

IMPERIAL

IMPERIAL COLLEGE LONDON

DEPARTMENT OF EARTH SCIENCE AND ENGINEERING

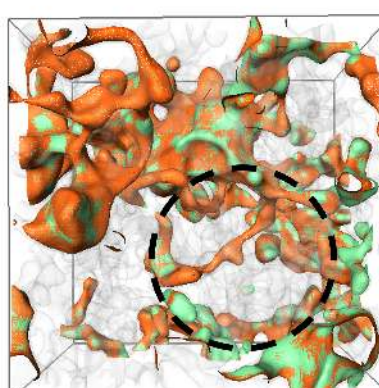
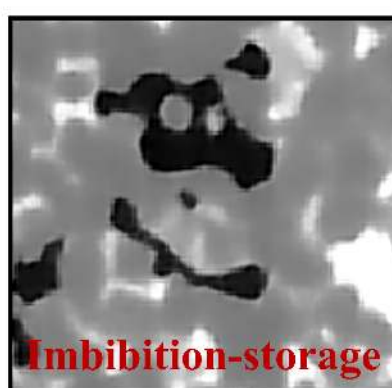
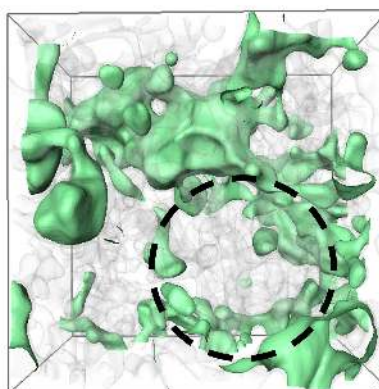
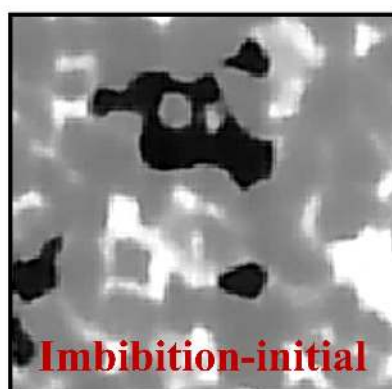
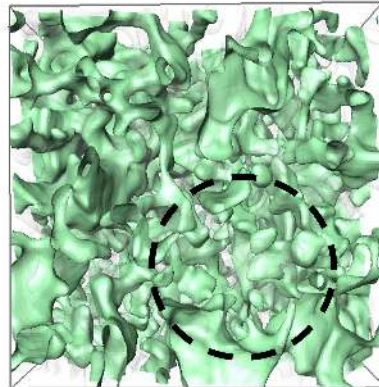
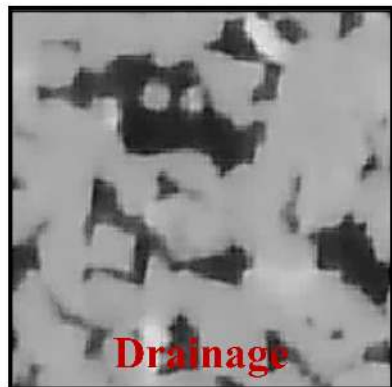
**Pore-Scale Investigation of Two-Phase Flow
Hysteresis in Hydrogen Storage Using
Micro-CT Imaging**

SEPIDEH GOODARZI

Supervisors: Prof. Martin J. Blunt
Dr. Branko Bijeljic

Submitted in partial fulfillment of the requirements for the degree of Doctor of Philosophy

May 2025



Hydrogen-initial

Hydrogen-16 h storage

Declaration of Originality

I hereby declare that the work presented in this thesis is my own and is the result of my own original research. I have not used any sources other than those referenced in the work. This thesis has not been previously submitted, either in whole or in part, for the award of any degree or diploma at any other educational institution. All quotations and paraphrases from other sources are properly cited and acknowledged. I confirm that this thesis complies with the rules and regulations of Imperial College London.

Sepideh Goodarzi, 2025

Copyright Declaration

© Sepideh Goodarzi, 2025. All rights reserved.

The copyright of this thesis rests with the author. Unless otherwise indicated, its contents are licensed under a Creative Commons Attribution 4.0 International License (CC BY). Under this license, you are free to copy, redistribute, and create derivative works of the material, provided that you credit the author and do not use it for commercial purposes. When sharing or adapting this work, you must make the license terms clear by naming the license and linking to its text. If you modify the work, indicate the changes made. For uses not covered under this license or permitted by UK Copyright Law, please seek permission from the copyright holder.

Creative Commons Attribution 4.0 International License) CC BY license

Abstract

With the increasing interest in hydrogen as a clean energy carrier, understanding its behaviour in subsurface porous media is essential for optimising geological storage systems. This PhD thesis investigates the pore-scale dynamics of hydrogen-brine systems, focusing on hysteresis, capillary pressure, and the role of Ostwald ripening in gas retention and connectivity. Traditional models—largely based on hydrocarbon systems—tend to overlook gas redistribution mechanisms like Ostwald ripening. This research addresses that gap by employing high-resolution X-ray tomography and Minkowski functionals to examine hydrogen behaviour in Bentheimer sandstone, offering new insights into gas-phase connectivity and trapping.

The work comprises three experimental investigations. The first study examined hydrogen and brine distribution during repeated injection and waterflooding cycles, with a 16-hour storage period. Results showed preferential hydrogen accumulation in larger pores and demonstrated that Ostwald ripening enhanced gas connectivity even in the absence of external flow. The second experiment focused on capillary pressure and saturation changes across three injection–flooding cycles. Residual gas saturation decreased from 40% in the first cycle to less than 18% by the third, suggesting reduced hysteresis relative to conventional expectations and reinforcing the significance of Ostwald ripening in mobilising trapped gas.

The final study extended the storage period to four days to observe longer-term effects on hydrogen distribution and connectivity. Using both hydrophilic and hydrophobic porous plates, contact angle measurements (50°) confirmed the water-wet nature of Bentheimer sandstone. Observations revealed a decrease in residual gas saturation from 85% after initial hydrogen injection to 22% after the third brine injection. These findings further highlight that hydrogen storage hysteresis is less pronounced than predicted by classical models.

By advancing the understanding of pore-scale fluid topology and gas connectivity, this thesis contributes important insights toward the design and optimisation of subsurface hydrogen storage systems, supporting the transition to cleaner energy solutions.

Acknowledgments

First and foremost, I would like to express my sincere appreciation to my supervisors, Prof. Martin Blunt and Dr. Branko Bijeljic, for their unwavering support and guidance throughout my PhD journey. Martin, your insightful ideas and direction were crucial to the accomplishments I achieved during my research. Your expertise and encouragement have profoundly shaped my academic path. Your belief in my potential has inspired me to strive for excellence, both in academia and beyond. Branko, I am deeply grateful for your mentorship and support throughout my PhD research and career development. Your constructive feedback and guidance have significantly enriched my academic experience and prospects.

I thank Shell through the Digital Rocks program and InFUSE Prosperity Partnership for funding this work. I am deeply grateful to Steffan Berg, Matthias Apple and Justin Freeman at Shell for their sponsorship and for believing in the importance of my research. Their support has enabled me to pursue my studies with dedication and focus.

To Dr. Yihuai Zhang, Dr. Sajjad Foroughi, Dr. Guanglei Zhang and Hussain M.A. Alzahrani and Waleed Dokhon, thank you for your collaboration, insightful discussions and camaraderie during our time at Imperial. Your contributions have enriched my research experience.

Many thanks to my dad and mum, your unwavering support and encouragement have been my guiding light throughout this journey. Despite the distance, your belief in me never wavered, and your love gave me the strength to pursue my dreams. To my dear sister, *Beh Dokht*, and brothers, your constant encouragement and understanding have meant the world to me. I am deeply grateful for your support, even from afar, and I am filled with joy knowing that I have made you proud. This thesis is a testament to the love and support I have received from each of you.

Finally, I would love to say thank you to my love, *Amin*, for your unwavering support, belief in me, and love that have been my strength. In every challenge, you've stood by me, encouraging me to reach for my goals. Your faith in my abilities has been my guiding light. Thank you for being my partner, confidant, and greatest supporter.

Dedication

To my dad—for your quiet strength, the values you passed on, and for always believing in me, even when I didn't believe in myself. And to my love—for being my calm, my constant, and my biggest cheerleader, even when I was too stressed to appreciate it. I carried your love with me every step of the way—and still, I owe you both more than I can ever say.

Table of Contents

Declaration of Originality	ii
Copyright Declaration	iii
Abstract	iv
Acknowledgments	v
Dedication	vi
List of Figures	xxii
List of Tables	xxiv
List of Symbols	xxv
List of Abbreviations	xxvii
List of Publications	xxviii
1 Introduction	1
1.1 Global Energy Demands	1
1.2 Grey, Blue and Green Hydrogen	4
1.3 Requirements and Infrastructure	5
1.4 Hydrogen Storage in Porous Media	7
1.4.1 Challenges	8
1.5 Research Motivation	10
1.6 Aim and Objectives	10
1.7 Structure of the Study	11
2 Scientific Background	12
2.1 Theory	12
2.1.1 Darcy's Law	12
2.1.2 Porosity and Fluid Saturation	14
2.1.3 Interfacial Tension and Capillary Number	14

Table of Contents

2.1.4	Wettability and Contact Angle	16
2.2	Fluid Flow in Porous Media	18
2.2.1	Hysteresis	18
2.2.2	Two-Phase Flow	19
2.2.2.1	Capillary Pressure and Saturation	19
2.2.2.2	Interfacial Area	20
2.2.2.3	Pore Size Distribution	21
2.2.3	Gas Trapping and Movement	22
2.2.3.1	Ostwald Ripening	22
2.2.3.2	Péclet Number	24
2.2.3.3	Minkowski Functionals	24
2.3	X-ray Imaging	25
2.3.1	Micro Computed Tomography	25
2.3.2	Synchrotron Tomography	27
2.4	Literature Review	28
2.4.1	Two-phase Flow	28
2.4.2	Distribution of Hydrogen at the Porescale	29
2.4.3	Hydrogen-Wettability	29
2.4.4	Capillary Pressure	30
2.4.5	Hysteresis	30
2.4.6	Ostwald Ripening	33
2.5	Research Questions	34
2.5.0.1	Scientific Significance	35
3	Trapping, Hysteresis and Ostwald Ripening in Hydrogen Storage	38
3.1	Summary	38
3.2	Materials and Methods	38
3.2.1	Rock Sample	38
3.2.2	Fluid Properties	40
3.2.3	Sample Preparation	40
3.2.4	Experimental Procedure	41
3.2.5	Image Acquisition	43
3.2.6	Image Processing	43
3.3	Results and Discussion	45
3.3.1	Three-dimensional Raw Images	45
3.3.1.1	Greyscale Images	45
3.3.1.2	Segmented Images	45
3.3.2	Analysis of Discrete Ganglia	47
3.3.3	Gas Saturation Profile	49
3.3.4	Capillary Pressure Analysis	51
3.3.5	Measurement of Interfacial Area	51

Table of Contents

3.3.6	Fluid Connectivity and Péclet Number	53
3.3.7	Pore and Throat Occupancy	55
3.4	Health and Safety	58
3.4.1	Hydrogen Hazards	58
3.4.2	Storage and Handling of Hydrogen	59
3.4.3	Safety Protocols for Brine	59
3.4.4	X-ray Safety Considerations	60
3.5	Final Remarks	60
4	Ostwald Ripening Leads to Less Hysteresis during Hydrogen Injection and Withdrawal	62
4.1	Summary	62
4.2	Materials and Methods	63
4.2.1	Porous Plate Disc	63
4.2.2	Equilibrating Brine with Gas	63
4.2.3	Rock and Fluid Properties	64
4.2.4	Experimental Procedure	65
4.2.5	Image Processing	67
4.3	Results and Discussion	69
4.3.1	Raw Greyscale Images	70
4.3.2	Fluid Configuration and Connectivity	71
4.3.3	Quantification of Capillary Pressure	75
4.3.4	Gas Saturation Profile	77
4.3.5	Wettability Characterisation	79
4.3.5.1	Specific Interfacial Area	79
4.3.5.2	Pore and Throat Occupancy	80
4.4	Health and Safety	80
4.5	Final Remarks	82
5	Pore-scale Insights into Wettability and Curvature for Hydrogen Storage	84
5.1	Summary	84
5.2	Materials and Methods	85
5.2.1	Discs, Rock and Fluid Properties	85
5.2.2	Experimental Procedure	85
5.2.3	Image Acquisition and Processing	88
5.3	Results and Discussion	91
5.3.1	Redistribution of Gas During Long-Term Storage	91
5.3.1.1	Fluid Connectivity	91
5.3.2	Wettability in a Brine-Hydrogen System	95
5.3.2.1	Contact Angles	95
5.3.2.2	Pore and Throat Occupancy Maps	97

Table of Contents

5.3.3	Minkowski Functionals	100
5.3.3.1	Gas Saturation Profile	100
5.3.3.2	Interfacial Area	101
5.3.3.3	Curvature Distributions	102
5.3.3.4	Capillary Pressure Analysis	104
5.4	Health and Safety	106
5.5	Final Remarks	106
6	Conclusions and Future Work	107
6.1	Conclusions	107
6.2	Future Work	109
Bibliography		128
A	Scientific Background	129
B	Trapping, Hysteresis and Ostwald Ripening in Hydrogen Storage ...	130
B.1	Sample preparation	130
B.2	Absolute permeability measurement	130
B.3	PEEK tubing, valves, and pumps	131
B.4	Differential pressure measurement	131
B.5	Micro computed tomography	132
B.6	Micro-CT scanning parameters	133
C	Ostwald Ripening Leads to Less Hysteresis during Hydrogen Injection ...	135
C.1	Reactor	135
C.2	Bubble size and cumulative distribution	136
C.3	Pore and throat occupancy	137
D	Pore-scale Insights into Wettability for Hydrogen Storage	139
D.1	Image processing	139

List of Figures

1.1	CO ₂ emissions associated with different energy sources, highlighting the significant contributions of oil, coal, and gas to global carbon emissions [1].	2
1.2	Great Britain's daily energy consumption (in GWh) from August 2021 to June 2024, showing the seasonal variation in gas usage, electricity demand, and renewable energy generation. The figure illustrates the significant fluctuations in energy demand across different months, with peaks during colder periods due to increased heating needs. The data also highlights the relatively stable transport energy usage and the growing yet variable contribution of renewable energy to the overall energy mix [2].	3
1.3	The three primary methods of hydrogen production—Grey, Blue, and Green Hydrogen. Grey Hydrogen is produced from natural gas or coal through steam reforming and gasification, resulting in CO ₂ emissions. Blue Hydrogen follows a similar process but incorporates Carbon Capture and Storage (CCS) technologies to reduce CO ₂ emissions. Green Hydrogen is produced via the electrolysis of water using renewable electricity, resulting in the emission-free production of hydrogen and oxygen [3].	4
1.4	Energy storage capacity in the UK as of 2019 across various technologies, using a logarithmic scale. The graph illustrates the existing energy storage capabilities and highlights the significant gap that needs to be addressed to meet future hydrogen storage requirements [4].	5
1.5	Map showing "Global Hydrogen Storage Projects Underway," highlighting regions where hydrogen storage is prioritized. The map illustrates global efforts to expand hydrogen infrastructure, with salt caverns (blue) and depleted gas fields (pink) as key storage methods. These projects underscore the strategic importance of hydrogen storage in supporting the transition to a low-carbon energy system, with ongoing developments across Europe, North America, and other regions [1, 5].	6
1.6	Illustration of underground hydrogen storage from renewable energy sources, showcasing various geological formations used for storage, including salt caverns, depleted hydrocarbon reservoirs, and saline aquifers. The image highlights the integration of wind and solar energy generation with hydrogen production via electrolysis, its distribution, and storage in underground structures to balance energy supply and demand [6].	7

1.7	Key challenges in underground hydrogen storage (UHS) within porous reservoirs, including geochemical interactions between hydrogen and brine, hydrodynamic processes such as gravity segregation and viscous fingering, dispersion and mixing with cushion or residual gases, and the influence of microbial activity on hydrogen purity and reservoir conditions [7].	9
2.1	An illustration of a cylindrical core sample used to determine the absolute permeability of a rock using Darcy's law. Where K is the permeability, A is the cross-sectional area, L is the length of the sample, Q is the volumetric flow rate, and P_1 and P_2 are the pressures at the inlet and outlet, respectively.	13
2.2	Example of relative permeability curves for primary drainage, imbibition, and secondary drainage for an oil-water system, showing a distinct hysteresis effect, evident from the difference between the drainage and imbibition curves for both water and oil [8]. This hysteresis is due to the differing pore-scale displacement mechanisms and fluid distribution during the two processes. The arrows indicate the direction of saturation change for each phase.	13
2.3	Examples of flat, positive and negative curvatures. The principal radii of curvature of this interface are denoted as R_1 and R_2	16
2.4	The wettability states of an oil droplet on a solid surface with water as the surrounding phase. The contact angle θ is measured through the water. Contact angles below 90° indicate a water-wet system, while those above 90° indicate an oil-wet system.	17
2.5	Visualisation of a contact angle (60°) using automated code, identifying the same point in the data visualisation software, and comparing it to a manual contact angle measurement at the same location (61°) [9].	17
2.6	Hysteresis behaviour illustrated in input-output graphs. The left graph shows a smooth hysteresis loop where the output w lags behind the input u , resulting in a delay and looping behaviour. The right graph represents an idealized rectangular hysteresis loop, highlighting two distinct process paths (ρ_1 and ρ_2) that do not follow the same track, illustrating the system's nonlinearity and memory effect [10].	19
2.7	Schematic of pore bodies and pore throats in a gas/water system. The diagram illustrates the larger pore spaces known as pore bodies and the narrow constrictions called pore throats that interconnect them, highlighting the pathways for fluid flow and storage within the rock matrix.	21
2.8	Schematic illustration of Ostwald ripening. Differences in local capillary pressure lead to differences in the concentration of dissolved gas and result in concentration gradients in the aqueous phase and diffusion of dissolved gas away from regions of high capillary pressure.	22
2.9	Continuous image projected onto a sensor array (discretised values), (1) 2D and (2) 3D.	26

2.10 Diagram of a micro-CT system. The X-ray source, rotating sample stage, and flat-panel detector are shown, illustrating how the instrument generates radiographic projections of a rock sample. These projections are then reconstructed into tomographic images and 3D voxel data for detailed analysis [11, 12].	27
2.11 A schematic of the traditional model of hysteresis in capillary pressure. It is assumed that subsequent displacements, regardless of starting and finishing capillary pressure and the order of imbibition and drainage, cannot lie in the capillary pressure-saturation plot outside the bounds indicated for imbibition and secondary drainage. We will show that Ostwald ripening facilitates the repositioning of gas within the pore space, leading to reduced trapping and capillary pressures that lie outside these bounding curves.	31
3.1 Comparison of three commonly used sandstone types in experimental studies. The top row shows macroscopic views of Berea sandstone (a), Fontainebleau sandstone (b), and Bentheimer sandstone (c), highlighting differences in texture and colouration. The bottom row shows microscopic views or pore structures, illustrating variations in grain shape, size, and porosity [13].	39
3.2 Three contrast scan images for the injection of deionised water-Potassium Iodide solutions (2.5 wt.% -, 3.5 wt.% - and 4.5 wt.% -KI) into a Bentheimer sample.	40
3.3 A schematic diagram for the two-phase hydrogen-brine experiment conducted with the X-ray microtomography scanner (micro-CT). The arrangement of the core holder, pumps, flow lines, valves, and pressure transducer used in the experiment are represented in the diagram. The micro-CT enclosure is indicated by the black dashed line.	42
3.4 Schematic illustrating the stitching of six overlapping sections to produce a complete 3D image of the Bentheimer sandstone sample. Each section was scanned with an overlap to ensure high-resolution reconstruction. The resulting images achieved a spatial resolution of $5.8 \mu\text{m}/\text{voxel}$. A selected subsection, with dimensions of $2069 \times 2187 \times 1142$ voxels, was extracted for further detailed analysis in this study to investigate localised pore-scale features.	44
3.5 Two-dimensional cross-sections of three-dimensional raw images of the Bentheimer sample before and after the three cycles of hydrogen injection (drainage) and water flooding (imbibition): the rock, gas and brine are medium grey, black and light grey, respectively.	46
3.6 Two-dimensional cross-sections of three-dimensional raw images of the Bentheimer sample before and after 16 hours of undisturbed gas storage. The blue dashed circles indicate gas shrinkage, while the red dashed circles highlight increased gas connectivity. Arrows emphasise the redistribution of gas within the pore space, revealing the effects of Ostwald ripening over time.	46

3.7	Two-dimensional cross-sections of three-dimensional raw images of the Bentheimer sample before and after 16 hours of undisturbed gas storage. The dashed circles highlight regions where gas redistribution occurs over time, which enhances phase connectivity.	47
3.8	3D visualisation of hydrogen gas distribution within the pore space during the first and second cycles of gas injection (drainage) and subsequent water flooding (imbibition). Distinct colours represent individual hydrogen gas ganglia, illustrating their distribution and size. After 16 hours of storage, the ganglia experience growth, leading to improved connectivity and the formation of larger, interconnected pathways. This enhanced connectivity is particularly visible in the zoomed-in regions on the right, where the hydrogen gas, depicted in green, occupies a more continuous and connected structure within the pore network.	48
3.9	The volume-weighted size distribution of gas ganglia, analysed in the sub-volume, reveals a significant shift towards larger ganglia spanning multiple pores after gas injection and imbibition, while the total gas volume remains approximately constant. The distributions are shown for the first (a,b) and second (c,d) cycles of gas and brine injection, using a uniform bin size in logarithmic space. The grey-shaded area represents the volume distribution of all the pores.	49
3.10	Cumulative volume distribution of hydrogen gas ganglia within the sub-volume near the top of the sample is presented for the first (a,b) and second (c,d) cycles of gas and brine injection. Over time, smaller bubbles gradually merge or dissipate, contributing to the growth of larger ganglia spanning multiple pores. Although the total gas volume remains approximately constant, the curves illustrate the transition towards a more connected gas structure. The vertical segment in the cumulative curve after 16 hours indicates the dominance of a single large ganglion, which enables hydrogen withdrawal through a continuous pathway.	50
3.11	Gas saturation profile measured from segmented images during three cycles of gas injection and water flooding at different gas flow rates and a constant water injection rate along the length of a Bentheimer sample. Gas is dissolved near the inlet after the water flooding stages. The subsection studied for further analysis is shown by the black dashed line.	50
3.12	The gas saturation profile of a sub-volume located near the top of the sample during three cycles of gas and water injection, including both the initial injection and after an additional 16-hour storage period. The region considered is indicated by the black dashed box in Fig. 3.11.	51
3.13	Capillary pressure values as a function of water saturation, derived from the mean interfacial curvature during gas injection and water flooding cycles. Different shades represent drainage and imbibition phases, with paired shaded markers (initial vs. 16-hour storage) indicating temporal variations. Dashed lines connect the initial and storage steps. The error bars reflect uncertainties arising from image segmentation in both capillary pressure and water saturation measurements.	52

3.14 The interfacial areas per unit volume for water-solid, gas-solid and gas-water in a voxel subvolume during three cycles of gas injection (D= Drainage) and water flooding (I= Imbibition), including both the initial stage and after an additional 16-hour storage period.	52
3.15 A two-dimensional cross-section of the dry scan of the Bentheimer sandstone sample (a), alongside segmented images showing the pore space (b) and solid grain distribution (c). These visualisations, derived from X-ray imaging, were used for pore-network analysis. The graph on the right (d) presents the probability distributions of pore and throat radii, characterising the structural variability of the sandstone's pore network.	55
3.16 Volume-weighted histograms of gas and water occupancy as a function of pore and throat radius, analysed during the first cycle of gas injection following water flooding. The first row (a-d) and third row (i-l) depict the probability distributions of pore and throat radii across different flow stages, while the second row (e-h) and fourth row (m-p) illustrate the corresponding volume fraction distributions. Green represents gas (hydrogen), blue represents water, and grey indicates the overall size distribution of all pores and throats. Each column corresponds to a specific stage of the process, comparing the initial state of injection and the state after a 16-hour storage period for drainage and imbibition.	56
3.17 Volume-weighted histograms of gas and water occupancy as a function of pore and throat radius, analysed during the second cycle of gas injection following water flooding. The first row (a-d) and third row (i-l) depict the probability distributions of pore and throat radii across different flow stages, while the second row (e-h) and fourth row (m-p) illustrate the corresponding volume fraction distributions. Green represents gas (hydrogen), blue represents water, and grey indicates the overall size distribution of all pores and throats. Each column corresponds to a specific stage of the process, comparing the initial state of injection and the state after a 16-hour storage period for drainage and imbibition.	57
3.18 Comparison of volume-weighted histograms showing gas occupancy distributions as a function of pore and throat radii during the first cycle of gas and water injections, highlighting differences between initial conditions and after 16 hours of storage.	58
4.1 Schematic of the hydrophilic porous plate used in the experiment, highlighting key features. Grooves were added to enhance water distribution, and Peek tubing was incorporated for differential pressure measurement. The inset illustrates the plate's pore structure and the water-wetting properties, depicted by the contact angle (θ).	63

4.2	Porosity distribution along the length of a Bentheimer sandstone sample (60 mm in length), demonstrating a relatively uniform porosity profile. The porosity values were derived through imaging techniques, with an associated error of 0.05% due to image segmentation processes. The slight variations observed are attributed to inherent heterogeneities in the sample and the precision of the imaging methodology.	64
4.3	Schematic of the experimental apparatus used in the study. The diagram highlights the arrangement of the flow cell, injection and receiving pumps, multiphase and confining flow lines, and the pressure transducer. The dashed box marks the micro-CT exposure region, where high-resolution imaging of the flow processes was conducted	67
4.4	A small section of two-dimensional raw greyscale images is shown the raw (a) and after filtering (b). Segmentation (c) highlights distinct phases: hydrogen gas (green), brine (blue), and rock (grey). The three-dimensional subvolume (right) visualises the distribution of hydrogen and brine within the pore space of Bentheimer sandstone.	68
4.5	Schematic representation of the Bentheimer sandstone sample used for analysis. The full sample has a height of 60 mm and a diameter of 12 mm. A subsection scan (14 mm \times 12 mm \times 12 mm) was extracted for further analysis, as shown in the magnified region. Within this subsection, a smaller volume (140 \times 166 \times 40 voxels) was selected for a closer examination of fluid distribution within the solid rock structure.	69
4.6	Two-dimensional slices of three-dimensional raw images from the sandstone sample illustrate changes observed before and after a 16-hour storage period. In these images, rock is depicted in medium grey, gas in black, and brine in light grey.	70
4.7	Two-dimensional cross-sectional views of the segmented three-dimensional images depicting the gas, brine, and rock phases in green, blue, and grey, respectively, for the first cycle at the initial state and after 16 hours of storage. The dashed lines highlight regions where noticeable rearrangements of the gas phase have occurred, leading to changes in connectivity.	71
4.8	The three-dimensional images illustrate the distribution of hydrogen within the pore space following three cycles of gas and water injections (D= Drainage, I= Imbibition). Diverse colours distinguish discrete gas ganglia: after a 16-hour storage, these ganglia merge, resulting in improved connectivity. The presence of connected ganglia, highlighted with a black arrow, demonstrates the influence of storage on hydrogen redistribution and pore-scale connectivity.	72

4.9	Zoomed-in images of the gas phase structures after initial displacement and then after waiting for 16 hours. The lighter green shade represents the gas arrangement and connections at the initial stage. The darker green shade displays how the configuration of gas changed after being left undisturbed for 16 hours (the red dashed circles). This comparison visually highlights the improved connections between the gas phase due to Ostwald ripening. (D= Drainage, I= Imbibition) .	73
4.10	The volume-weighted size distribution (a, b) and cumulative volume distribution (c, d) of ganglia are shown for the third cycle of gas and brine injection. The graphs compare the initial stage with the distribution after 16 hours of storage. The shaded grey area represents the volume distribution across all pores. A distinct vertical segment in (b) and a highlighted region in (d) indicate the emergence of a single large ganglion, which dominates the volume after storage.	74
4.11	Measured differential pressures during the three drainage cycles, corresponding to capillary pressure endpoints of 20, 9, and 3 kPa, following gas injection. The results indicate consistent pressure stabilisation over the last 12 hours at each injection.	75
4.12	Estimated capillary pressure for drainage and imbibition measured on a 600^3 voxel subvolume near the top of the sample. The black lines show independent experimental measurements in the literature where Ostwald ripening is not considered [14]. The points are our measurements and the error bars represent the uncertainty in the determination of capillary pressure and saturation from the segmented images.	76
4.13	The gas saturation profile averaged along the flow direction during three cycles of hydrogen injection and water flooding across the length of a Bentheimer sample, illustrating both the initial injection and after a 16-hour waiting period. The black dashed line indicates the specific subsection selected for detailed analysis. .	77
4.14	Illustration of the variation in gas saturation profiles for sandstone samples from the literature: Higgs et al. [15], Yekta et al. [16], Boon and Hajibeygi [17], Goodarzi et al. [18], Thaysen et al. [19], Jha et al. [20] and Boon et al. [21] including the present study. The error bars represent the uncertainty due to image segmentation.	78
4.15	Measurements of interfacial area per unit volume between fluid-fluid and fluid-solid phases within a subvolume over three cycles of gas and water injection (D= Drainage, I= Imbibition). Results are presented for both the initial stage and after a 16-hour storage period, alongside gas saturation trends. Error bars indicate uncertainties in image segmentation.	79

4.16 The probability distribution of pore and throat radii occupied by hydrogen (green) and water (blue) is shown for the first cycle. (a)-(c) and (g)-(i) show the initial occupancy immediately after imbibition and after 16 hours, highlighting the redistribution of fluids within pores and throats. (d)-(f) and (j)-(l) illustrate the volume fraction of hydrogen and water as a function of pore and throat size, demonstrating the extent of gas entrapment and subsequent fluid redistribution over time.	81
4.17 Comparison of volume-weighted histograms show the probability distribution of pore (a) and throat (b) radii occupied by water immediately after imbibition (pink) and after 16 hours (striped). The histograms illustrate a shift in gas occupancy, particularly in smaller pore and throat sizes, indicating redistribution over time.	82
5.1 Illustration of hydrophilic and hydrophobic porous plates. The hydrophilic plate, depicted on the left (a), allows water to pass through while acting as a barrier to gas. The hydrophobic plate, shown on the right (b), repels water, ensuring it remains confined within the rock sample. Insets highlight the pore structure of each plate, with the respective wetting properties depicted by contact angles (θ) of water.	85
5.2 Schematic representation of the two-phase hydrogen-brine experiment using an X-ray micro-CT scanner. The setup includes the core holder, pumps, flow lines, valves, pressure transducer, and hydrophilic and hydrophobic porous plates. Hydrogen gas is injected from the top, while brine, equilibrated in the stirred reactor, is injected from the bottom. The micro-CT scanning region is highlighted within the black dashed enclosure.	87
5.3 Illustration of the rock sample scanned using the Heliscan micro-CT scanner. The full-length scan was obtained at $4.68\ \mu\text{m}$ resolution, while a high-resolution region of interest (ROI, $12\ \text{mm} \times 5\ \text{mm}$) was scanned at $3.04\ \mu\text{m}$ resolution for detailed analysis. The zoomed region highlights the enhanced resolution, facilitating pore-level investigations.	89
5.4 Visualisation of fluid distribution in a porous rock sample during drainage, initial imbibition, and after four days of storage. The top row (a-c) presents greyscale segmented images, where rock appears in grey, brine in light grey, and gas in dark regions. The middle row (d-f) shows phase-segmented images highlighting brine in blue and hydrogen gas in green within the rock pores. The bottom row (g-i) isolates the hydrogen phase, illustrating gas redistribution over time. During drainage (a, d, g), hydrogen is initially dispersed within the pores. Upon imbibition (b, e, h), brine invades, partially displacing hydrogen. After four days of storage (c, f, i), Ostwald ripening causes smaller gas clusters to dissolve and redeposit into larger connected clusters, enhancing hydrogen connectivity. Coloured arrows in (g-i) indicate regions where gas rearrangement has occurred.	90

5.5	A small section of two-dimensional raw greyscale images, highlighting gas structure and connectivity evolution over time. The top row (a–c) represents the initial stage, while the bottom row (d–f) shows the same region after four days of storage. Images were captured using X-ray tomography at three different resolutions: (a, d) $3.04\ \mu\text{m}/\text{voxel}$, (b, e) $4.68\ \mu\text{m}/\text{voxel}$, and (c, f) $9.37\ \mu\text{m}/\text{voxel}$. The greyscale intensity distinguishes brine (light grey), rock matrix (medium grey), and hydrogen gas (dark regions). Over four days, Ostwald ripening led to an increase in gas-phase connectivity and structural coalescence, as observed in the dark regions.	92
5.6	Structural evolution of hydrogen gas ganglia during storage, visualised through sequential 3D scans over four days. Panels (a–e) illustrate the progressive morphological changes of the hydrogen ganglia at key intervals: after water injection, 24 hours, 48 hours, 72 hours and 96 hours. The dashed red circle highlights regions where connectivity increases due to the Ostwald ripening process, resulting in larger, more interconnected ganglia over time.	92
5.7	Three-dimensional visualisation of gas and water distributions in the sample at various stages of the experiment such as after gas injection, first water flooding, and second water flooding. The last column (After 4 days) demonstrates structural changes in the gas phase after storage. The distinct colours represent individual clusters of the gas and water phases, highlighting their spatial distribution and connectivity within the pore space. The grey colour arrows show the direction of fluid injection.	93
5.8	Cumulative volume distribution of gas ganglia after gas injection (a) and water flooding (b–d), during the initial stage and after 4 days of storage. Each curve represents the cumulative gas volume as a function of ganglia size, highlighting the redistribution of gas. The vertical line observed after 4 days of storage indicates the dominance of a single large ganglion, resulting from the dissolution of smaller clusters and reprecipitation onto larger ones through Ostwald ripening.	95
5.9	Two-dimensional visualisation of hydrogen and brine distributions within Bentheimer sandstone during gas injection and successive water flooding cycles. The figure illustrates different experimental stages, beginning with gas injection (G1), followed by first water flooding (WF1), second water flooding (WF2), and third water flooding (WF3). The blue regions represent the water phase, while the green regions indicate the gas phase. Key transitions are annotated to track the evolution of fluid distribution over time.	96
5.10	Probability density functions of contact angles during imbibition are shown in (a) and (b), indicating a predominantly water-wet system. (c) provides visual confirmation through CT-based visualisations of a zoomed-in subvolume. The bottom row shows a side-by-side comparison before and after 4 days, reinforcing that brine preferentially coats pore walls while hydrogen remains in the pore centre, with minimal wettability alteration over time.	97

5.11 Probability distribution of pore sizes occupied by gas and brine, along with the corresponding volume fractions, after water injection. The comparison between the initial stage (a-c) and after four days of storage (g-i) highlights fluid redistribution. The volume fraction of gas and brine in the pores is shown in (d-f) for the initial stage and (j-l) for the four-day storage period, illustrating the increasing brine occupancy over time.	98
5.12 Probability distribution of throat sizes occupied by gas and brine, alongside their respective volume fractions, following water injection. The initial stage (a-c) and after four days of storage (g-i) show how brine gradually invades larger throats. The volume fraction of gas and brine in the throats is depicted in (d-f) for the initial stage and (j-l) for the four-day storage period, highlighting the role of capillary forces in fluid redistribution.	99
5.13 The gas saturation profile averaged along the flow direction during cycles of hydrogen injection and water flooding across the length of a Bentheimer sample, illustrating both the initial injection and the state after a 4-day waiting period (storage). The results highlight the role of porous plates in enhancing gas retention and achieving a more uniform saturation profile, while also minimising capillary end effects. Minor fluctuations observed after storage are attributed to gas redistribution driven by Ostwald ripening.	100
5.14 Illustration of the normalised frequency distribution of mean curvature following (a) gas injection and (b) water flooding in a Bentheimer sandstone. The mean curvature is classified into three categories: mixed curvature ($k_1 k_2 \leq 0$) represented in green, convex structures ($k_1 > 0, k_2 > 0$) shown in pink and concave structures ($k_1 < 0, k_2 < 0$), depicted in blue. The overall mean curvature distribution is represented by the grey line.	102
5.15 Mean curvature distribution of hydrogen-brine interfaces before (orange) and after four days of storage (blue) following water flooding. The histogram shows a slight narrowing of the curvature distribution over time, suggesting fluid redistribution and interface relaxation due to Ostwald ripening. This process results in smoother and more connected gas ganglia. The insets (a) and (b) provide 3D visualisations of the extracted interface between hydrogen (green) and brine (blue) within the pore space at the initial and post-storage stage, respectively.	103
5.16 Measured capillary pressure evolution during drainage and successive imbibition cycles, with a precision of ± 0.03 kPa. The drainage phase shows an initial stabilisation at 14.2 kPa with a gas saturation of 0.85 (a). During subsequent imbibition cycles (b-d), capillary pressure and gas saturation progressively decrease, indicating improved fluid connectivity and reduced gas trapping. A 2% error applies to the gas saturation due to the segmentation method.	104

5.17	Estimated capillary pressure for drainage and imbibition measured on a 600^3 voxel subvolume in the middle of the sample. The black lines represent independent experimental measurements from the literature [14, 22] where Ostwald ripening is not considered. The data points correspond to our direct pressure measurements and curvature-derived values, with error bars indicating uncertainty in the determination of capillary pressure and saturation from segmented images. The results demonstrate a reduction in hysteresis in later imbibition cycles, attributed to enhanced gas redistribution and pore-scale connectivity.	105
A.1	Diamond Light Source building, a large ring-shaped facility that accelerates electrons to produce intense beams of synchrotron light, enabling the study of atoms and molecules in extraordinary detail [23].	129
B.1	Example of a rubber sleeve (Viton, nitrile, or silicone) used for enclosing the sample, sealed with PTFE tape to prevent gas leakage and Aluminium foil at the ends for additional sealing. This setup ensures a secure environment for the experimental process, minimising fluid and gas escape.	130
B.2	Pressure transducer (Keller PD-33X) used in the experiments. The left side shows a sketch of the setup with dimensions in millimetres, while the right side shows the actual pressure transducer used for measuring pressure during the experiments [24].	132
B.3	Images of the two advanced micro-CT scanners used in this study. Left: The Zeiss Xradia 510 X-ray Scanner, equipped with a flat-panel detector. Right: The Heliscan micro-CT scanner, featuring a helical scanning setup with an X-ray source, detector, and sample platform, enabling seamless imaging without artifacts.	133
C.1	Parr Instrument Company Bench Top Reactor, featuring a 1L capacity chamber and advanced controls for precise temperature and pressure adjustments. This reactor is designed for high-pressure and high-temperature experiments, ensuring reliable and safe operation in laboratory settings [25].	135
C.2	The volume-weighted size distribution of ganglia is illustrated for the two cycles of gas and brine injection, with a uniformly spaced bin size in logarithmic space. These graphs compare the initial stage with the distribution after 16 hours of storage. The shaded grey area represents the volume distribution across all pores.	136
C.3	The cumulative volume distribution of ganglia is illustrated across two cycles of gas and brine injection. These graphs compare the initial stage with the distribution after 16 hours of storage. A distinct vertical segment indicates the emergence of a single large ganglion, which dominates the volume following the storage period.	136
C.4	Volume-weighted histograms of gas occupancy as a function of pore radius, plotted for the second cycle of gas injection following water flooding. Green indicates gas, blue indicates water, and grey represents the size distribution of all pores. Each plot corresponds to a specific cycle of injection and flooding, shown for both the initial stage and after a 16-hour storage period.	137

C.5	Volume-weighted histograms of gas occupancy as a function of pore radius, plotted for the third cycle of gas injection following water flooding. Green indicates gas, blue indicates water, and grey represents the size distribution of all pores. Each plot corresponds to a specific cycle of injection and flooding, shown for both the initial stage and after a 16-hour storage period.	138
D.1	Two-dimensional cross-sections of three-dimensional raw images of the Bentheimer sandstone sample showing the distribution of rock, gas and brine during three cycles of hydrogen and brine injection. The images compare initial and post-4-day stages for each cycle, with a scale bar representing 3222 μm	139

List of Tables

1.1	Physical properties of hydrogen [26].	8
2.1	Summary of published pore-scale hydrogen displacement in sandstone and experimental conditions.	36
3.1	Thermophysical properties of the fluids used in the experiment, including density (ρ) measured at ambient temperature, dynamic viscosity (μ), and interfacial tension (σ). The values for brine are sourced from [27,28], while hydrogen properties are obtained from [29].	40
3.2	Capillary numbers, $Ca = \mu q / \sigma$, where μ is the viscosity of the injected fluid, σ is the interfacial tension, and q is the Darcy velocity for the flooding cycles.	41
3.3	Summary of scanning parameters for the Zeiss X-ray microtomography scanner used in the experiment. Initial scans include dry, wet, gas injection, and water injection steps, each comprising six overlapping sections to cover the entire sample length. After 16 hours, additional detailed scans of sections 2 and 5 were performed to monitor localised changes over time.	43
3.4	The Euler characteristic of a gas undergoing an unsteady-state two-phase experiment, both for the initial state and after 16 hours, following three cycles of hydrogen and brine injection. The results indicate that higher Euler characteristic values correspond to lower gas phase connectivity, with imbibition steps generally showing less connectivity compared to drainage steps. Over time, the decreasing values suggest an increase in gas phase connectivity.	54
3.5	The Péclet number, Eq. (2.20), for gas undergoing an unsteady-state two-phase experiment, presented for three cycles of hydrogen and brine injection. The results demonstrate a significant decrease in the Péclet number during imbibition steps compared to drainage steps, indicating that diffusion plays a dominant role in mass transport during imbibition. The first drainage cycle exhibits the highest Péclet number, suggesting that advective transport is more significant in this phase. In subsequent cycles, lower Péclet values suggest an increasing contribution of diffusive transport relative to advection.	54

4.1	Thermophysical properties of the fluids used in the experiment, including density (ρ) measured at ambient temperature, dynamic viscosity (μ), and interfacial tension (σ). The values for brine are sourced from [27,30], while hydrogen properties are obtained from [29,31].	65
4.2	Capillary numbers, $Ca = \mu q / \sigma$, where μ is the viscosity of the injected fluid, σ is the interfacial tension, and q is the Darcy velocity for the flooding cycles. . . .	66
4.3	Summary of scanning parameters for the Zeiss X-ray microtomography scanner used in the experiment. Initial scans include dry, wet, gas injection, and water injection steps, each comprising six overlapping sections to cover the entire sample length. After 16 hours, additional detailed scans of sections 1 to 6 were performed to monitor localised changes over time.	68
4.4	Normalised Euler characteristic [mm^{-3}] throughout three cycles of hydrogen and brine injection, capturing the initial state and the subsequent 16-hour storage period.	75
5.1	Capillary numbers, $Ca = \mu q / \sigma$, where μ is the viscosity of the injected fluid, σ is the interfacial tension, and q is the Darcy velocity for the flooding cycles. . . .	88
5.2	Summary of scanning parameters for the Heliscan micro-CT scanner used in the experiment. Two scanning modes were employed: a full-length helical scan to capture overall saturation distribution and volumetric assessments, and a high-resolution region-of-interest (ROI) scan to focus on detailed pore-level investigations. The scanning parameters, including exposure time, projections, total time, and voxel resolution for each mode, are detailed in the table.	88
5.3	Normalised Euler characteristic [mm^{-3}] throughout hydrogen and brine injections, capturing the initial state and the subsequent 4-days storage period. . . .	94
5.4	Interfacial area per unit volume and gas saturation at different stages of drainage (G) and imbibition (WF). Gas saturation (S_g) and interfacial areas between gas-solid (a_{gr}), gas-water (a_{gw}) and water-solid (a_{wr}) are measured in $1/\text{mm}$. Results are presented for both the initial stage and after a 4-days storage period.	102

List of Symbols

Latin symbols	Meaning	SI unit
C	Concentration	$mol \cdot m^{-3}$
Ca	Capillary number	—
Cf	Connectivity functional	—
D	Diffusion coefficient	$m \cdot s^{-2}$
Ec	Euler characteristic	—
g	Acceleration to gravity	$m \cdot s^{-2}$
H	Henry's constant	$mol \cdot (m^3 \cdot Pa)^{-1}$
F	Diffusive flux	$mol \cdot s^{-1}$
I	Intensity	—
k_{eff}	Effective permeability	m^2
k_r	Relative permeability	m^2
K	Absolute permeability	m^2
l	characteristic length	m
L	Sample length	m
M	Characteristic diffusion length	m
n	Number of gas moles in the ganglion	—
P	Pressure	Pa
P_c	Capillary pressure	Pa
Pe	P'eclet number	—
r	Radius of curvature of the fluid interface	m
R	Universal gas constant	$J \cdot (mol \cdot K)^{-1}$
S	Fluid saturation	—
q	Volume flowrate	$m^3 \cdot s^{-1}$
x	Length of X-ray path through the material	m

Greek symbols	Meaning	SI unit
λ	Linear attenuation coefficient	m^{-1}
μ	Viscosity	$\text{Pa} \cdot \text{s}$
ϕ	Porosity	—
ψ	Mobility	$(\text{Pa} \cdot \text{s})^{-1}$
ρ	Density	$\text{kg} \cdot \text{m}^{-3}$
σ	Interfacial tension	$\text{N} \cdot \text{m}^{-1}$
τ	Distance between pores	m
θ	Contact angle	<i>radians</i>
ξ	Mean radius of a throat	m
φ	Curvature	m^{-1}
κ	Total curvature	m^{-1}
Ω	Principal radii of curvature	m

List of Abbreviations

Abbreviation	Meaning	Page
CCS	Carbon Capture and Storage	4
CPRICE	Capillary Pressure and Resistivity Index by Continuous Injection	20
CO ₂	Carbon Dioxide	1
COBR		17
CT	Computed Tomography	20
D	Dimension	20
EOR	Enhanced Oil Recovery	23
EU	European Union	5
GW	Gigawatt	2
H ₂	Hydrogen	8
KI	Potassium Iodide	40
MIP	Mercury Intrusion Porosimetry	21
MICP	Mercury Injection Capillary Pressure	75
NMR	Nuclear Magnetic Resources	20
PPE	personal protective equipment	59
PTFE	Polytetrafluoroethylene	41
RGB	Red Green Blue	25
ROI	Region of Interest	89
TW	Terawatt	2
UHS	Underground Hydrogen Storage	28
USBM	United States Bureau of Mines	17
UK	United Kingdom	2
US	United State	5

List of Publications

Journal publications:

1. **S. Goodarzi**, G. Zhang, B. Bijeljic, M. J. Blunt, “Ostwald Ripening Leads to Less Hysteresis during Hydrogen Injection and Withdrawal: A Pore-Scale Imaging Study,” International Journal of Hydrogen Energy, vol. 114, pp. 475-485, 2025.
2. **S. Goodarzi**, Y. Zhang, S. Foroughi, B. Bijeljic, M. J. Blunt, “Trapping, hysteresis and Ostwald ripening in hydrogen storage: A pore-scale imaging study,” International Journal of Hydrogen Energy, vol. 56, pp. 1139–1151, 2024.
3. R. Chai, Q. Ma, **S. Goodarzi**, F. Y. Yow, B. Bijeljic and M. J. Blunt, “Multiphase Reactive Flow During CO₂ Storage in Sandstone,” Engineering, 2024.
4. W. Dokhon, **S. Goodarzi**, H. M. Alzahrani, B. Bijeljic, M. J. Blunt, and A. Niemi, “Pressure decline and gas expansion in underground hydrogen storage: A pore-scale percolation study,” Journal of Hydrogen Energy, vol. 86, pp. 261–274, 2024.
5. R. Moghadasi, **S. Goodarzi**, Y. Zhang, B. Bijeljic, M. J. Blunt, and A. Niemi, “Pore-scale characterisation of residual gas remobilisation in CO₂ geological storage,” Advances in Water Resources, p. 104499, 2023.
6. Y. Zhang, B. Bijeljic, Y. Gao, **S. Goodarzi**, S. Foroughi, and M. J. Blunt, “Pore-scale observations of hydrogen trapping and migration in porous rock: Demonstrating the effect of Ostwald ripening,” Geophysical Research Letters, vol. 50, no. 7, p.e2022GL102383, 2023.
7. R. Moghadasi, S. Foroughi, **S. Goodarzi**, Y. Zhang, B. Bijeljic, M. J. Blunt, and A. Niemi, “Trapping, Remobilisation during Geological CO₂ Storage: A Pore-Scale Imaging and Modelling Study,” Submitted to Advances in Water Resources, 2025.
8. R. Chai, **S. Goodarzi**, F. Y. Yow, B. Bijeljic and M. J. Blunt, “Pore-scale Imaging; Ostwald Ripening; Trapped CO₂ Reduction; Ganglia Structure Evolution,” 2025, *In progress*
9. M. H. Liseroudi, M. Bzhani, M. J. Blunt, A. W. Kingston, **S. Goodarzi**, O. H. Ardakani. “Shale-CO₂ Reactivity: Implication for Caprock Integrity of Carbon Storage Reservoirs,” 2025, *In progress*.

10. M. Li, **S. Goodarzi**, S. Foroughi, B. Bijeljic and M. J. Blunt, “Minimal Surfaces in Mixed-Wet Bead Packs: Insights from 3D X-Ray Imaging,” 2025, *In progress*

Conferences and Consortium Meetings:

1. **S. Goodarzi**. Ostwald Ripening Leads to Less Hysteresis during Hydrogen Injection and Withdrawal: A Pore-Scale Imaging Study. *Consortium on Pore-Scale Modelling and Imaging, London, UK, 2025*.
2. **S. Goodarzi**, G. Puyou, J. P. Duneau. Improvement of X-ray Analyses in the Lab. *TotalEnergies, Pau, France, 2024*.
3. **S. Goodarzi**, G. Zhang, B. Bijeljic, M. J. Blunt. Enhanced Hydrogen Storage in Bentheimer Sandstone: High-Pressure Investigation with Equilibrated Brine and Porous Plate. *EGU General Assembly, Vienna, Austria, 2024*.
4. **S. Goodarzi**, G. Zhang, B. Bijeljic, M. J. Blunt. Enhanced Hydrogen Storage in Bentheimer Sandstone: High-Pressure Investigation with Equilibrated Brine and Porous Plate. *2nd International Summer School on UHS, Delft, The Netherlands, 2024*.
5. **S. Goodarzi**, G. Zhang, B. Bijeljic, M. J. Blunt. Enhanced Hydrogen Storage in Bentheimer Sandstone: High-Pressure Investigation with Equilibrated Brine and Porous Plate. *AGU Annual Meeting, San Francisco, US, 2024*.
6. **S. Goodarzi**. Enhanced Hydrogen Storage in Bentheimer Sandstone: High-Pressure Investigation with Equilibrated Brine and Porous Plate. *InFUSE Prosperity Partnership, Amsterdam, The Netherlands, 2024*.
7. **S. Goodarzi**. Enhanced Hydrogen Storage in Bentheimer Sandstone: High-Pressure Investigation with Equilibrated Brine and Porous Plate. *Consortium on Pore-Scale Modelling and Imaging, London, UK, 2024*.
8. **S. Goodarzi**. Trapping, Hysteresis and Ostwald Ripening in Hydrogen Storage: A Pore-Scale Imaging Study. *Shell Annual Review, London, UK, 2023*.
9. **S. Goodarzi**. Trapping, Hysteresis and Ostwald Ripening in Hydrogen Storage: A Pore-Scale Imaging Study. *CSSR Annual Conference, Bergen, Norway, 2023*.
10. **S. Goodarzi**. Trapping, Hysteresis and Ostwald Ripening in Hydrogen Storage: A Pore-Scale Imaging Study. *International Women in Engineering Day, London, UK, 2023*.
11. **S. Goodarzi**, Y. Zhang, S. Foroughi, B. Bijeljic, M. J. Blunt. Trapping, Hysteresis and Ostwald Ripening in Hydrogen Storage: A Pore-Scale Imaging Study. *Interpore annual meeting, Edinburgh, UK, 2023*.
12. **S. Goodarzi**. Trapping, Hysteresis and Ostwald Ripening in Hydrogen Storage: A Pore-Scale Imaging Study. *Toward Net Zero Seminars, London, UK, 2023*.

13. **S. Goodarzi.** Trapping, Hysteresis and Ostwald Ripening in Hydrogen Storage: A Pore-Scale Imaging Study. *InFUSE Prosperity Partnership. Amsterdam, The Netherlands, 2023.*
14. **S. Goodarzi.** Trapping, Hysteresis and Ostwald Ripening in Hydrogen Storage: A Pore-Scale Imaging Study. *Consortium on Pore-Scale Modelling and Imaging, London, UK, 2023.*
15. **S. Goodarzi**, Y. Zhang, S. Foroughi, B. Bijeljic, M. J. Blunt. Trapping, Hysteresis and Ostwald Ripening in Hydrogen Storage: A Pore-Scale Imaging Study, poster presentation. *Gordon Research Conference. Les Diablerets, Switzerland, 2022.*
16. **S. Goodarzi.** Hysteresis in Multiphase Flow and Application to Hydrogen Storage. *Interpore annual meeting. Abu Dhabi, UAE, 2022.*
17. **S. Goodarzi.** Trapping, Hysteresis and Ostwald Ripening in Hydrogen Storage: A Pore-Scale Imaging Study. *Consortium on Pore-Scale Modelling and Imaging, London, UK, 2022.*

Available Data and Code

- High-resolution versions of the referenced images in this work are available for download at <https://zenodo.org/records/10426407>.
- The code used for the generation of pore and throat occupancy maps, contact angle and pore network extraction are available on GitHub in the following links <https://github.com/ImperialCollegeLondon/porescale>.

Chapter 1

Introduction

This chapter provides an overview of the motivation for investigating hysteresis in multiphase flow and its critical application to hydrogen storage, the central focus of this PhD research. It begins by emphasising the urgent need for sustainable and clean energy solutions in the face of growing global energy demands and climate goals, highlighting hydrogen's role as a key enabler of future energy systems. The discussion then explores the specific challenges associated with hydrogen storage in porous media, where the complex dynamics of multiphase flow and hysteresis significantly impact storage efficiency and reliability. The chapter concludes with a roadmap of the thesis structure, outlining how subsequent chapters build toward a deeper understanding of hysteresis in multiphase flow and its implications for scalable hydrogen storage solutions.

1.1 Global Energy Demands

The global energy landscape is undergoing a profound transformation, driven by the urgent need to reduce carbon emissions and mitigate the effects of climate change. As illustrated in Fig. 1.1, fossil fuels  specifically oil, coal, and gas- are the predominant sources of global energy but are also the largest contributors to carbon dioxide (CO₂) emissions, with oil contributing 11.84 billion tonnes, coal 14.98 billion tonnes, and gas 7.92 billion tonnes of CO₂ annually [1]. This staggering impact on the environment emphasises the necessity of transitioning from these carbon-intensive energy sources to renewable alternatives.

As nations worldwide work towards transitioning from fossil fuels to renewable energy sources, hydrogen is emerging as a pivotal component of the future energy mix. With its dual capacity as both an energy carrier and a storage medium, hydrogen holds the potential to address some of the most pressing challenges in achieving a sustainable and resilient energy system. This global shift towards hydrogen is reflected in numerous international initiatives and strategies aimed at harnessing its potential to decarbonise critical sectors such as transportation, industry, and heating.

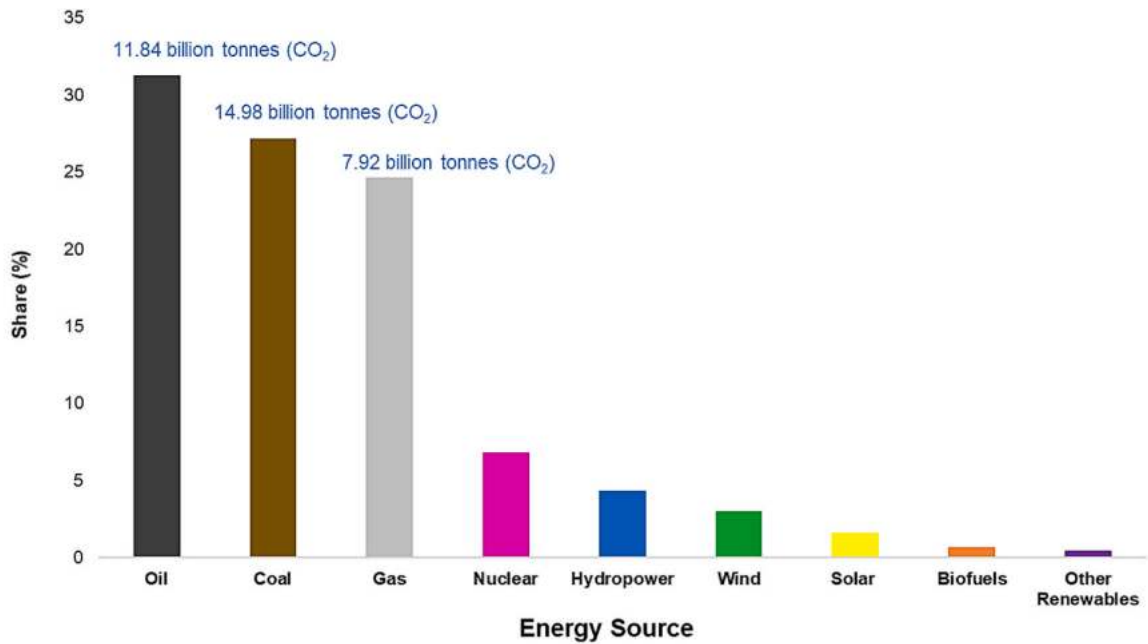


Figure 1.1: CO₂ emissions associated with different energy sources, highlighting the significant contributions of oil, coal, and gas to global carbon emissions [1].

In the UK, these global trends are mirrored by the nation's ambitious targets for carbon reduction and energy transition. Projects like HyNet North West [32] exemplify this commitment, leveraging salt caverns for hydrogen storage to balance energy supply and support decarbonisation. Such initiatives align with the UK's Net Zero target, which anticipates a hydrogen demand of up to 500 T_{Wh}/year by 2050 under high-resource scenarios. The growing demand for energy in the UK, driven by industrial activities, population growth, and the increasing electrification of various sectors, presents significant challenges to achieving the nation's carbon reduction goals. As the UK transitions towards a more sustainable energy mix, there is a pressing need to develop reliable and scalable energy storage solutions that can complement renewable energy sources such as wind and solar. In this context, hydrogen, with its versatility as an energy carrier, is emerging as a crucial component of the UK's strategy to meet these demands while minimising carbon emissions.

The demand for energy in Great Britain fluctuates significantly throughout the year, as illustrated in Fig. 1.2, which depicts the country's daily energy usage from August 2021 to June 2024. The data reveals marked increases in gas consumption, particularly during the colder months when heating needs drive demand up by approximately 2000 GWh/day. In contrast, transport energy usage remains relatively stable across the year, with a daily demand of around 1500 G_{Wh}, which is predominantly met by fossil fuels. Electricity demand, although more consistent, also exhibits seasonal peaks. Meanwhile, the contribution of renewable energy, despite its growth, varies and still constitutes a smaller portion of the total energy mix. These seasonal variations underscore the critical challenge of ensuring a reliable energy supply that meets demand year-round, especially as the UK strives to reduce its reliance on fossil fuels and increase the share

of renewable energy in its overall energy mix. Hydrogen emerges as a promising solution in this context, offering a versatile means of storing energy during periods of low demand or high renewable generation and releasing it when needed. However, the effectiveness of hydrogen as an energy carrier hinges on the development of efficient and safe storage systems.

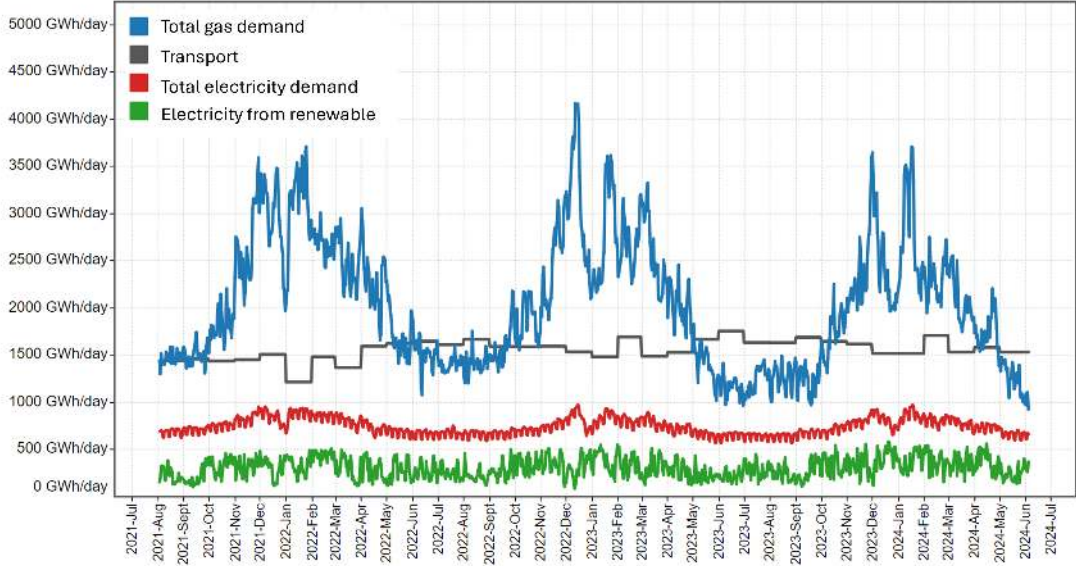


Figure 1.2: Great Britain's daily energy consumption (in GWh) from August 2021 to June 2024, showing the seasonal variation in gas usage, electricity demand, and renewable energy generation. The figure illustrates the significant fluctuations in energy demand across different months, with peaks during colder periods due to increased heating needs. The data also highlights the relatively stable transport energy usage and the growing yet variable contribution of renewable energy to the overall energy mix [2].

As the UK works towards achieving its ambitious Net Zero target by 2050, hydrogen is expected to play a pivotal role in the energy transition. Its ability to decarbonise sectors such as transportation, industry, and heating has brought hydrogen to the forefront as a crucial energy carrier in future energy scenarios. The versatility of hydrogen, coupled with its potential to store and deliver energy from renewable sources, positions it as a key enabler of a sustainable energy system. Projections from the UK's Net Zero scenarios indicate a significant increase in hydrogen demand by 2050. Under the High Electrification Scenario, it is estimated that 240 TWh/year of hydrogen will be required, potentially rising to 500 TWh/year under the High Resource Scenario. Similarly, the National Grid's Future Energy Scenarios predict that even under a scenario of high electrification, hydrogen demand could reach 113 TWh/year, with a possible rise to 591 TWh/year if hydrogen is widely adopted for heating. These scenarios reflect the growing importance of hydrogen in the UK's future energy landscape. These projections underscore the critical need for efficient and scalable hydrogen storage solutions to meet future energy demands [33, 34].

1.2 Grey, Blue and Green Hydrogen

Hydrogen can be produced through various methods, each with differing impacts on carbon emissions and environmental sustainability. The most common form, Grey Hydrogen, is produced from natural gas or coal through reforming or gasification processes, see Fig 1.3. However, this method is highly carbon-intensive, releasing significant amounts of approximately 10 to 20 kg CO_2 per kilogram of hydrogen produced. As of 2022, grey hydrogen accounted for around 98% of the global hydrogen supply, contributing significantly to global carbon emissions. To address the environmental concerns associated with grey hydrogen, Blue Hydrogen has been developed. Like grey hydrogen, blue hydrogen is produced from fossil fuels but incorporates carbon capture and storage (CCS) technologies to mitigate emissions. The captured CO_2 is securely stored in geological formations, reducing the greenhouse gas intensity to around 20 g $\text{CO}_2/\text{e}/\text{MJ}$ of hydrogen produced or even less. Despite its lower environmental impact compared to grey hydrogen, blue hydrogen production in the UK remains limited, although several projects, such as Acorn, HyTeeside, and HyNet, are currently in development.

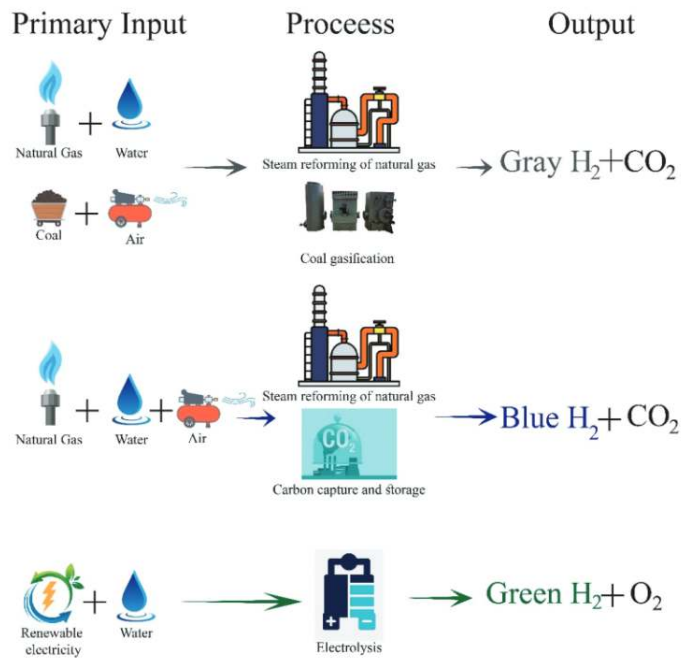


Figure 1.3: The three primary methods of hydrogen production—Grey, Blue, and Green Hydrogen. Grey Hydrogen is produced from natural gas or coal through steam reforming and gasification, resulting in CO_2 emissions. Blue Hydrogen follows a similar process but incorporates Carbon Capture and Storage (CCS) technologies to reduce CO_2 emissions. Green Hydrogen is produced via the electrolysis of water using renewable electricity, resulting in the emission-free production of hydrogen and oxygen [3].

On the other end of the spectrum, Green Hydrogen represents the most sustainable form of hydrogen production. It is generated through the electrolysis of water, powered by renewable energy sources such as wind or solar. This method produces hydrogen with minimal carbon emissions, positioning green hydrogen as a critical player in global decolonisation efforts. The

UK has been actively developing its green hydrogen capacity, with around 14 sites currently producing approximately 2.21 metric tonnes (26 GWh) of green hydrogen. The global market for green hydrogen is expected to expand rapidly, with initiatives like Germany's Salzgitter Green Hydrogen Plant and the EU's RePowerEU Plan illustrating its role in decarbonising industries and increasing energy independence. These projects demonstrate the economic viability and scalability of green hydrogen as nations push for a sustainable energy transition. While grey and blue hydrogen dominate the current market, green hydrogen is anticipated to play a crucial role in the UK's strategy to achieve Net Zero by 2050, particularly in sectors where electrification is challenging [35–37]. The focus of this research aligns with the broader goal of scaling up green hydrogen production and storage to meet future energy demands sustainably.

1.3 Requirements and Infrastructure

As the world transitions to a low-carbon energy future, hydrogen is becoming increasingly vital as a key energy carrier and storage medium. Projections from the UK National Grid Future Energy Scenarios, alongside estimates from Gas Infrastructure Europe and the US DOE National Clean Hydrogen Strategy, indicate a significant rise in hydrogen storage needs by 2050. For instance, the UK anticipates a requirement of 56 TWh/year of hydrogen energy storage by 2050 [38], while the EU and the US foresee needs of up to 450 TWh/year [39] and 264 TWh/year [40], respectively. These projections underscore the critical importance of developing large-scale hydrogen storage infrastructure to ensure a stable and reliable energy supply. The transition to a renewable-based energy system heavily depends on the availability of such storage solutions to mitigate the intermittent nature of renewable energy sources, see Fig. 1.4.

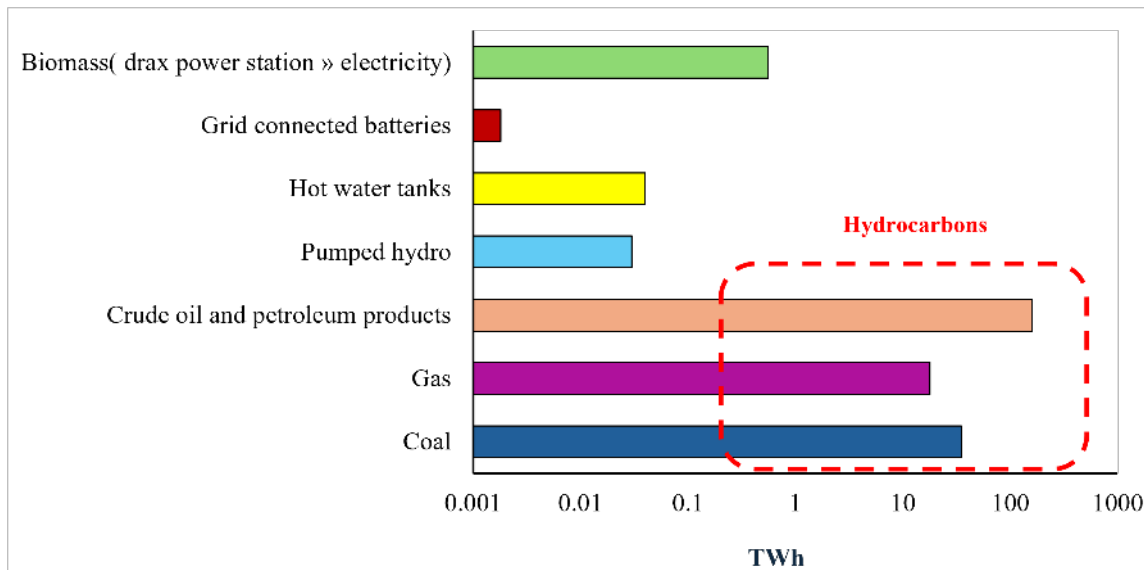


Figure 1.4: Energy storage capacity in the UK as of 2019 across various technologies, using a logarithmic scale. The graph illustrates the existing energy storage capabilities and highlights the significant gap that needs to be addressed to meet future hydrogen storage requirements [4].

Hydrogen storage in underground formations, such as salt caverns and aquifers, has been practiced for decades, providing valuable insights into large-scale hydrogen storage. Projects like France's Manosque Salt Cavern facility and Germany's HyPSTER program are at the forefront of demonstrating how these technologies can integrate with renewable energy sources and stabilize energy supply [41–43]. Figure 1.5 showcases various underground hydrogen storage projects globally, including aquifer storage in Germany and France, salt cavern storage in the UK and the US, and hydrogen storage for biomethane production in Argentina and Austria. These historical and ongoing projects demonstrate the proven track record of underground hydrogen storage, particularly the widespread use of salt caverns, which offer excellent containment properties and the ability to store large volumes of hydrogen.

The experience gained from these projects is essential for the future expansion of hydrogen storage infrastructure, especially as the demand for hydrogen continues to grow. The increasing demand for hydrogen storage is reflected in the numerous projects currently being undertaken worldwide, which are at the forefront of developing new technologies and expanding the capacity of existing storage solutions.

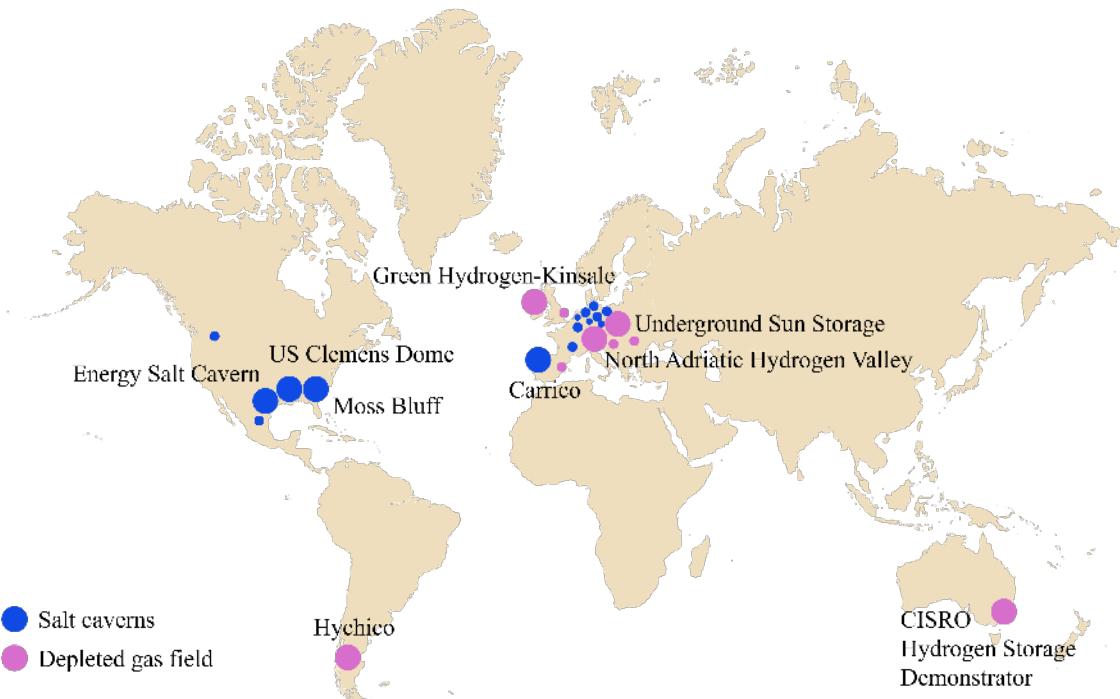


Figure 1.5: Map showing "Global Hydrogen Storage Projects Underway," highlighting regions where hydrogen storage is prioritized. The map illustrates global efforts to expand hydrogen infrastructure, with salt caverns (blue) and depleted gas fields (pink) as key storage methods. These projects underscore the strategic importance of hydrogen storage in supporting the transition to a low-carbon energy system, with ongoing developments across Europe, North America, and other regions [1, 5].

1.4 Hydrogen Storage in Porous Media

Hydrogen can be produced by several processes and it can be stored using different methods such as bonding chemically in ionic and covalent compounds, absorbing in materials with a large specific area or keeping it at high-pressure gas cylinders or cryogenic tanks [44, 45]. Hydrogen is one of the vital components in the energy supply chain, which can be safely combusted, burning one cubic metre of hydrogen (0.082 kg) produces around 12.7 MJ of energy compared to methane (0.554 kg) which has the energy potential of 44 MJ [26]. Since the energy consumed to produce a unit of hydrogen is higher than released energy, hydrogen is not considered as an energy source. However, it is capable of transporting and storing energy so it can easily be converted into electricity or heat and be considered as an efficient energy carrier. In 1915, gas storage in geological formations was accomplished in Canada for the first time and in 1986, underground storage of gaseous hydrogen in large quantities was stated as the cheapest method, according to Taylor et al. [20, 46].

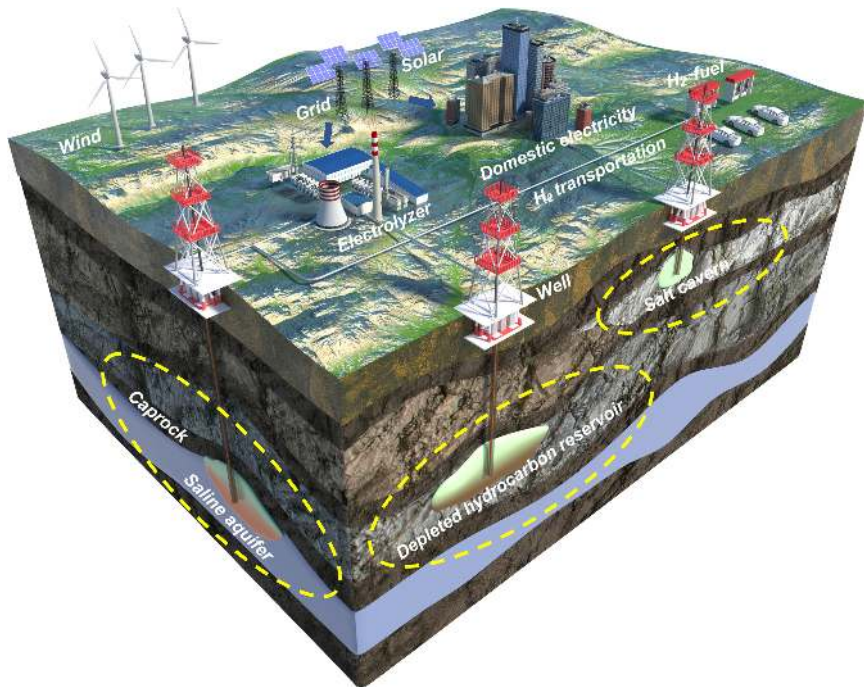


Figure 1.6: Illustration of underground hydrogen storage from renewable energy sources, showcasing various geological formations used for storage, including salt caverns, depleted hydrocarbon reservoirs, and saline aquifers. The image highlights the integration of wind and solar energy generation with hydrogen production via electrolysis, its distribution, and storage in underground structures to balance energy supply and demand [6].

The reason for attention to underground storage energy is to regulate the fluctuations in the consumption and production of energy. Temporary storing the excess of electricity in the form of hydrogen in underground structures such as aquifers, caverns, or depleted natural oil/gas reservoirs is already being demonstrated in projects like the UK's Teesside Net Zero project, which aims to use porous reservoirs to balance seasonal energy demands while reducing carbon

emissions. These initiatives highlight the feasibility and importance of such storage methods for future energy resilience, see Fig. 1.6. The underground storage of hydrogen not only is safer due to the absence of contact with atmospheric oxygen but also makes the operation economically viable [26,47]. Numerous authors have studied hydrogen storage in different aspects of storage efficiencies such as cryogenic and compressed tanks, metals or chemical hybrids, but not many reviews exist on the concept of underground hydrogen storage in the geological formations [48–54].

1.4.1 Challenges

Hydrogen storage in underground reservoirs, such as depleted gas fields, presents unique challenges arising from its physical and chemical properties. As the lightest and simplest element, hydrogen exhibits a low density (see Table 1.1) and low critical pressure and temperature, behaving as a supercritical fluid under typical reservoir conditions. One of the primary challenges is hydrogen’s limited solubility in water and brines, which varies with reservoir pressure, temperature, and fluid composition. While solubility increases with pressure and exhibits a non-linear relationship with temperature, it decreases in higher-salinity environments [55–57].

Table 1.1: Physical properties of hydrogen [26].

Properties	H_2
Molecular Weight	2.016
Density @ 25°C and 1 atm	0.082 kg/m ³
Viscosity @ 25°C and 1 atm	0.89×10^{-5} Pa·s
Solubility in pure water @ 25°C and 1 atm	7.9×10^{-4} mol·kg ⁻¹ H ₂ (g)
Normal boiling point	−253°C
Critical Pressure	12.8 atm
Critical Temperature	−239.95°C
Heating Value	120–142 kJ/g
Diffusion in pure water @ 25°C	5.13×10^{-9} m ² /s

Another significant challenge is hydrogen’s high diffusivity, which promotes mixing with other fluids in the reservoir, see Fig. 1.7. Its small molecular size results in a relatively high diffusion coefficient that depends on factors like reservoir conditions, fluid properties, and temperature. This mixing, driven by molecular diffusion and chemical potential gradients, can lead to hydrogen loss or contamination, adversely affecting storage efficiency [58]. Hydrogen’s low density and viscosity relative to reservoir fluids contribute to hydrodynamic instabilities, such as gravity segregation, where buoyant hydrogen rises unevenly within the reservoir. Additional instabilities include viscous fingering, where hydrogen forms preferential flow paths during injection, and lateral spreading, which can leave significant amounts of injected hydrogen unrecoverable [59]. In depleted oil and gas reservoirs, miscible flow conditions dominate, increasing the risk of hydrogen mixing with cushion gas or residual hydrocarbons and reducing the purity of withdrawn hydrogen. Conversely, in aquifers without cushion gas, immiscible flow processes like capillary trapping may occur, leading to inefficient displacement and challenging retrieval during

withdrawal cycles.

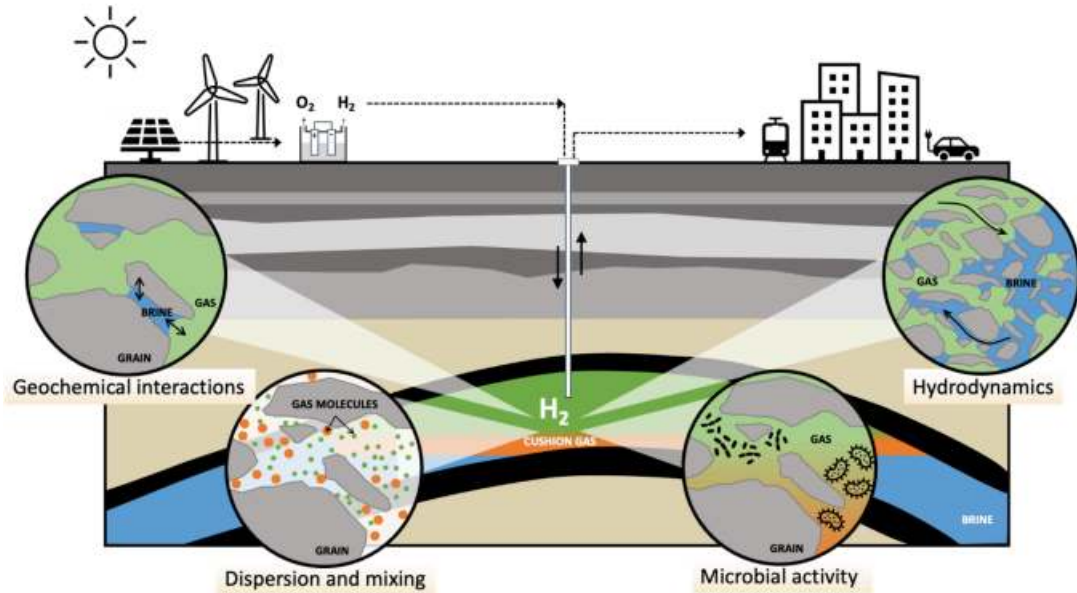


Figure 1.7: Key challenges in underground hydrogen storage (UHS) within porous reservoirs, including geochemical interactions between hydrogen and brine, hydrodynamic processes such as gravity segregation and viscous fingering, dispersion and mixing with cushion or residual gases, and the influence of microbial activity on hydrogen purity and reservoir conditions [7].

Hydrogen's interactions with other fluids and reservoir rock are governed by properties such as interfacial tension, wettability, and relative permeability, which have posed significant engineering challenges in projects such as Germany's large-scale aquifer storage pilot, where hydrogen blending led to purity and recovery inefficiencies. These real-world difficulties underscore the importance of addressing such factors for effective deployment [60]. These parameters influence hydrogen's mobility and distribution in porous media. For example, mixing with hydrocarbons or cushion gas decreases hydrogen purity, impacting its utility in subsequent cycles.

Immiscible displacement, while enhancing retention, also poses risks of trapping, further complicating recoverability [61]. Additionally, hydrogen storage may be influenced by microbial activity within porous reservoirs, where specific bacteria can consume or produce hydrogen, altering its purity or leading to byproducts that impact reservoir integrity. Such processes are particularly relevant in aquifers and must be accounted for in reservoir management strategies. The experience gained from these projects is essential for the future expansion of hydrogen storage infrastructure, especially as the demand for hydrogen continues to grow. The increasing demand for hydrogen storage is reflected in the numerous projects currently being undertaken worldwide, which are at the forefront of developing new technologies and expanding the capacity of existing storage solutions.

1.5 Research Motivation

Multiphase flow in porous media is a fundamental area of study with wide-ranging applications, including enhanced oil recovery, carbon sequestration, and underground hydrogen storage. A critical aspect of these systems is the phenomenon of hysteresis, which arises during cyclic processes such as injection and withdrawal, significantly impacting fluid distribution, recovery, and trapping mechanisms. Despite its importance, hysteresis in multiphase flow remains poorly understood, particularly at the pore scale where key interactions between fluids and reservoir rock occur.

Hydrogen storage presents an ideal application to investigate hysteresis in multiphase flow due to its reliance on cyclic injection and withdrawal operations. The storage process is inherently influenced by complex flow regimes, including capillary trapping, residual saturation, and interfacial dynamics, all of which are governed by hysteresis. Current methods, however, lack the resolution to directly observe and quantify these pore-scale processes under realistic reservoir conditions.

To address this gap, this research utilises micro X-ray Computed Tomography (micro-CT) to visualise and analyse fluid flow and phase distribution in porous media at high resolution. This novel technique enables precise measurement of properties such as relative permeability, saturation profiles, and trapping behaviour, offering unparalleled insights into the mechanics of hysteresis and its implications for hydrogen storage. By focusing on the intersection of hysteresis and UHS, this study aims to advance the fundamental understanding of multiphase flow and inform the design of more efficient energy storage systems.

1.6 Aim and Objectives

The aim of this research is to investigate the role of hysteresis in multiphase flow within porous media, with a specific focus on its application to underground hydrogen storage. By utilizing advanced imaging techniques such as micro-CT, the study seeks to enhance the understanding of pore-scale fluid dynamics and their implications for hydrogen injection, storage, and withdrawal processes. The objectives are as below,

- Quantify the effects of hysteresis on fluid flow properties, such as ~~relative permeability~~, capillary pressure, and residual trapping, during cyclic injection and withdrawal.
- Study hydrogen-brine displacement processes to understand their relationship with hysteresis and recovery efficiency.
- Employ micro-CT technology to visualise and measure pore-scale fluid distribution, phase interactions, and flow regimes under realistic reservoir conditions.
- ~~Evaluate the influence of porosity, permeability variations, and rock wettability on hysteresis and hydrogen recoverability in porous media.~~



1.7 Structure of the Study

This thesis is structured into six chapters, each building towards a comprehensive understanding of hysteresis in multiphase hydrogen-brine flow within porous media. The experimental focus involves three hydrogen-brine two-phase flow experiments conducted under static conditions, using advanced X-ray tomography. These experiments represent a significant novelty by employing hydrogen as a test fluid, refining the methodology with each iteration to achieve improved results, and leveraging pore-scale imaging to investigate the behaviour of hydrogen-brine systems in unprecedented detail. The thesis will be structured as follows:

Chapter 2 begins with an overview of the fundamental equations and concepts governing multiphase flow in porous media, followed by a synthesised review of pore-scale two-phase flow studies, focusing on experimental investigations. The chapter highlights critical knowledge gaps, such as the limited understanding of hysteresis during cyclic injection and withdrawal.

Chapter 3 examines hysteresis in hydrogen-brine flow using X-ray tomography. An unsteady-state experiment with a Bentheimer sandstone sample to observe fluid distribution during drainage and imbibition cycles.

Chapter 4 investigates three cycles of hydrogen injection and brine injection, with images taken immediately after each cycle and after a 16-hour resting period. The chapter focuses on the experimental setup, methodology, and the role of Ostwald ripening in hydrogen storage.

Chapter 5 explores unsteady-state hydrogen-brine flow through a Bentheimer sandstone sample using porous plate experiments and high-resolution micro-CT imaging. It quantifies capillary pressure, contact angle, and meniscus curvature over three imbibition cycles, showing a progressive reduction in capillary pressure and residual gas saturation.

Chapter 6 summarises the key findings of this research and discusses their implications. It also outlines potential avenues for future work, highlighting areas where further investigation could enhance understanding of hydrogen storage in porous media and improve storage strategies.

Chapter 2

Scientific Background

This chapter begins with an overview of the key principles of multiphase flow at the pore scale, detailing the main forces that influence flow in porous media. It introduces Darcy's law, which applies to flow at larger scales. The chapter then delves into displacement processes like imbibition and drainage, which affect fluid movement. Additionally, it covers the connectivity of gas ganglia and the flow regimes identified through X-ray imaging. Finally, we will identify gaps in the existing literature and connect them to our experiments to emphasise the importance and originality of our work.

2.1 Theory

Studying the rock-fluid system on a pore-by-pore basis results in a better understanding of multiphase flow at larger scales, which is an important aspect in hydrocarbon recovery, carbon or hydrogen storage and groundwater hydrology. Understanding pore-scale physics requires investigation of the fluid flow dynamics and the processes that control the fluid movement in porous materials [22, 62].

2.1.1 Darcy's Law

The transport of fluids through reservoir rocks is complex and current theories of multiphase flow are based on Darcy's law, which is an empirical equation that relates the macroscopic velocity (actually the flux or volume flowing per unit area) of a fluid to the average pressure gradient of individual phases, see Fig. 2.1. For phase 'm', it can be expressed as,

$$\mathbf{q}_m = -\frac{k_{rm}K}{\mu_m}(\nabla \mathbf{P}_m - \rho_m \mathbf{g}), \quad (2.1)$$

where the acceleration due to gravity is \mathbf{g} and the volume of fluid flowing per unit of time per unit of area is \mathbf{q} . The viscosity, density and pressure of the fluid are given by μ_m , ρ_m and \mathbf{P}_m , respectively. K is the absolute permeability with a unit of length squared m^2 or Darcy and k_{rm} is the relative permeability [63, 64]. Generally, permeability is a measurement of the ability of porous materials to conduct flow and if there is more than one fluid, the ability

of each fluid is decreased by the presence of other fluids. In multiphase systems, measuring the ratio of effective permeability of fluids (k_{eff}) to the absolute permeability of the rock can represent relative permeability, which has a first-order dependency on saturation and typically plotted against it. Relative permeability also depends on other properties such as wettability and saturation history.

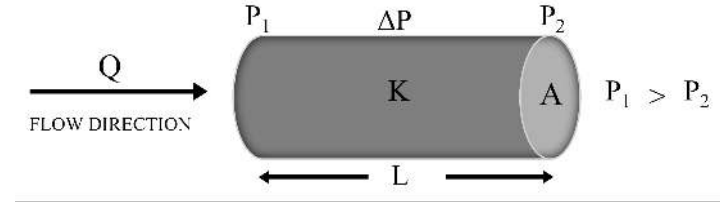


Figure 2.1: An illustration of a cylindrical core sample used to determine the absolute permeability of a rock using Darcy's law. ~~Where~~ K is the permeability, A is the cross-sectional area, L is the length of the sample, Q is the volumetric flow rate, and P_1 and P_2 are the pressures at the inlet and outlet, respectively.

In porous media, the wetting phase tends to coat the solid surfaces and occupies small pores and corners, while the non-wetting phase resides in the centres of larger pores. This distribution, influenced by surface wettability, affects the flow potential and relative permeability of each phase. For example, in a water-wet system, gas (or oil) flows more readily through larger pores, whereas water is confined to smaller spaces, leading to higher gas relative permeability at the same saturation. The relative permeability curves differ depending on the saturation history, such as during drainage, where the non-wetting phase displaces the wetting phase, and during imbibition, where the wetting phase displaces the non-wetting phase. This difference, known as hysteresis, results from varying pore-scale displacement mechanisms and fluid distribution, see Fig. 2.2.

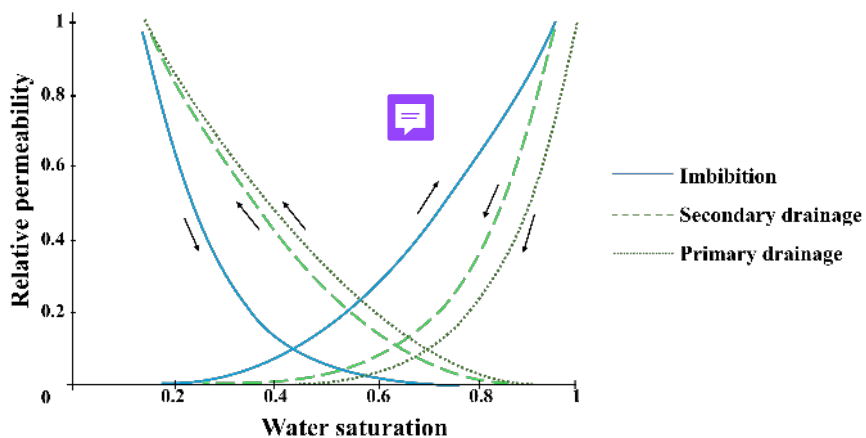


Figure 2.2: Example of relative permeability curves for primary drainage, imbibition, and secondary drainage for an oil-water system, showing a distinct hysteresis effect, evident from the difference between the drainage and imbibition curves for both water and oil [8]. This hysteresis is due to the differing pore-scale displacement mechanisms and fluid distribution during the two processes. The arrows indicate the direction of saturation change for each phase.

The relative permeability of multiphase flow in experiments can be obtained by ignoring gravitational forces and assuming that two phases experience the same pressure drop [64]

$$k_{rw} = \frac{\mathbf{q}_w \mu_w L}{\Delta \mathbf{P} K}, \quad (2.2)$$

$$k_{rg} = \frac{\mathbf{q}_g \mu_g L}{\Delta \mathbf{P} K}, \quad (2.3)$$

where (L defines the sample length). Relative permeability has an impact on trapping; therefore, calculation of fluid relative permeability helps to estimate ultimate recovery and productivity besides planning operation of productions [22,65].

2.1.2 Porosity and Fluid Saturation

Porosity ϕ in a porous medium is the measure of the void spaces within the material, defined as the ratio of the volume of these void spaces (pores) to the total volume of the medium, which includes both the voids and the solid matrix,

$$\phi = \frac{\text{void volume}}{\text{total volume}}. \quad (2.4)$$

This characteristic can be expressed in two forms: total porosity and effective porosity. Effective porosity ϕ_e is particularly significant in practical applications as it accounts for the volume of connected void spaces that contribute to fluid flow through the medium, providing a more accurate representation of the medium's capacity to transmit fluids [64,66]. Saturation refers to the fraction of the pore volume occupied by a specific fluid phase in a porous medium. In a multiphase flow system, the combined saturation values of all fluids (such as water, oil, and gas) must sum to one, indicating that they collectively occupy the entire pore space. These saturation levels are typically denoted with subscripts, such as S_w for water saturation, S_o for oil saturation, and S_g for gas saturation. When a medium is fully saturated with a single fluid, that fluid's saturation is equal to one,

$$S_w + S_o + S_g = 1. \quad (2.5)$$

Porosity and saturation are closely related concepts; the amount of void space, defined by porosity, determines the capacity of the medium to hold fluids, while saturation indicates the specific proportion of this void space that each fluid occupies.

2.1.3 Interfacial Tension and Capillary Number

In the study of multiphase flow in porous media, understanding the forces at play is essential for explaining fluid distribution and movement. Among these forces, interfacial tension, denoted as σ , is the energy per unit area at the interface between two immiscible fluids. It arises from the imbalance of intermolecular forces at the interface, causing the fluids to rearrange themselves to minimise the surface area. For example, a gas bubble in water forms a spherical shape because

a sphere has the lowest surface area for a given volume, thus minimising the interfacial tension. This property plays a crucial role in the distribution and behaviour of fluids within porous media, influencing phenomena such as capillary pressure. The interfacial tension between the two fluids influences the ease with which one fluid can displace the other. Lower interfacial tension generally facilitates fluid displacement but may also lead to reduced trapping of the non-wetting phase.

There is an empirical relationship between capillary pressure and saturation. The difference of fluid pressures is assumed to be equal to the capillary pressure, which is assumed as a function of wetting phase saturation only [67]. In a system of two-phase flow such as gas/water, the capillary pressure is defined as a difference of pressure between gas and water

$$P_c = P_g - P_w, \quad (2.6)$$

where c , g and w are known as the capillary, gas and water, respectively. The capillary pressure can be calculated based on the Young-Laplace equation, where P_c is a multiplication of interfacial tension (σ) divided by the radius of curvature of the fluid interface (r),

$$P_c = \frac{2\sigma}{r}. \quad (2.7)$$

If pressure and interfacial forces are balanced, the geometry of the interface is related to the pressure difference, which can be determined from the two principal radii of curvature (Ω)

$$P_c = 2\sigma\kappa = \sigma\left(\frac{1}{\Omega_1} + \frac{1}{\Omega_2}\right), \quad (2.8)$$

where κ is the total curvature of the interface. The radii of the curvature can be either positive (bulging out) or negative (concave), see Fig. 2.3. For gas/water systems, if κ is positive, water is at a lower pressure than gas; if κ is negative, it means water has the higher pressure. However, it cannot be measured analytically for a complex rock system because of complicated pore morphology and contact angle effects [64, 68]. By considering a constant pressure difference between phases, the equality between gas pressure and water pressure can be assumed. If the effects of gravity are neglected then the total Darcy flux ($\mathbf{q}_t = \mathbf{q}_g + \mathbf{q}_w$) can be written as a multiplication of mobility, permeability and pressure gradient, where (ψ_t) is the total mobility

$$\mathbf{q}_t = -\psi_t K \nabla \mathbf{P}. \quad (2.9)$$

For a gas/water system, the total mobility can be written as follow [69],

$$\psi_t = \psi_w + \psi_g, \quad (2.10)$$

$$\psi_t = \frac{k_{rw}}{\mu_w} + \frac{k_{rg}}{\mu_g}. \quad (2.11)$$

To examine the effect of flowrate, capillary number (Ca) is defined as a multiplication of total Darcy flux by the average dynamic viscosity of the two fluids divided by interfacial tension

between two phases,

$$Ca = \mu \mathbf{q}_t / \sigma. \quad (2.12)$$

At the pore-scale, if viscous forces dominate, $Ca > Ca^v$, then Ca^v approximately equals to $K/\tau\xi$, where τ represents the distance between pores and ξ is the mean radius of a throat. ~~When Ca approximately equals 1, then no transition displacement occurs between capillary-controlled and viscous-controlled.~~ Viscous effects can be ignored if $Ca \ll Ca^v$ meaning that the capillary forces dominate [22, 63, 64].

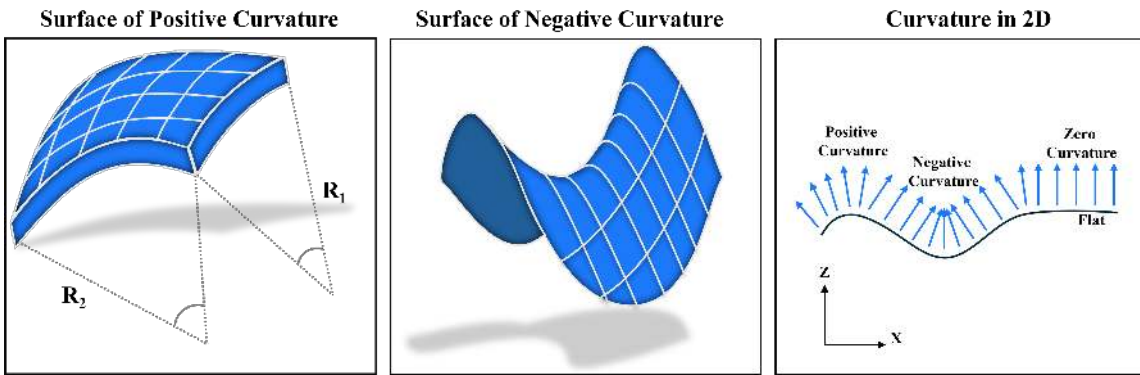


Figure 2.3: Examples of flat, positive and negative curvatures. The principal radii of curvature of this interface are denoted as R_1 and R_2 .

2.1.4 Wettability and Contact Angle

Wettability is referring to the tendency of a solid surface to be preferentially wetted by one fluid in the presence of another immiscible fluid. This property significantly influences the distribution and movement of fluids within porous rock formations, affecting fluid recovery and reservoir performance. In porous media saturated with water and oil, the rock can exhibit different wetting preferences: water-wet surfaces favour contact with water, while oil-wet surfaces prefer contact with oil. Most reservoir rocks display mixed wettability, with smaller pores typically being strongly water-wet and larger pores exhibiting a range of wettabilities from water-wet to oil-wet.

The characterisation of wettability is commonly achieved by measuring the contact angle θ , which is the angle formed at the junction where the solid surface, gas/oil, and water meet. This angle is influenced by various factors, including the mineral composition of the rock, the chemistry of the formation brine, the composition of the gas/oil, and the reservoir temperature [70–72]. The contact angle provides a direct quantification of wettability, ranging from 0° (strongly water-wetting) to 180° (strongly oil-wetting). The contact angle is measured in the denser phase, typically water, at the point of three-phase contact, see Fig. 2.4. Wettability can be understood through the balance of forces at the interfaces between the different phases, as described by Young's equation [64]:

$$\sigma_{nws} = \sigma_{\text{gas}} + \sigma_{\text{cos}\theta}, \quad (2.13)$$

where σ_{nws} is the interfacial tension between the solid and non-wetting phase, σ_{ws} is the interfacial tension between the solid and wetting phase. This relationship indicates how the contact angle is determined by the relative magnitudes of these interfacial tensions. The rock wettability can be assessed using indirect methods, such as the Amott wettability index and the United States Bureau of Mines (USBM) wettability index, which infer wettability from macroscopic measurements of capillary pressure. However, the most effective direct method is contact angle geometry, which measures the contact angle on an external surface, although it is challenging to apply within porous materials.

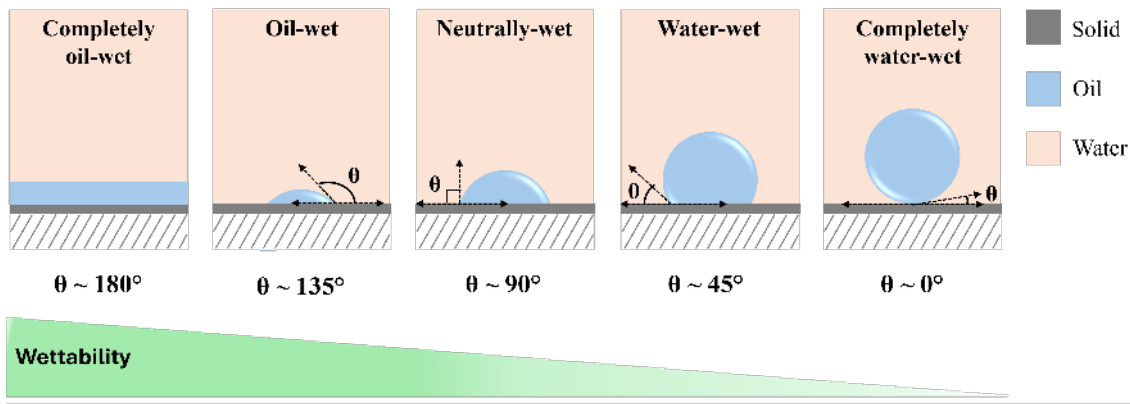


Figure 2.4: The wettability states of an oil droplet on a solid surface with water as the surrounding phase. The contact angle θ is measured through the water. Contact angles below 90° indicate a water-wet system, while those above 90° indicate an oil-wet system.

Recent advancements in high-resolution imaging techniques, particularly pore-scale X-ray imaging, have led to innovative methods for characterising wettability within the pore space. Utilising micro tomography, specifically micro-CT imaging, allows for direct visualisation of the pore space and measurement of the contact angle at the COBR interface on rock surfaces under reservoir conditions, see Fig. 2.5.

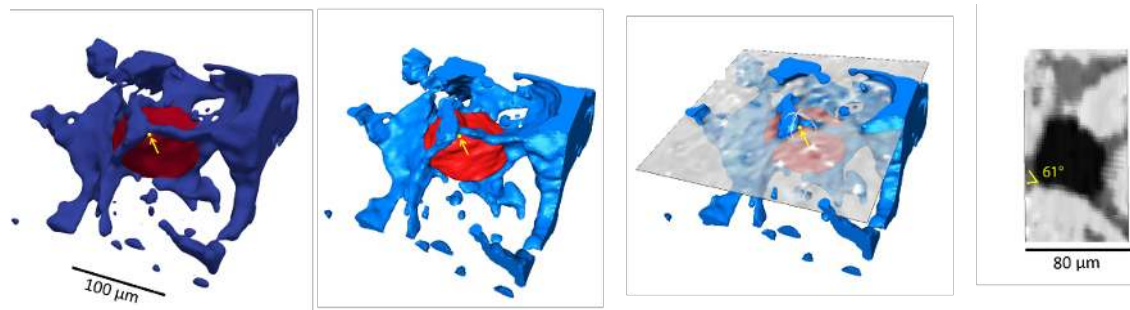


Figure 2.5: Visualisation of a contact angle (60°) using automated code, identifying the same point in the data visualisation software, and comparing it to a manual contact angle measurement at the same location (61°) [9].

This approach provides a more accurate measurement of contact angles by accounting for geological textures, surface roughness, and displacement effects typically absent on ideal flat surfaces.

Moreover, it enables the measurement of contact angles across numerous points within multiple pores, enhancing the precision of wettability characterisation. Known as the geometric contact angle, it is measured between a vector tangential to the fluid-fluid interface and the rock surface. Additionally, ~~X-ray imaging advancements~~ have facilitated the calculation of the thermodynamic contact angle, associated with fluid displacement based on energy balance. These innovations have significantly enhanced our pore-scale understanding  of wettability in complex systems and will be employed to determine contact angles in multiphase experiments.

2.2 Fluid Flow in Porous Media

Multiphase flow in porous media is observed in many natural and engineered processes such as gas storage in oil reservoirs, enhanced oil recovery, manufacturing contexts, drug delivery, wastewater treatment and fluid separation. At the pore-scale, capillary forces mainly control the fluid displacement, which depends on the wettability and geometry of the porous medium. A porous medium is made of void spaces which can be represented as a network composed of ~~pores, throats and wide regions~~. Flow can be transient displacement or steady state. In steady-state ~~condition~~, both fluids flow through the media simultaneously at a constant flowrate [73]. For transient displacement, a porous medium can have a different filling sequences known as drainage or imbibition which apply to strictly hydrophobic or hydrophilic systems. The process is called drainage when a wetting phase is displaced by a nonwetting phase where the wetting phase moves from the pore centres to the corners of the pore spaces [64, 74]. Imbibition happens when the wetting phase displaces the nonwetting phase, the capillary pressure is positive and contact angles are less than 90° [75].

2.2.1 Hysteresis

The relationship between the capillary pressure and saturation has been investigated in different experiments that concluded the capillary pressure not only depends on the saturation but also on the saturation history, which introduced a new concept known as hysteresis. The word 'hysteresis' is an ancient Greek word meaning to lag behind or deficiency, which can express the quantitative properties of a system [10]. Let us consider there is an input u and output w in a system, increasing u results in a rise in w . If the input direction reverses, the pair u and w do not flow the original path, Fig. 2.6. This behaviour of the system indicates that predicting the output depends on the input and history of the process [76, 77]. In other words, when a system experiences a certain delay in a looping behaviour of the input and output graph, it means the two process paths are not following the same track [78, 79].

Hysteresis phenomenon has specific attention in a wide range of engineering disciplines such as electrical engineering, civil engineering and petroleum engineering. Hysteresis is defined based on the fundamental of the fields and it defers from one field to another [80, 81]. However, in this report, the hysteresis phenomenon focuses on the area of multiphase flow. The concept of hysteresis was first introduced for magnetism in the 1910s. Many papers have studied how

hysteresis behaviour can affect rocks and fluid properties and how understanding this new phenomenon can help to improve the performance of reservoir productions [82]. Studying hysteresis also is important for oil and gas reservoirs because of the significant effects that it has on the accuracy of the reservoir simulation results. Ignoring the hysteresis leads to large errors in the simulation results, therefore this phenomenon should be accounted for and considered in the modelling processes.

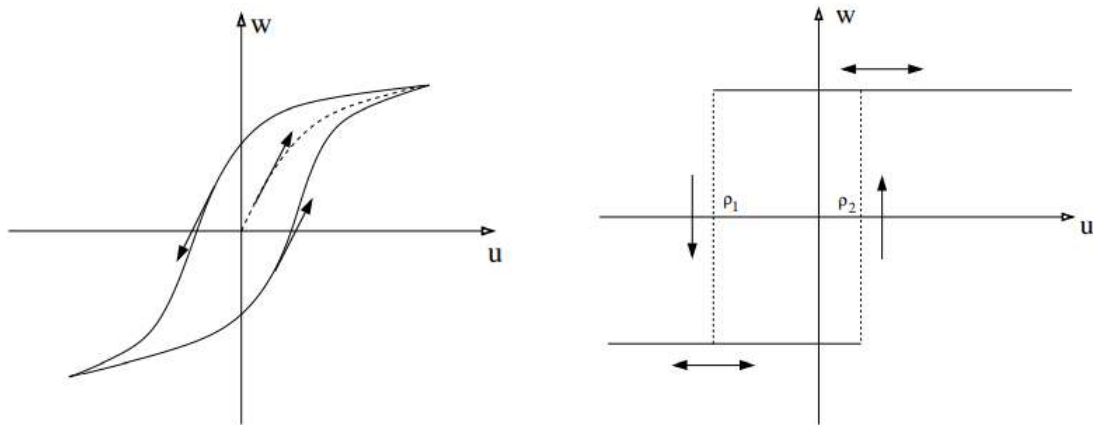


Figure 2.6: Hysteresis behaviour illustrated in input-output graphs. The left graph shows a smooth hysteresis loop where the output w lags behind the input u , resulting in a delay and looping behaviour. The right graph represents an idealized rectangular hysteresis loop, highlighting two distinct process paths (ρ_1 and ρ_2) that do not follow the same track, illustrating the system's nonlinearity and memory effect [10].

2.2.2 Two-Phase Flow

2.2.2.1 Capillary Pressure and Saturation

Capillary pressure is one of the important factors in multiphase flow, geological CO₂ sequestration, water-alternating gas injection and enhanced oil recovery methods [83–86]. Having a better understanding of hysteresis in capillary pressure can help to gain the knowledge of the distribution of saturation in the reservoirs and accurate process designs. There are several methods to measure capillary pressure on rock samples [87]. One of the major static methods is mercury injection, used to interpret the size of restrictions (throats). It only works for primary drainage and it is not useful for the study of hysteresis [88].

Another technique to measure capillary pressure was proposed by Hassler and Brunner [89] known as the centrifuge technique. This technique only works for the denser phase (water) displacing oil and it is limited to the hysteresis test because only one phase can displace the other [90].  The porous-plate technique is considered the most accurate way to measure capillary pressure where fluid is injected at a known pressure and the non-wetting phase cannot escape because of the presence of a low permeability high-capillary-entry-pressure porous plate. Although, it takes weeks or months to reach the equilibrium state for each point of capillary pressure, it can be used to investigate arbitrary displacement cycles [91, 92].

As most of the mentioned experimental techniques have the difficulty in the measurements, several studies developed mathematical models for hysteresis in capillary pressure. Killough [93] developed an empirical model which reproduced the hysteresis curve by applying saturation history. Although his model is accurate, the experimental data is needed to provide parameter values for his equations. Ismail et al., [94] studied water-oil capillary pressure in a carbonate reservoir and proposed a model by using Killough's equation. While Killough mainly studied two-phase flow systems, Leverett [95] suggested a new model for three-phase systems. Based on Leverett's assumptions a new model was developed and proposed by Parker and Lenhard. This model expressed a new scaled saturation-capillary pressure function. Comparing this model with experimental results showed a good agreement especially for scanning paths [96].

More recently, some advanced methods have been developed such as X-ray CT [97], Nuclear Magnetic Resonance (NMR) [92], Capillary Pressure and Resistivity Index by Continuous Injection (CPRICE) [98]. These techniques can overcome the limitations of conventional methods. For example, the Nuclear Magnetic Resonance technique reduces the time requirement and X-ray computed tomography provides direct observation of pore network structure during ~~multi-phase~~ flow [99–101]. This method helps to have a better understanding of pore networks, pore size distribution and pore network tortuosity [102]. However, the complexity and small sizes of the pore structure make it difficult for direct images of multiphase flow in porous media as it requires a lot of 3D image processing and a high computational power [103].

The only new method that can be used for measuring the capillary pressure is X-ray imaging and by applying Eq. 2  the capillary pressure for displacement can be calculated from interfacial curvature. X-ray imaging provides a method to measure curvature that I will apply in my work.

2.2.2.2 Interfacial Area

Since capillary pressure is not a unique function of saturation, we need to describe it through another variable as well. Hassanzadeh and Gray [104] proposed that capillary pressure could be described by a unique function of saturation and interfacial area. The problem though has been the measurement of interfacial area. Culligan et al. [105] presented a measurement of interfacial per volume based on ~~computed microtomography~~ images. Cheng et al. [106] studied the interfacial area per volume between wetting and non-wetting fluids and they observed that the interfacial area per volume of the capillary-dominated interfaces lifts the pressure-saturation hysteresis. Chen et al. [107] used a two-dimensional micromodel and proposed that each system has a unique pressure-saturation-interfacial area.

Porter et al. [108] verified the Chen et al. findings by using three-dimensional ~~X-ray microtomography~~. They showed defining the main branches can describe the relationship among capillary pressure, saturation and interfacial area without scanning the curve data. The relationship between interfacial area and saturation based on pore sizes and also capillary pressure-saturation relationship was predicted by Diamantopoulos et al. [109].

2.2.2.3 Pore Size Distribution

Pore size distribution refers to the variety and abundance of pores of different sizes within a rock matrix. Understanding the distribution of pore sizes is crucial because it directly impacts the rock's ability to store and transmit fluids. The pores within a rock can range from nanometers to millimeters in diameter, and their distribution can be influenced by several factors including the rock's genesis, mineral composition, and diagenetic history. These pores are often interconnected, forming a network that dictates the flow paths of fluids. The geometry and connectivity of these pores are essential parameters that influence the rock's porosity and permeability, as explained in subsections 2.1.1 and 2.1.2. There is no single definition of "pore diameter" or "pore size," as each method of determination uses a model suited to the specific experiment. Similarly, "void space" typically refers to the space between solid surfaces. The irregular network of pores in rocks includes narrow constrictions called ~~pore~~ throats or necks and larger spaces known as ~~pore~~ bodies, see Fig. 2.7.

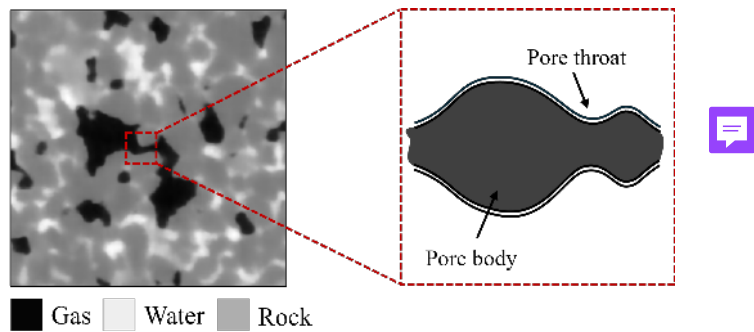


Figure 2.7: Schematic of ~~pore~~ bodies and ~~pore~~ throats in a gas/water system. The diagram illustrates the larger pore spaces known as ~~pore~~ bodies and the narrow constrictions called ~~pore~~ throats that interconnect them, highlighting the pathways for fluid flow and storage within the rock matrix.

Measurement of pore size distribution is typically carried out using techniques such as mercury intrusion porosimetry (MIP) [110], nuclear magnetic resonance (NMR) spectroscopy [92], and ~~micro-computed tomography (micro-CT)~~ [100] scanning. MIP involves forcing mercury into the rock pores under controlled pressures and measuring the volume of mercury intruded to infer pore sizes. NMR spectroscopy exploits the magnetic properties of hydrogen nuclei in the pore fluids to determine pore sizes based on relaxation times. Micro-CT scanning provides high-resolution, three-dimensional images of the rock's internal structure, allowing for detailed analysis of pore geometry and connectivity [111, 112].

In the context of hydrogen and brine systems, understanding pore size distribution is particularly important. Hydrogen, being a small and light molecule, can diffuse through very small pores, but its storage and transport are influenced by the rock's microstructure. Brine, which has a higher viscosity and density, will interact differently with the pore surfaces, affecting its flow and retention. The interplay between these fluids and the rock's pore size distribution can significantly influence properties such as relative permeability, capillary pressure, and wettability.

2.2.3 Gas Trapping and Movement

One of the aspect of gas storage is that the trapping and movement of gas in its own phase might be affected by the transport of dissolved gas. In oilfield operations, it is commonly assumed that the dissolution of hydrocarbons is insignificant and that hysteresis is caused by the displacement between completely immiscible phases. This assumption is reflected in the use of hydrocarbon-water properties to describe gas storage. However, both with hydrogen and carbon dioxide, this assumption is not valid [113–115].

2.2.3.1 Ostwald Ripening

The movement of gas through Ostwald ripening is crucial for understanding the behaviour of trapped gases in porous structures. When a gas phase exists in porous media, such as subsurface reservoirs or sedimentary rock formations, variations in pore size and surface tension create non-uniform capillary pressures. These differences drive a diffusion process where dissolved gas molecules move from regions of higher concentration, associated with higher capillary pressure, to areas of lower concentration. As gas dissolves and diffuses through the aqueous phase, smaller gas bubbles, which experience higher internal pressure, shrink, while larger bubbles with lower internal pressure grow. This process, driven by the lower solubility in smaller bubbles, gradually leads to a redistribution of gas, where larger bubbles dominate, and the system moves toward equilibrium with a more stable gas configuration, see Fig. 2.8.

According to Henry's Law, dissolved gas concentrations in the aqueous phase depend on the partial pressure of gas at the gas-liquid interface. In the context of Ostwald ripening, Henry's Law helps explain how dissolved gas diffuses to eliminate concentration gradients between different regions of gas ganglia (bubbles). The result is that smaller bubbles, with higher internal pressures and lower solubility, dissolve more readily, while larger bubbles accumulate the diffused gas, reinforcing the process of bubble coarsening.

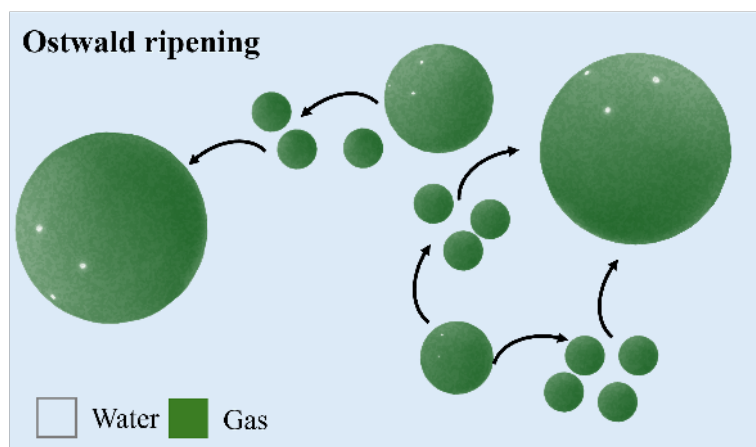


Figure 2.8: Schematic illustration of Ostwald ripening. Differences in local capillary pressure lead to differences in the concentration of dissolved gas and result in concentration gradients in the aqueous phase and diffusion of dissolved gas away from regions of high capillary pressure.

In a gas-brine system, the equilibrium concentration of gas depends on the gas pressure, P_g , as described by Henry's law:

$$C = HP_g, \quad (2.14)$$

where C is the concentration of gas dissolved in the aqueous phase in units of $\text{mol} \cdot \text{m}^{-3}$, P_g is the gas pressure in pascals and H is the Henry's law constant with SI units of $\text{mol} \cdot \text{m}^{-3} \cdot \text{Pa}^{-1}$. Consequently, the typical concentration gradient between ganglia can be approximated as

$$\Delta C \approx \frac{H\sigma}{r}, \quad (2.15)$$

assuming that the pressure variation between ganglia is on the order of a characteristic capillary pressure, with σ denoting the interfacial tension and r representing a characteristic radius of curvature for a gas-brine meniscus.

The diffusive flux F of dissolved gas, in units of $\text{mol} \cdot \text{s}^{-1}$, is governed by Fick's law:

$$F = \frac{DA\Delta C}{M}, \quad (2.16)$$

where D is the diffusion coefficient of gas in the aqueous phase, A is a representative pore cross-sectional area, and M is the characteristic diffusion length.

This flux allows us to approximate the time scale required for the complete dissolution of a ganglion, as observed in experiments:

$$t = \frac{n}{F}, \quad (2.17)$$

where n represents the number of moles of gas in the ganglion. Applying the ideal gas law,

$$PV = nRT, \quad (2.18)$$

where V is the ganglion volume, T is the temperature, and R is the universal gas constant, we estimate the dissolution time. Here, we assume that all gas is lost through Ostwald ripening, neglecting the alternative possibility that very small ganglia might migrate through the pore space and merge with larger neighboring ganglia.

The time required for small ganglia to dissolve can be estimated as

$$t \approx \frac{VM}{DAH\sigma}. \quad (2.19)$$

In porous media, understanding how Henry's Law interacts with Ostwald ripening is essential for various applications. In enhanced oil recovery (EOR), for example, the dynamics of gas movement are critical for optimising injection strategies of gases like CO_2 , which can lead to more efficient oil displacement. Similarly, in carbon sequestration, Ostwald ripening affects the stability and migration of CO_2 trapped in subsurface formations. By promoting a uniform capillary pressure through gas redistribution, the system minimises its energy, resulting in a more stable gas distribution. This illustrates the complex relationship between gas solubility, capillary

pressure, and fluid mechanics in porous media, guided by principles like Henry's Law [116–118].

2.2.3.2 Péclet Number

The concept of the Péclet number is pivotal in various fields, including chemical engineering, hydrology, and environmental engineering. For instance, in subsurface hydrology, the Péclet number helps in understanding the dispersion of contaminants in groundwater. In chemical reactors, it assists in designing efficient systems by balancing advective and diffusive transport to optimise reaction rates and product distribution. In the context of gas transport in porous media, such as the hydrogen-water system, the Péclet number aids in predicting how gases will move through the porous structure, considering both the flow dynamics and the molecular diffusion. The Péclet number (Pe) is a dimensionless quantity used extensively in the study of transport phenomena within fluid mechanics and porous media. Named after the French physicist Jean Claude Eugène Péclet, it quantifies the relative importance of advective transport (due to bulk fluid motion) to diffusive transport (due to molecular diffusion) within a flow system. The Péclet number is particularly useful in characterising the transport of substances such as heat, mass, or momentum in various engineering and scientific applications.

In porous media, the Péclet number provides insights into the dominant transport mechanisms and helps in predicting the behaviour of fluids under different flow conditions. It is defined by the following equation:

$$Pe = \frac{\mathbf{q} \cdot l}{D}, \quad (2.20)$$

where \mathbf{q} is the Darcy velocity, representing the volumetric flow rate of fluid per unit area of the porous medium. The term l is the characteristic length, often taken as the average distance between the centres of two neighbouring pores, and D is the diffusion coefficient of the solute in the solvent [119, 120]. The Péclet number allows for a distinction between different regimes of transport: low Péclet Numbers ($Pe < 1$): Diffusion-dominated transport. In this regime, molecular diffusion is the primary mechanism for the movement of solutes, and advective transport is relatively insignificant. This is typical in systems with low flow rates or high diffusivity. High Péclet Numbers ($Pe > 1$): Advection-dominated transport. Here, the bulk fluid motion predominantly drives the transport process, overshadowing the effects of molecular diffusion. This scenario is common in systems with high flow rates or low diffusivity.

2.2.3.3 Minkowski Functionals

To quantitatively analyse the morphology and topology of the gas and brine phases within the porous medium, Minkowski functionals were employed. These functionals provide a rigorous mathematical framework for describing the geometrical properties of structures in three-dimensional space, making them highly valuable in the study of multiphase flow in porous media. Four key functionals are considered in this study: volume, surface area, mean curvature, and connectivity [121, 122].

The volume functional (S) represents the total space occupied by a given phase. In the context of core flooding, it corresponds to the saturation of gas and brine, which is a fundamental parameter in understanding displacement and trapping mechanisms. The gas saturation (S_g) is calculated based on the volume of gas present in the pore space relative to the total porous volume. The surface area functional (a) measures the total interfacial area between different phases, such as gas-brine, gas-solid, and brine-solid interfaces. The specific interfacial area provides insights into phase distribution and fluid-fluid interactions, which influence capillary trapping and displacement efficiency.

The mean curvature functional (κ) is related to the shape of the fluid interfaces and can be used to infer capillary forces within the pore structure. It can be related to the capillary pressure (P_c) through the interfacial tension (σ) using the Young-Laplace equation (Eq. 2.8) [123]. By analysing the distribution of mean curvature, it is possible to understand the stability of fluid configurations and how they evolve over time, particularly during imbibition and gas trapping processes. The connectivity functional (C_f) is linked to the topology of the fluid phase, describing how isolated or connected the gas structures are within the porous medium. The Euler characteristic (χ) is derived from this functional and provides a measure of the number of isolated clusters or interconnected ganglia. Changes in connectivity, such as the transition from multiple small gas clusters to a single large gas structure due to Ostwald ripening, can be captured through this metric.

2.3 X-ray Imaging

Over the last two decades, pore-scale imaging has developed rapidly to describe the geometry of the rock and the multiphase flow dynamics. In 1987, Flannery et al. [124] obtained grey-scale images by a scanner. The images contain details of the pore space of rocks for segmentation. Development of this imaging technique continued by building a laboratory facility (Australian National University in collaboration with the University of New South Wales) to image a wide range of rock samples and predict different properties of fluids [125]. An image can be two or three dimensional and is defined by $f(x, y, z)$. Each value represents the brightness of the pixel/voxel, as shown in Fig. 2.9. They can be represented in different types such as 8bit, RGB, 16 bit or 32 bit float.

2.3.1 Micro-Computed Tomography

Computed tomography can be described in four types: conventional, high resolution, ultra high resolution and microtomography with the scale of resolution mm , $100 \mu m$, $10 \mu m$ and μm , respectively. The simplest elements of X-ray tomography are the X-ray source and a signal set of X-ray intensity measurements, known as a view. In computed tomography, multiple sets of views of an object are required over a range of angular orientations. The X-ray intensity, the spectrum of X-ray energies generated and the size of the focal spot are required to determine the effectiveness of X-ray on a sample.

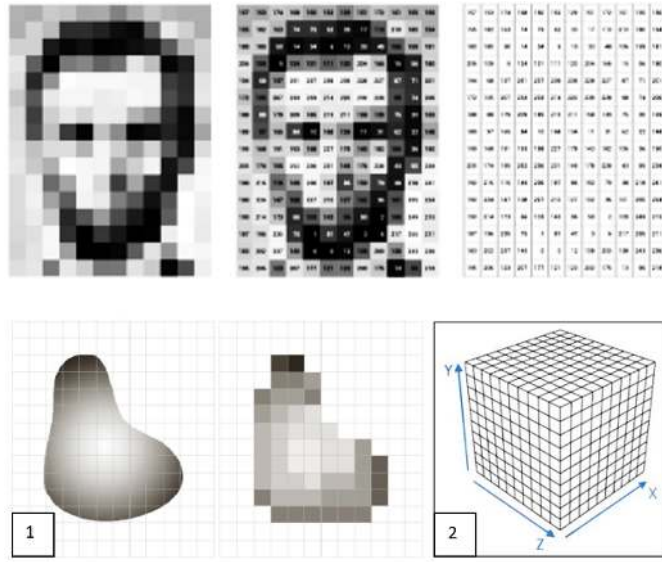


Figure 2.9: Continuous image projected onto a sensor array (discretised values), (1) 2D and (2) 3D.

When photons interact with solids, they transmit through the materials and the attenuation of X-ray follows Lambert-Beer's law. This law is only valid if all photons have the same energy and wavelength [126],

$$I = I_0 \exp(-\lambda x), \quad (2.21)$$

where x is the length of the X-ray path through the material, λ is the linear attenuation coefficient for the material being scanned and I_0 is the initial X-ray intensity. The quality of an image is directly related to the detectors. Several detectors show the amount of gathered data and the amount of an averaged sample can be determined from the size of an individual detector. Fitting the sample inside of the field view and avoiding any movement of the sample during the scan is necessary. Reconstruction technique is a method to convert sinograms into two-dimensional image slices to have a range which is determined by the computer system [11, 126]. Using a micro-CT scanner is a new approach to image a rock sample, which is a laboratory instrument and provides its source of X-ray, as shown in Fig. 2.10.

A three-dimensional representation of rocks and fluids is produced from a series of two-dimensional projections taken at different angles. The energy spectrum generated from micro-CT machines is in the range 30-60 keV with corresponding wavelengths 0.04-0.1 nm, which produces images of around 1000^3 - 2000^3 voxels. Two factors governing the image resolution are the sample size and the proximity of the sample to the beam. When the images are obtained, they are reconstructed and aligned as 3D images. Noises and artefacts should be removed before the segmentation step. Then, the images are segmented into the grain and different fluid phases such as water, oil or gas [126, 127].

2.3.2 Synchrotron Tomography

Recently, synchrotron light has been used to explore the dynamic displacement processes of multiphase flow in porous media. The history of ~~synchrotron goes to~~ 1873, when Clerk Maxwell changed the understanding of light. Some years later, this theory was expanded and X-ray light was identified. In 1946, the first synchrotron was built and designed to study collisions among high energy particles. Over the years, the number of experiments using synchrotron light increased and in 1980, the world's first synchrotron was built in the UK at Daresbury in Cheshire. Now there are around 40 large synchrotron light sources around the world to support a wide range of experiments with different applications in e.g. health and medicine, engineering, environmental science and many more [128].

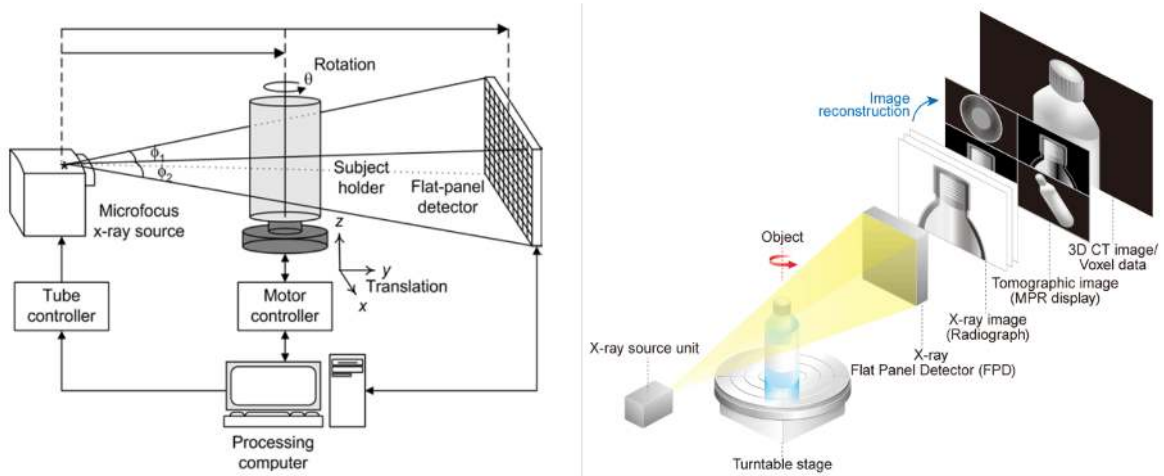


Figure 2.10: Diagram of a micro-CT system. The X-ray source, rotating sample stage, and flat-panel detector are shown, illustrating how the instrument generates radiographic projections of a rock sample. These projections are then reconstructed into tomographic images and 3D voxel data for detailed analysis [11, 12].

A synchrotron is a circular particle accelerator that uses a guiding magnetic field to increase the kinetic energy of beam particles. The fast-moving charged electrons produce very bright light, known as synchrotron light. It is 10 million times brighter than the sun and millions of times brighter than light produced from conventional sources. ~~Synchrotron can be described as source of synchrotron light and high energy physics machines.~~ This method has a great advantage for capturing sample images, as it provides a higher time resolution compared to the lab-based micro-CT. In a lab-based micro-CT a conical X-ray beam makes geometrical magnification, while the X-ray beam for the synchrotron light source is almost parallel, which results in a stronger intensity at synchrotron sources. A polychromatic X-ray beam is created in the synchrotron and it passes through the monochromator, and a thin scintillator screen detects the high flux of X-ray and converts it into visible light [129]. An example of synchrotron light building is shown in Appendix Fig. A.1.

2.4 Literature Review

This section reviews recent studies on two-phase flow dynamics within porous media, particularly concerning gas-liquid systems like hydrogen and water. As these processes are fundamental to various energy and environmental applications, including underground hydrogen storage, understanding the interplay of factors such as hysteresis, capillary pressure, wettability, and Ostwald ripening is critical. We will examine recent experimental and numerical studies, highlighting advancements in measurement techniques like micro-CT imaging and *in-situ* observations. By synthesising findings from the latest research, this review aims to provide a comprehensive overview of the current state of knowledge, identify gaps, and outline future directions in the study of two-phase flow (hydrogen-water) in porous media.

2.4.1 Two-phase Flow

~~Two-phase flow in porous media refers to the simultaneous movement of two immiscible fluids, such as gas and liquid, through a porous medium. This phenomenon is critical in various fields, including petroleum engineering, chemical processing, and environmental science, as well as in emerging technologies like underground hydrogen storage (UHS). Understanding two-phase flow dynamics is essential for optimising processes like oil recovery, CO₂ sequestration, and hydrogen storage, where the interaction between the two phases significantly influences system performance. The behaviour of two-phase flow in porous media is governed by a set of equations, including the continuity equation and Darcy's law for multiphase flow. These equations are often coupled with empirical relationships such as the capillary pressure-saturation curve and relative permeability-saturation functions. The flow regimes, ranging from bubbly to annular flow, depend on the flow rates and fluid properties, and these regimes are characterised by distinct patterns of phase distribution and movement [118, 130–133].~~

 Core flooding experiments, micro-CT imaging, and microfluidic devices are commonly used to study two-phase flow. These techniques allow for the visualisation and quantification of fluid distributions and flow patterns at the pore scale. For instance, micro-CT imaging provides detailed 3D images of fluid saturation and distribution within rock samples, offering insights into phenomena like snap-off and capillary trapping. Numerical simulations, including pore-scale modelling and continuum-scale approaches, are used to predict two-phase flow behaviour in porous media. These models help in understanding complex interactions and scale-up from laboratory experiments to field-scale applications. Advances in computational power and algorithms have enabled more accurate and detailed simulations, capturing the impact of pore-scale heterogeneities and fluid properties [126, 134, 135].

Recent studies have focused on the unique characteristics of hydrogen in two-phase flow, particularly in the context of UHS. Due to hydrogen's low viscosity and high diffusivity, it exhibits different flow behaviour compared to other gases like methane or CO₂. For instance, hydrogen tends to migrate through preferential pathways in heterogeneous rock formations, affecting storage efficiency and recovery. Recent experimental work has demonstrated that capillary trapping can significantly reduce hydrogen recovery, and small-scale heterogeneities in rock samples can

lead to unexpected flow and trapping behaviours. Accurately modelling two-phase flow remains challenging due to the complexity of interactions between the phases and the porous medium. Factors such as pore-scale heterogeneity, wettability alterations, and the presence of mixed-wet systems add layers of complexity. Additionally, phenomena like Ostwald ripening, where dissolved gases can affect the redistribution of phases, are often overlooked but crucial for accurate modelling [136–139].

2.4.2 Distribution of Hydrogen at the Porescale

Earlier studies using X-ray imaging focused on studying unsteady-state two-phase displacement, which provided valuable information on trapping and recovery efficiency for carbon dioxide storage and oil recovery applications, but it is not known if hydrogen behaves similarly in subsurface rocks [140–143]. Recent studies have used non-invasive high-resolution 3D X-ray imaging to study hydrogen trapped within rock that is otherwise saturated with water. These studies have revealed that hydrogen can be trapped to a significant degree, which may impact the effectiveness of storage and retrieval processes [136, 144]. Boon and Hajibeygi [17] characterised hydrogen transport in geological porous, using medical X-ray CT scanning. At the centimeter scale, the interplay of viscous, capillary and viscous forces determines the amount of hydrogen trapping. Jangda et al. [145] studied, cyclic hydrogen flow visualisation experiments on a layered rock sample with varying pore and throat sizes showed that hydrogen follows larger pores and throats through low permeability layers during drainage, reducing storage capacity. Imbibition unexpectedly resulted in higher hydrogen saturation due to rock heterogeneity. These findings emphasise the importance of considering small-scale heterogeneity and dissolution effects in reservoir models for efficient underground hydrogen. Thaysan et al. [144] showed that during secondary imbibition, hydrogen recovery decreased with pressure, with lower recoveries at higher pressures. They suggested that future hydrogen storage operations in porous media should consider more shallow and lower-pressure sites to optimise recoverability.

2.4.3 Hydrogen-Wettability

~~Wettability refers to the preference of a solid surface to be in contact with one fluid over another. It is quantified by the contact angle, which is the angle at which a fluid interface meets the solid surface.~~ Several methods have been employed in recent studies to investigate hydrogen wettability, such as measuring contact angles, using the tilted plate technique [140], the captive bubble cell approach [141], direct X-ray imaging inside the rock [142] and in microfluidics devices [143]. These studies have found similar contact angles for hydrogen, methane, nitrogen, and carbon dioxide, despite the different multiphase flow parameters expected for hydrogen and water due to the interplay of viscous, capillary, and gravitational forces [143, 146–148]. Jangda et al. [136] initially investigated the trapping of hydrogen after injecting brine that was both pre-equilibrated and non-pre-equilibrated with hydrogen at high pressure and high temperature. They found average contact angles of 54° and 53°, respectively, with a reduction in residual saturation using non-H₂-equilibrated brine, suggesting that hydrogen dissolution affects the

gaseous phase presence. Iglauer et al. [140] investigated hydrogen wettability of reservoir rocks at various geo-storage conditions. They found increasing pressure, temperature, and organic surface concentrations increases hydrogen wettability. However, in all cases hydrogen was the non-wetting phase in the presence of brine.

Recently, physicochemical interactions of hydrogen with a solid surface on wettability has been studied on sandstone rocks. For the first time, Higgs et al. [142] studied the characterisation of the wettability and interfacial tension of a hydrogen-brine-quartz system, using **in-situ** methods for contact angle measurements. They continued their work on Underground Hydrogen Storage (UHS) in Bentheimer sandstone and found that hydrogen has low relative permeability and significant capillary trapping, resulting in a residual gas saturation of 0.4. Micro-CT imaging confirmed a water-wet system with slight hysteresis. High capillary numbers increased initial gas saturation, but high capillary pressures pose challenges for commercial application [15]. Jha et al. [20] used X-ray imaging to examine the hydrogen saturation in initially brine-saturated sandstone. These studies found initial hydrogen saturation of up to 65% after primary drainage and a maximum residual saturation of 41% after imbibition. They also investigated the H₂/brine/rock wettability and measured the contact angle by direct measurement on the images using the method of AlRatout et al. [149] that we will employ in our work. Reviewing these papers concludes that hydrogen is a non-wetting phase, which occupies the centre of the largest pores.

2.4.4 Capillary Pressure

Capillary pressure arises from the interaction between the fluids and the solid matrix of the porous medium. It is a function of the interfacial tension between the fluids and the wetting properties of the solid surface. Capillary pressure plays a pivotal role in determining the distribution of fluids within the porous structure, influencing factors such as fluid displacement and trapping. Yekta et al. [16] studied capillary pressure and relative permeability for hydrogen-water systems. They conducted a series of steady-state core floods using a Triassic sandstone sample and measured capillary pressures using the mercury injection method. The results of capillary number calculations showed a capillary flow regime for the hydrogen-water system. They also reported the interfacial tension value between hydrogen and water 0.051 N/m, which is less than interfacial tension for a methane-water system at the same experimental conditions.

2.4.5 Hysteresis

An underground hydrogen storage project generally follows a cyclic operation with alternate periods of injection and withdrawal, depending on energy demand and the type of storage field used. The timing of injection and withdrawal can vary based on seasonal energy demand. These cycles involve primary drainage (hydrogen injection), secondary imbibition (hydrogen withdrawal), and secondary drainage (re-injection) followed by repeated withdrawal and injection. This is different from carbon dioxide storage, where only primary drainage (initial injection) and secondary imbibition (water displacement and capillary trapping) occur. The design and management of hydrogen storage require the consideration of hysteresis during multiple cycles of drainage and

imbibition; this hysteresis controls the amount of hydrogen that can be recovered and how much is trapped in the pore space [20, 26, 113, 150].

To thoroughly examine hysteresis, it is imperative to study multiple fluid injection cycles. The reason for this is that capillary pressure is not solely dependent on saturation, but also on the saturation history [77–79]. Hysteresis is caused by different displacement processes and trapping at the pore scale. Hysteresis in capillary pressure – the pressure difference between the gaseous and aqueous phases – leads to differences between primary drainage, imbibition and secondary drainage, as illustrated schematically in Fig. 2.11. Herring et al. [151] used time-resolved X-ray imaging to study three cycles of drainage and imbibition with supercritical CO_2 and brine. They observed increased trapping after the first cycle, possibly due to dissolution effects in subsequent cycles during the 30 pore volumes of water flooding, whereas we find reduced trapping.

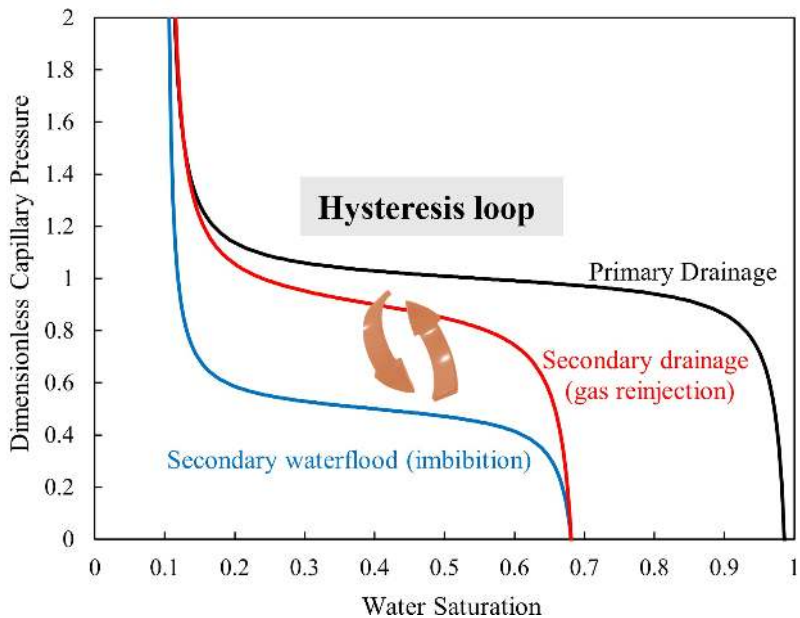


Figure 2.11: A schematic of the traditional model of hysteresis in capillary pressure. It is assumed that subsequent displacements, regardless of starting and finishing capillary pressure and the order of imbibition and drainage, cannot lie in the capillary pressure-saturation plot outside the bounds indicated for imbibition and secondary drainage. We will show that Ostwald ripening facilitates the repositioning of gas within the pore space, leading to reduced trapping and capillary pressures that lie outside these bounding curves.

Recent work by Kumbhat and Ebigo [152] underscores the significant role of hysteresis in underground hydrogen storage, showing that hysteresis affects UHS operations, particularly during early cycles. They found that relative permeability hysteresis leads to increased hydrogen trapping, resulting in a less mobile plume and a more dispersed hydrogen mass. This behaviour negatively impacts hydrogen recovery, particularly in initial storage cycles. Pan et al. [153] studied also the effects of relative permeability hysteresis on UHS in saline aquifers and their results showed that lowering the hydrogen withdrawal factor reduces the efficiency of hydrogen extraction from storage, but it also leads to higher purity in the withdrawn hydrogen gas. Additionally, this adjustment influences the flow dynamics, affecting the interaction between hy-

drogen and brine and altering the overall performance of the storage system. Lysyy et al. [154] examined hydrogen storage in aquifers and found that neglecting relative permeability hysteresis significantly impacts the accuracy of storage estimates, leading to an overestimation of annual working gas capacity by 34% and recovered hydrogen volume by 85%. Hysteresis causes reductions in both working gas capacity and recovery factor, with a 15% decrease observed after the first cycle. Furthermore, it influences injection and withdrawal rates, ultimately reducing the efficiency of hydrogen recovery.

Recent studies have further advanced the understanding of hysteresis and capillary trapping in hydrogen storage. For example, Khan et al. [155] performed a pore-to-reservoir scale analysis of capillary trapping in underground hydrogen storage and their findings suggest that capillary forces play a significant role in hydrogen entrapment, leading to increased hysteresis and reduced recovery in subsurface environments. Shiran et al. [156] showed that higher injection rates enhance hydrogen saturation. However, cyclic injection and withdrawal resulted in increased residual hydrogen trapping after each cycle, which they attributed to hysteresis effects. The authors suggested that hydrogen dissolution into brine might contribute to this residual trapping; however, their experiments did not involve pre-equilibrated brine. This contrasts with our findings, where pre-equilibration of brine with hydrogen minimised dissolution effects and led to reduced residual trapping over three cycles.

Bahrami et al. [157] developed a quasi-2D microfluidic system to investigate hydrogen-water flow dynamics and their findings highlight the preferentially water-wet nature of hydrogen in porous media and the significant hysteresis between drainage and imbibition stages. Lysyy et al. [146] conducted microfluidic experiments and observed that an increase in the capillary number enhances hydrogen saturation following the drainage phase. Adding to this understanding, Yu et al. [158] analysed the effects of pore geometry and injection rate on residual trapping through dead-end bypassing. Their findings revealed that a higher pore height-to-width ratio increases residual trapping up to a critical threshold before decreasing and that a converging-shaped pore reduces trapping volume. Song et al. [159] observed that flow is more obstructed in regions with low pore-throat ratios and that flow behaviour changes suddenly when transitioning from wide pores to narrow throats. In addition, Wang et al. [160] studied hydrogen transport under varying wetting conditions and found that less water-wet conditions led to fewer instances of snap-off and greater storage efficiency during drainage, promoting the formation of larger hydrogen clusters during imbibition.

Regardless of the type of displacement, for immiscible phases with no alteration of wettability, in capillary equilibrium, it is impossible for the capillary pressure to lie outside the region between the secondary drainage and imbibition values for subsequent displacement cycles [64]. However, if the gas has any solubility in the aqueous phase, there is an additional constraint: local differences in local capillary pressure lead to slightly different solubilities, resulting in concentration gradients of dissolved gas. The dissolved gas will diffuse to achieve a constant concentration in the aqueous phase, which is only possible once the local capillary pressure is everywhere constant. This leads to rearrangement of the gaseous phase, over time-scales of hours to days at the millimetre scale mediated by transport of dissolved species in a process called

Ostwald ripening [161].

2.4.6 Ostwald Ripening

Another aspect of hydrogen storage is that the trapping and movement of hydrogen in its own phase might be affected by the transport of dissolved gas. In oilfield operations, it is commonly assumed that the dissolution of hydrocarbons is insignificant and that hysteresis is caused by the displacement between completely immiscible phases. This assumption is reflected in the use of hydrocarbon-water properties to describe hydrogen storage. However, both with hydrogen and carbon dioxide, this assumption is not valid [113–115]. ~~Ostwald ripening impacts the distribution of fluids in porous media. Differences in local capillary pressure lead to differences in the concentration of dissolved gas from Henry's law. This in turn results in concentration gradients in the aqueous phase and diffusion of dissolved gas away from regions of high capillary pressure. Equilibrium is reached when the capillary pressure is uniform throughout the system.~~

Several studies have investigated the effect of Ostwald ripening in porous media on the distribution of gases, such as carbon dioxide and air. Zhang et al. [27] explored hydrogen injection and withdrawal dynamics, comparing results with a parallel nitrogen experiment. Their findings revealed the disappearance of smaller hydrogen ganglia and expansion of larger ones maintaining the overall gas volume—a phenomenon not observed with nitrogen, where the fluid configuration remained unchanged. They suggested that this redistribution of hydrogen is facilitated by Ostwald ripening. Singh et al. [162,163] explored Ostwald ripening in different pore geometries and their simulations demonstrated that Ostwald ripening plays a crucial role in heterogeneous or fractured porous media, influencing gas storage in transition zones between oil and water.

Garing et al. [138] and De-Chalendar et al. [114] conducted comprehensive studies combining experimental observations and theoretical analyses. Their research evaluated how Ostwald ripening influences the micro-scale distribution of carbon dioxide within pores. In line with these studies, the experiment by Boon et al. [21] demonstrated that during no-flow periods, medium-sized hydrogen ganglia fragmented, while larger ganglia grew, providing direct evidence of Ostwald ripening.

 A recent study utilised X-ray tomography to investigate hysteresis from repeated hydrogen injection and withdrawal cycles in a Bentheimer sandstone sample. The results revealed capillary pressure hysteresis and hydrogen migration through Ostwald ripening due to gas diffusion in brine. Sixteen hours post-injection, hydrogen aggregated into larger ganglia with improved connectivity, as evidenced by a decreased Euler characteristic. This study suggests that Ostwald ripening reduces hysteresis and enhances connectivity, a factor often overlooked in hydrocarbon flow models [18]. Blunt [161] predicted the rearrangement of gas under capillary-gravity equilibrium and determined the time required to reach these states. His research showed that significant reorganisation of gas can occur over periods ranging from hours to months and across distances from millimetres to centimetres. However, the impact on residual saturation and capillary pressure hysteresis has not been quantified: this is the aim of this research.

Hysteresis in capillary pressure and relative permeability for repeated cycles of gas injection and

withdrawal has been studied in the literature [164–167]. However, there has been no discussion of time-dependent behaviour due to Ostwald ripening and the difference with oil/water systems where this effect is negligible. Herring et al. [168] used time-resolved X-ray imaging to study three cycles of drainage and imbibition with supercritical CO₂ and brine. They found more trapping after the first cycle, whereas we find less, but their result could be due to dissolution in subsequent cycles during the 30 pore volumes of water flooding. Recently Li et al. [169] found Ostwald ripening was identified as a key phenomenon affecting long-term CO₂ storage during CO₂-WAG injection experiments in carbonate rocks. This process, driven by diffusion, allows for the local reconnection of capillary-trapped CO₂, potentially reducing the amount of CO₂ trapped over time and enhancing its migration. Although capillary trapping is crucial for maintaining CO₂ storage, Ostwald ripening facilitates gas ganglia rearrangement due to concentration differences in dissolved CO₂, gradually moving the system toward gravity-capillary equilibrium. The study found that while the height of the transition zone where capillary trapping occurs is relatively small (less than 1 meter), the time required for equilibrium to be reached is substantial—ranging from 0.36 to 2 million years, depending on the rock type.

Several studies have investigated hydrogen storage in Bentheimer sandstone under various conditions, as summarised in Table 2.1. Higgs et al. [142] highlighted that the recovery of hydrogen gas from porous reservoir rocks is significantly influenced by the wettability of the sandstone. They reported that the hydrogen-brine-quartz system exhibits a water-wet nature, enabling a large percentage of gas to be recovered. A more recent study by Higgs et al. [15] measured relative permeability hysteresis during co-injection core floods of hydrogen and water. Their findings indicate that capillary trapping results in a high residual gas saturation, which significantly impacts the injectivity and the storage efficiency of hydrogen. Jangda et al. [136] identified that the strongly water-wet nature of Bentheimer sandstone contributes to reduced capillary hysteresis, thereby enhancing fluid displacement efficiency during hydrogen storage. We will study Bentheimer sandstone in this study as an exemplar of a permeable formation used for hydrogen storage.

2.5 Research Questions

Hysteresis is a critical phenomenon in multiphase flow, describing the non-unique relationship between capillary pressure and saturation. Its understanding is particularly crucial in the context of hydrogen storage, where efficient injection and withdrawal depend on minimising trapping and maximising recovery. Hydrogen storage in porous media poses unique challenges due to its susceptibility to hysteresis effects, which traditional hydrocarbon models fail to adequately capture. By addressing these limitations, this research aims to enhance the reliability of hydrogen storage systems. This work leverages Minkowski functionals—saturation, interfacial area, curvature, and Gaussian curvature—which offer a complete geometric description of fluid behaviour in porous media. While these functionals have theoretical significance, their role in hysteresis has remained underexplored, primarily due to the lack of experimental techniques capable of capturing these properties at the pore scale. Recent ~~advancements~~ in high-resolution X-ray

tomography now provide the tools to bridge this gap, enabling a detailed investigation of the interplay between Minkowski functionals and hysteresis.

The research addresses the following scientific questions:

- How does the trapping of hydrogen in porous media evolve during repeated injection and withdrawal cycles?
- How does Ostwald ripening influence these changes, and what implications does this have for residual saturation and recovery efficiency?
- Can high-resolution X-ray imaging reveal reduced hysteresis and trapping during cyclic hydrogen injection compared to traditional hysteresis models that neglect Ostwald ripening?
- What is the role of Minkowski functionals in characterising hysteresis, and how do their interrelationships influence capillary pressure and fluid connectivity?

2.5.0.1 Scientific Significance

This research contributes to the growing field of hydrogen storage by addressing key challenges in the understanding and modelling of hysteresis in multiphase flow. By studying the interplay of Minkowski functionals and leveraging high-resolution X-ray imaging, this work advances the theoretical understanding of hysteresis while providing experimental data that challenge traditional hydrocarbon-based models. The outcomes of this research have significant implications for renewable energy technologies, particularly the development of reliable and efficient underground hydrogen storage systems. The insights gained may also extend to related fields, such as carbon sequestration and hydrology, where hysteresis plays a critical role.

To achieve the stated objectives, high-resolution three-dimensional X-ray imaging experiments were conducted using Bentheimer sandstone as the porous medium. This experimental ~~setup~~ enabled the direct observation of gas-phase rearrangements, quantification of pore occupancy, and estimation of capillary pressure from meniscus curvature. Additionally, the experiments systematically analysed the time-dependent effects of Ostwald ripening on hysteresis, residual saturation, and recovery efficiency. The data collected provide a foundation for establishing a unique relationship among Minkowski functionals and understanding their role in multiphase flow hysteresis.

Table 2.1: Summary of published pore-scale hydrogen displacement in sandstone and experimental conditions.

Study	Sample	Displacement	P & T	Main Results	Year
Jha et al. [20]	Gosford sandstone	Unsteady-state	0.1 MPa, ~20°C	Sandstone aquifers are favourable for hydrogen storage.	2021
Lysyy et al. [150]	Berea sandstone	Steady-state	3 MPa, 30°C	Strong hysteresis effects during primary drainage, imbibition, and secondary drainage.	2022
Thayesen et al. [19]	Clashach sandstone	Unsteady-state	2 MPa, 20°C	Higher pressures lead to increased hydrogen trapping and lower recovery, while high capillary numbers improve recovery.	2022
Rezaei et al. [170]	Sandstone	Unsteady-state	0.1-20.68 MPa, 80°C	Rock type influences hydrogen flow, pressure reduces permeability, and salinity has minimal effects.	2022
Boon and Hajibeygi [17]	Berea sandstone	Steady-state	10 MPa, 18°C	Capillary forces can create barriers that temporarily prevent hydrogen from moving freely, leading to increased overall hydrogen coverage.	2022
Higgs et al. [139]	Bentheimer sandstone	Unsteady-state	2.13 MPa, 24.85°C	Hydrogen behaves similarly to methane in shallow and low-pressure reservoirs.	2023
Zhang et al. [27]	Bentheimer sandstone	Unsteady-state	1 MPa, 23°C	After 12 hours of no flow, a significant rearrangement of trapped hydrogen occurred, driven by Ostwald ripening, which helped reduce capillary pressure hysteresis.	2023

Jangda et al. [136]	Bentheimer sandstone	Unsteady-state	10 MPa, 50°C	Hydrogen dissolution into brine is a critical factor for understanding hydrogen recovery during underground storage. 2023
Dokhan et al. [171]	Bentheimer sandstone	Unsteady-state	1 MPa, 20°C	Gas expansion increased the average gas saturation and, during withdrawal, can enhance hydrogen recovery by remobilising trapped hydrogen. 2024
Goodarzi et al. [18]	Bentheimer sandstone	Unsteady-state	1 MPa, 25°C	Ostwald ripening, driven by the diffusion of dissolved gas in brine, leads to less hysteresis and improved connectivity in H ₂ storage. 2024
Bijay et al. [172]	Berea sandstone	Unsteady-state	20 MPa, 20°C	Early H ₂ breakthrough and low initial saturation were observed due to the formation of capillary fingers. 2024
Medina et al. [173]	Silicon-wafer	Unsteady-state	3 MPa, 20°C	Hydrogen saturation, contact angle, and dissolution depend on brine type, salinity, and pressure. 2024
Jangda et al. [145]	Clashach sandstone	Unsteady-state	10 MPa, 50°C	Capillary pressure complicates fluid displacement in heterogeneous rocks. 2024
Higgs et al. [15]	Bentheimer sandstone	Steady-state	2.12 MPa, 25°C	High capillary numbers are needed for complete pore space saturation. 2024

Chapter 3

Trapping, Hysteresis and Ostwald Ripening in Hydrogen Storage

The contents of this chapter have been published in:

S. Goodarzi, Y. Zhang, S. Foroughi, B. Bijeljic, M. J. Blunt, “Trapping, hysteresis and Ostwald ripening in hydrogen storage: A pore-scale imaging study,” International Journal of Hydrogen Energy, vol. 56, pp. 1139–1151, 2024.

3.1 Summary

This study used X-ray tomography to investigate hysteresis during repeated hydrogen injection and withdrawal in a Bentheimer sandstone sample. An unsteady state experiment evaluated the distribution of hydrogen and brine after drainage and imbibition cycles, with imaging conducted immediately after injection and 16 hours later. Hydrogen was injected at 1 MPa and ambient temperature over three cycles, followed by water flooding. The results revealed capillary pressure hysteresis and hydrogen migration via Ostwald ripening, driven by gas diffusion in the brine. These processes were characterised by analysing interfacial curvature, area, connectivity, and pore occupancy. Hydrogen preferentially occupied larger pore spaces, consistent with water-wet conditions. After 16 hours, hydrogen aggregated into larger ganglia, with a single large connected ganglion dominating the volume. The Euler characteristic decreased over this period, indicating improved connectivity. The work implies that Ostwald ripening – mass transport of dissolved gas – leads to less hysteresis and better connectivity than would be assumed ignoring this effect, as done in assessments of hydrocarbon flow and trapping.

3.2 Materials and Methods

3.2.1 Rock Sample

Bentheimer sandstone is a highly homogeneous and well-sorted quartz sandstone. It originates from the Lower Cretaceous period and is primarily found in the Bentheim region of Germany.

This rock has been widely studied and is recognised for its consistent properties, making it a standard material in geological and petrophysical research. Bentheimer sandstone has high porosity (approximately 20-25%) and permeability (ranging from 1 to 2 Darcy). These properties make it ideal for experiments requiring detailed fluid flow and pore structure analysis. The mineral composition is predominantly quartz (approximately 90-95%), with minor feldspar and clay minerals [174]. The grains are well-rounded and cemented with silica, contributing to the rock's mechanical stability.

Among other potential rock types, see Fig. 3.1, Bentheimer sandstone stood out for its unique combination of desirable properties. For instance, Berea sandstone, another widely used rock, is known for its moderate porosity (15-20%) and permeability, but it can exhibit heterogeneity in mineral composition and pore structure, complicating experimental repeatability [175, 176]. Similarly, Fontainebleau sandstone, while highly homogeneous and composed predominantly of quartz, has much lower porosity (7-10%), making it less suitable for experiments that require high pore connectivity [177].

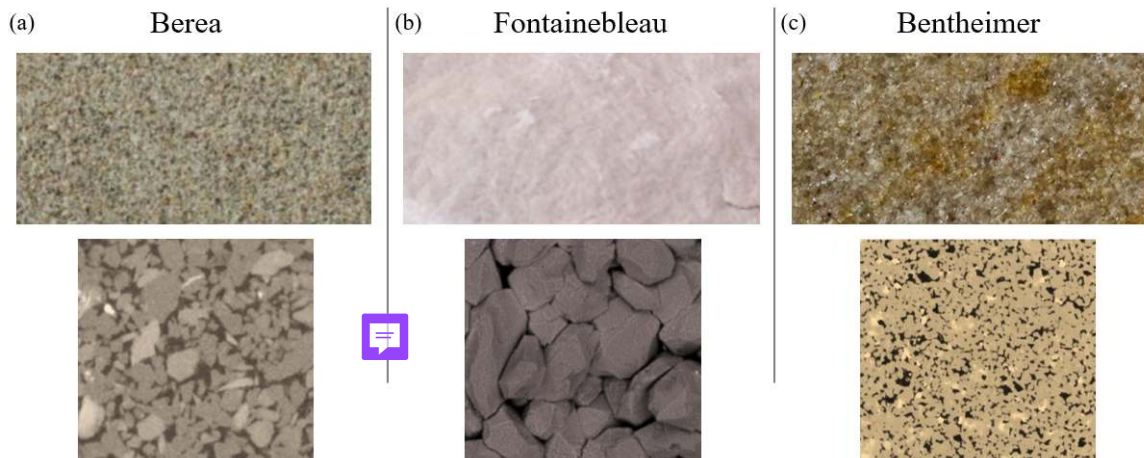


Figure 3.1: Comparison of three commonly used sandstone types in experimental studies. The top row shows macroscopic views of Berea sandstone (a), Fontainebleau sandstone (b), and Bentheimer sandstone (c), highlighting differences in texture and colouration. The bottom row shows microscopic views or pore structures, illustrating variations in grain shape, size, and porosity [13].

This sandstone was chosen for this experimental studies due to its uniform pore structure and predictable behaviour under laboratory conditions. Its high porosity and permeability facilitate the visualisation and quantification of fluid flow and transport properties using advanced techniques like X-ray micro-tomography. Additionally, the well-documented properties of Bentheimer sandstone in the literature [168, 178, 179] provide a robust baseline for comparison and validation of experimental results. Its consistent properties allow researchers to isolate and study specific physical phenomena without the complications of heterogeneous materials. By centralising this information, this subsection serves as a reference point for understanding the relevance of Bentheimer sandstone in the context of this thesis. Details provided here will be referred to throughout the experimental chapters as needed.

3.2.2 Fluid Properties

For this experiment, hydrogen was selected as the gas phase, and brine doped with potassium iodide (KI) was used as the liquid phase. The doping process was essential for improving the contrast between gas, water, and rock phases during imaging. Potassium ~~Iodide~~ (KI) was dissolved in deionised water to increase the brightness of the fluid phases, making them more distinguishable in the resulting CT images. The presence of KI, with its higher atomic radius, enhances phase contrast, enabling clearer imaging of the different fluid phases within the rock's pore network. Results from the doping process, shown in Fig. 3.2, demonstrate the optimal contrast achieved, where KI significantly improved the differentiation between phases. The greatest contrast between the phases was observed when KI was dissolved in deionised water with a weight percentage of 3.5%, as indicated in Fig. 3.2 (b). The fluid properties, including dynamic viscosity and interfacial tension are summarised in Table 3.1.

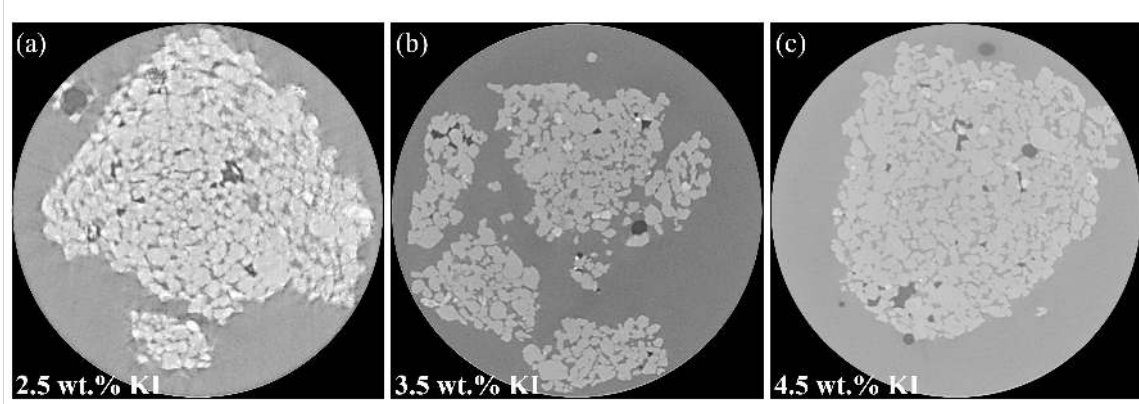


Figure 3.2: Three contrast scan images for the injection of deionised water-~~Potassium Iodide~~ solutions (2.5 wt.% - , 3.5 wt.% - and 4.5 wt.% -KI) into a Bentheimer sample.

Table 3.1: Thermophysical properties of the fluids used in the experiment, including density (ρ) measured at ambient temperature, dynamic viscosity (μ), and interfacial tension (σ). The values for brine are sourced from [27, 28], while hydrogen properties are obtained from [29].

Fluid	ρ (kg.m ⁻³)	μ (Pa.s)	σ (N.m ⁻¹)
Water-3.5 wt% KI	1011	0.821×10^{-3}	7.29×10^{-2} (σ_{wg})
Gas-H ₂	0.0354	8.8×10^{-5}	7.29×10^{-2} (σ_{gw})

3.2.3 Sample Preparation

The sample preparation process began with drilling a rock core of 12.8 mm in diameter and approximately 60 mm in length—larger than typical samples in the literature—constrained only by the available space in the CT scanner. After drying the sample in an oven for 24 hours, it was securely enclosed in a rubber. The rubber sleeve plays a crucial role in the experimental setup by providing flexibility, chemical resistance, and a reliable seal, preventing interaction with the confining fluid and isolating the sample from external influences. To further ensure sealing

integrity, PTFE tape was wrapped around the sleeve to prevent gas leakage, and aluminium foil was applied to seal the sample ends. Additional details about these materials can be found in Appendix B.1.

3.2.4 Experimental Procedure

The experiment was conducted under capillary-controlled conditions and with unsteady-state flooding. During the experiment, the pore pressure and confining pressure were maintained at a constant level of 1 MPa and 2 MPa, respectively, and the temperature was kept at 25° C. The capillary number (Ca) is calculated from Eq. 2.12 for 3 cycles, see Table 3.2. To investigate the saturation history, the flooding cycles were repeated three times, with the brine flow rate being held constant while the gas flow rate was varied.

Table 3.2: Capillary numbers, $Ca = \mu q / \sigma$, where μ is the viscosity of the injected fluid, σ is the interfacial tension, and q is the Darcy velocity for the flooding cycles.

Cycle	Flooding step	Flow Rate [ml.min ⁻¹]	$Ca_{[gw]}$	$Ca_{[wg]}$
1	1 st Drainage	2.00	3.22×10^{-7}	-
1	1 st Imbibition	0.06	-	8.93×10^{-8}
2	2 nd Drainage	0.40	6.45×10^{-8}	-
2	2 nd Imbibition	0.06	-	8.93×10^{-8}
3	3 rd Drainage	0.08	1.29×10^{-8}	-
3	3 rd Imbibition	0.06	-	8.93×10^{-8}

The protocol for initiating the unsteady-state two-phase flow micro-CT imaging experiment was as follows:

1. The sample was securely enclosed within a silicone rubber to prevent any interaction with the surrounding fluid. The top and bottom parts of the rubber were connected to the production and injection pieces, respectively, as shown in Fig. 3.3.
2. The coreholder was then positioned within the micro-CT scanner (Zeiss Xradia 510), and the necessary flowlines and pumps were set up to introduce the fluid phases. Further details on the pump types and materials can be found in Appendix B.3. To eliminate any air and prepare for hydrogen injection, the sample, lines, and gas pump were thoroughly vacuumed for several hours to ensure that no potentially hazardous hydrogen-air mixture could form. Basic health and safety precautions were followed throughout the procedure, with further details provided in Section 3.4.
3. The confining and back pressures of 1 MPa and 2 MPa, respectively, were applied. The pressure drop across the sample was accurately measured with a differential pressure transducer (Keller PD-33X), which was connected to the sample's inlet and outlet, with a precision of ± 0.03 kPa, see Appendix B.4 for more details.

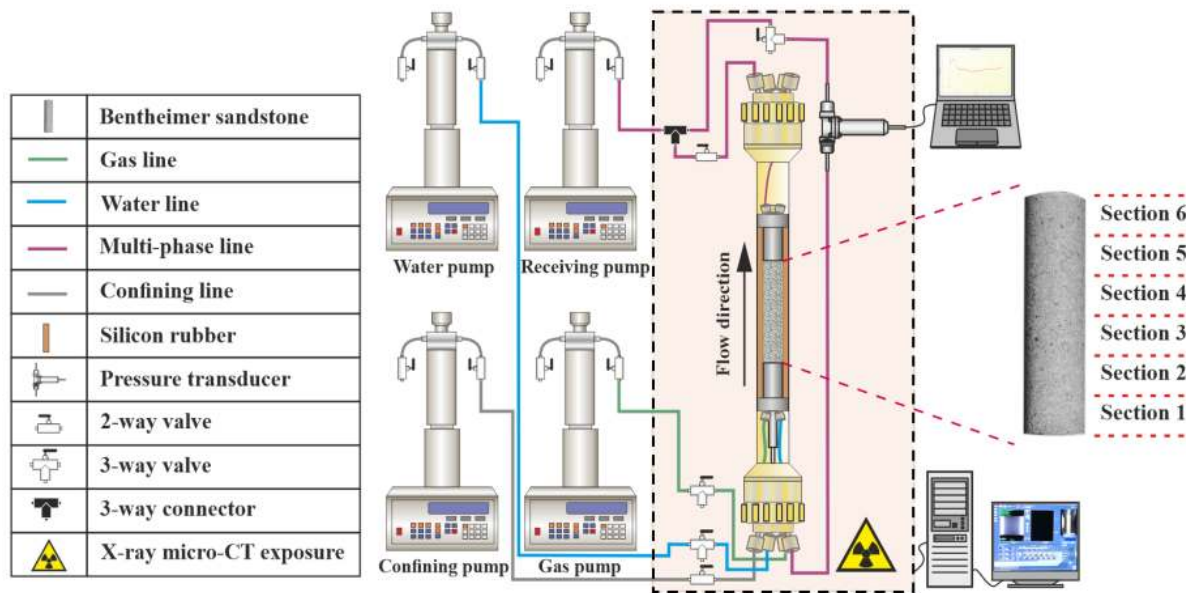


Figure 3.3: A schematic diagram for the two-phase hydrogen-brine experiment conducted with the X-ray microtomography scanner (micro-CT). The arrangement of the core holder, pumps, flow lines, valves, and pressure transducer used in the experiment are represented in the diagram. The micro-CT enclosure is indicated by the black dashed line.

4. The initial phase of the experiment involved scanning a dry sample. Subsequently, brine was introduced into the sample at a flow rate of 0.1 ml/min, starting from the bottom of the sample to achieve full saturation of the pore space. The brine flow rate was increased after 18 hours by 0.5 ml/min and the pressure drop was continuously monitored until it stabilised. At this stage, the sample's absolute permeability was determined as 1.4 ± 0.1 D ($1.4 \times 10^{-12} \pm 0.1 \times 10^{-12} \text{ m}^2$), as measured under the experimental conditions, more details are provided in Appendix B.2. The low flow rate brine injection continued overnight at 0.05 ml/min and the brine-saturated sample was simultaneously scanned.
5. Three flooding cycles were conducted consecutively using the same procedure, with the gas flow rate being reduced. Each cycle began by introducing 10 pore volumes of gas at a specified flow rate. For cycle one the gas flow rate was 2 ml/min, for cycle two was 0.4 ml/min and for cycle 3 was 0.08 ml/min. The duration of gas injection varied across the cycles, with a time of 2 hours for cycle 1, 8 hours for cycle 2 and 12 hours for cycle 3.
6. Once the gas injection (drainage) was completed after 2 hours, the valve was closed, and the gas pump was switched off. A bottom-to-top scan of the sample was performed for 12 hours, with each scan divided into six sections overlapping by 25%. Subsequently, after an additional 4 hours had passed, making it a total of 16 hours since the gas injection was stopped, images of sections 2 and 5 were captured over a period of four hours.
7. Ten pore volumes of brine were then injected (imbibition) at a steady flow rate of 0.06 ml/min for 6 hours, followed by another 12 hour bottom-to-top scan of the sample. After

a further 4 hours, images were taken of sections 2 and 5.

8. After completing the three cycles (steps 4-6), a scan of the entire sample was carried out 24 hours later to evaluate the residual gas content.

3.2.5 Image Acquisition

The imaging was performed using the Zeiss Xradia 510 X-ray scanner equipped with a flat panel detector. Further details about the scanner are provided in Appendix B.5, while the exposure time and number of projections are summarised in Table 3.3. The X-ray source was configured with a photon energy of 80 keV and a power of 7 W, with a 360° rotation angle of the sample. A single air filter was utilised between the source and sample. The detector provided three-dimensional images with a voxel size of 5.8 μm , which determines the spatial resolution of the scan and was selected to achieve a balance between resolution and scan duration. During each scan, a total of six images were taken with a vertical overlap of 4 mm to ensure the entire length of the sample was captured. In total, the images covered 2069 voxels in the x-direction, 2187 voxels in the y-direction, and 9594 voxels in the z-direction. Further details regarding the selection of scanning parameters, including projection number, exposure time, and voltage settings, are provided in Appendix B.6.

Table 3.3: Summary of scanning parameters for the Zeiss X-ray ~~microtomography~~ scanner used in the experiment. Initial scans include dry, wet, gas injection, and water injection steps, each comprising six overlapping sections to cover the entire sample length. After 16 hours, additional detailed scans of sections 2 and 5 were performed to monitor localised changes over time.

Step	Sections	Exposure time [s]	Projections	Total time [mins]
Dry scan	1-6	1.2	3001	120 \times 6
Wet scan	1-6	1.2	3001	120 \times 6
Gas injection	1-6	1.2	3001	120 \times 6
Water injection	1-6	1.2	3001	120 \times 6
16 hours storage	2,5	1.2	3001	120 \times 2

3.2.6 Image Processing

Image processing is a vital step for preparing datasets and extracting quantitative information. This involves preprocessing operations, such as noise reduction with Gaussian or median filters, to improve clarity and minimise artefacts, ensuring datasets are optimised for analysis. Segmentation, a key step in isolating regions of interest like solid phases or fluid boundaries, was performed using methods such as watershed segmentation and interactive thresholding. Specialised software like Avizo (ThermoFisher Scientific) [180, 181] was employed for visualisation, segmentation, and analysis of complex 3D datasets. Its advanced tools enable 3D reconstruction and interactive exploration, making it ideal for micro-tomography data. Additionally, ImageJ, with its customisation and automation capabilities [182, 183], complements workflows for specific

tasks. By integrating these tools, the transition from raw data to actionable insights is achieved, enabling accurate and reproducible measurements that align with research objectives.

The image processing workflow began with reconstructing all the images to make them compatible with the Avizo software for further processing [184]. Since the sample was captured in six individual scans that covered its entire length, these scans were stitched together to form a single, continuous image of the whole sample, as shown in Fig 3.4. Any unwanted regions, such as the rubber, were cropped out after stitching. This process was repeated for the other scans as well. Once the scans were stitched and the extraneous parts removed, the two-phase images were registered to the dry scan, allowing for a direct comparison of the pore-throat structures to facilitate detailed analysis. Then, we applied a non-local mean filter to reduce noise in our images [185].

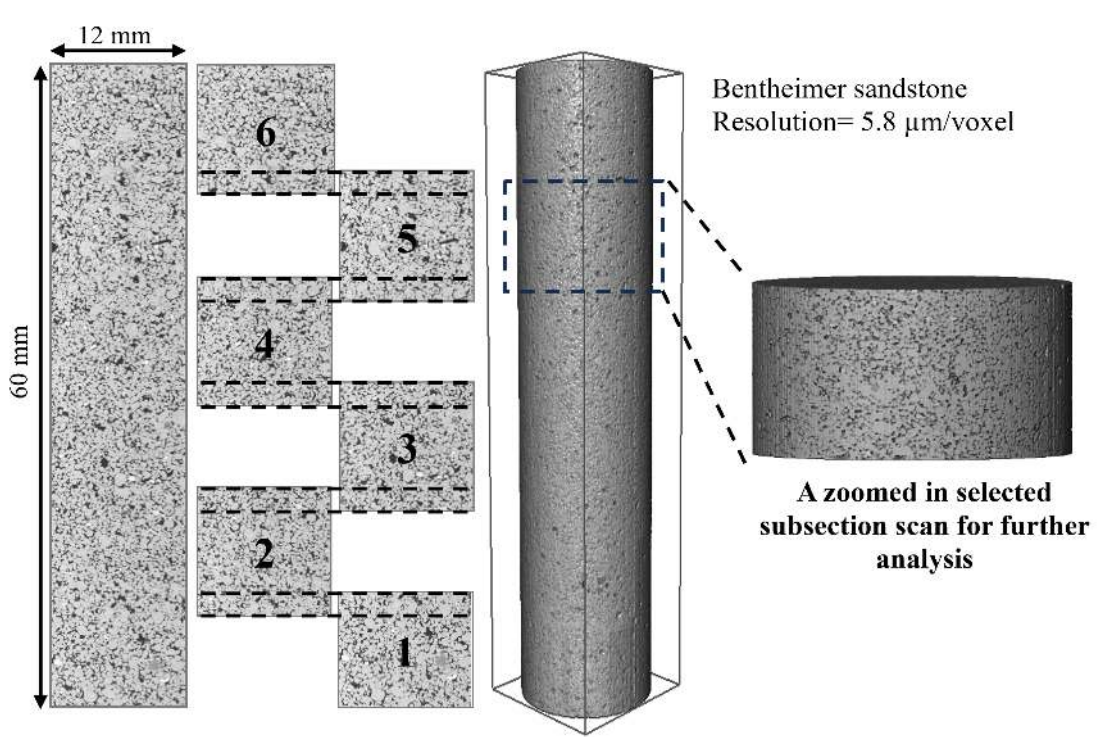


Figure 3.4: Schematic illustrating the stitching of six overlapping sections to produce a complete 3D image of the Bentheimer sandstone sample. Each section was scanned with an overlap to ensure high-resolution reconstruction. The resulting images achieved a spatial resolution of $5.8 \mu\text{m}/\text{voxel}$. A selected subsection, with dimensions of $2069 \times 2187 \times 1142$ voxels, was extracted for further detailed analysis in this study to investigate localised pore-scale features.

Next, we used the Interactive Thresholding technique in Avizo to segment the gas, brine, and rock phases. This method involves selecting grayscale intensity ranges for each phase, allowing for precise and real-time adjustments to ensure accurate separation. By combining visual feedback with histogram analysis, this approach ensures that transitions between phases are well-defined, even in areas with overlapping intensities. The segmentation process enabled the extraction of key parameters such as curvature, surface areas, and fluid saturation.

3.3 Results and Discussion

In this section, we present the key findings from our experiments. Section 3.3.1 details the pore-scale analysis derived from raw images. Section 3.3.2 explores the movement of gas within discrete ganglia, confirming gas migration towards larger bubbles after 16 hours. In Section 3.3.3, we describe the gas saturation profiles measured across the sample during three cycles of gas injection and water flooding. We also include a gas saturation profile for a sub-volume, both at its initial state and after 16 hours of waiting. Section 3.3.4 focuses on the local capillary pressure observed after gas and water injection during these three cycles. Section 3.3.5 presents the measurements of fluid-fluid and fluid-solid specific interfacial areas, plotted alongside the gas connectivity data from Section 3.3.6 and a quantification of the Pécelt number. Finally, Section 3.3.7 characterises the pore occupancy, including the distribution and arrangement of the fluids within the pore space.

3.3.1 Three-dimensional Raw Images

3.3.1.1 Greyscale Images

After analysing the full-cycle core flooding experiment, we observed the dynamic behaviour of gas, brine, and rock phases across multiple drainage and imbibition steps, see Fig. 3.5. The greyscale images illustrate how gas distribution evolves as brine is injected and displaced over successive cycles. While these images provide a broad overview of the fluid displacement process, a closer examination of a specific subvolume reveals additional insights into the behaviour of trapped gas over time.

Figure 3.6 focuses on a selected region within the sample, comparing its state immediately after gas injection to its configuration following 16 hours of undisturbed storage. Two key phenomena emerge: (i) some gas clusters shrink (blue dashed circles), and (ii) previously disconnected gas pockets merge, increasing phase connectivity (red dashed circles).

These observations indicate that gas redistribution occurs within the pore space even without active flow, likely driven by mechanisms such as Ostwald ripening. This provides direct evidence that, beyond primary drainage and imbibition, gas mobility and connectivity continue to evolve at the microscale, influencing long-term storage and recovery processes.

3.3.1.2 Segmented Images

Due to the scanning procedure described in Table 3.3, the sample was scanned after a 16-hour waiting period only for Sections 2 and 5. These specific sections were selected for further analysis to better capture the effects of gas redistribution over time. Figure 3.7 illustrates the arrangement of gas in the pore space after gas injection (drainage) and during the first two imbibition (water flooding) cycles.

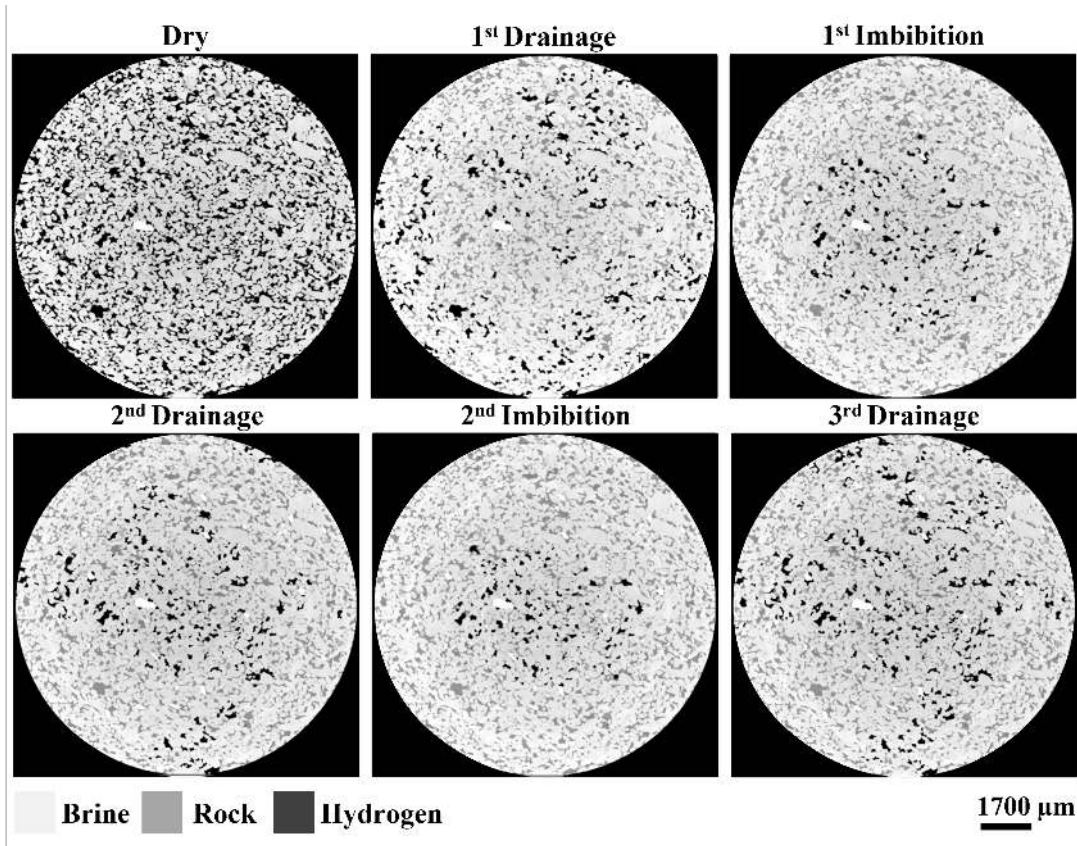


Figure 3.5: Two-dimensional cross-sections of three-dimensional raw images of the Bentheimer sample before and after the three cycles of hydrogen injection (drainage) and water flooding (imbibition): the rock, gas and brine are medium grey, black and light grey, respectively.

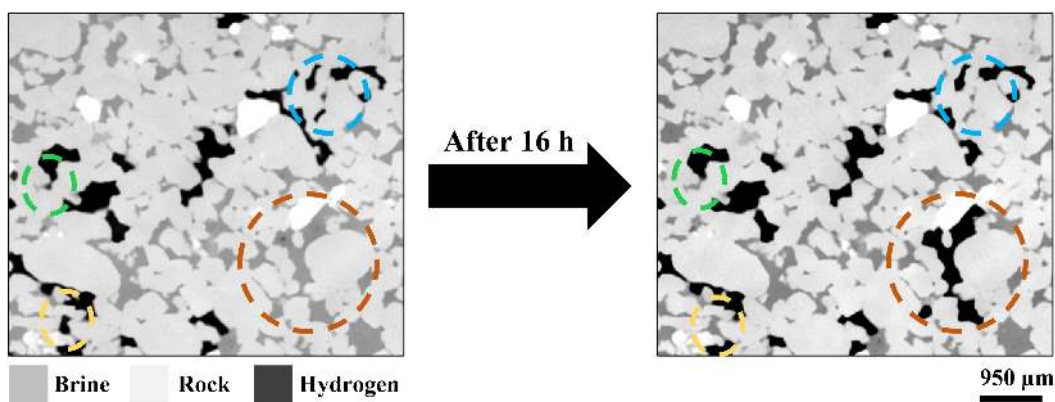


Figure 3.6: Two-dimensional cross-sections of three-dimensional raw images of the Bentheimer sample before and after 16 hours of undisturbed gas storage. The blue dashed circles indicate gas shrinkage, while the red dashed circles highlight increased gas connectivity. Arrows emphasise the redistribution of gas within the pore space, revealing the effects of Ostwald ripening over time.

The dashed lines in the figure highlight the rearrangement of gas and brine phases between the initial scan and the 16-hour storage scan at each stage. For example, the red and yellow dashed outlines emphasise regions where significant gas redistribution or dissolution occurred, demonstrating changes in phase occupancy and connectivity. We did not include the third imbibition because, after the third cycle, all the hydrogen dissolved in the brine, as confirmed by the absence of any visible gas phase in these regions.

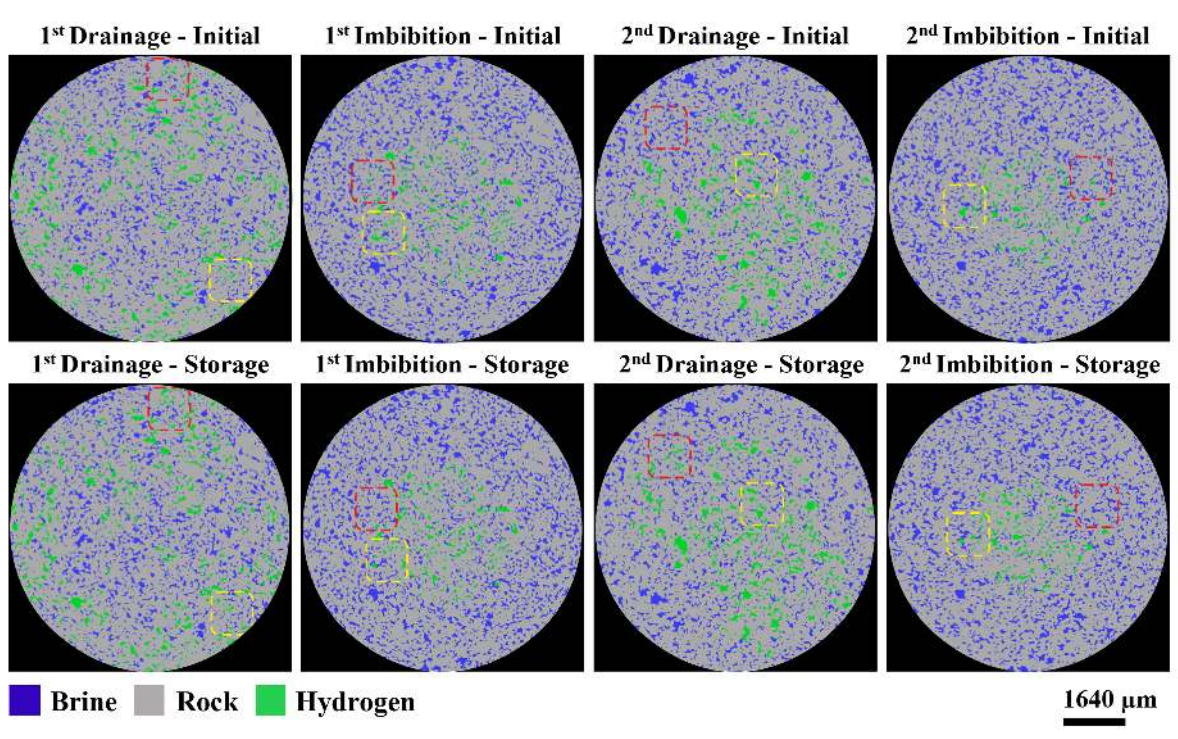


Figure 3.7: Two-dimensional cross-sections of three-dimensional raw images of the Bentheimer sample before and after 16 hours of undisturbed gas storage. The dashed circles highlight regions where gas redistribution occurs over time, which enhances phase connectivity.

3.3.2 Analysis of Discrete Ganglia

3D images of gas phase ganglia trapped inside the rock are shown in Figs. 3.8. These images were obtained for a sub-volume image size of $900 \times 900 \times 1373$ voxels located near the top of the sample (this is the central part of section 5, shown in Fig. 3.4). The trapped ganglia were imaged after injecting gas and water to the initial state and then waiting for 16 hours for cycles one and two. During the drainage stage, hydrogen injection followed by an additional 16-hour waiting period resulted in the formation of a single, large connected ganglion which is shown in green.

Additionally, we measured the ganglion size distributions in the sub-volume shown in Fig. 3.3, which revealed a significant movement of gas bubbles towards larger ganglia, spanning several pores, after gas injection and imbibition, see Fig. 3.9. It should be noted that the total gas volume remains approximately constant. Figure 5.8 illustrates the cumulative volume distribution of

ganglia. The graph highlights the phenomenon of bubble rearrangement, as smaller bubbles tend to disappear and contribute to the larger bubbles [161, 162].

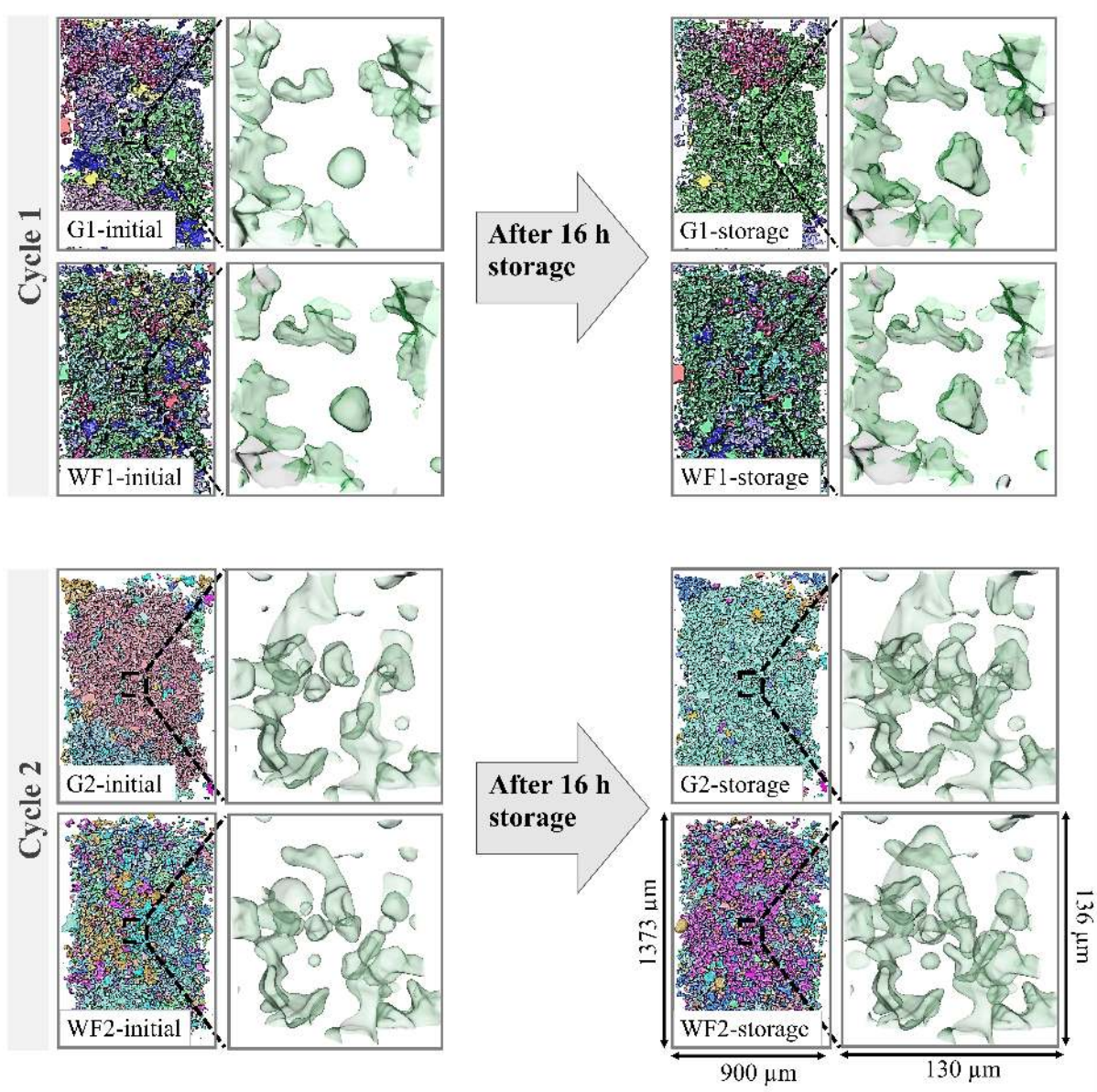


Figure 3.8: 3D visualisation of hydrogen gas distribution within the pore space during the first and second cycles of gas injection (drainage) and subsequent water flooding (imbibition). Distinct colours represent individual hydrogen gas ganglia, illustrating their distribution and size. After 16 hours of storage, the ganglia experience growth, leading to improved connectivity and the formation of larger, interconnected pathways. This enhanced connectivity is particularly visible in the zoomed-in regions on the right, where the hydrogen gas, depicted in green, occupies a more continuous and connected structure within the pore network.

After 16 hours, one large ganglion dominates the volume, as evidenced by the vertical portion in the cumulative curve at a large volume. This feature permits the withdrawal of hydrogen through a connected pathway, thus highlighting its potential significance in the remobilization of gas. This is aligned with the previous studies of gas-brine systems, where a significant rearrangement

of the trapped gas was observed after brine injection [27, 138].

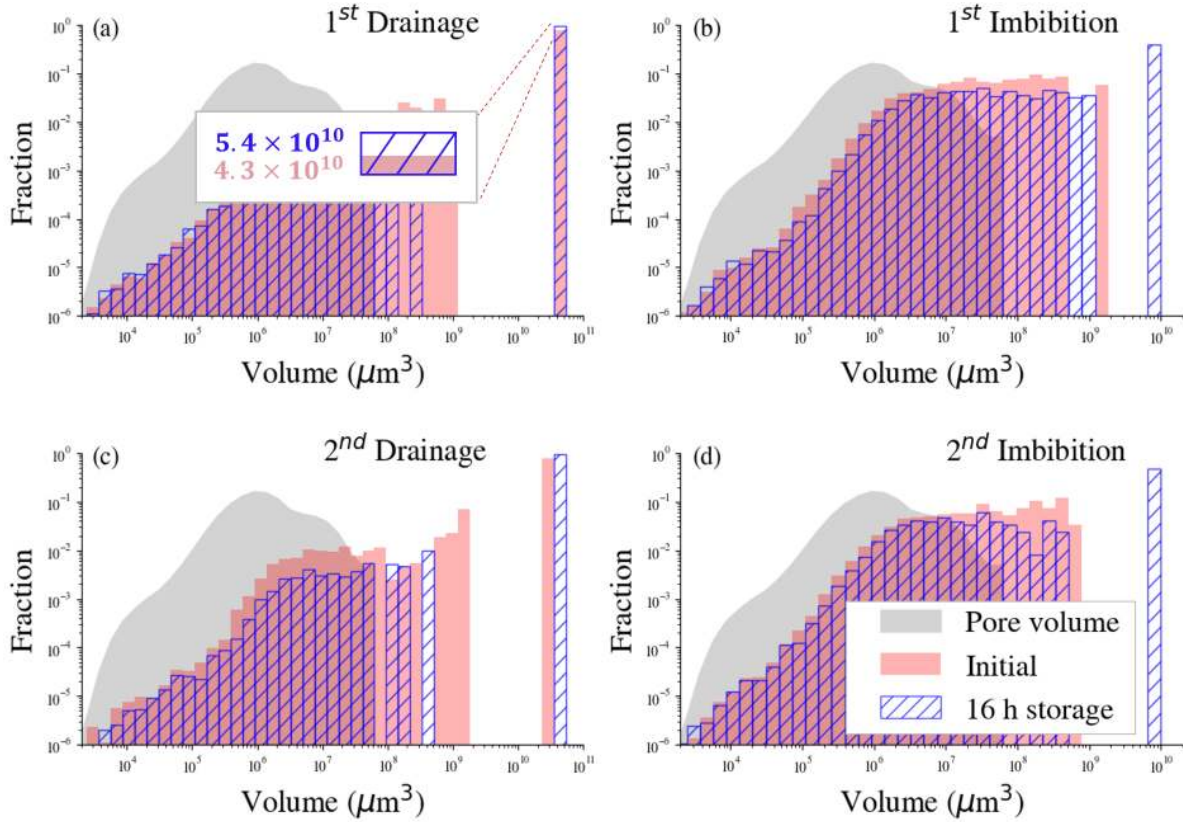


Figure 3.9: The volume-weighted size distribution of gas ganglia, analysed in the sub-volume, reveals a significant shift towards larger ganglia spanning multiple pores after gas injection and imbibition, while the total gas volume remains approximately constant. The distributions are shown for the first (a,b) and second (c,d) cycles of gas and brine injection, using a uniform bin size in logarithmic space. The grey-shaded area represents the volume distribution of all the pores.

3.3.3 Gas Saturation Profile

The cross-sectionally-averaged gas saturation along the entire sample length was measured, as depicted in Fig. 3.11. The flow rate used in the drainage cycles decreased from the first to the second to the third cycle with a consequent decrease in hydrogen saturation. The maximum average gas saturation reached was approximately 30%. The residual hydrogen saturation was approximately 10%, but hydrogen was dissolved near the inlet and was completely dissolved in brine after the third imbibition cycle. We also plotted a gas saturation profile for a sub-volume located near the top of the sample (section 5, illustrated in Fig. 3.4). A comparison was made between the gas saturation during the initial cycle and after an additional 16-hour storage period, following three cycles of fluid injection, as shown in Fig. 3.12. The analysis indicated that gas saturation in the studied volume slightly increases after 16 hours, suggesting that a small amount of gas may have migrated upward from lower sections of the sample.

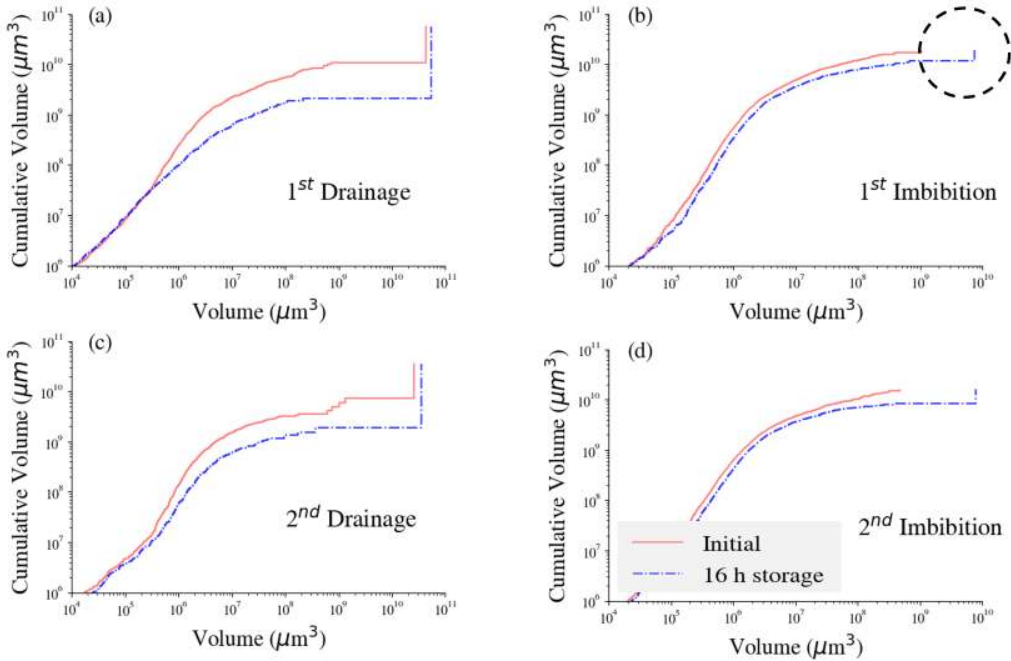


Figure 3.10: Cumulative volume distribution of hydrogen gas ganglia within the sub-volume near the top of the sample is presented for the first (a,b) and second (c,d) cycles of gas and brine injection. Over time, smaller bubbles gradually merge or dissipate, contributing to the growth of larger ganglia spanning multiple pores. Although the total gas volume remains approximately constant, the curves illustrate the transition towards a more connected gas structure. The vertical segment in the cumulative curve after 16 hours indicates the dominance of a single large ganglion, which enables hydrogen withdrawal through a continuous pathway.

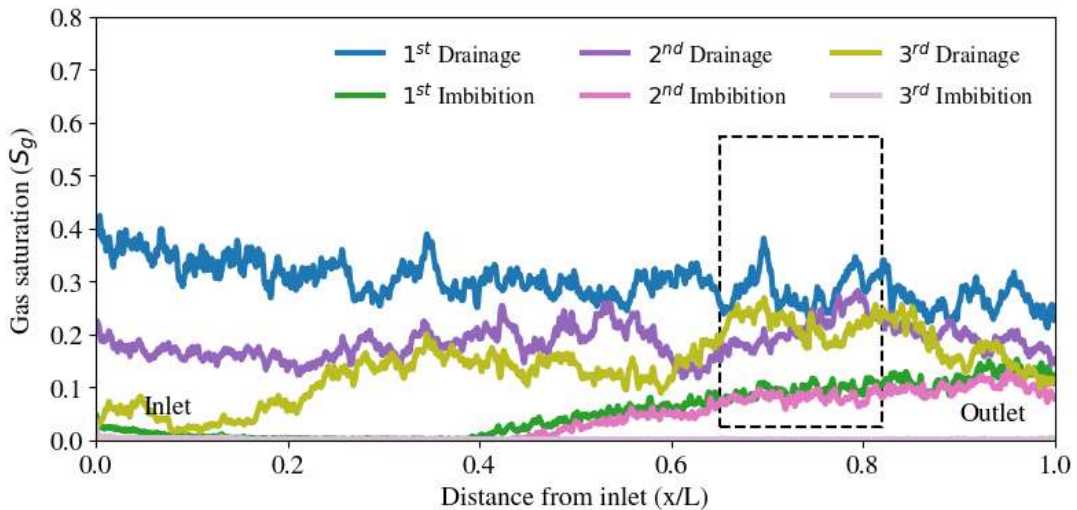


Figure 3.11: Gas saturation profile measured from segmented images during three cycles of gas injection and water flooding at different gas flow rates and a constant water injection rate along the length of a Bentheimer sample. Gas is dissolved near the inlet after the water flooding stages. The subsection studied for further analysis is shown by the black dashed line.

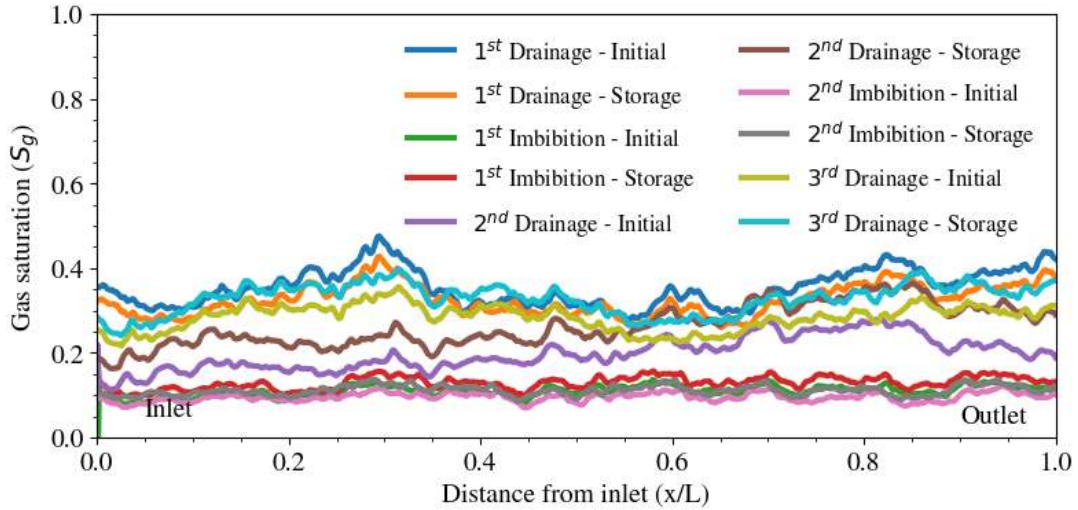


Figure 3.12: The gas saturation profile of a sub-volume located near the top of the sample during three cycles of gas and water injection, including both the initial injection and after an additional 16-hour storage period. The region considered is indicated by the black dashed box in Fig. 3.11.

3.3.4 Capillary Pressure Analysis

Figure 3.13 presents the capillary pressure distribution for all cycles within a sub-volume of $500 \times 500 \times 500$ voxels (part of section 5, shown in Fig.3.4). The capillary pressure at each stage was determined using a curvature-based measurement approach, previously established in the literature [123, 186]. To calculate capillary pressure, the interfacial curvature between hydrogen and brine was extracted from the segmented pore-scale images. The mean curvature was obtained by averaging the curvature distribution, and the Young-Laplace equation [64] was then applied to derive capillary pressure, as explained in Chapter 2, Section 2.1.3.

The measurement of capillary pressure provides an average value and showed the capillary pressure after drainage is slightly higher than that after imbibition with no significant difference after the Ostwald ripening process. Nevertheless, the accuracy of the pressure measurements is limited due to the inherent uncertainty in the estimation of interfacial curvature from the pore-space images. The analysis of the capillary pressure data did not reveal any clear trends between the initial state and the 16-hour waiting period, as the results can fluctuate either upward or downward, with any changes potentially being drowned out by measurement errors.

3.3.5 Measurement of Interfacial Area

We conducted measurements to quantify the specific interfacial areas, defined as the area per unit volume ($500 \times 500 \times 500$ voxels, part of section 5, shown in Fig.3.4). The interfacial areas between water and gas, as well as between the fluids and the solid rock surface, were measured both at the initial state and after a 16-hour waiting period, as shown in Fig.4.15.

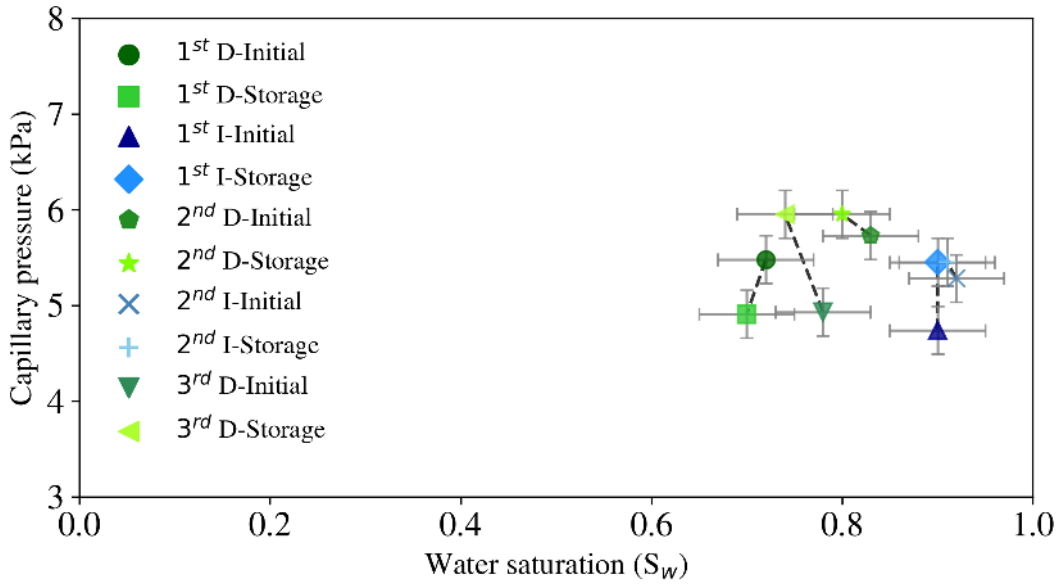


Figure 3.13: Capillary pressure values as a function of water saturation, derived from the mean interfacial curvature during gas injection and water flooding cycles. Different shades represent drainage and imbibition phases, with paired shaded markers (initial vs. 16-hour storage) indicating temporal variations. Dashed lines connect the initial and storage steps. The error bars reflect uncertainties arising from image segmentation in both capillary pressure and water saturation measurements.

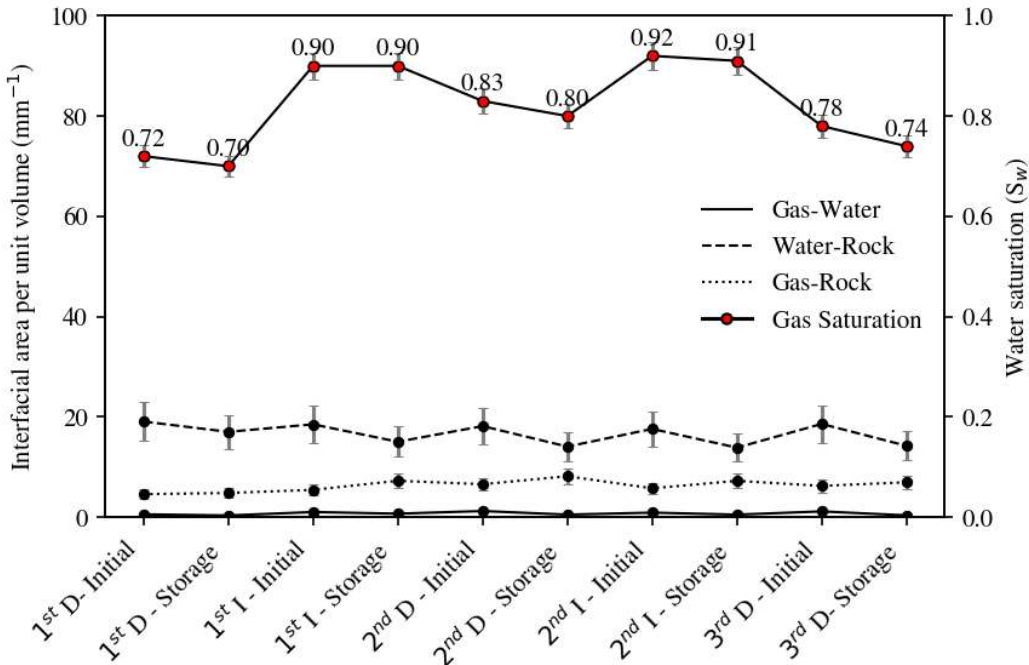


Figure 3.14: The interfacial areas per unit volume for water-solid, gas-solid and gas-water in a voxel subvolume during three cycles of gas injection (D= Drainage) and water flooding (I= Imbibition), including both the initial stage and after an additional 16-hour storage period.

The results confirmed that the sample is water-wet, as indicated by the consistently higher water-solid interfacial area compared to the gas-solid interfacial area. This suggests that water preferentially adheres to the rock surface. The observed variations in interfacial area are closely linked to changes in water saturation (S_w), shown on the secondary y-axis. Initially, during drainage cycles, lower water saturation values correspond to an increase in the gas-solid interfacial area, as gas displaces water and makes greater contact with the solid. Conversely, during imbibition, higher water saturation reduces gas presence, leading to a decrease in the gas-solid interfacial area while the water-solid interfacial area increases.

Over the 16-hour waiting period, the water-solid interfacial area shows a slight decline, suggesting minor water redistribution or film thinning due to capillary forces. In contrast, the gas-solid interfacial area increases, which can be attributed to gas redistribution through mechanisms such as Ostwald ripening, where gas tends to migrate to larger pores or less water-wet regions, enhancing its contact with the rock surface. The gas-water interfacial area, which is relatively small compared to other interfaces, follows a decreasing trend with increasing water saturation, implying that as water saturation rises, gas becomes more isolated in the pore space, resulting in a reduced interface between the two phases.

3.3.6 Fluid Connectivity and Péclet Number

Here, we took a closer look at the connectivity of fluids within the pore space, evaluating it qualitatively and quantitatively. We achieved this by isolating fluids from segmented images and giving each one a distinct colour in the isolated phase, see Fig. 3.8. Table 3.4 provides a quantitative assessment of fluid connectivity from the Euler characteristic, measured in a sub-volume image size of $900 \times 900 \times 1373$ voxels located near the top of the sample (section 5, shown in Fig. 3.4) as in the previous section. The Euler characteristic, or Euler number, represents the number of objects (ganglia) in a phase, minus the number of redundant loops within those ganglia. A large positive Euler characteristic indicates that the phase is trapped within numerous discrete ganglia, while a large negative Euler characteristic suggests a phase that is interconnected with many loops [187].

To ensure accuracy in our measurements, we have filtered out any features smaller than 10 voxels in size. As expected the Euler characteristic is negative after drainage, when the gas is well connected in the pore space, and positive after imbibition when the gas is trapped. In all cases, we see that after waiting 16 hours the Euler characteristic decreases: this indicates an improvement in connectivity. This result is consistent with the formation and swelling of a single large connected ganglion shown in Fig. 5.8, and an overall tendency for the gas to congregate in fewer, larger ganglia as a result of Ostwald ripening, Fig. 3.9.

To understand the nature of displacement and fluid arrangement we also calculated the Péclet number, which is defined as the ratio of advective to diffusive transport of gas in a material [119, 120]. The Péclet number is given by $Pe = \frac{q \cdot l}{D}$ (Eq. 2.20), where q is the Darcy velocity (volume of injected fluid flowing per unit time per unit area), l is the average distance between the centers of two neighboring pores, and D is the diffusion coefficient of the gas in brine, measured

outside a porous medium. For the hydrogen-water system, D is $5.13 \times 10^{-9} \text{ m}^2/\text{s}$ [188] and l is 150 μm obtained from a pore-network analysis of the pore space described in the next section [189]. Equation (2.20) compares the transport of hydrogen in its own phase by advection according to Darcy's law to the timescale for the diffusion-driven transport of hydrogen dissolved in the aqueous phase. A more detailed discussion of the Péclet number and its implications is provided in Section 2.20. The values are shown in Table 3.5.

Table 3.4: The Euler characteristic of a gas undergoing an unsteady-state two-phase experiment, both for the initial state and after 16 hours, following three cycles of hydrogen and brine injection. The results indicate that higher Euler characteristic values correspond to lower gas phase connectivity, with imbibition steps generally showing less connectivity compared to drainage steps. Over time, the decreasing values suggest an increase in gas phase connectivity.

Normalised Euler characteristic [mm^{-3}]			
Cycle	Flooding step	Initial	16 h storage
1	1 st Drainage	-5	-16
1	1 st Imbibition	18	10
2	2 nd Drainage	-4	-8
2	2 nd Imbibition	30	14
3	3 rd Drainage	-3	-4

Note. The Euler characteristic was measured on segmented images of a sub-volume and normalised to the total volume.

This analysis indicates that even during displacement, transport of dissolved gas can be significant in comparison with advective displacement. With the exception of the first drainage cycle, the time for hydrogen to move a pore length is shorter by diffusion through brine, than by displacement in its own phase. This indicates that in our experiments, with time-scales for displacement of order an hour and waiting times of 16 hours, diffusive transport in the aqueous phase can play a significant role in the redistribution of the gas phase.

Table 3.5: The Péclet number, Eq. (2.20), for gas undergoing an unsteady-state two-phase experiment, presented for three cycles of hydrogen and brine injection. The results demonstrate a significant decrease in the Péclet number during imbibition steps compared to drainage steps, indicating that diffusion plays a dominant role in mass transport during imbibition. The first drainage cycle exhibits the highest Péclet number, suggesting that advective transport is more significant in this phase. In subsequent cycles, lower Péclet values suggest an increasing contribution of diffusive transport relative to advection.

Flooding step	Darcy velocity [$\text{mm} \cdot \text{s}^{-1}$]	Capillary number Ca	Péclet number Pe
1 st Drainage	0.260	3.22×10^{-7}	7.61
1 st Imbibition	0.008	8.93×10^{-8}	0.23
2 nd Drainage	0.052	6.45×10^{-8}	1.52
2 nd Imbibition	0.008	8.93×10^{-8}	0.23
3 rd Drainage	0.010	1.29×10^{-8}	0.30
3 rd Imbibition	0.008	8.93×10^{-8}	0.23

3.3.7 Pore and Throat Occupancy

To understand the Bentheimer sandstone's pore structure and connectivity, we utilised differential imaging based on segmented X-ray scans [190]. Figure 3.15 presents three distinct representations of the sample: the dry scan, the segmented pore space, and the solid grain distribution. These images were used to quantify the total porosity, which was calculated as 22.6%, and to characterise the structural arrangement of the rock.

A pore-network analysis was performed on the segmented image to identify pores and throats, where pores represent the larger void regions and throats are the narrow restrictions connecting them [191]. The probability distributions of pore and throat sizes, also shown in Figure 3.15, reveal a mean pore radius of approximately $30 \mu\text{m}$ [28, 51] and a mean throat radius of $24 \mu\text{m}$ [64]. These measurements indicate that the pore space is well-resolved using X-ray imaging and provide key information about the connectivity and geometry of the pore network. These baseline measurements and visualisations serve as critical groundwork for interpreting fluid behaviour within the pore network. The subsequent discussion on pore occupancy will build on this analysis to explore how gas distributes and interacts with the sandstone's pore structure under different displacement conditions.

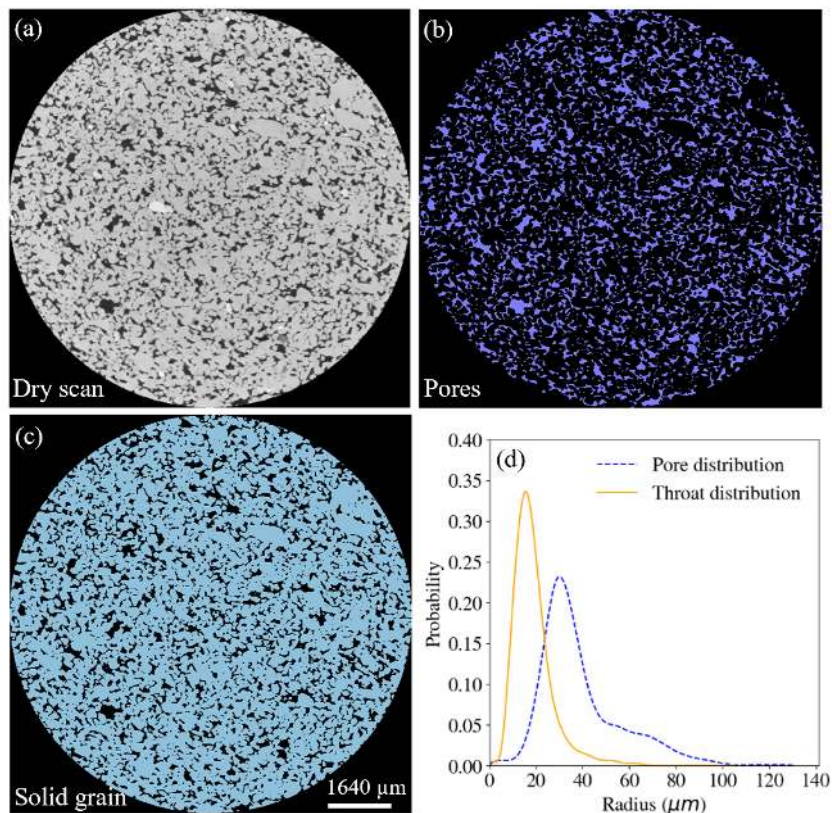


Figure 3.15: A two-dimensional cross-section of the dry scan of the Bentheimer sandstone sample (a), alongside segmented images showing the pore space (b) and solid grain distribution (c). These visualisations, derived from X-ray imaging, were used for pore-network analysis. The graph on the right (d) presents the probability distributions of pore and throat radii, characterising the structural variability of the sandstone's pore network.

Figures 3.16 and 3.17 display the pore and throat size distributions, along with the volume-weighted fraction of gas-filled pore elements determined using the generalised pore network extraction tool. This method involves using the extracted pore network structures from the dry scan image as an image analysis tool, following Foroughi et al. [189]. Specifically, during pore network extraction from the dry scans, the inscribed spheres in each pore (a wide region in the void space) and throat (a restriction between pores) identified by the pore network extraction are calculated. These inscribed spheres were identified using the maximal ball method described by Dong and Blunt [192], and the generalised network extraction algorithm of Raeini et al. [191].

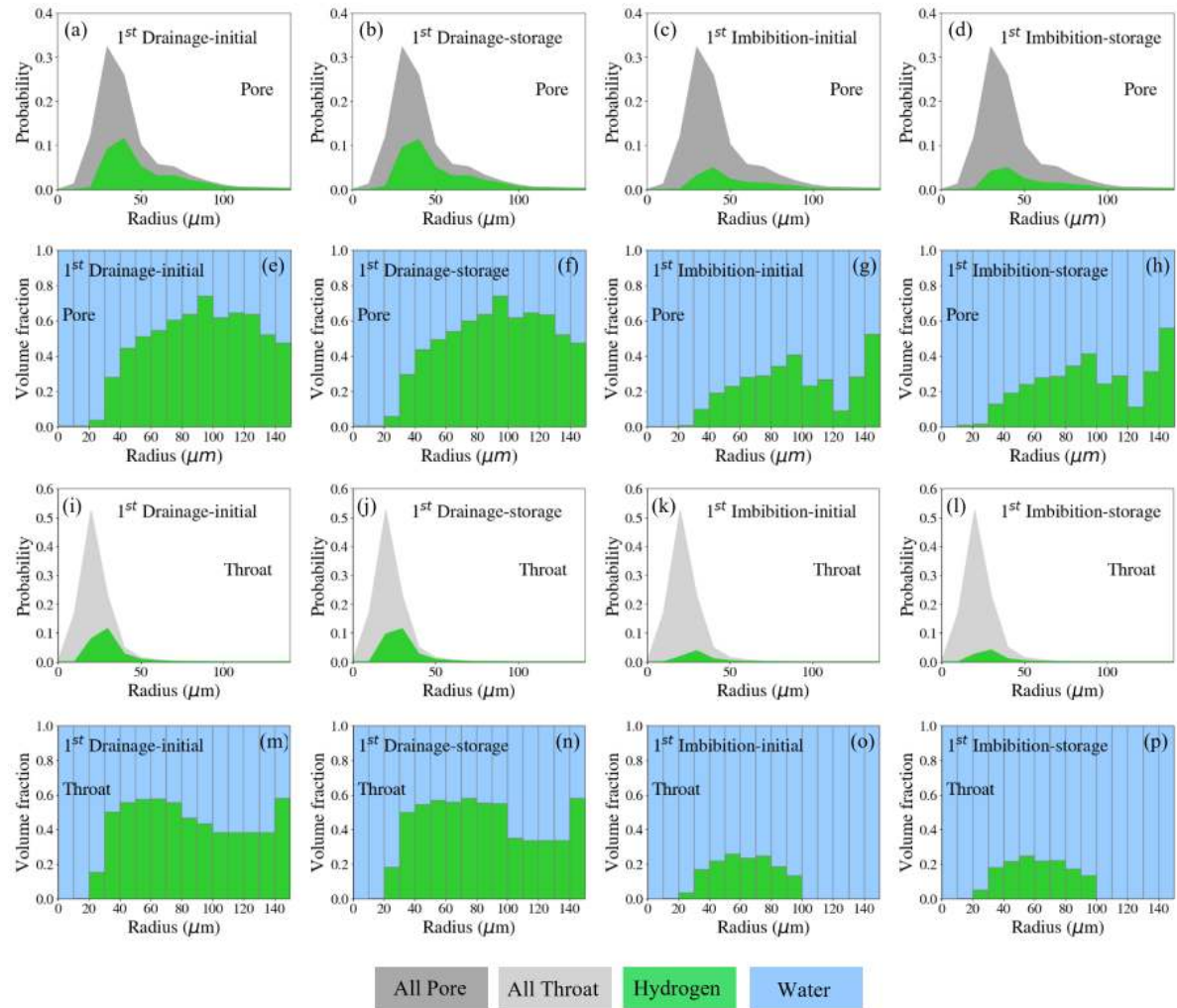


Figure 3.16: Volume-weighted histograms of gas and water occupancy as a function of pore and throat radius, analysed during the first cycle of gas injection following water flooding. The first row (a-d) and third row (i-l) depict the probability distributions of pore and throat radii across different flow stages, while the second row (e-h) and fourth row (m-p) illustrate the corresponding volume fraction distributions. Green represents gas (hydrogen), blue represents water, and grey indicates the overall size distribution of all pores and throats. Each column corresponds to a specific stage of the process, comparing the initial state of injection and the state after a 16-hour storage period for drainage and imbibition.

In pores, the largest spheres centered on each pore, which lie completely in the pore space, are identified. In throats, the largest spheres that can fit in the void space ~~centered~~ on the throat surface are identified. The inscribed spheres represent the local maxima (dilations) and minima (constrictions) in the distance map of the pore space, which are the locations where a non-wetting phase resides when it has just entered a pore or throat during drainage or the last location within a pore or throat where it can reside during imbibition.

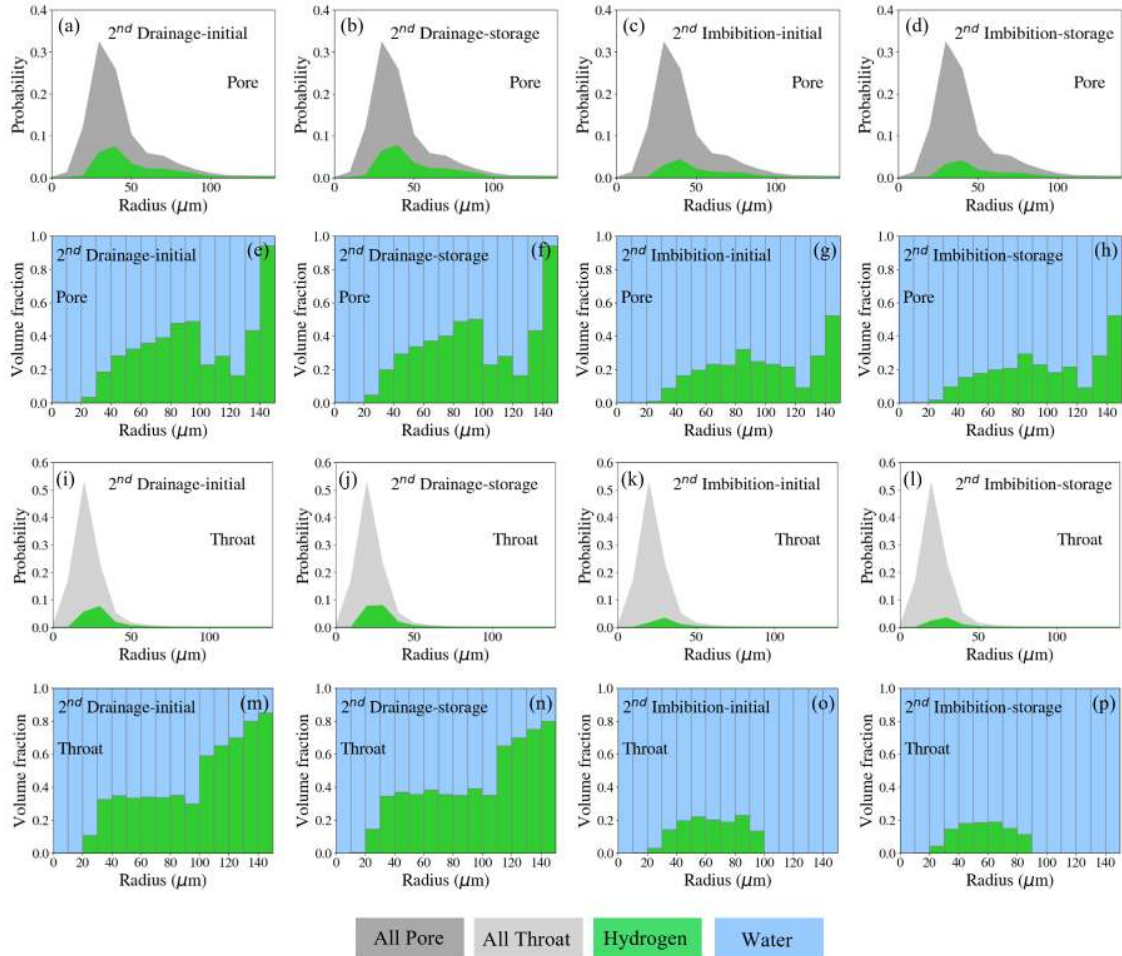


Figure 3.17: Volume-weighted histograms of gas and water occupancy as a function of pore and throat radius, analysed during the second cycle of gas injection following water flooding. The first row (a-d) and third row (i-l) depict the probability distributions of pore and throat radii across different flow stages, while the second row (e-h) and fourth row (m-p) illustrate the corresponding volume fraction distributions. Green represents gas (hydrogen), blue represents water, and grey indicates the overall size distribution of all pores and throats. Each column corresponds to a specific stage of the process, comparing the initial state of injection and the state after a 16-hour storage period for drainage and imbibition.

To determine which fluid resides in each inscribed sphere, we spatially registered the micro-CT images to each other so that the same voxel in each of the images corresponds to the same physical location in the sample. The mean square grey-scale value differences between the

different images were minimised for this purpose. The images containing the inscribed spheres labeled with their corresponding pore number or throat number (as extracted from the dry scan) were then overlaid on each image acquired during the flow experiments. Based on the fluid phase which dominantly fills (more than 50%) the inscribed spheres of a pore or throat in the micro-CT image, we considered that phase as occupying the pore or throat.

Figure 3.16 indicates that after the first drainage, gas displaced brine from the larger and medium-sized pores, leaving most of the smaller pores filled with brine, consistent with the system being water-wet. The resolution of the images is, however, insufficient to measure contact angle directly. Little change in occupancy was seen after 16 hours, implying that ganglion rearrangement is not principally the migration of gas into larger pores, but instead the aggregation of ganglia to occupy several connected pores. After imbibition, gas tended to be trapped in some of the larger and medium-sized pores, but again little change in occupancy was observed after 16 hours, see Fig. 3.18. As shown in Fig. 3.17, we noticed a similar trend of gas filling in the pores and throats for cycle 2.

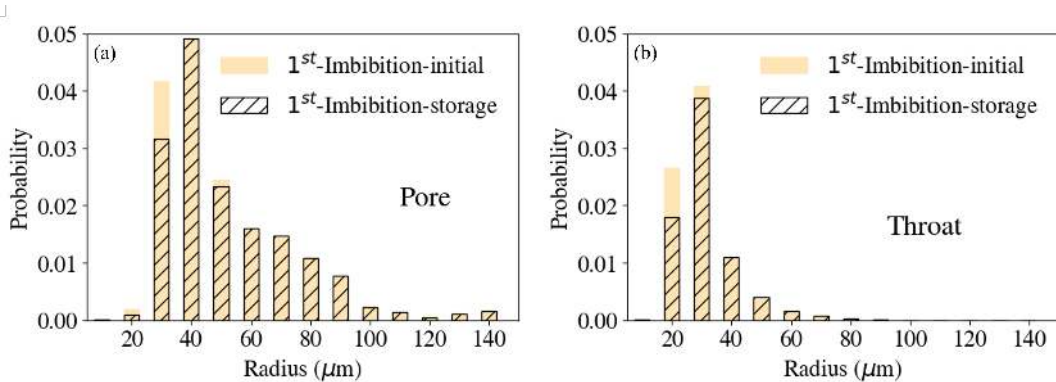


Figure 3.18: Comparison of volume-weighted histograms showing gas occupancy distributions as a function of pore and throat radii during the first cycle of gas and water injections, highlighting differences between initial conditions and after 16 hours of storage.

3.4 Health and Safety

Working with gas in a laboratory environment involves several safety risks that must be carefully managed to ensure the safety of people and the integrity of the experiment. For example, hydrogen is a highly flammable gas, and its unique physical properties require specific precautions, especially when used in combination with other substances like brine. This section outlines the key safety risks, measures, and protocols implemented during hydrogen-brine experiments.

3.4.1 Hydrogen Hazards

Hydrogen is highly flammable and can ignite at low concentrations (as low as 4% in air). The ignition energy for hydrogen is very low, meaning that even static electricity can ignite it. When hydrogen mixes with air or oxygen, hydrogen forms highly explosive mixtures. The wide range of concentrations (4% to 75% in air) makes these mixtures dangerous even in small amounts.

Hydrogen molecules are very small and can easily leak through tiny openings, including through some materials that are impermeable to other gases. Hydrogen is difficult to detect without specialised equipment because it is colourless and odourless. This increases the risk of undetected leaks. Several standard safety measures were adopted during hydrogen-brine experiments to mitigate the risks associated with hydrogen. The experiments were conducted in well-ventilated spaces with hydrogen detectors placed near potential leak points. Since hydrogen is prone to leakage due to its small molecular size, pressure systems were regularly tested for leaks using soap solutions or electronic leak detectors before each experiment [193, 194].

3.4.2 Storage and Handling of Hydrogen

Hydrogen cylinders were stored upright in a well-ventilated area, away from direct sunlight, and secured to prevent them from falling over. Appropriate gas cylinder signage and fire hazard warnings were clearly posted in the storage area. Only regulators designed specifically for hydrogen were used to prevent accidents caused by incorrect equipment. All valves were opened slowly to minimise the risk of pressure surges. Before introducing hydrogen into the experimental setup, special attention was given to preparing the system to ensure a safe and controlled environment. The lines and the experimental chamber were vacuumed to remove any residual air, moisture, or contaminants. This minimised the risk of forming explosive hydrogen-oxygen mixtures and reduced the possibility of hydrogen interacting with impurities, which could affect experimental results or compromise safety.

After vacuuming, the lines were purged with an inert gas (such as nitrogen) to further displace any remaining oxygen and ensure that the system was in an ideal state for hydrogen flow. This procedure ensured that the lines were free from any unwanted gases or particulates that could react with hydrogen. Brine is highly corrosive to many metals, including those commonly used in hydrogen handling systems. To avoid equipment degradation and potential leaks, corrosion-resistant materials such as stainless steel and compatible plastics were used in the setup.

3.4.3 Safety Protocols for Brine

Brine, due to its high salinity, is highly corrosive and poses additional safety challenges in laboratory experiments. Its corrosive nature can degrade materials in the experimental setup, particularly metals, leading to equipment failure or leaks. To address this, only corrosion-resistant materials, such as stainless steel or compatible plastics, were used for components that come into contact with brine. Regular inspections of the equipment were conducted to identify any signs of corrosion, ensuring timely maintenance or replacement of affected parts. Contact with brine can also cause irritation to the skin and eyes. To prevent exposure, laboratory personnel wore appropriate personal protective equipment (PPE), including gloves, goggles, and lab coats. Any accidental spills were promptly cleaned using appropriate neutralising agents to prevent long-term damage to surfaces or equipment. Waste brine was disposed of according to environmental and chemical safety regulations, ensuring minimal environmental impact and adherence to laboratory safety protocols [195, 196].

3.4.4 X-ray Safety Considerations

In addition to the safety precautions associated with hydrogen handling, High-resolution 3D X-ray micro-computed tomography systems, require strict adherence to radiation safety protocols to protect laboratory personnel from potential harm. X-ray systems emit ionising radiation, which can pose significant health risks, including damage to living tissue and an increased risk of cancer with prolonged or excessive exposure. Although modern X-ray systems are designed with shielding to protect operators, safety measures must still be rigorously enforced. The X-ray CT system used in the experiments was enclosed within a fully shielded cabinet, designed to contain and block harmful radiation. The shielding materials, typically lead or other dense metals ensured that X-ray exposure outside of the system remained well below permissible limits. The X-ray CT system was equipped with interlock systems that automatically disable the X-ray source if the enclosure is opened or if there is a system malfunction. This safeguard prevents accidental exposure during the operation or maintenance of the equipment [197].

Radiation levels around the X-ray system were continuously monitored using dosimeters to ensure that the radiation levels remained within safe limits. Access to the X-ray scanning area was restricted to trained personnel only. All operators of the X-ray CT system underwent specialised training in radiation safety and proper system usage. To reduce the risk of unnecessary radiation exposure, the X-ray system was operated only for the duration required to capture the necessary scans. The system was powered down when not in use to prevent inadvertent X-ray emissions [198].

3.5 Final Remarks

This study investigated the effects of drainage and imbibition cycles on hydrogen saturation in a Bentheimer sandstone sample (12.8 mm in diameter and approximately 60 mm in length), with high-resolution imaging used to track gas distribution. Imaging was conducted after each hydrogen or water injection, as well as 16 hours post-injection, to assess fluid redistribution over time. A progressive reduction in flow rate across successive drainage cycles led to a corresponding decline in hydrogen saturation, with a peak average gas saturation of approximately 30%. Residual hydrogen saturation was measured at around 10%; however, hydrogen dissolution was observed near the inlet and became complete in brine after the third imbibition cycle. These findings provide valuable insight into hydrogen retention and transport mechanisms within porous media. The main conclusions of the work are as follows:

1. Hydrogen is the non-wetting phase and tends to occupy the larger regions of the pore space. It is trapped by the injection of water in the largest pores.
2. Even with no flow there is a significant rearrangement of the hydrogen within the pore space over length-scales of a centimeter and time-scales of 16 hours. We hypothesise that this is caused by Ostwald ripening: the transfer of gas dissolved in the aqueous phase to equilibrate the local capillary pressure.

3. Ostwald ripening leads to the aggregation of hydrogen in larger ganglia with, in most cases, a single large ganglion dominating the volume.
4. The connectivity of the gas phase also increases after 16 hours, as quantified by the Euler characteristic.

Our work implies that there may be less hysteresis in hydrogen storage than implied by the use of models based on hydrocarbons which ignore Ostwald ripening. This is favourable for hydrogen injection and withdrawal.

The next chapter could extend this study to work on more representative pressures to acquire higher-resolution images to investigate the effect of pressure changes on the behaviour [199]. Additionally, it would be valuable to inject brine that is pre-equilibrated with hydrogen to avoid the complicating effects of dissolution. The porous plate technique could be used to allow a higher initial hydrogen saturation to be reached in drainage. More accurate measurements of capillary pressure over a wide saturation range may allow the determination of a model of capillary pressure hysteresis applicable for hydrogen storage.

Chapter 4

Ostwald Ripening Leads to Less Hysteresis during Hydrogen Injection and Withdrawal

The contents of this chapter have been published in:

S. Goodarzi, G. Zhang, B. Bijeljic, M. J. Blunt, “Ostwald Ripening Leads to Less Hysteresis during Hydrogen Injection and Withdrawal: A Pore-Scale Imaging Study,” International Journal of Hydrogen Energy, vol. 114, pp. 475-485, 2025.

4.1 Summary

This study explores hydrogen storage in Bentheimer sandstone using high-resolution 3D X-ray imaging during hydrogen injection and brine flooding cycles. The results reveal a reduction in hysteresis during hydrogen injection and withdrawal, attributed to Ostwald ripening—the transport of dissolved hydrogen in the aqueous phase to balance local capillary pressure. Hydrogen saturation reached 82% after injection, while the residual saturation decreased significantly from 40% in the first cycle of brine injection (imbibition) to less than 18% in the third. End-point capillary pressure during gas injection was directly measured as 20, 9, and 3 kPa in the first, second, and third cycles, respectively. During the imbibition steps, the gas saturation decreased consistently, reflecting reduced trapping effects and improved gas connectivity. After 16 hours of rest, a single large connected ganglion formed, further reducing the Euler characteristic per unit volume from -10 mm^{-3} to -23 mm^{-3} during the third drainage cycle. These findings highlight that traditional hysteresis models that ignore the effect of Ostwald ripening over-estimate the amount of residual trapping in hydrogen storage.

4.2 Materials and Methods

4.2.1 Porous Plate Disc

Porous ceramic plates are crucial components in core flooding experiments, serving to control the flow of different fluid phases through the rock core. These plates are typically made from materials like alpha alumina, which have a specific pore size that allows the wetting phase to pass through while preventing the non-wetting phase from penetrating when a threshold pressure is applied. For experiments using porous ceramic plates, one or two plates were employed, depending on the setup. The hydrophobic plate, being water-repellent, prevented water from escaping the rock sample, ensuring it remained saturated within the sample. Conversely, the hydrophilic plate acted as a gas barrier, allowing only water to pass through while confining the gas inside.

After selecting the hydrophilic porous plate for this experiment, it was cut to match the diameter of the rock sample. To improve water distribution, grooves were added to one side of the plate, see Fig. 4.1 for a schematic representation of the plates. To measure the differential pressure across the sample, small holes were drilled in the porous plate to align with the injection piece. To prevent gas from escaping through these holes, glue was applied around the drilled areas, ensuring a secure seal.

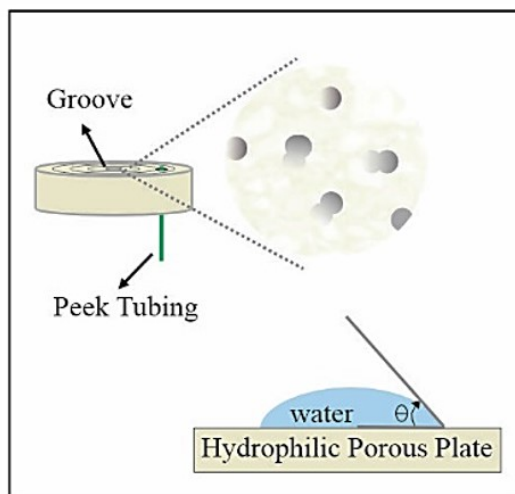


Figure 4.1: Schematic of the hydrophilic porous plate used in the experiment, highlighting key features. Grooves were added to enhance water distribution, and Peek tubing was incorporated for differential pressure measurement. The inset illustrates the plate's pore structure and the water-wetting properties, depicted by the contact angle (θ).

4.2.2 Equilibrating Brine with Gas

A crucial step in the experimental process involved equilibrating the brine with hydrogen gas before injecting it into the sandstone sample. The high-pressure reactor used in this study was a Parr Instrument Company Bench Top Reactor, see Appendix C.1, designed to safely handle elevated pressures and temperatures while providing a controlled environment for experiments.

This reactor featured a chamber with a capacity of 1 liter, capable of storing liquid samples under high-pressure conditions. Equipped with advanced temperature and pressure controls, the reactor allowed precise adjustments to simulate a wide range of experimental conditions. Its robust construction, using materials compatible with reactive gases such as hydrogen and nitrogen, ensured chemical durability and operational safety.

Additionally, the reactor was equipped with a stirrer drive, facilitating uniform mixing of reactants during experiments. The brine was placed in the reactor, and hydrogen gas was gradually injected into the chamber while compressing the gas to reach the desired pressure. Once the target pressure was achieved, the brine was stirred gently at a low speed for 24 hours to ensure complete saturation with hydrogen. This preparation step was critical to ensure that the brine was fully equilibrated with hydrogen, replicating the conditions necessary for accurate and reliable experimental results.

4.2.3 Rock and Fluid Properties

Bentheimer sandstone, known for its uniform pore structure, was selected for this investigation. This material has been extensively used as a benchmark in prior studies [168, 178, 179], it offers a consistent framework for comparative analysis. Detailed information about the properties and characteristics of this rock can be found in Chapter 3, Section 3.2.1.

The overall porosity of the Bentheimer sandstone sample was determined to be 20.4% using differential imaging techniques [190]. In this method, the porosity is identified by subtracting a dry image of the sample from one where it is fully saturated with a high-contrast solution. Figure 4.2 presents the porosity distribution along the sample length, revealing a relatively uniform profile, which underscores the homogeneity of the sandstone.

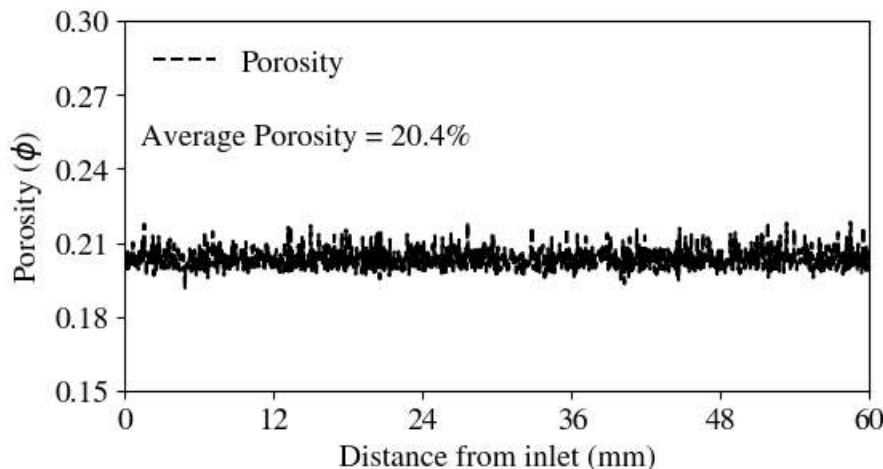


Figure 4.2: Porosity distribution along the length of a Bentheimer sandstone sample (60 mm in length), demonstrating a relatively uniform porosity profile. The porosity values were derived through imaging techniques, with an associated error of 0.05% due to image segmentation processes. The slight variations observed are attributed to inherent heterogeneities in the sample and the precision of the imaging methodology.

The rock sample was prepared by drilling a cylinder with a diameter of 12 mm and a length of approximately 60 mm. To optimise phase contrast during imaging, the aqueous (wetting) phase was doped with 20% weight percent Potassium-Iodide (KI) dissolved in deionised water. The details of the doping process are elaborated in Chapter 3, Section 3.2.2. A summary of the fluid properties, including dynamic viscosity and interfacial tension, is provided in Table 4.1.

Table 4.1: Thermophysical properties of the fluids used in the experiment, including density (ρ) measured at ambient temperature, dynamic viscosity (μ), and interfacial tension (σ). The values for brine are sourced from [27, 30], while hydrogen properties are obtained from [29, 31].

Fluid	Density ρ [kg.m ⁻³]	Viscosity μ [Pa.s]	Interfacial Tension σ [N.m ⁻¹]
Water-20 wt.% KI	1263	0.821×10^{-3}	7.23×10^{-2} (σ_{gw})
Gas-H ₂	0.0354	9.11×10^{-6}	7.23×10^{-2} (σ_{gw})

4.2.4 Experimental Procedure

To investigate gas behaviour, cycles of injection and withdrawal were performed to achieve varying levels of saturation-high, medium, and low. The sample was kept at a constant confining pressure of 10 MPa and maintained at a pore pressure of 8 MPa under ambient temperature (25°C). The pressure difference between the inlet and outlet was measured using a pressure transducer, see Appendix B.4 for more details. The experiment was conducted under capillary-controlled conditions and with unsteady state flooding. The capillary number (Ca) is calculated from Eq. 2.12 for 3 cycles, as tabulated in Table 4.2.

The experimental sequence was as follows.

1. The sample was initially prepared by ensuring it was completely dry and sealing it within a nitrile rubber enclosure to prevent any interactions with the confining fluid, as explained in Chapter 3, Section 3.2.3. Before connecting the top and bottom parts of the rubber enclosure, a water-wet porous ceramic plate, matching the diameter of the sample, was placed within the enclosure. This plate worked as a barrier, keeping the gas inside the sample and providing a uniform saturation after fluid injection while allowing the flow of the aqueous phase. The upper part of the rubber was connected to the production component, while the injection component was linked to the lower part, as illustrated in Fig. 4.3.
2. Prior to introducing brine into the sample, we employed a high-pressure reactor to equilibrate the brine with hydrogen (mixing at 176 rpm), ensuring that the brine was thoroughly saturated with hydrogen gas.
3. The sealed sample was then located within the micro-CT apparatus. Flowlines and pumps injected the fluid phases and applied confining and back pressures. A Keller PD-33X differential pressure transducer was connected to the top and bottom of the sample to measure differential pressure during fluid injections, with a precision of ± 0.03 kPa. To

eliminate any air and prepare for hydrogen injection, the sample, lines, and gas pump were thoroughly vacuumed for several hours, ensuring that no potentially dangerous hydrogen-air mixture could form.

4. The experiment began by scanning the dry sample at a confining pressure of 2 MPa with zero pore pressure. Next, 100 pore volumes of brine were introduced from the bottom, allowing the pore space to gradually reach full saturation. Once saturated, the sample was scanned again under conditions of 8 MPa pore pressure and 10 MPa confining pressure.
5. We executed three consecutive flooding cycles, each following a similar procedure. In each cycle, we introduced gas from the top of the sample under a specified differential pressure. The first cycle aimed to achieve high gas saturation, and it took 2 days to stabilise at 20 kPa differential pressure, as shown in Table 4.2. The second cycle was designed to target medium gas saturation, requiring 3 days to reach a steady state at 8 kPa differential pressure. The last cycle was intended to achieve low gas saturation, and it took 4 days to reach a differential pressure of 3 kPa.
6. Following the completion of gas injection (drainage), the valve was closed, and the gas pump was turned off. A comprehensive bottom-to-top scan of the sample was conducted over 7.5 hours, divided into six sections with a 25% overlap. After an additional 8.5 hours, totaling 16 hours since the cessation of gas injection, images of all sections were captured.
7. After completing the gas injection and scanning phases, We injected 2 pore volumes of brine, maintaining a constant flow rate of 0.06 ml/min for a period of 45 minutes. The experiment was performed under conditions controlled by capillary forces.
8. After completing brine injection, the entire length of the sample was scanned from bottom to top for 7.5 hours. Eight and a half hours later, images were taken of sections 1 to 6.
9. Upon completion of the three cycles, a final bottom-to-top scan of the sample was conducted 24 hours later to assess the residual gas content.

Table 4.2: Capillary numbers, $Ca = \mu q / \sigma$, where μ is the viscosity of the injected fluid, σ is the interfacial tension, and q is the Darcy velocity for the flooding cycles.

Cycle	Flooding step	Ca_{gw}	Flow rate [ml.min ⁻¹]	Capillary pressure [kPa]
1	1 st Drainage	-	-	20
1	1 st Imbibition	1.1×10^{-7}	0.06	-
2	2 nd Drainage	-	-	9
2	2 nd Imbibition	1.1×10^{-7}	0.06	-
3	3 rd Drainage	-	-	3
3	3 rd Imbibition	1.1×10^{-7}	0.06	-

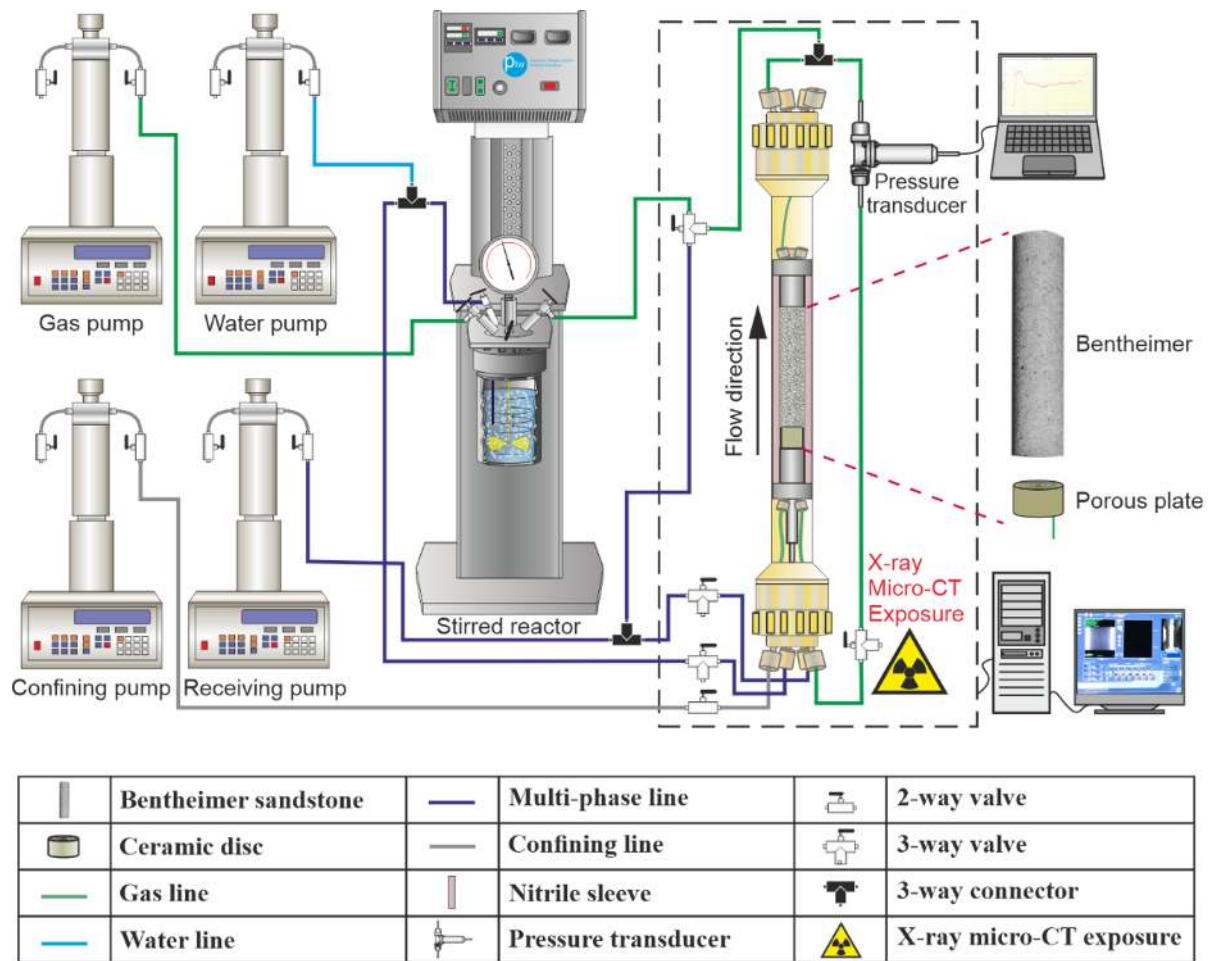


Figure 4.3: Schematic of the experimental apparatus used in the study. The diagram highlights the arrangement of the flow cell, injection and receiving pumps, multiphase and confining flow lines, and the pressure transducer. The dashed box marks the micro-CT exposure region, where high-resolution imaging of the flow processes was conducted

4.2.5 Image Processing

The same scanner and image acquisition parameters as described in Section 3.2.5 were used in this study. The scan times and parameters are summarised in Table 4.3. This time, however, the entire length of the sample was scanned after 16 hours to achieve a more accurate quantification of fluid behaviour following storage. Each scanning session captured six overlapping images, ensuring complete coverage of the sample's length, with a vertical overlap of 4 mm. The generated three-dimensional images had a voxel size of $5.4 \mu\text{m}$, covering 3023 voxels along the x-axis, 3064 along the y-axis, and 11586 along the z-axis, resulting in over 100 billion voxels in total.

Once the images were obtained, reconstruction, normalisation, registration, cropping, and stitching were performed using Avizo (ThermoFisher Scientific) to create three-dimensional renderings of the gas, water, and rock at each cycle [184], more details are provided in Chapter 3,

Section 3.2.6. To reduce image noise, a non-local mean filter was applied [185].

Image segmentation was performed using the seeded watershed algorithm [200] to accurately delineate phase boundaries and minimise misclassification caused by partial volume effects. In this method, a greyscale intensity range was assigned to each phase based on prior knowledge of material properties. These predefined intensity ranges served as initial seeds, ensuring that the segmentation process was constrained to realistic phase distributions. The watershed algorithm then expanded these seeds based on intensity gradients, allowing segmentation to grow proportionally while ensuring that phase boundaries were formed at the steepest gradient points. This approach effectively minimised over-segmentation and provided a precise distinction between different fluid and solid phases within the sample, see Fig. 4.4. By applying this method, key parameters such as gas saturation, ganglion sizes, fluid connectivity, and surface areas involving solid-fluid interactions were extracted with high accuracy.

Table 4.3: Summary of scanning parameters for the Zeiss X-ray ~~microtomography~~ scanner used in the experiment. Initial scans include dry, wet, gas injection, and water injection steps, each comprising six overlapping sections to cover the entire sample length. After 16 hours, additional detailed scans of sections 1 to 6 were performed to monitor localised changes over time.

Step	Sections	Exposure time [s]	Projections	Total time [mins]
Dry scan	1-6	1.2	3001	75 × 6
Wet scan	1-6	1.2	3001	75 × 6
Gas injection	1-6	1.2	3001	75 × 6
Water injection	1-6	1.2	3001	75 × 6
16 hours storage	1-6	1.2	3001	75 × 6

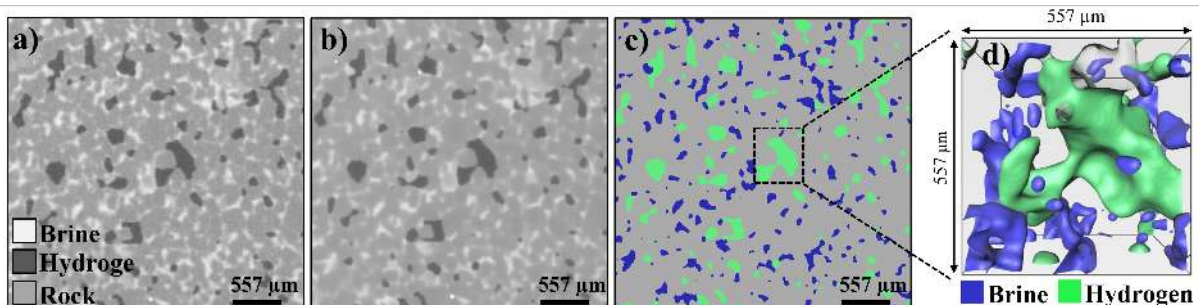


Figure 4.4: A small section of two-dimensional raw greyscale images is shown the raw (a) and after filtering (b). Segmentation (c) highlights distinct phases: hydrogen gas (green), brine (blue), and rock (grey). The three-dimensional subvolume (right) visualises the distribution of hydrogen and brine within the pore space of Bentheimer sandstone.

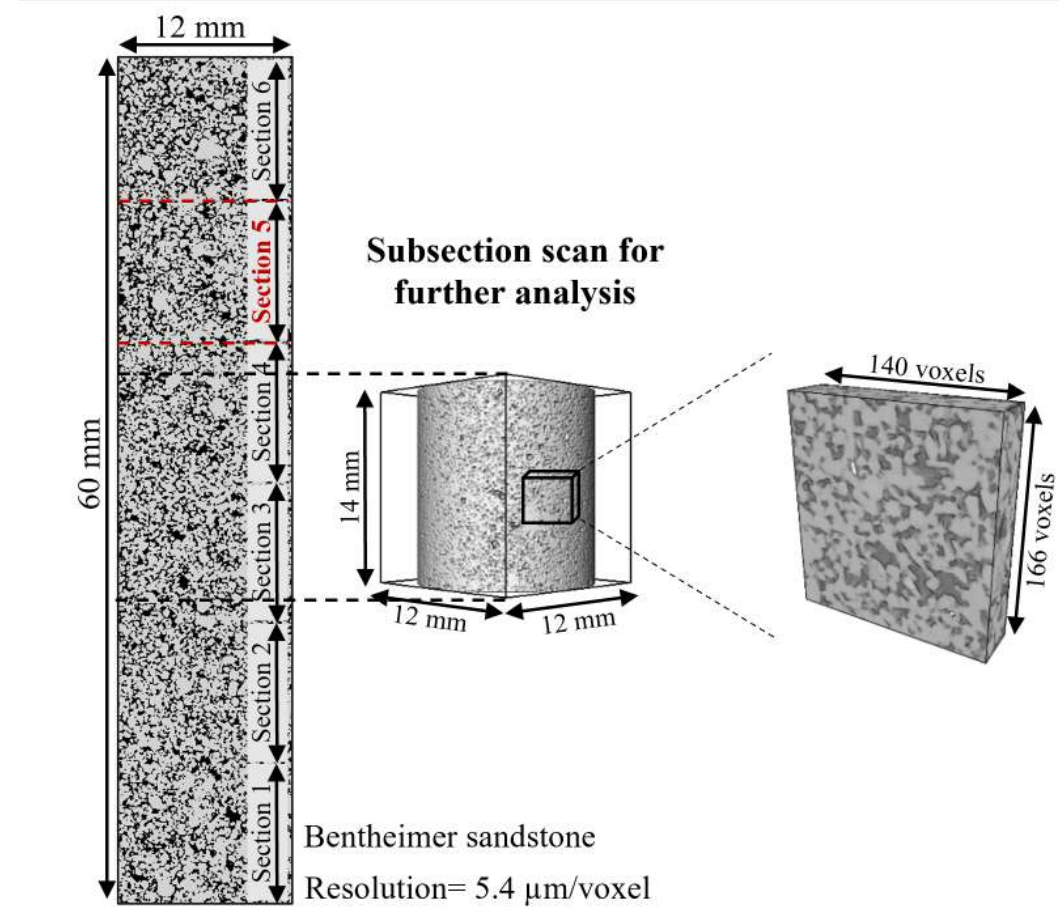


Figure 4.5: Schematic representation of the Bentheimer sandstone sample used for analysis. The full sample has a height of 60 mm and a diameter of 12 mm. A subsection scan (14 mm \times 12 mm \times 12 mm) was extracted for further analysis, as shown in the magnified region. Within this subsection, a smaller volume (140 \times 166 \times 40 voxels) was selected for a closer examination of fluid distribution within the solid rock structure.

4.3 Results and Discussion

In Section 4.3.1, we analyse the greyscale images, which demonstrate improved uniform hydrogen distribution. Our examination focuses on discrete ganglia to validate the process of gas aggregation into larger bubbles following an additional waiting period of 16 hours. These results are presented alongside a discussion of gas connectivity in Section 4.3.2. In Section 4.3.3, we examine the dynamics of capillary pressure following gas and water injections over three cycles. We discuss the gas saturation profiles observed across the entire sample during three cycles of gas injection and subsequent water flooding in Section 4.3.4. Finally, the measurements of specific interfacial areas between gas-water, gas-rock, and water-rock, as well as details of pore occupancy, including fluid distribution and arrangement within the pore space are provided in section 4.3.5.

4.3.1 Raw Greyscale Images

Significant ~~advancements in the experimental setup~~ and methodology have allowed for improved hydrogen saturation and reduced dissolution effects, as evidenced by the greyscale images captured at various experimental stages. These improvements are demonstrated in Figure 4.6, which highlights ~~a significant enhancement in saturation uniformity~~ across all cycles compared to Figure 3.7, Section 3. This uniformity can be attributed to the use of a hydrophilic porous plate combined with brine pre-equilibrated with hydrogen. By pre-equilibrating the brine, the complicating effects of hydrogen dissolution during the injection phases were minimised, resulting in a more stable and homogeneous hydrogen phase distribution throughout the sample.

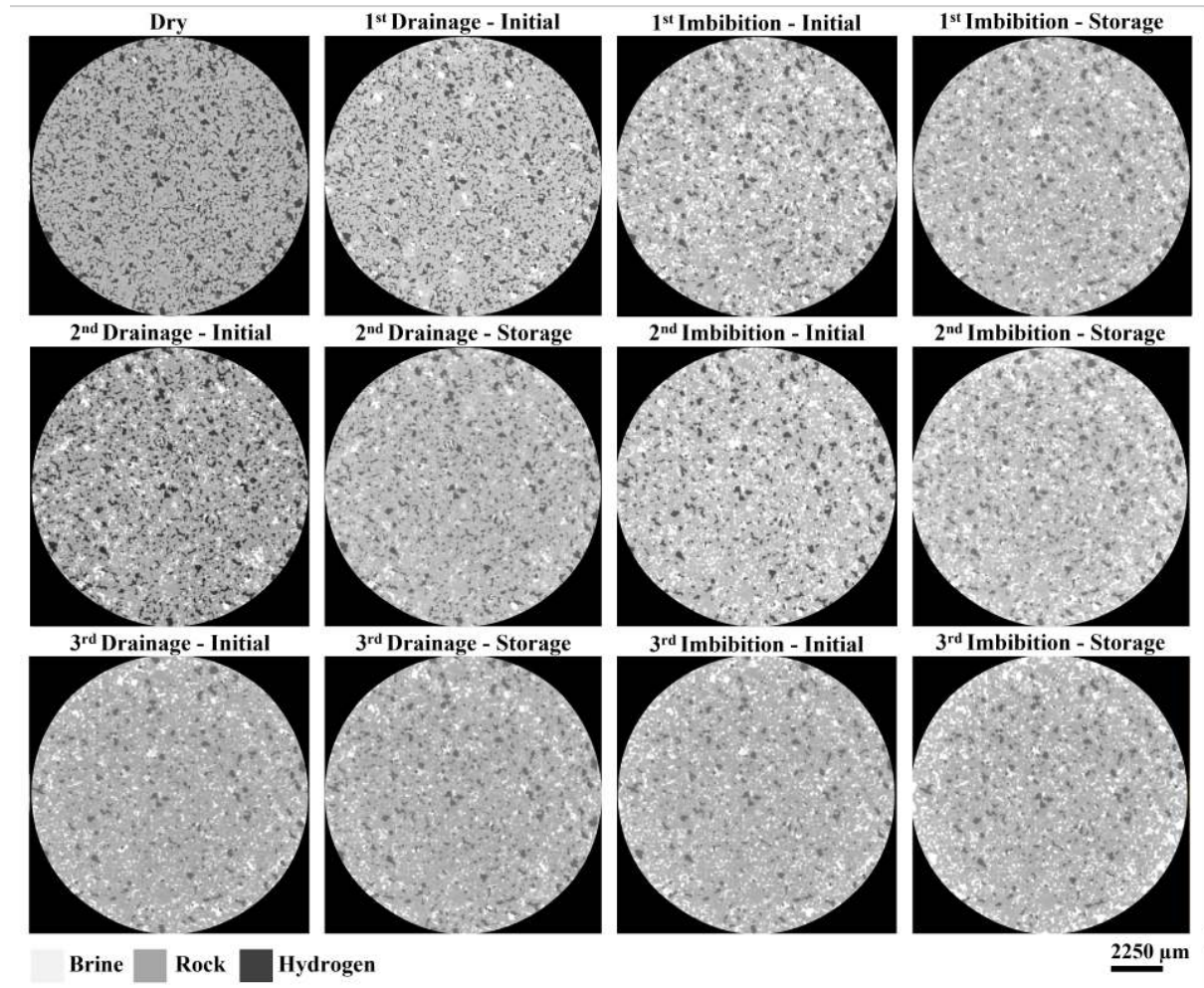


Figure 4.6: Two-dimensional slices of three-dimensional raw images from the sandstone sample illustrate changes observed before and after a 16-hour storage period. In these images, rock is depicted in medium grey, gas in black, and brine in light grey.

~~To further investigate localised phase behaviour~~, Figure 4.7 examines a subvolume extracted from the sandstone sample, showcasing the spatial distribution of gas, brine, and rock phases both at the initial state and after 16 hours of storage. The dashed circles in the images identify regions where significant rearrangements in the gas phase have occurred, leading to changes

in connectivity and morphology. These observations suggest localised redistribution of the gas phase during storage, likely influenced by capillary pressure adjustments or minor dissolution and re-precipitation effects.

The improved visibility of phase boundaries in the raw images underscores the effectiveness of the methodological ~~advancements~~. The stabilisation of the gas phase through brine pre-equilibration ensured more reliable and reproducible observations of redistribution phenomena, further validating the robustness of the experimental approach.

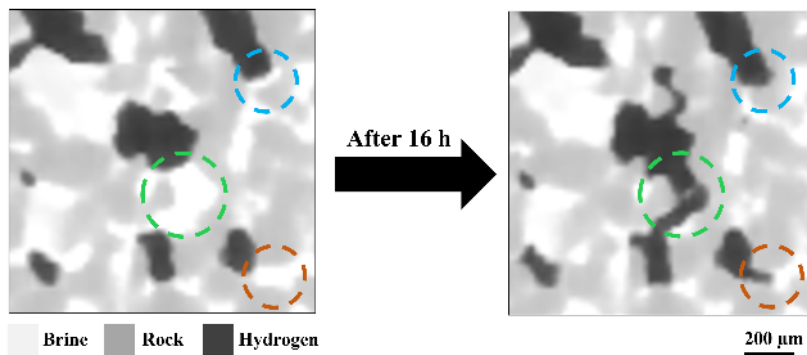


Figure 4.7: Two-dimensional cross-sectional views of the segmented three-dimensional images depicting the gas, brine, and rock phases in green, blue, and grey, respectively, for the first cycle at the initial state and after 16 hours of storage. The dashed lines highlight regions where noticeable rearrangements of the gas phase have occurred, leading to changes in connectivity.

4.3.2 Fluid Configuration and Connectivity

Figure 4.8 displays the side view of three-dimensional images of the gas phase captured at an image size of $2150 \times 2150 \times 2560$ voxels (Fig. 4.5, located upper part of the sample). These images were obtained after the initial stage of gas injection and water flooding, followed by each cycle being observed for an additional 16-hour waiting period. Each colour in the figures represents a discrete ganglion of gas: a wide variety of colours reflects a poorly connected phase, whereas a narrow range of colours indicates a well-connected phase. During the drainage cycles, after injection of hydrogen and an additional 16-hour waiting period, a single large connected ganglion formed, as highlighted with the red arrow (Fig. 4.8, 2^{nd} D-16 h storage).

Additionally, during the imbibition cycles, after water injection and another 16-hour wait, the results revealed increased gas connectivity, with larger and more unified ganglia forming (Fig. 4.8, 2^{nd} I-16 h storage). This observation shows the dynamic nature of gas phase rearrangement, driven primarily by Ostwald ripening, which allows smaller ganglia to dissolve and migrate, ultimately joining larger structures.

Further insight into the enhanced connectivity is provided in Fig. 4.9, displaying a magnified view of gas phase ganglia. These images are extracted from a sub-volume of $166 \times 140 \times 40$ voxels (upper part of the sample, illustrated in Fig. 4.8). The visual comparison between the initial stage (light green) and the expanded volume after the 16-hour storage period (dark green) distinctly illustrates the transition from a fragmented to a more connected gas phase.

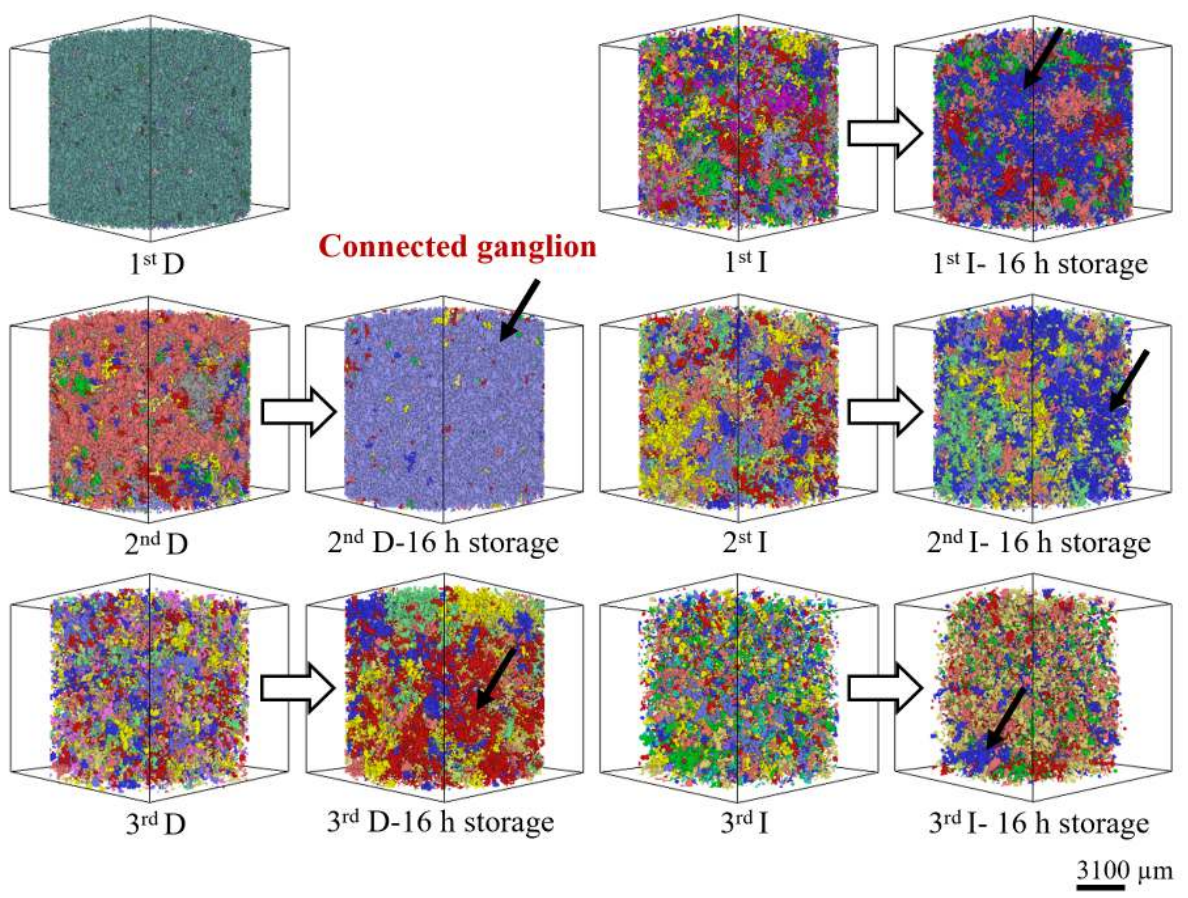


Figure 4.8: The three-dimensional images illustrate the distribution of hydrogen within the pore space following three cycles of gas and water injections (D= Drainage, I= Imbibition). Diverse colours distinguish discrete gas ganglia: after a 16-hour storage, these ganglia merge, resulting in improved connectivity. The presence of connected ganglia, highlighted with a black arrow, demonstrates the influence of storage on hydrogen redistribution and pore-scale connectivity.

This evolution is indicative of gas mass transfer mechanisms, which preferentially stabilise larger ganglia while reducing the overall capillary pressure. This suggests that allowing sufficient time for storage can mitigate residual trapping, enhancing the mobility and hydrogen withdrawal efficiency in subsequent injection and withdrawal cycles. There is a tendency to see more gas in the centre of the sample near the injection inlet (the lower part of the sample). This could be due to channelling from the injection port, or diffusion of hydrogen through the nitrile sleeve. To remove this artefact, we perform the remaining quantitative analysis on the upper part of the images, away from the inlet.

In Figure 4.10, the ganglion size distribution within section 5 (Fig. 4.5) illustrates the gas movement across the last cycle following the injection of hydrogen and after water flooding. The volume-weighted fraction of ganglia sizes, plotted logarithmically against gas volume, displays a significant shift of gas bubbles towards larger ganglia from the initial stage to the 16-hour storage, observed consistently after both gas injection and water flooding. This trend parallels the hydrogen distribution within the pore space, as shown in Fig. 4.8. Despite nearly constant

overall gas volume, the ganglia distribution (Fig. 4.10, c,d) reveals a process of smaller bubbles merging with larger ones [161, 162]. The results for the first and second cycles are provided in Appendix C.2 and C.3.

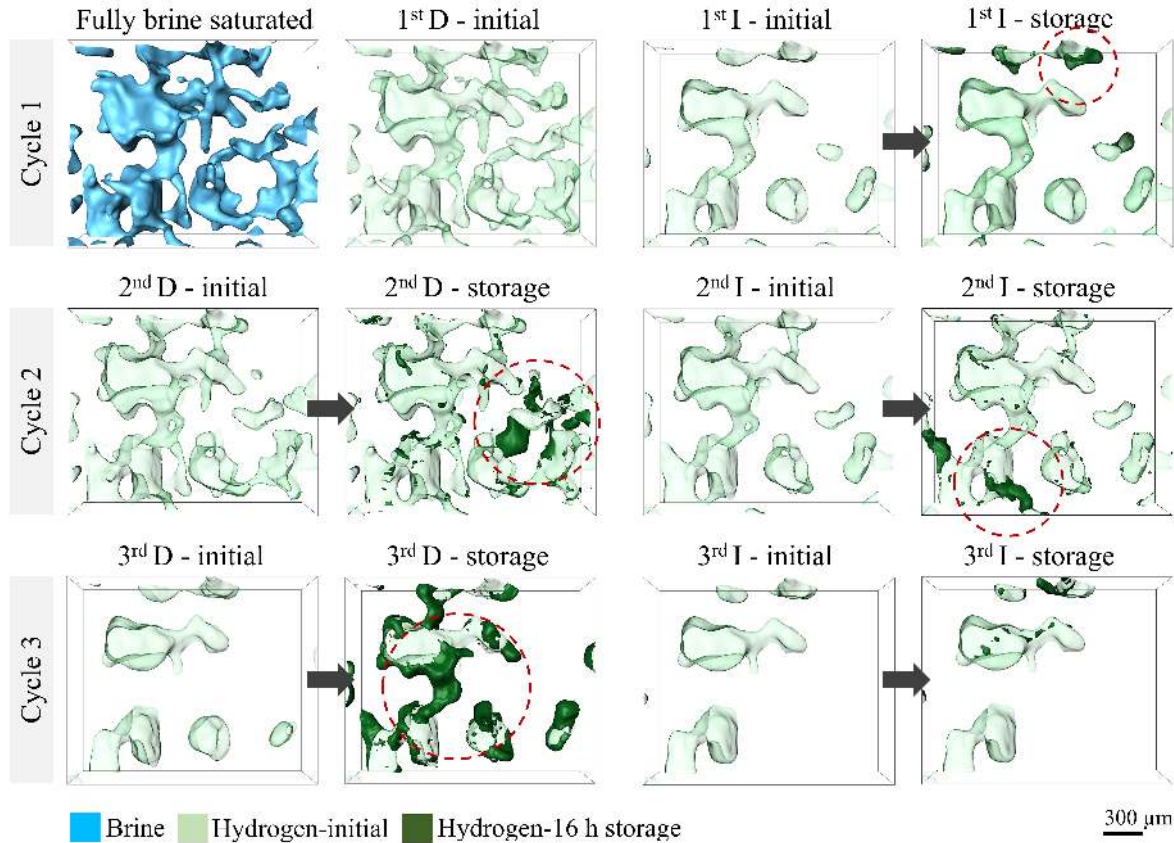


Figure 4.9: Zoomed-in images of the gas phase structures after initial displacement and then after waiting for 16 hours. The lighter green shade represents the gas arrangement and connections at the initial stage. The darker green shade displays how the configuration of gas changed after being left undisturbed for 16 hours (the red dashed circles). This comparison visually highlights the improved connections between the gas phase due to Ostwald ripening. (D= Drainage, I= Imbibition)

After 16 hours, a significant increase in the volume of the single largest ganglion is evident, especially in cycle 3. This characteristic facilitates hydrogen withdrawal through connected pathways, indicating its potential role in gas remobilisation. These observations align with prior studies on gas-brine systems, highlighting significant rearrangements in trapped gas following brine injection [21, 27, 138].

For a comprehensive quantitative evaluation of fluid connectivity, Table 4.4 shows the computed Euler characteristic using a sub-volume image size of $1723 \times 1723 \times 1461$ voxels (section 5, Fig. 4.5). The Euler characteristic is a topological measure that helps quantify the connectivity and structure of complex shapes or configurations, such as the arrangement of gas ganglia within porous media. It is calculated by subtracting the number of redundant loops or holes (loops that can be removed without cutting a ganglion into two pieces) from the number of distinct

components or objects present in the system (gas ganglia).

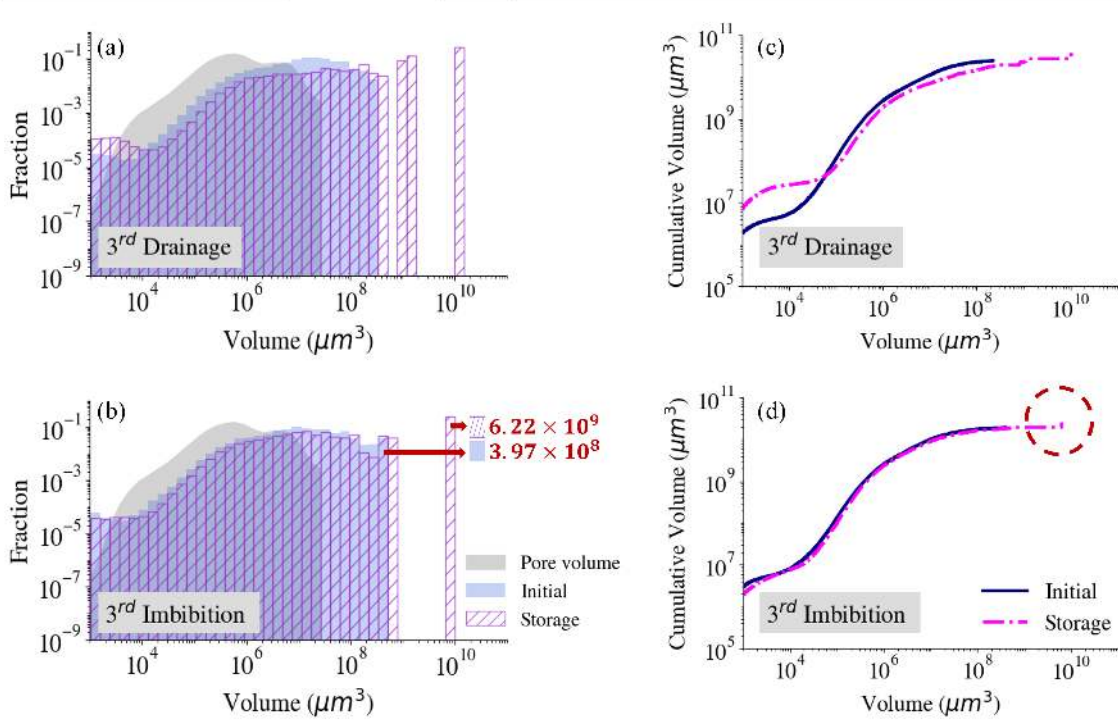


Figure 4.10: The volume-weighted size distribution (a, b) and cumulative volume distribution (c, d) of ganglia are shown for the third cycle of gas and brine injection. The graphs compare the initial stage with the distribution after 16 hours of storage. The shaded grey area represents the volume distribution across all pores. A distinct vertical segment in (b) and a highlighted region in (d) indicate the emergence of a single large ganglion, which dominates the volume after storage.

To facilitate comparison across different sub-volumes, we compute a normalised Euler characteristic by dividing the Euler characteristic by the volume of the sub-image in mm^3 . This normalisation yields a density-like measure, allowing us to account for the influence of volume size on connectivity calculations and to make direct comparisons between different conditions or stages of the experiment. A positive value implies many discrete ganglia and disconnected or poorly connected gas while a negative value shows a well-interconnected phase containing numerous loops [201].

Following gas injection (drainage), the observed negative Euler characteristic signifies robust gas connectivity within the pore network. Conversely, the positive values observed after water flooding (imbibition) are consistent with gas trapping. For all cycles, a consistent decrease in the Euler characteristic after 16 hours denotes improved connectivity. This aligns with the formation of a single, expanded ganglion and the observed pattern of gas merging into larger ganglia due to Ostwald ripening (Fig. 4.10).

Table 4.4: Normalised Euler characteristic [mm^{-3}] throughout three cycles of hydrogen and brine injection, capturing the initial state and the subsequent 16-hour storage period.

Cycle	Flooding step	Normalised Euler characteristic [mm^{-3}]	
		Initial	16 h storage
1	1 st Drainage	-98	—
1	1 st Imbibition	+23	+18
2	2 nd Drainage	-16	-29
2	2 nd Imbibition	+35	+22
3	3 rd Drainage	-10	-23
3	3 rd Imbibition	+29	+22

Note. The Euler characteristic was measured on segmented images of a sub-volume and normalised to the total volume.

4.3.3 Quantification of Capillary Pressure

Capillary pressure refers to the equilibrium pressure difference between two immiscible fluid phases in porous media [64], as mentioned in Chapter 2, Section 2.1.3. The analysis of capillary pressure involved measuring capillary pressure endpoints after drainage in each of the three cycles, with varying pressures: 20, 9, and 3 kPa, following gas injection, shown in Fig. 4.11. These measurements align well with independent measurements of the mercury injection capillary pressure (MICP) [22] once we have corrected for differences in interfacial tension.

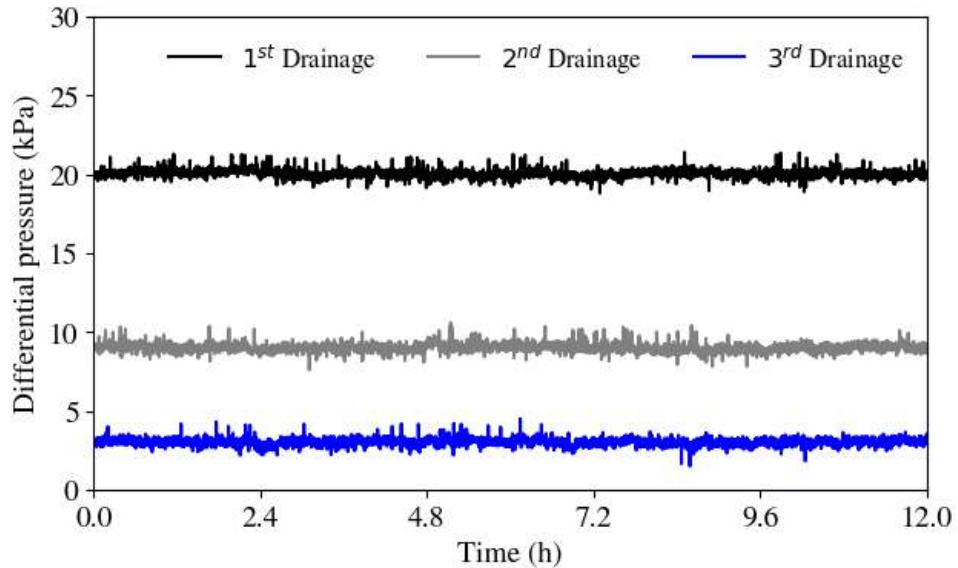


Figure 4.11: Measured differential pressures during the three drainage cycles, corresponding to capillary pressure endpoints of 20, 9, and 3 kPa, following gas injection. The results indicate consistent pressure stabilisation over the last 12 hours at each injection.

Additionally, we compared the capillary pressures measured during injection of gas (drainage) and water flooding (imbibition) using the porous plate technique on Bentheimer sandstone for a gas/water system [14]. We estimated the capillary pressure as a function of local saturation

in a subvolume of $600 \times 600 \times 600$ voxels (part of section 5, Fig. 4.5), from the average interfacial curvature of the gas-water menisci and then applying the Young-Laplace equation [64], same method as mentioned in Chapter 3, Section 3.3.4. The interfacial curvature and local water saturation were measured within the same subvolume. The capillary pressure derived from curvature analysis agrees with the direct pressure measurements to within experimental uncertainty.

Less trapping was observed after the second imbibition cycle than after the first. Furthermore, a drop in gas saturation occurred in the third cycle as under a low imposed pressure, gas cycled back into the injection pump. During this cycle, intermittent gas connections and disconnections led to fluctuations in the recorded differential pressure readings. Subsequent imbibition during the third cycle revealed even less gas trapping.

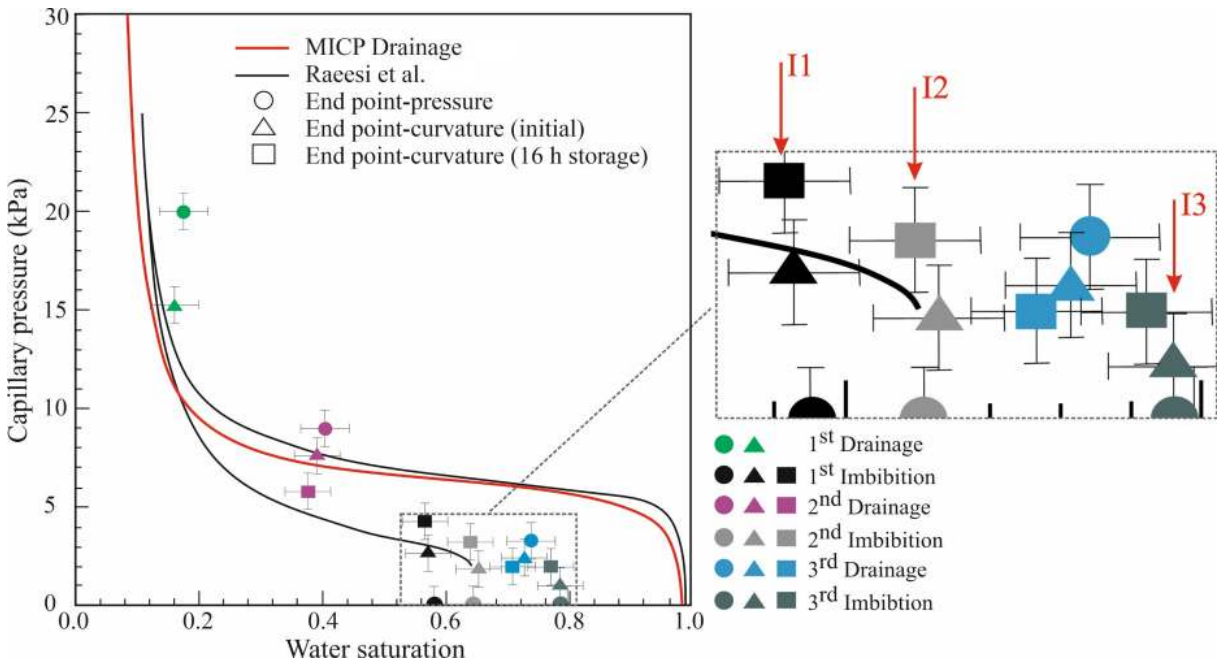


Figure 4.12: Estimated capillary pressure for drainage and imbibition measured on a 600^3 voxel subvolume near the top of the sample. The black lines show independent experimental measurements in the literature where Ostwald ripening is not considered [14]. The points are our measurements and the error bars represent the uncertainty in the determination of capillary pressure and saturation from the segmented images.

The results in Fig. 4.12 have three features which cannot be explained by a traditional hysteresis model Fig. 2.11, but which are fully consistent with the analysis of connectivity presented previously.

1. The residual saturation decreases from the first to second imbibition cycle and is further reduced after the third cycle. This is only possible because the gas phase rearranges and reconnects, allowing more displacement in subsequent injection cycles.
2. There is a tendency for the capillary pressure to increase on waiting after imbibition and to decrease after drainage. Without Ostwald ripening the capillary pressure should be

constant once flow has stopped.

3. Related to point 2, this leads to less hysteresis between drainage and imbibition, once the gaseous phase has been allowed to rearrange to achieve local capillary equilibrium. The results suggest – within experimental uncertainty – a unique capillary pressure with no hysteresis, as indicated by the trend line. However, there is no theoretical reason why hysteresis is eliminated: there is still trapping, likely contact angle hysteresis and different pore-scale displacement processes. What we can say though is that there is significantly less hysteresis than observed when Ostwald ripening can be ignored.

4.3.4 Gas Saturation Profile

We measured the gas saturation throughout the entire sample, as presented in Fig. 4.13. Throughout the drainage cycles, we progressively adjusted pressure differences, resulting in a reduction in hydrogen saturation. The hydrophilic porous plate technique facilitated higher initial hydrogen saturations by effectively manipulating capillary forces, enhancing hydrogen retention within the pore spaces. The peak average hydrogen saturation achieved was around 82%, with the largest measured residual hydrogen saturation averaging around 40%, consistent with previous measurements on sandstones [20, 142]. The comparison in Fig. 4.13 between initial gas saturation and that after a further 16-hour storage period during the three cycles of fluid injection revealed a consistency in total gas saturation: this indicates that the gas phase rearranges in the pore space – there is no injection or production. However, fluctuations in the saturation profiles were observed after 16 hours, which suggests local gas redistribution and migration, likely driven by Ostwald ripening [161].

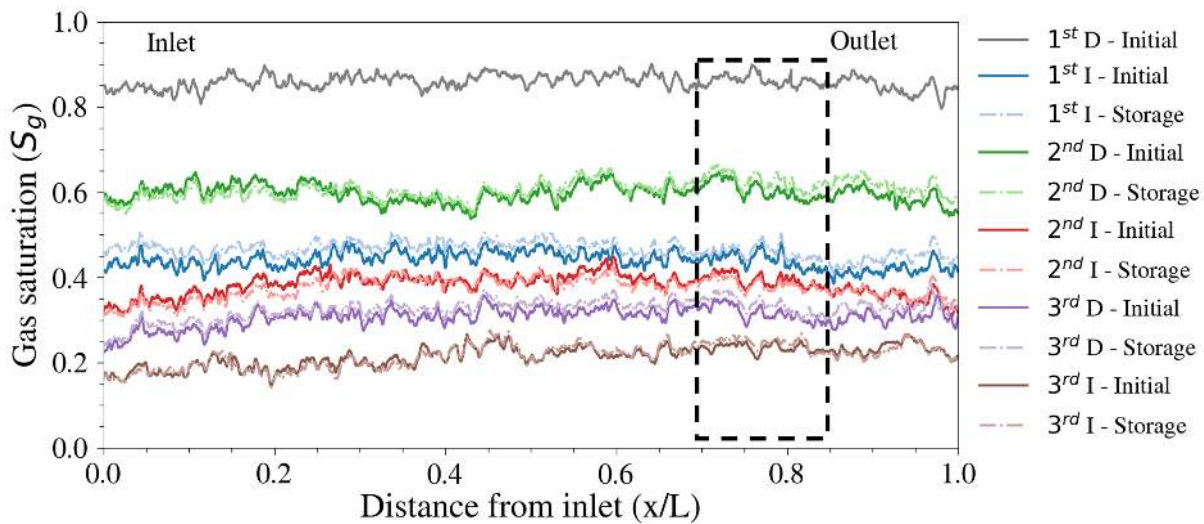


Figure 4.13: The gas saturation profile averaged along the flow direction during three cycles of hydrogen injection and water flooding across the length of a Bentheimer sample, illustrating both the initial injection and after a 16-hour waiting period. The black dashed line indicates the specific subsection selected for detailed analysis.

Furthermore, the stability of the gas distribution across cycles, as indicated by the near-uniform

profiles along the sample length, highlights the effectiveness of hydrogen retention in Bentheimer sandstone. However, small variations in saturation between the inlet and outlet during storage may reflect differences in local pore structure and capillary forces, which could lead to heterogeneous gas displacement dynamics.

A comparison of specific gas saturations (S_{gi} and S_{gr}) from studies in the literature using sandstone samples is provided in Fig. 4.14. The relatively high S_{gr} (40%) observed in our experiments may be partially attributed to the pre-equilibration of brine with hydrogen. This procedure likely reduced gas dissolution during injection, enhancing retention in the pore structure.

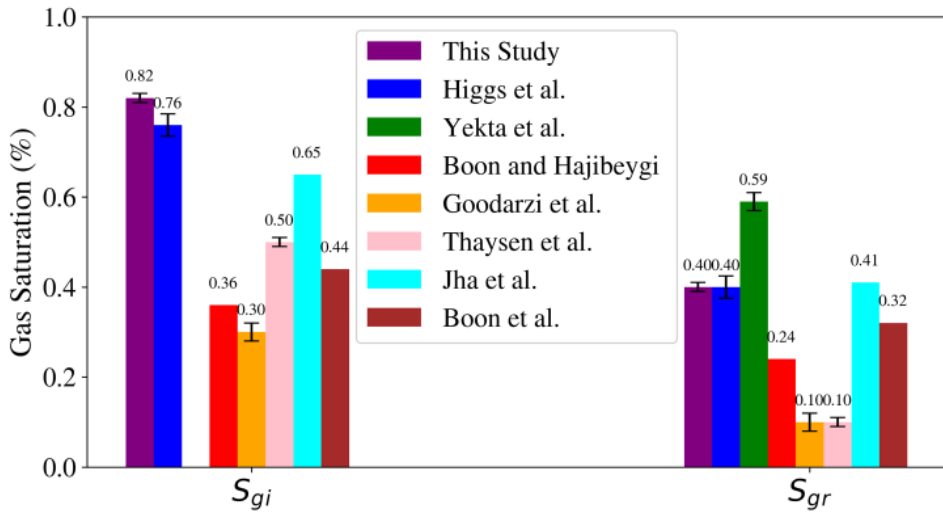


Figure 4.14: Illustration of the variation in gas saturation profiles for sandstone samples from the literature: Higgs et al. [15], Yekta et al. [16], Boon and Hajibeygi [17], Goodarzi et al. [18], Thaysen et al. [19], Jha et al. [20] and Boon et al. [21] including the present study. The error bars represent the uncertainty due to image segmentation.

Additionally, the 16-hour waiting period may have allowed Ostwald ripening to occur, enabling the redistribution of gas and stabilising larger gas clusters. While these conditions likely played a role, other factors, such as pore structure and capillary forces, may also have contributed to the observed values. Compared to Jha et al. [20], who reported a slightly higher residual saturation, the differences can be attributed to variations in pore structure and capillary pressure dynamics. Finally, the consistency of trends across studies, despite variations in S_{gi} and S_{gr} magnitudes, underscores the importance of experimental parameters such as pressure, flow rates, and capillary forces.

The gas injection rate, although not kept constant in this study (pressure-controlled) to focus on saturation effects, remains a critical parameter influencing storage and recovery performance [202]. Higher injection rates typically accelerate gas saturation and enhance initial storage efficiency by rapidly displacing brine [156]. However, they may also amplify pressure gradients, leading to increased capillary trapping in smaller pores and potentially reducing recovery efficiency. In contrast, lower injection rates promote a more uniform gas distribution by allowing equilibrium between phases, even at the cost of extended operational durations. Con-

versely, water injection was conducted at a constant flow rate, ensuring steady and controlled imbibition.

4.3.5 Wettability Characterisation

4.3.5.1 Specific Interfacial Area

The specific interfacial area per unit volume ($600 \times 600 \times 600$ voxels, upper part of the sample, shown in Fig. 4.5) was calculated for fluid and solid phases both initially and after a 16-hour storage period, as shown in Fig. 4.15. The results confirm the water-wet nature of the sample, as indicated by the consistently higher water-rock interfacial area compared to the gas-rock interfacial area. This preference reflects the natural tendency of water to maintain contact with the solid surface in a water-wet porous medium.

During the storage periods, the water-rock interfacial area exhibited a notable decline following water injection. This reduction suggests a relaxation process in which water redistributes to energetically favourable configurations, thereby decreasing its contact with the solid surface. Similarly, the gas-rock interfacial area consistently decreased after gas injection, particularly in the second cycle. This observation reflects the displacement of gas from regions in contact with the solid surface, likely driven by capillary forces that favour water-solid interactions. The gas-water interfacial area, although smaller in magnitude, also exhibited a slight reduction during the waiting period, which may be attributed to minor equilibration processes between the two fluids under static conditions.

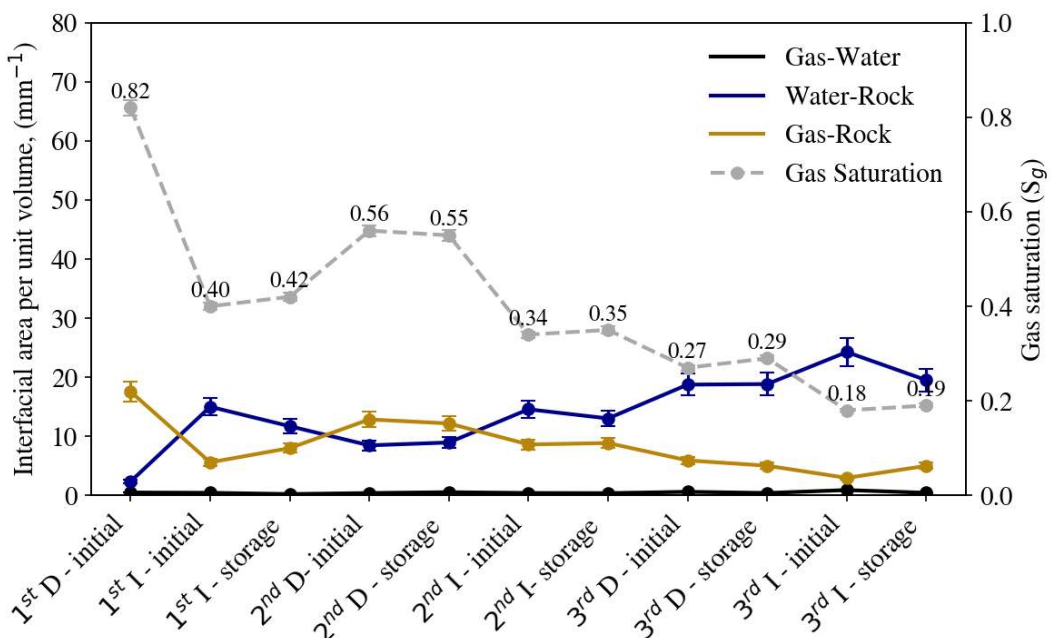


Figure 4.15: Measurements of interfacial area per unit volume between fluid-fluid and fluid-solid phases within a subvolume over three cycles of gas and water injection (D= Drainage, I= Imbibition). Results are presented for both the initial stage and after a 16-hour storage period, alongside gas saturation trends. Error bars indicate uncertainties in image segmentation.

The gas saturation data reveal a consistent trend as gas saturation remains stable after injection and during the storage periods across all cycles. This constancy confirms that no additional gas displacement or production occurs during storage. Despite this stability, the observed reductions in gas-solid and gas-water interfacial areas indicate a redistribution of the gas phase within the pore network. This redistribution likely reflects pore-scale adjustments, such as the coalescence of gas ganglia into larger, more stable structures, driven by mechanisms like Ostwald ripening. These findings are consistent with other works [18, 145, 157], which also confirmed the water-wet nature of the sample. In that study, the water-rock interfacial area decreased slightly during the waiting period, while the gas-rock area increased. However, the present study, conducted under higher pressure conditions, demonstrates more consistent trends, particularly for the gas-rock interface.

4.3.5.2 Pore and Throat Occupancy

To better understand the spatial distribution of gas and brine within the pore structure, both immediately after fluid injection and following a 16-hour storage period, a detailed 3D pore and throat occupancy analysis was performed on the middle part of the sample. This analysis is based on pore network structures extracted from dry scan images, as described in Chapter 3, Section 3.3.7. The methodology was applied across all experimental cycles, with results for gas injection and subsequent water flooding provided in the Appendix C.3. However, in this section, we focus on the first drainage and imbibition phase to illustrate the key mechanisms governing fluid redistribution.

Following the initial drainage phase, gas displaced brine from the majority of the pore space, resulting in a high initial gas saturation. During subsequent imbibition, water infiltrated the pore network, trapping gas within larger and medium-sized pores due to capillary forces. The distribution of gas and brine at this stage is consistent with a water-wet system, where water preferentially occupies smaller pores and throats, while gas remains trapped in larger elements. After the 16-hour waiting period, some changes in the pore and throat occupancy were observed. The probability distribution of pore and throat radii occupied by gas and brine, as well as the volume fraction of each phase over time, is presented in Fig. 4.17. Redistribution of the trapped gas phase suggests potential mechanisms such as Ostwald ripening, led to a reorganisation of the trapped gas phase.

4.4 Health and Safety

In this chapter, the experimental procedure involved equilibrating brine with hydrogen gas using a high-pressure reactor before injecting it into the sandstone sample. The general health and safety measures related to hydrogen handling, brine storage, and X-ray safety remain the same as outlined in Chapter 3, Section 3.4, and only the additional safety considerations specific to reactor operation are detailed here.

The Parr Bench Top Reactor used for equilibrating brine with hydrogen operates under elevated pressure and temperature conditions, requiring strict adherence to pressure vessel safety proto-

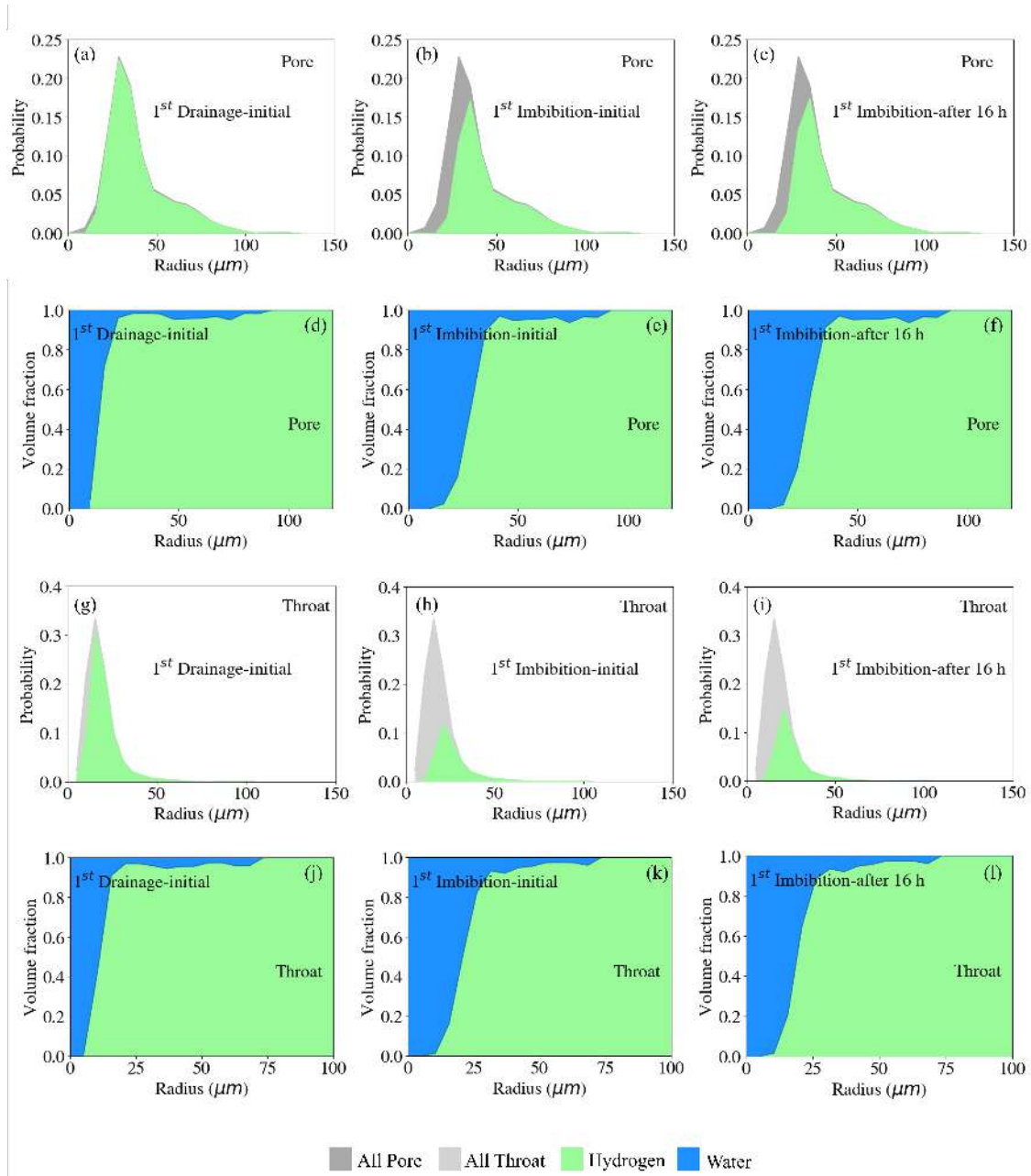


Figure 4.16: The probability distribution of pore and throat radii occupied by hydrogen (green) and water (blue) is shown for the first cycle. (a)-(c) and (g)-(i) show the initial occupancy immediately after imbibition and after 16 hours, highlighting the redistribution of fluids within pores and throats. (d)-(f) and (j)-(l) illustrate the volume fraction of hydrogen and water as a function of pore and throat size, demonstrating the extent of gas entrapment and subsequent fluid redistribution over time.

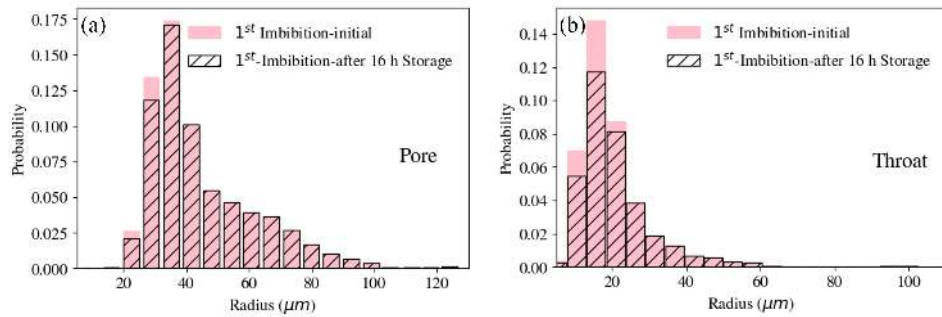


Figure 4.17: Comparison of volume-weighted histograms show the probability distribution of pore (a) and throat (b) radii occupied by water immediately after imbibition (pink) and after 16 hours (striped). The histograms illustrate a shift in gas occupancy, particularly in smaller pore and throat sizes, indicating redistribution over time.

cols. The primary risks associated with its operation include high-pressure hazards, potential hydrogen leaks, and mechanical failures. To mitigate these risks, the following safety measures were implemented:

- The reactor was fitted with pressure relief valves and pressure gauges to continuously monitor internal conditions. Experiments were conducted within the recommended operating limits of the reactor, and safety interlocks ensured that excessive pressure buildup was prevented.
- Since hydrogen is highly flammable and prone to leakage, the reactor system was tested for leaks before each experiment using soap solution tests. Gas flow rates were carefully controlled to avoid sudden pressure fluctuations.
- Hydrogen was introduced gradually to minimise rapid pressurisation risks. The system was vacuumed before hydrogen injection to eliminate residual oxygen, reducing the risk of explosive gas mixtures.

4.5 Final Remarks

In this study, we performed a porous plate experiment to measure capillary pressure and saturation, involving three cycles of hydrogen injection followed by water flooding on a Bentheimer sandstone sample, 60 mm in length and 12 mm in diameter. The experiment was conducted at 25°C and 8 MPa under capillary-dominated conditions. Pre-equilibrated brine was used to ensure no significant dissolution of hydrogen in the brine during either drainage or imbibition, even at pressures as high as 8 MPa. High-resolution images (5.4 μm voxel size) were captured to observe the pore-scale configuration of gas after each injection. Following each gas and water injection, a 16-hour no-flow period was implemented to examine the hydrogen distribution during the gas storage phase. As a result, the peak average hydrogen saturation achieved was approximately 82%, while the largest measured residual hydrogen saturation averaged around

40%. Additionally, the meniscus curvature between gas and water provided an independent estimate of local capillary pressure. Our results indicate the following.

1. Once flow has stopped, the gas redistributes within the pore space without altering the overall volume. Our hypothesis attributes this phenomenon to Ostwald ripening which leads to a uniform local capillary pressure mediated by transport of dissolved gas in the aqueous phase.
2. This rearrangement leads to better gas connectivity and, in most cases, the growth of a single, large connected ganglion.
3. The capillary pressure measurements are not consistent with traditional hysteresis models. Repeated drainage and imbibition cycles led to lower residual saturations. This was associated with pore-scale rearrangement of gas in the pore space leading to better connectivity. The experimental data acquired so far may suggest less hysteresis between drainage and imbibition than conventionally assumed.

In this chapter, the storage time for hydrogen trapping was 16 hours. In the next chapter, we will extend the storage duration to four days, allowing for a longer-term analysis. This will be combined with intermediate imaging and higher-resolution CT scans to enable a more detailed investigation of interfacial curvature and contact angle. This approach may provide deeper insights into the correlation between local capillary pressure and Ostwald ripening. A key focus of future work will be measuring capillary pressure at the endpoints of both imbibition and drainage. This will be complemented by differential pressure measurements to more precisely determine capillary pressure throughout the injection process.

Chapter 5

Pore-scale Insights into Wettability and Curvature for Hydrogen Storage

This chapter presents an experimental study on hydrogen-brine multiphase flow in Bentheimer sandstone. The findings contribute to an ongoing research effort aimed at integrating experimental data with numerical modelling. While this chapter is not yet published as a standalone study, the data and results will be included in a forthcoming publication in collaboration with modelling researchers.

5.1 Summary

This study explores hydrogen and brine flow dynamics in Bentheimer sandstone under high-pressure conditions using X-ray micro-CT imaging. By employing a porous plate setup with both hydrophilic and hydrophobic plates, the experiment assessed gas saturation, wettability, capillary pressure, and interfacial curvature. Following an initial hydrogen injection, three successive brine injections were performed, with fluid redistribution monitored over a four-day storage period. The results showed notable changes in gas-phase connectivity due to Ostwald ripening, where smaller gas clusters dissolved and reprecipitated onto larger ones. Gas saturation initially reached 82% after hydrogen injection and progressively decreased to 40% after the first brine injection, 30% after the second, and 20% after the third. Contact angle measurements confirmed a strongly water-wet system, with values around 50°, aligning with Bentheimer sandstone's hydrophilic nature. Direct curvature measurements from segmented images provided independent estimates of capillary pressure, which were consistent with experimental data. Minkowski functionals further quantified pore-scale structural evolution, highlighting reductions in residual gas saturation across successive imbibition cycles. The observed reduction in capillary pressure hysteresis suggests improved gas redistribution over time. These findings contribute to the understanding of hydrogen trapping and storage mechanisms in porous media, with implications for subsurface energy applications.

5.2 Materials and Methods

5.2.1 ~~Discs~~, Rock and Fluid Properties

To achieve better flow control during the experiment, two porous ceramic plates were used. Their hydrophilic and hydrophobic properties provided selective phase control, improving the stability of saturation within the rock sample. For further details on the plate preparation and functionality, refer to Chapter 4, Section 4.2.2. The design and function of the porous plates are shown in Fig. 5.1.

Bentheimer sandstone was chosen for this study due to its extensive use in laboratory experiments and suitability as a benchmark material, as discussed in Chapter 3, Section 3.2.1. The cylindrical core sample measured 12 mm in diameter and 37 mm in length, the latter chosen to accommodate scanner limitations and ensure the entire sample could be imaged effectively. The overall porosity of the sample was measured at 23% using the same method as mentioned in Chapter 4, Section ??.

The aqueous (wetting) phase used in this study was prepared by dissolving 20wt.% ~~Potassium Iodide~~ (KI) in deionised water to enhance phase contrast during imaging. This allowed for a clear distinction between the fluid phases in the pore network. Gas properties included a dynamic viscosity of 5.99×10^{-6} Pa.s [29] and an interfacial tension of $\sigma = 7.23 \times 10^{-2}$ N.m⁻¹ with brine [31].

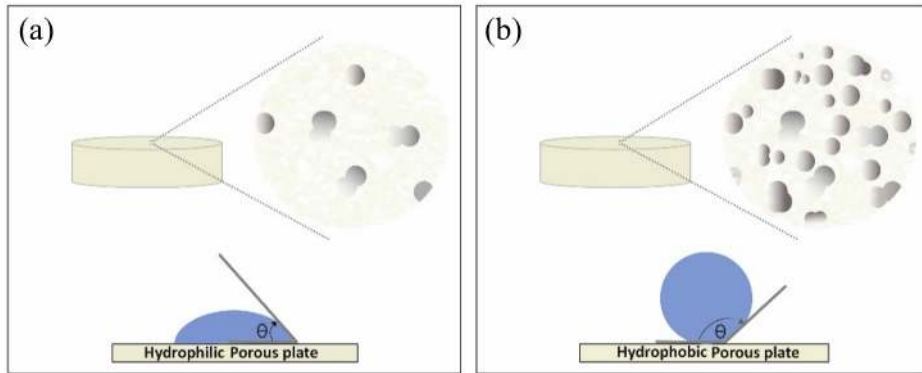


Figure 5.1: Illustration of hydrophilic and hydrophobic porous plates. The hydrophilic plate, depicted on the left (a), allows water to pass through while acting as a barrier to gas. The hydrophobic plate, shown on the right (b), repels water, ensuring it remains confined within the rock sample. Insets highlight the pore structure of each plate, with the respective wetting properties depicted by contact angles (θ) of water.

5.2.2 Experimental Procedure

The experimental procedure aimed to evaluate gas saturation after repeated water injections, focusing on the quantity of trapped gas at high initial gas saturation levels. Water was injected three times under a pore pressure of 3500 kPa and a confining pressure of 4500 kPa, while maintaining a temperature of 25° C. The capillary number (Ca) is calculated from Eq. 2.12 for

3 cycles, see Table 5.1. The steps for initiating the unsteady-state two-phase flow micro-CT imaging experiment were as follows:

1. For fluid preparation, the brine was equilibrated with hydrogen gas in a high-pressure reactor at a mixing rate of 176 rpm. This process ensured that the brine became fully saturated with hydrogen before being injected into the sample.
2. The experimental sequence then proceeded with the preparation of the sample. The rock sample was thoroughly dried and enclosed in a nitrile rubber to prevent interaction with the confining fluid. Two porous ceramic plates, one hydrophobic and the other hydrophilic, were placed at opposite ends of the sample. The hydrophilic plate acted as a barrier to retain the gas within the sample, while the hydrophobic plate ensured that water remained inside the sample during gas injection. The upper portion of the rubber was connected to the production assembly, and the lower end was linked to the injection assembly, as shown in Fig 5.2.
3. The coreholder was placed inside a Heliscan micro-CT scanner, and the required flowlines and pumps were configured for fluid phase injection. To remove any air and prepare for hydrogen injection, the sample, lines, and gas pump were thoroughly vacuumed for several hours, ensuring the prevention of any potentially hazardous hydrogen-air mixture.
4. A confining pressure of 4.5 MPa and a pore pressure of 3.5 MPa were applied. To accurately monitor the pressure drop across the sample, a differential pressure transducer (Keller PD-33X) with a precision of ± 0.04 kPa was used. The transducer was connected to the sample's inlet and outlet through holes drilled in the porous plates, ensuring reliable pressure measurements.
5. The experiment began with scanning a dry sample. Brine was then introduced from the bottom at a flow rate of 0.1 ml/min to ensure full saturation of the pore space. After 18 hours, the flow rate was increased to 0.5 ml/min while continuously monitoring the pressure drop until stabilisation. At this point, the absolute permeability of the sample was determined to be $(1.5 \pm 0.1) D$ $(1.5 \times 10^{-12} \pm 0.1 \times 10^{-12} \text{ m}^2)$ under experimental conditions, with details of the measurement method provided in Appendix B.2. The low-flow-rate brine injection was maintained overnight at 0.02 ml/min while the brine-saturated sample was scanned.
6. The first gas injection (drainage) began at a low flow rate to allow gas to enter the sample while the scanner was active, making it possible to observe gas bubbles entering from the top. For the first cycle, gas was injected at 0.5 ml/min, with half a pore volume introduced initially, followed by a quick scan to assess gas saturation. This process was repeated incrementally to complete the first drainage step.
7. After the gas injection was completed, the valve was closed, and the gas pump was switched off. A full-length helical scan was then performed at a low resolution to evaluate overall

saturation distribution and volume. Additionally, a region-of-interest (ROI) scan was conducted at a finer resolution, focusing on the middle section of the rock.

8. After allowing a few hours for gas equilibrium, brine was then injected (imbibition) at a steady flow rate of 0.05 ml/min for approximately one hour. Following this, all valves were closed, and the sample was scanned. The sample was left undisturbed for four days, during which scans were performed twice daily to monitor fluid rearrangement over time.
9. After four days, a second brine injection was conducted following the same injection and scanning procedure. To complete three imbibition cycles, a third brine injection was performed, followed by another four-day observation period with periodic scans.
10. Upon completing the three imbibition cycles, a final full-length scan of the sample was conducted 24 hours later to evaluate the residual gas content.

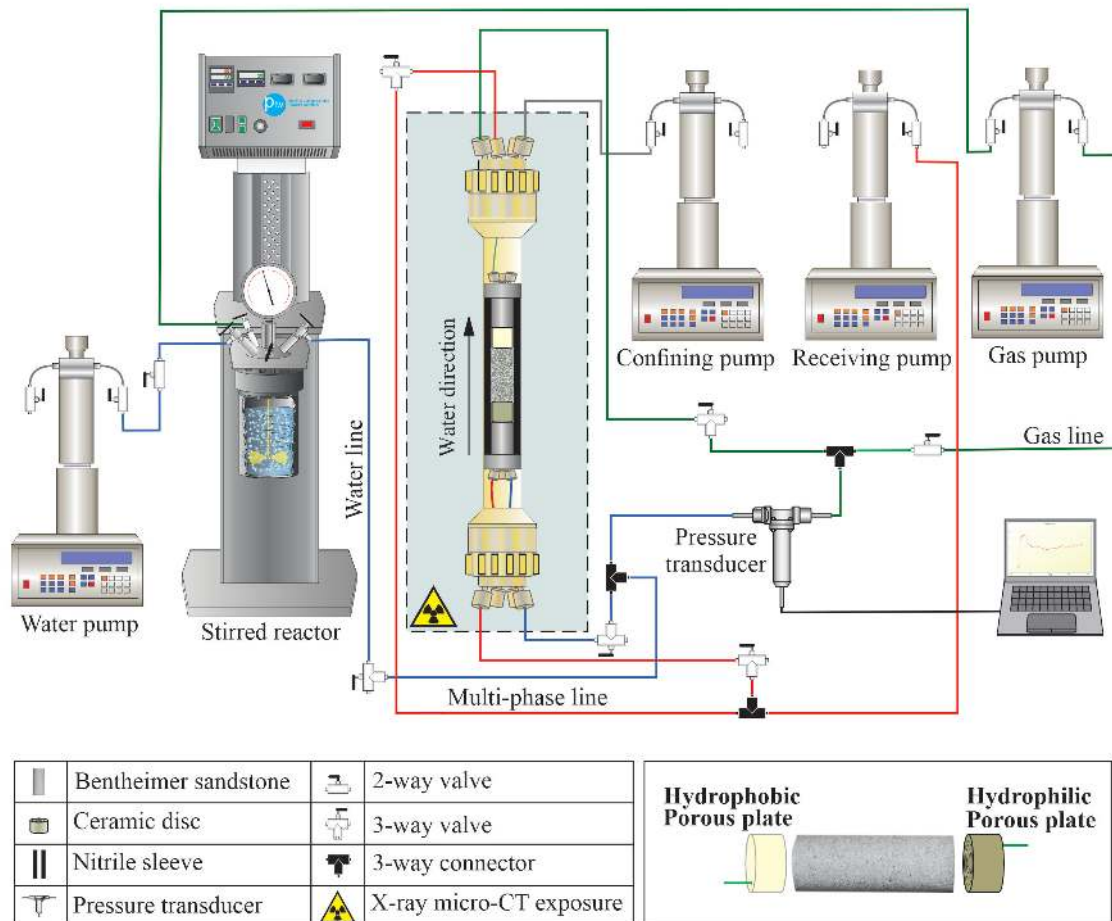


Figure 5.2: Schematic representation of the two-phase hydrogen-brine experiment using an X-ray micro-CT scanner. The setup includes the core holder, pumps, flow lines, valves, pressure transducer, and hydrophilic and hydrophobic porous plates. Hydrogen gas is injected from the top, while brine, equilibrated in the stirred reactor, is injected from the bottom. The micro-CT scanning region is highlighted within the black dashed enclosure.

Table 5.1: Capillary numbers, $Ca = \mu q / \sigma$, where μ is the viscosity of the injected fluid, σ is the interfacial tension, and q is the Darcy velocity for the flooding cycles.

Cycle	Flooding step	Flow Rate [ml.min ⁻¹]	$Ca_{[gw]}$	$Ca_{[wg]}$
1	1 st Drainage	0.08	9.79×10^{-10}	-
1	1 st Imbibition	0.05	-	8.39×10^{-8}
2	2 nd Imbibition	0.05	-	8.39×10^{-8}
3	3 rd Imbibition	0.05	-	8.39×10^{-8}

5.2.3 Image Acquisition and Processing

For 3D imaging, a Heliscan micro-CT scanner was utilised, operating at a tube voltage of 100 kV and a target current of approximately 50 μ A. The exposure time and number of projections are detailed in Table 5.2, while additional specifications regarding the scanner can be found in Section B.5. Two distinct scanning modes were employed: a full-length helical scan at a resolution of 9.37 μ m and 4.68 μ m per voxel, designed to capture overall saturation distribution and volumetric assessments, and a high-resolution region-of-interest (ROI) scan at 3.04 μ m per voxel, focusing on a central segment of the rock. This dual approach facilitated both macroscopic saturation analysis and detailed pore-scale investigations, including interfacial curvature and ganglia volume measurements. The acquired images spanned 1480 voxels in the x-direction, 1480 voxels in the y-direction, and 3360 voxels in the z-direction. A comprehensive discussion of the scanning parameter selection, including the number of projections, exposure time, and voltage settings, is provided in Appendix B.6

Table 5.2: Summary of scanning parameters for the Heliscan micro-CT ~~scanner~~ used in the experiment. Two scanning modes were employed: a full-length helical scan to capture overall saturation distribution and volumetric assessments, and a high-resolution region-of-interest (ROI) scan to focus on detailed pore-level investigations. The scanning parameters, including exposure time, projections, total time, and voxel resolution for each mode, are detailed in the table.

Scan type	Exposure time [s]	Projections	Total time [mins]	Voxel resolution [μ m]
Heliscan (Full)	0.3	2997	97	9.37
Heliscan (Full)	0.3	2997	505	4.68
Region-of-interest (ROI)	0.3	3261	185	3.04

The image processing workflow began with reconstructing the images to ensure compatibility with the Avizo software for further analysis [184]. Unlike conventional micro-CT imaging workflows that require stitching multiple scans, the Heliscan micro-CT scanner produced a single, continuous image of the entire sample, eliminating the need for stitching. To prepare the im-

ages for analysis, extraneous regions, such as the rubber surrounding the sample, were cropped from the dataset. This process was carried out for both the full-length helical scans and the high-resolution region-of-interest (ROI) scans, as illustrated in Fig. 5.3. Since the Heliscan system inherently registers scans during acquisition, only minimal adjustments were necessary for alignment.

A non-local means filter was then applied to reduce noise in the reconstructed images [185]. More details of greyscale images provided in Appendix D.1. Subsequently, the watershed segmentation technique was used to distinguish the gas, brine, and rock phases. This segmentation allowed the extraction of critical metrics, including curvature, surface areas, and fluid saturation. Representative results of the segmented phases are presented in Figs. 5.4.

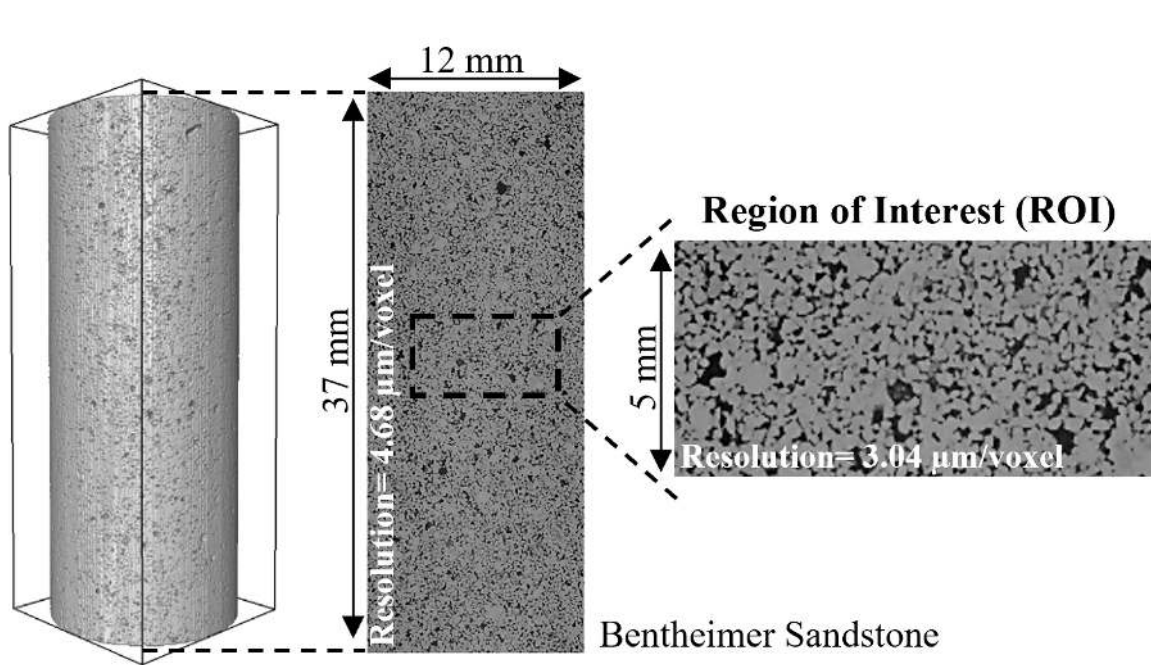


Figure 5.3: Illustration of the rock sample scanned using the Heliscan micro-CT scanner. The full-length scan was obtained at $4.68 \mu\text{m}$ resolution, while a high-resolution region of interest (ROI, 12 mm \times 5 mm) was scanned at $3.04 \mu\text{m}$ resolution for detailed analysis. The zoomed region highlights the enhanced resolution, facilitating pore-level investigations.

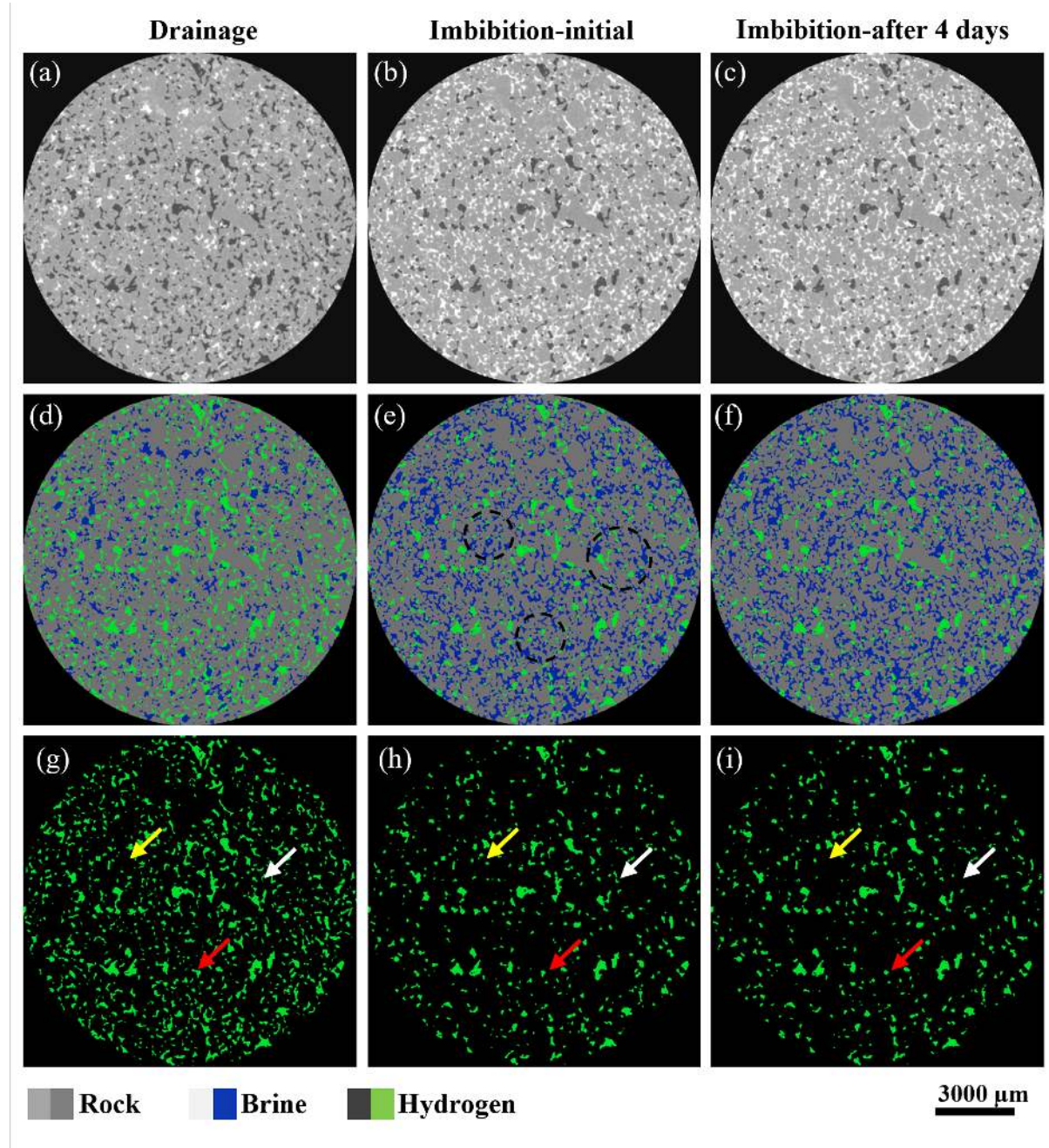


Figure 5.4: Visualisation of fluid distribution in a porous rock sample during drainage, initial imbibition, and after four days of storage. The top row (a–c) presents greyscale segmented images, where rock appears in grey, brine in light grey, and gas in dark regions. The middle row (d–f) shows phase-segmented images highlighting brine in blue and hydrogen gas in green within the rock pores. The bottom row (g–i) isolates the hydrogen phase, illustrating gas redistribution over time. During drainage (a, d, g), hydrogen is initially dispersed within the pores. Upon imbibition (b, e, h), brine invades, partially displacing hydrogen. After four days of storage (c, f, i), Ostwald ripening causes smaller gas clusters to dissolve and redeposit into larger connected clusters, enhancing hydrogen connectivity. Coloured arrows in (g–i) indicate regions where gas rearrangement has occurred.

5.3 Results and Discussion

This section is structured into distinct subsections, each addressing a key aspect of fluid behaviour within the sample. First, in Section 5.3.1, we explore long-term gas rearrangement and ganglia dynamics, highlighting how gas redistributes over time due to capillary forces and diffusion. In Section 5.3.2, we investigate wettability characteristics, discussing the role of contact angles in governing fluid-fluid and fluid-solid interactions. Next, in Section 5.3.3.4, we discuss the Minkowski Functionals by analysing the gas saturation distribution along the sample length, providing insights into saturation variations and displacement efficiency. Then, we examine the interfacial area, quantifying the spatial distribution of phases and the extent of fluid-fluid interfaces. Following this, we present capillary pressure measurements, illustrating the relationship between capillary forces and saturation within the porous structure. Finally, we will discuss the connectivity.

5.3.1 Redistribution of Gas During Long-Term Storage

Here we explore the evolution of gas ganglia connectivity and redistribution during 4-days storage following gas and water injection. The analysis focuses on the structural changes in the gas phase at the pore scale, highlighting the processes that govern gas connectivity and redistribution over time. The two-dimensional cross-sectional images in Fig. 5.5 highlight the effect of imaging resolution on the analysis of gas connectivity and redistribution.

The images, captured at resolutions of 3.04 $\mu\text{m}/\text{voxel}$, 4.68 $\mu\text{m}/\text{voxel}$, and 9.37 $\mu\text{m}/\text{voxel}$, reveal structural changes in the gas phase before and after 4 days of storage. Initially, as seen in the top row, the gas clusters appear isolated and dispersed across the pore space. After 4 days of storage (bottom row), the clusters show a clear trend of merging, becoming larger and more connected. This transformation is observed consistently across all resolutions, though finer resolutions provide greater clarity in detecting smaller gas ganglia.

Figure 5.6 provides a closer look at the redistribution of gas ganglia during the 96-hour storage period. The three-dimensional rendering subvolume snapshots (subfigures a–e) demonstrate that smaller gas clusters dissolve, and the gas reprecipitates onto larger clusters over time. The red dashed circles in subfigures a–e highlight regions where significant redistribution occurs. This transformation emphasises the critical role of Ostwald ripening in gas connectivity. Over 96 hours, larger clusters grow at the expense of smaller ones, leading to a more connected gas network.

5.3.1.1 Fluid Connectivity

Fluid connectivity within the pore space is analysed through a combination of qualitative visualisation and quantitative measurements. To examine connectivity qualitatively, segmented images of the fluid phase are processed to isolate the disconnected objects. Each separate fluid body is assigned a unique colour, allowing for a clear visual representation of connectivity. A broad spectrum of colours suggests a fragmented phase with poor connectivity, whereas a more uniform colour distribution indicates a well-connected network, see Fig. 5.7.

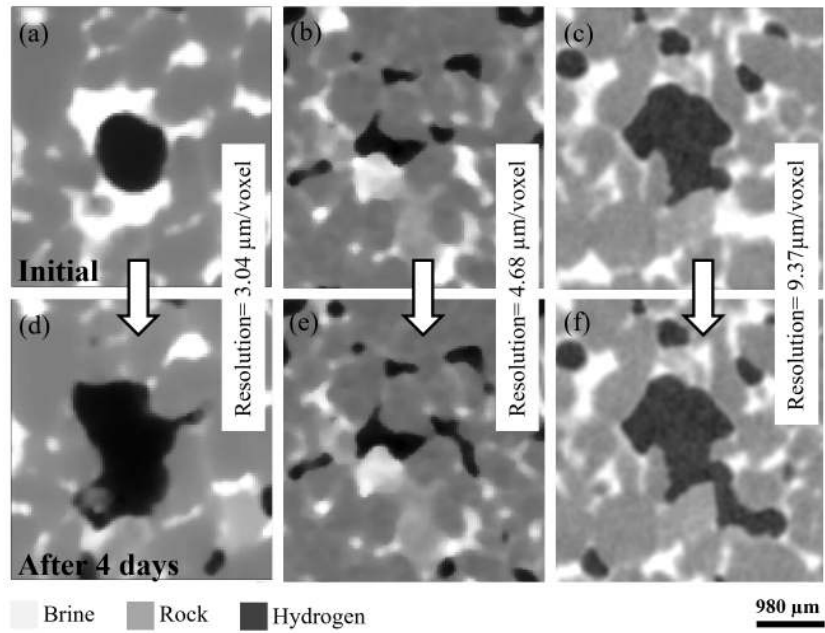


Figure 5.5: A small section of two-dimensional raw greyscale images, highlighting gas structure and connectivity evolution over time. The top row (a–c) represents the initial stage, while the bottom row (d–f) shows the same region after four days of storage. Images were captured using X-ray tomography at three different resolutions: (a, d) $3.04 \mu\text{m}/\text{voxel}$, (b, e) $4.68 \mu\text{m}/\text{voxel}$, and (c, f) $9.37 \mu\text{m}/\text{voxel}$. The greyscale intensity distinguishes brine (light grey), rock matrix (medium grey), and hydrogen gas (dark regions). Over four days, Ostwald ripening led to an increase in gas-phase connectivity and structural coalescence, as observed in the dark regions.

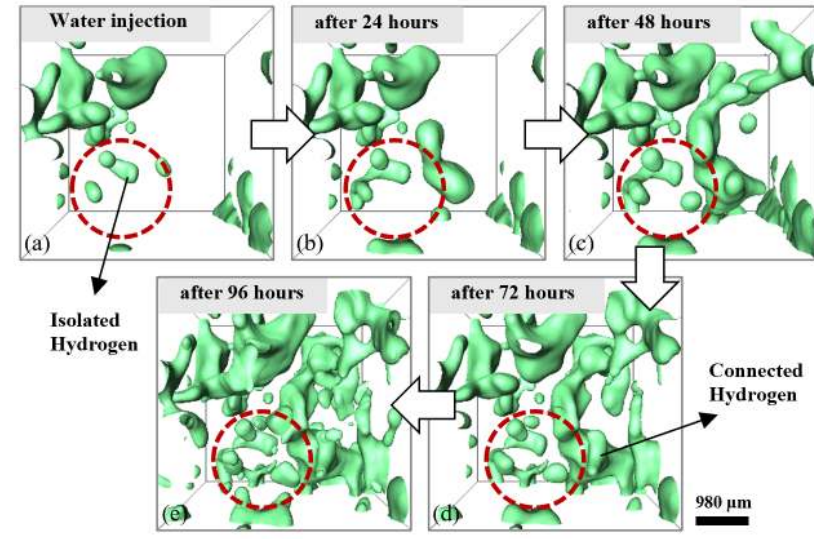


Figure 5.6: Structural evolution of hydrogen gas ganglia during storage, visualised through sequential 3D scans over four days. Panels (a–e) illustrate the progressive morphological changes of the hydrogen ganglia at key intervals: after water injection, 24 hours, 48 hours, 72 hours and 96 hours. The dashed red circle highlights regions where connectivity increases due to the Ostwald ripening process, resulting in larger, more interconnected ganglia over time.

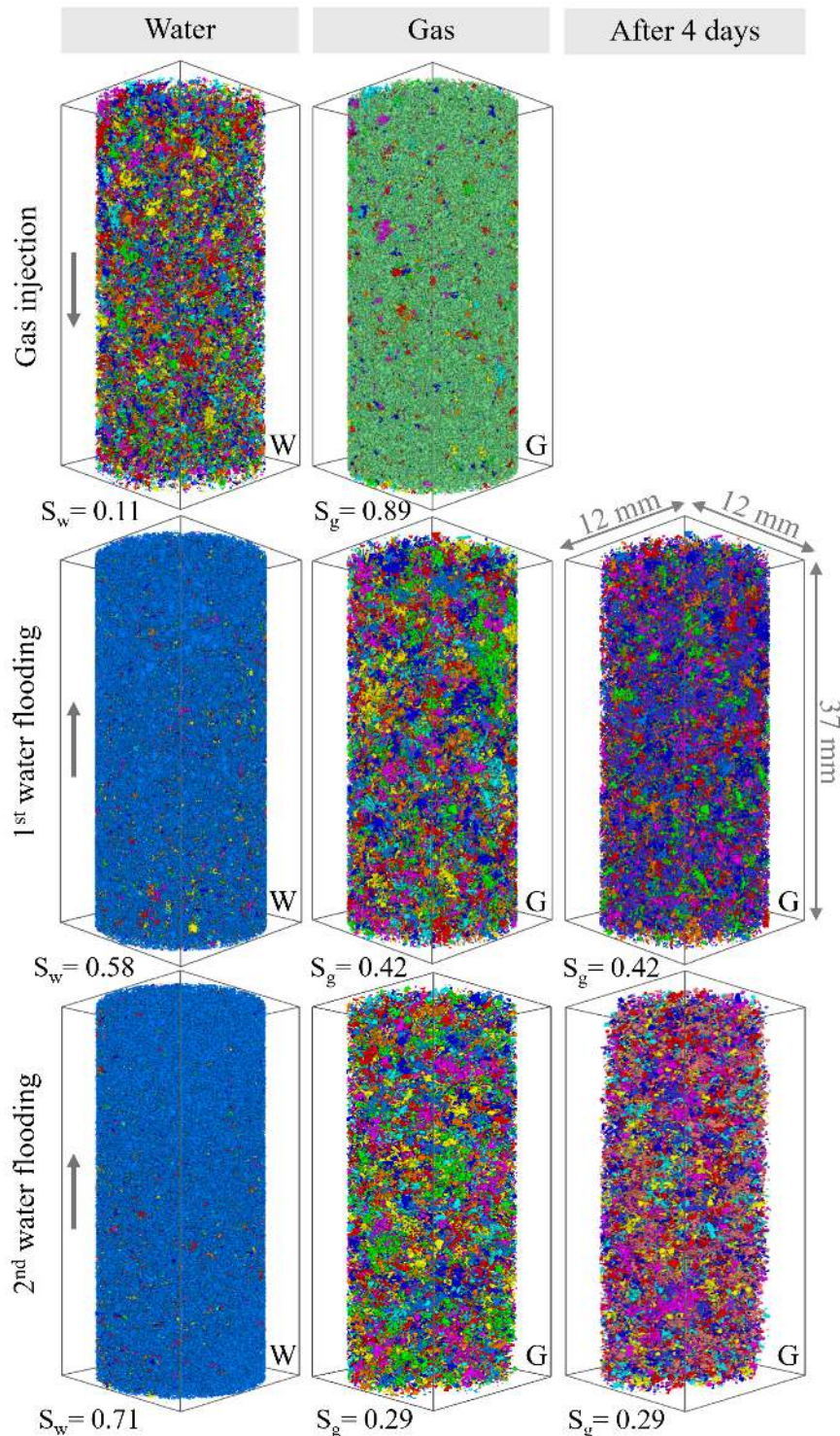


Figure 5.7: Three-dimensional visualisation of gas and water distributions in the sample at various stages of the experiment such as after gas injection, first ~~water flooding~~, and second ~~water flooding~~. The last column (After 4 days) demonstrates structural changes in the gas phase after storage. The distinct colours represent individual clusters of the gas and water phases, highlighting their spatial distribution and connectivity within the pore space. The grey colour arrows show the direction of fluid injection.

Figure 5.7 illustrates the initial gas injection creates a connected gas network spanning the pore space. During the first waterflooding, a significant portion of the gas phase is displaced, leaving behind residual gas ganglia. The second waterflooding stage further reduces the gas saturation, but some larger ganglia remain intact due to capillary trapping. The last column (After 4 days) shows changes in the gas structure after storage. These changes indicate a shift in the distribution of the gas phase, with larger ganglia becoming more dominant. This redistribution aligns with observations from the ~~resolution~~ analysis (Fig. 5.5), suggesting that the residual gas reorganises during storage to form more stable configurations.

For a quantitative assessment, the Euler characteristic is employed as a topological measure of connectivity, see Table 5.3. By normalising the Euler characteristic with respect to the sub-volume in mm^3 , a density-like metric is derived, ensuring comparability across different conditions. As previously described in Chapter 4, a positive Euler characteristic denotes a predominance of isolated gas ganglia and limited connectivity, whereas a negative value indicates a well-connected phase with numerous loops [201].

The results show distinct connectivity trends during gas injection (drainage) and ~~water flooding~~ (imbibition). Initially, gas injection results in a negative Euler characteristic (-5.3), reflecting strong connectivity within the pore network. In contrast, the subsequent ~~water flooding~~ stages exhibit positive Euler characteristic values, signifying increased gas trapping due to capillary forces. Over time, the Euler characteristic systematically declines during storage, indicating progressive coalescence of gas ganglia and improved connectivity. This trend is particularly evident in the imbibition cycles, where values decrease from 24.0 to 21.2 (1st imbibition), 22.4 to 20.8 (2nd imbibition), and 25.5 to 19.2 (3rd imbibition) over four days. These observations align with the physical process of Ostwald ripening, whereby smaller ganglia merge into larger, more stable clusters, enhancing connectivity over storage periods.

Table 5.3: Normalised Euler characteristic [mm^{-3}] throughout hydrogen and brine injections, capturing the initial state and the subsequent 4-days storage period.

Normalised Euler characteristic [mm^{-3}]			
Cycle	Flooding step	Initial	4-days Storage
1	1 st Drainage	-5.3	-
1	1 st Imbibition	+24.1	+21.2
2	2 nd Imbibition	+22.4	+20.8
3	2 nd Imbibition	+25.5	+19.2

Note. The Euler characteristic was measured on segmented images of a sub-volume and normalised to the total volume.

To complement the qualitative observations, a cumulative graph (Fig 5.8) has been added to illustrate the volume distribution of gas ganglia during gas injection and waterflooding. The graph reveals that the majority of gas volume is increasingly concentrated in larger clusters as the storage period progresses. This trend aligns with the visual evidence from Fig. 5.5, confirming that Ostwald ripening mechanisms drive the redistribution process. Larger ganglia grow at the expense of smaller clusters, stabilising the system by enhancing connectivity.

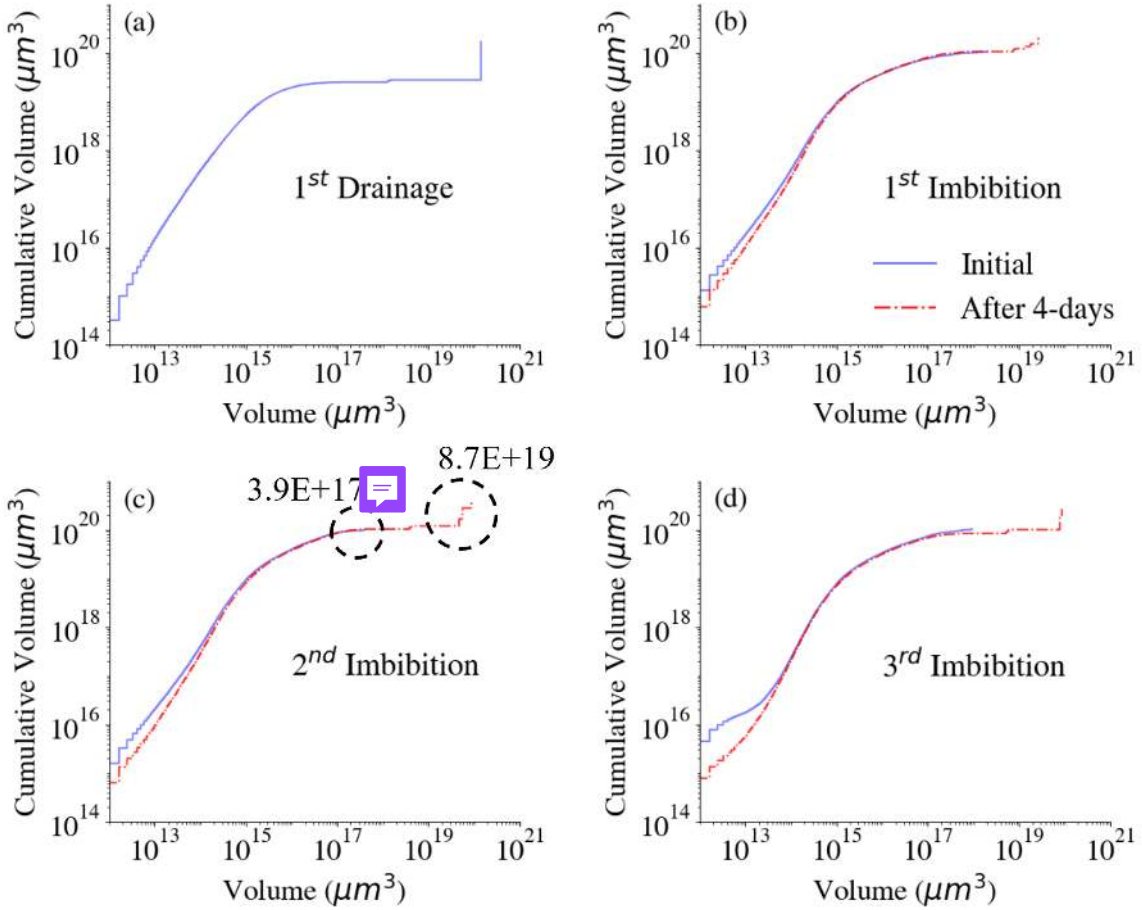


Figure 5.8: Cumulative volume distribution of gas ganglia after gas injunction (a) and water flooding (b-d), during the initial stage and after 4 days of storage. Each curve represents the cumulative gas volume as a function of ganglia size, highlighting the redistribution of gas. The vertical line observed after 4 days of storage indicates the dominance of a single large ganglion, resulting from the dissolution of smaller clusters and reprecipitation onto larger ones through Ostwald ripening.

5.3.2 Wettability in a Brine-Hydrogen System

5.3.2.1 Contact Angles

This section investigates the wettability in a water-gas system, analysed through contact angle measurements derived from CT imaging. The contact angle measurement methodology follows the geometric and topological approaches introduced by Wang et al. [203], incorporating the extended topological method to improve accuracy. This method enhances sensitivity to contact loop identification by accounting for solid surface orientation, thereby providing a more reliable estimation of wettability at the pore scale.

Initially, the sample is fully brine-saturated, ensuring no trapped gas. After gas injection (G1), a significant portion of the pore space is occupied by hydrogen, forming a connected gas phase. Following the first water flooding cycle (WF1), a noticeable reduction in gas saturation is ob-

served as water invades and displaces the gas. The subsequent flooding cycles (WF2 and WF3) continue this trend, progressively decreasing gas saturation, see Fig.5.9.

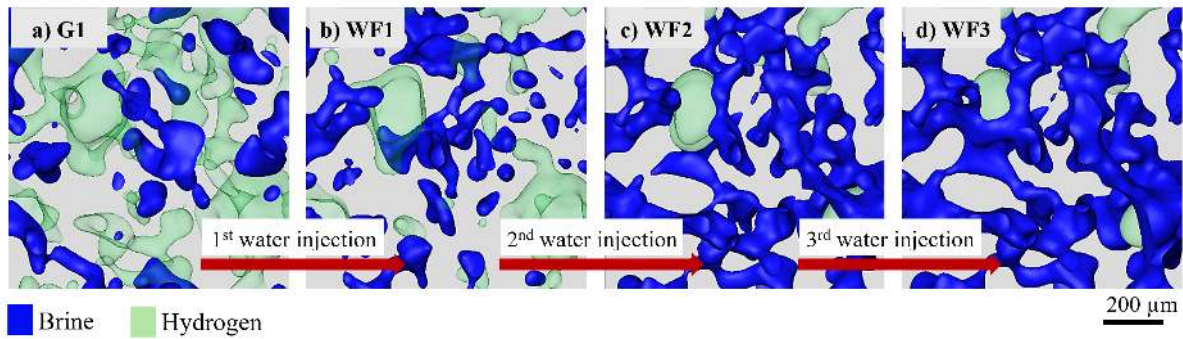


Figure 5.9: Two-dimensional visualisation of hydrogen and brine distributions within Bentheimer sandstone during gas injection and successive ~~water flooding~~ cycles. The figure illustrates different experimental stages, beginning with gas injection (G1), followed by first ~~water flooding~~ (WF1), second ~~water flooding~~ (WF2), and third ~~water flooding~~ (WF3). The blue regions represent the water phase, while the green regions indicate the gas phase. Key transitions are annotated to track the evolution of fluid distribution over time.

To ensure a representative assessment, a subvolume of $300 \times 300 \times 300$ voxels was extracted from the central region of the sample. Wettability was analysed across three sequential ~~water~~ flooding stages to track its evolution over time. Figure 5.10 (a) presents the probability density functions of contact angles at different imbibition cycles. Initially, the brine-hydrogen contact angle exhibited a mean value of approximately 50° , indicating a strongly water-wet condition. In water-wet systems, contact angles below 90° confirm that the rock surface preferentially attracts brine over hydrogen. This behaviour aligns with Bentheimer sandstone's high quartz content, a mineral known for its hydrophilic nature [174].

Similar wettability characteristics have been reported by Jangda et al. [136]. They found contact angles of 54° and 53° in Bentheimer sandstone under high-pressure conditions. The similarity in contact angles supports the strong water-wet nature of Bentheimer sandstone across different experimental conditions.

As ~~water flooding~~ progressed, the contact angle distribution shifted slightly, with a minor decrease in angles observed over time. Figure 5.10 (b) compares the contact angle distributions before and after four days. The solid black line represents the initial imbibition, while the dashed blue line captures the evolution of wettability. The contact angle distribution shows minimal change after 4 days, with a slight shift towards higher angles. This suggests that the rock remains predominantly water-wet, with no significant alteration due to brine-rock interactions or hydrogen exposure. Unlike mixed-wet or oil-wet systems, where higher contact angles ($>90^\circ$) are expected due to oil-affinity, Bentheimer sandstone's predominantly water-wet nature ensures that brine preferentially coats the pore walls while hydrogen resides in the pore centres.

To visually confirm these findings, Figure 5.10 (c) presents reconstructions of a zoomed-in subvolume, highlighting fluid distribution within pores. The images reveal that brine preferentially coats the pore walls, while hydrogen remains in the pore centre, a classic indicator of strongly

water-wet conditions. The side-by-side comparison of initial and post-4-day imbibition further emphasises that the rock's wettability remains consistently water-wet, with minimal alteration over time. This strong water-wet characteristic has significant implications for hydrogen storage, as it enhances hydrogen displacement efficiency and capillary trapping behaviour. Water-wet conditions promote hydrogen mobility while reducing the risk of retention in pore throats, thereby influencing long-term storage stability.

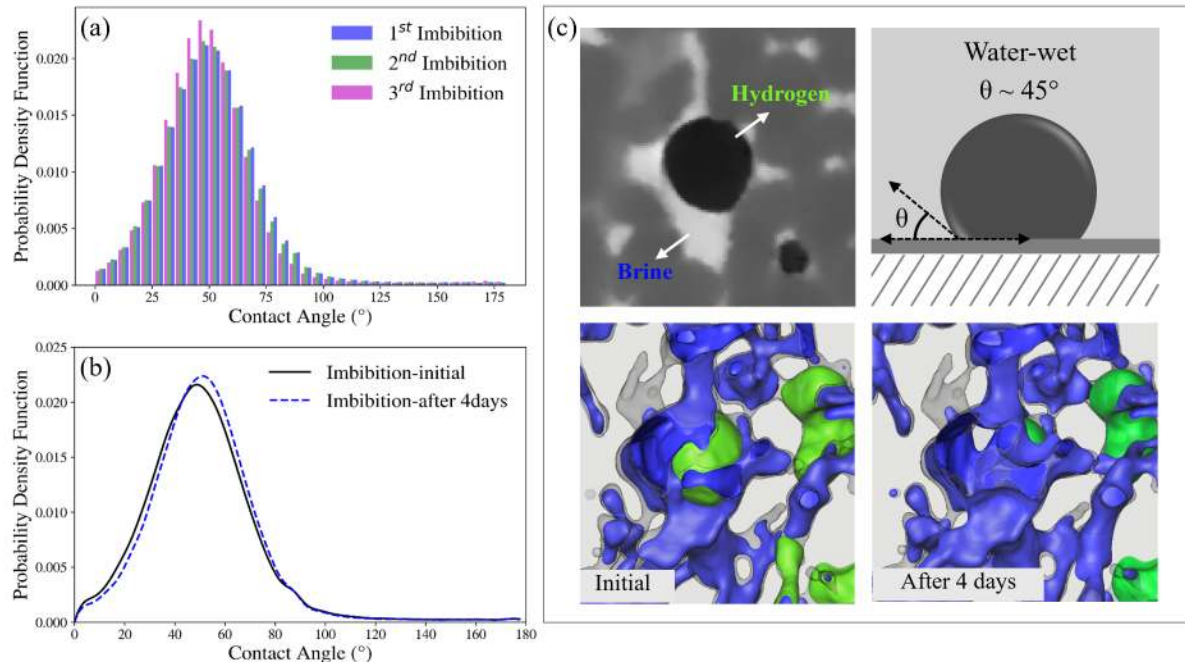


Figure 5.10: Probability density functions of contact angles during imbibition are shown in (a) and (b), indicating a predominantly water-wet system. (c) provides visual confirmation through CT-based visualisations of a zoomed-in subvolume. The bottom row shows a side-by-side comparison before and after 4 days, reinforcing that brine preferentially coats pore walls while hydrogen remains in the pore centre, with minimal wettability alteration over time.

5.3.2.2 Pore and Throat Occupancy Maps

Following the contact angle analysis, we now examine how fluids distribute within ~~the pore bodies~~ and throats following water injection. Figures 5.11 and 5.12 present the probability distribution of pore and throat sizes occupied by gas and water, alongside their respective volume fractions. This analysis is based on pore network structures derived from dry scan images to characterise fluid arrangement and phase distribution, as described in Chapter 3, Section 3.3.7.

Immediately after water injection, hydrogen predominantly resides in larger pores and throats, while brine preferentially occupies smaller ~~pores and throats~~. Over the course of four days, a gradual shift in fluid occupancy is observed as brine progressively infiltrates larger voids, thereby reducing hydrogen retention. This redistribution process is governed by capillary forces, leading to the displacement of hydrogen. Similarly, throat occupancy trends indicate a higher proportion of brine-filled throats after water injection, further emphasising the influence of capillarity on

fluid reorganisation.

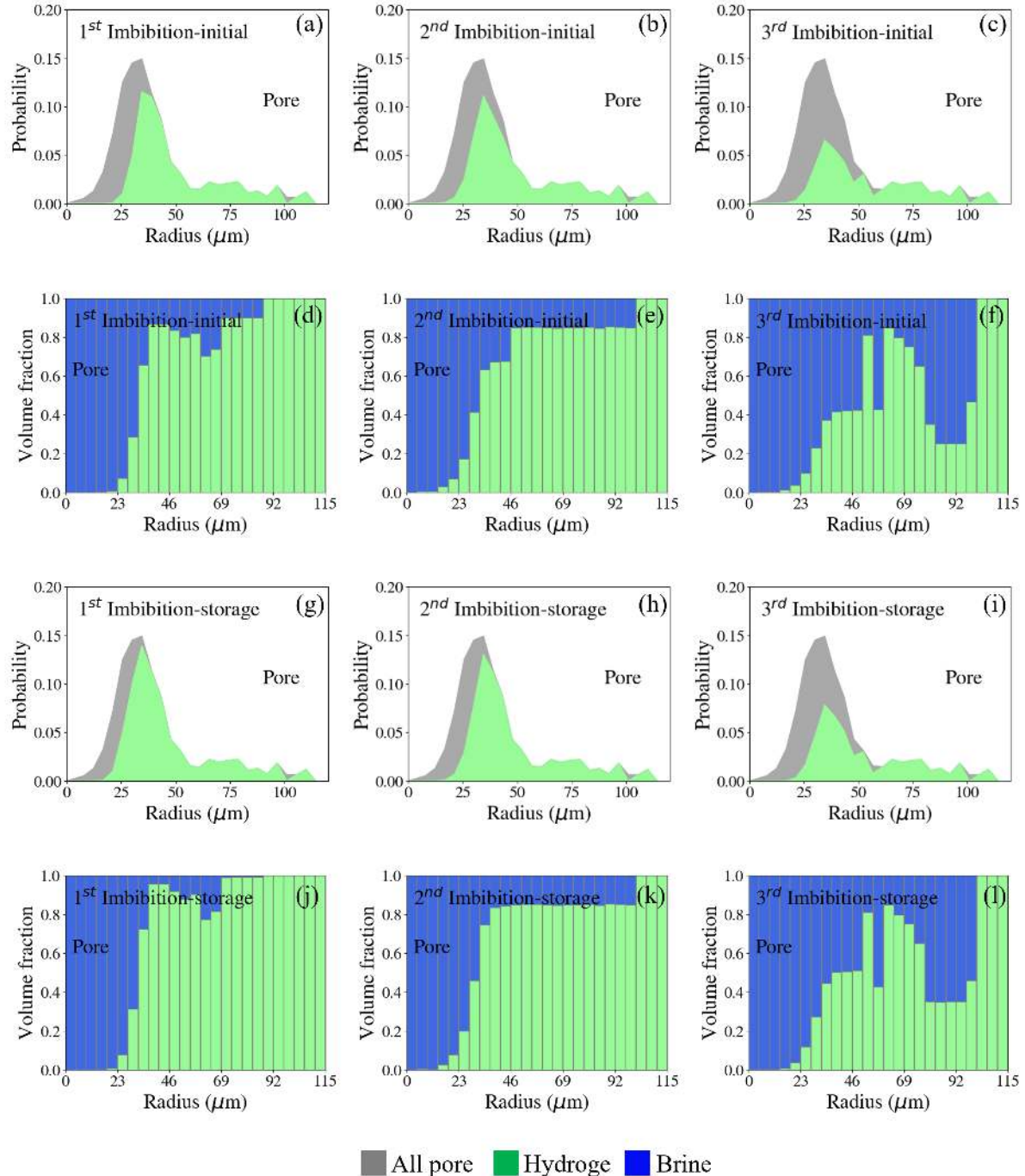


Figure 5.11: Probability distribution of pore sizes occupied by gas and brine, along with the corresponding volume fractions, after water injection. The comparison between the initial stage (a-c) and after four days of storage (g-i) highlights fluid redistribution. The volume fraction of gas and brine in the pores is shown in (d-f) for the initial stage and (j-l) for the four-day storage period, illustrating the increasing brine occupancy over time.

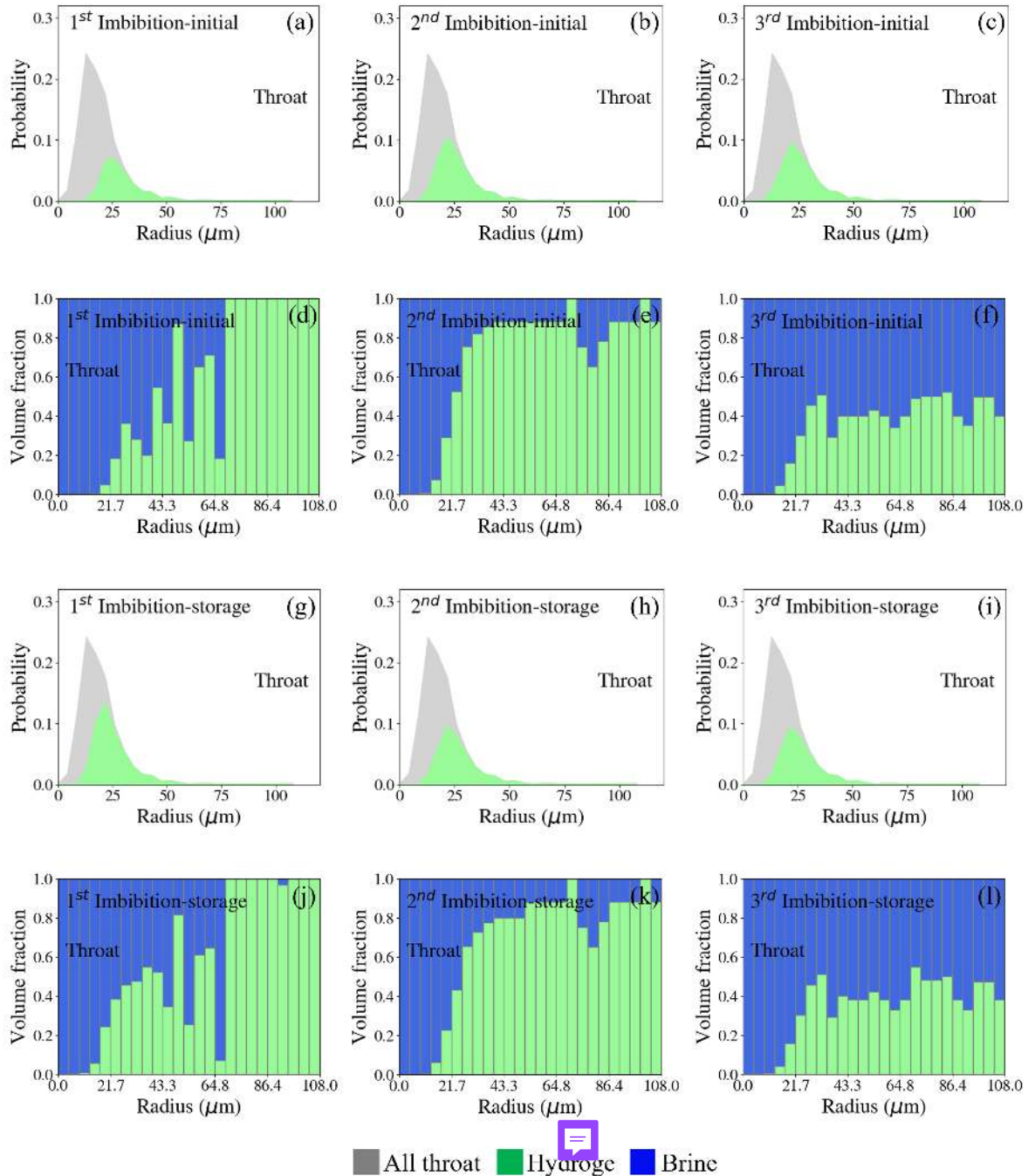


Figure 5.12: Probability distribution of throat sizes occupied by gas and brine, alongside their respective volume fractions, following water injection. The initial stage (a-c) and after four days of storage (g-i) show how brine gradually invades larger throats. The volume fraction of gas and brine in the throats is depicted in (d-f) for the initial stage and (j-l) for the four-day storage period, highlighting the role of capillary forces in fluid redistribution.

During imbibition, water infiltrates the pore network, leading to the entrapment of gas within larger and intermediate-sized pores due to capillary action. The spatial distribution of gas and brine at this stage aligns with the characteristics of a water-wet system, where brine preferentially

saturates smaller pores and throats while gas remains confined within larger structural elements. The probability distribution of gas- and brine-filled pores and throats, along with changes in volume fractions over time, suggests ongoing phase redistribution. This reorganisation of the trapped gas phase is likely driven by processes such as Ostwald ripening, which facilitates the merging of smaller gas ganglia into larger, more stable clusters.

5.3.3 Minkowski Functionals

To quantitatively analyse the morphology and topology of the gas and brine phases within the porous medium, Minkowski functionals were employed. As mentioned in Chapter 2, these functionals provide a rigorous mathematical framework for describing the geometrical properties of structures in three-dimensional space, making them highly valuable in the study of multiphase flow in porous media [121, 122]. Four key functionals are considered in this study: saturation, surface area, mean curvature and connectivity. In the following subsections, the results of these Minkowski functionals are presented, highlighting the evolution of gas and brine distribution throughout the experiment, including after gas injection, water flooding, and storage.

5.3.3.1 Gas Saturation Profile

The quantitative evolution of gas saturation across the sample length is presented in Fig. 5.13. Initially, after gas injection, a high gas saturation of approximately $89 \pm 2\%$ is achieved. However, successive water flooding cycles lead to a gradual reduction in gas saturation, with values dropping to $42 \pm 2\%$ after first water flooding, $29 \pm 2\%$ after the second imbibition, and $22 \pm 2\%$ after the last water injection.

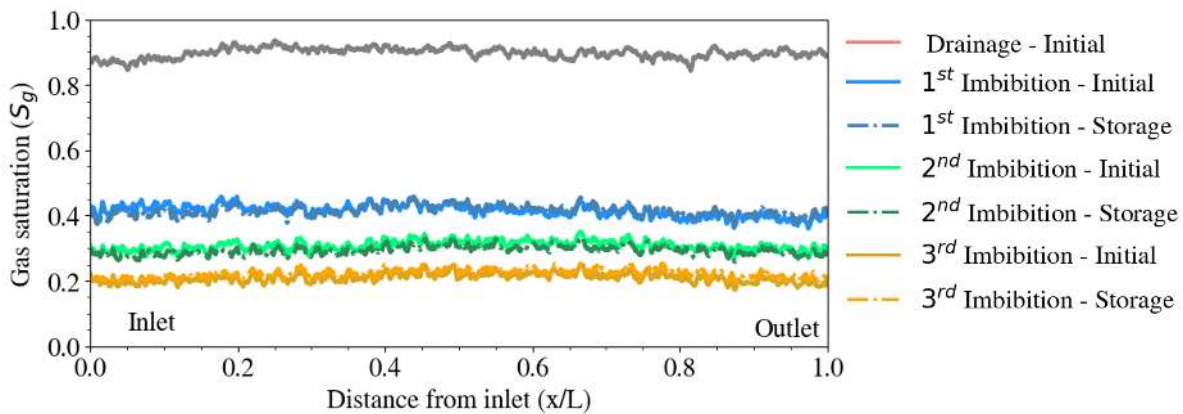


Figure 5.13: The gas saturation profile averaged along the flow direction during cycles of hydrogen injection and water flooding across the length of a Bentheimer sample, illustrating both the initial injection and the state after a 4-day waiting period (storage). The results highlight the role of porous plates in enhancing gas retention and achieving a more uniform saturation profile, while also minimising capillary end effects. Minor fluctuations observed after storage are attributed to gas redistribution driven by Ostwald ripening.

A comparison with the previous experiment in Chapter 4, Section 4.3.4, where only a hydrophilic

porous plate was used, highlights the impact of incorporating both hydrophilic and hydrophobic porous plates. In the previous experiment, the residual gas saturation after the first imbibition was 40%, which is slightly lower than the 42% observed in the current study. However, a more pronounced difference emerges in the later flooding stages. After the second ~~water flooding~~, the residual gas saturation was 34%, whereas it dropped now to 29%, indicating improved gas displacement efficiency. This demonstrates the increasing efficiency of gas displacement with continued water injection.

The most significant difference is observed after ~~WF3~~, where the residual gas saturation was 18%, compared to 22% in the current study. This suggests that the presence of a hydrophobic porous plate may contribute to slightly higher gas retention after multiple flooding cycles, possibly by reducing the extent of gas phase reconnection and mobilisation during water invasion. (The same error margin applies to this comparison, as the same segmentation method was used for both experiments).

Furthermore, the results confirm that saturation profiles exhibit minimal capillary end effects, leading to a more homogeneous distribution of gas across the sample length. The use of hydrophilic and hydrophobic porous plates significantly influences gas retention by controlling capillary forces, thereby ensuring uniform displacement. Observations from long-term storage indicate that gas saturation remains relatively stable, with minor fluctuations attributed to gas redistribution through Ostwald ripening [161].

5.3.3.2 Interfacial Area

In addition to contact angle measurements, we also assessed wettability by analysing interfacial area measurements on a subvolume of $500 \times 500 \times 500$ voxels was extracted from the central region of the sample. Table 5.4 presents the evolution of gas-solid (a_{gs}), gas-water (a_{gw}), and water-solid (a_{ws}) interfacial areas at different drainage and imbibition stages. A key parameter for evaluating wettability is the ratio f_w/S_w , where f_w represents the wetting phase fraction. According to Garfi et al. [204], a ratio greater than 1 indicates a water-wet system, as it suggests that the wetting phase occupies more solid surface area relative to its saturation. Throughout the imbibition and storage cycles, f_w/S_w remains above 1, confirming a predominantly water-wet condition in the analysed subvolume.

Examining the interfacial trends, we observe that as water saturation (S_w) increases from 0.15 in the gas-invaded stage (G1) to 0.81 after the final storage period (~~WF3-storage~~), the water-solid interfacial area (a_{ws}) also increases, reaching 14.2 1/mm. Simultaneously, the gas-solid interface (a_{gs}) decreases significantly, from 9.06 1/mm in the drainage stage to 0.85 1/mm in the final storage stage, indicating a progressive transition towards a more water-dominated system. The observed decrease in a_{gw} (gas-water interfacial area) during storage phases ~~suggests that gas becomes increasingly disconnected, further supporting the system's transition to stronger water wetting~~. Additionally, the wetting phase fraction f_w increases steadily from 0.31 in the initial drainage stage to 0.94 in the final storage stage, further reinforcing the water-wet nature of the system.



Table 5.4: Interfacial area per unit volume and gas saturation at different stages of drainage (G) and imbibition (WF). Gas saturation (S_g) and interfacial areas between gas-solid (a_{gr}), gas-water (a_{gw}) and water-solid (a_{ws}) are measured in $1/\text{mm}$. Results are presented for both the initial stage and after a 4-days storage period.

Steps	S_w	a_{gs} [1/mm]	a_{gw} [1/mm]	a_{ws} [1/mm]	f_w	f_w/S_w
G1	0.15	9.06	0.26	4.09	0.31	2.07
WF1	0.57	4.17	0.24	9.32	0.69	1.21
WF1-storage	0.59	2.27	0.08	5.25	0.69	1.18
WF2	0.69	3.55	0.24	9.09	0.72	1.04
WF2-storage	0.67	1.89	0.15	10.5	0.85	1.26
WF3	0.78	1.67	0.19	10.6	0.86	1.11
WF3-storage	0.81	0.85	0.09	14.2	0.94	1.17

Note. The ratio f_w/S_w is a measure of wettability, where $f_w = a_{ws}/(a_{gs} + a_{ws})$. If this ratio is greater than 1 it represents water-wet conditions.

5.3.3.3 Curvature Distributions

The interfacial curvature of the extracted gas-water interface was measured on the same subvolume and plotted in Fig 5.14. Following gas injection, the curvature distribution is approximately centred around zero, with a slight positive skew. The dominant feature appears to be saddle-like or mixed curvature, which suggests the presence of gas filled pore spaces forming interconnected structures. Convex and concave curvatures are also present but occur less frequently. This distribution is indicative of the capillary driven displacement of brine by hydrogen gas, forming fluid-fluid interfaces within the pore network.

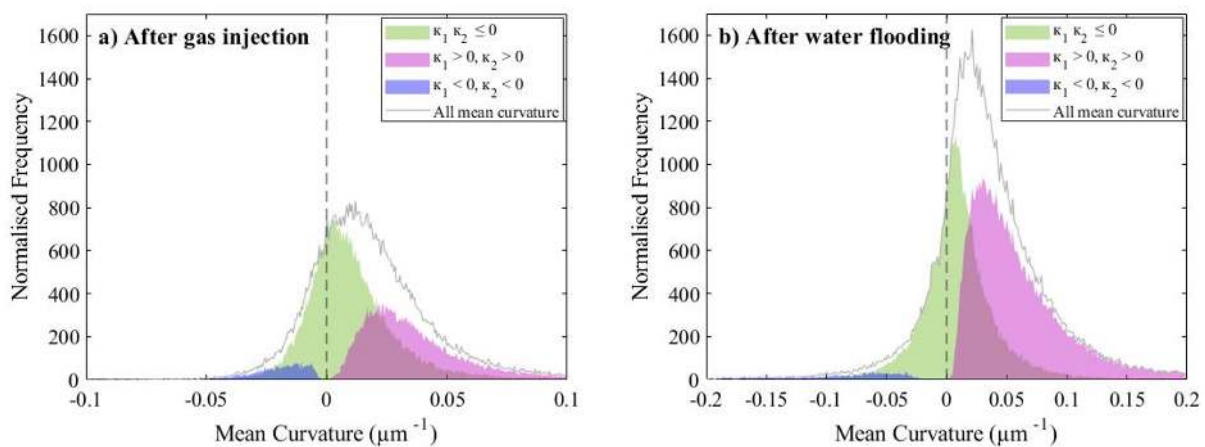


Figure 5.14: Illustration of the normalised frequency distribution of mean curvature following (a) gas injection and (b) water flooding in a Bentheimer sandstone. The mean curvature is classified into three categories: mixed curvature ($k_1 k_2 \leq 0$) represented in green, convex structures ($k_1 > 0, k_2 > 0$) shown in pink and concave structures ($k_1 < 0, k_2 < 0$), depicted in blue. The overall mean curvature distribution is represented by the grey line.

After ~~water flooding~~, the curvature distribution exhibits a shift towards more positive values. This shift suggests that brine displacement results in the formation of convex menisci, likely due to capillary forces acting on the receding gas phase. The increase in convex structures implies that hydrogen is being displaced from the pore spaces, leaving behind residual gas ~~in smaller, isolated regions~~. Meanwhile, the reduction in ~~concave structures suggests a decrease in trapped gas clusters with negative curvature~~. The presence of saddle-like structures remains significant, albeit with a slightly altered distribution compared to the drainage phase.

Additionally, curvature analysis was conducted after four days of storage (see Fig. 5.15), revealing that while the overall shape of the curvature distribution remains similar, there is a noticeable shift in the frequency of certain curvature values. The slight narrowing of the distribution after storage suggests a reduction in extreme curvature values, likely due to fluid redistribution over time. This process leads to the relaxation of highly curved menisci and the smoothing of fluid-fluid interfaces. Initially, the gas ganglia exhibit a broad and widely distributed curvature spectrum due to variations in capillary pressure. However, over time, some ganglia merge, increasing connectivity and imposing a more uniform pressure across the trapped gas structures. As a result, the curvature distribution becomes sharper and more defined. It is important to acknowledge that uncertainties in these measurements exist, as highlighted by Akai et al. [205].

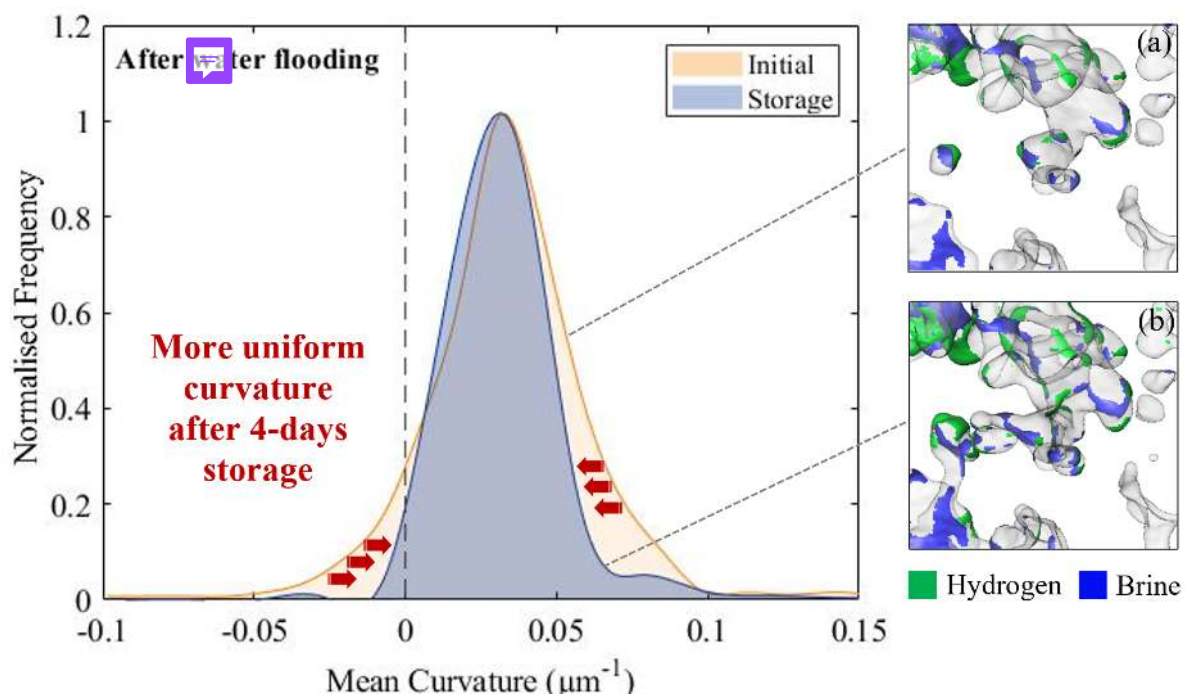


Figure 5.15: Mean curvature distribution of hydrogen-brine interfaces before (orange) and after four days of storage (blue) following water flooding. The histogram shows a slight narrowing of the curvature distribution over time, suggesting fluid redistribution and interface relaxation due to Ostwald ripening. This process results in smoother and more connected gas ganglia. The insets (a) and (b) provide 3D visualisations of the extracted interface between hydrogen (green) and brine (blue) within the pore space at the initial and post-storage stage, respectively.

5.3.3.4 Capillary Pressure Analysis

The relationship between capillary pressure and saturation is analysed through direct experimental measurements. This subsection discusses how capillary forces influence gas retention and displacement within the porous medium. The experimental data are compared with theoretical predictions and previous studies to assess the validity of current models under relevant storage conditions.

The implementation of two porous plates in this study enabled direct measurement of capillary pressure during drainage and subsequent imbibition cycles, significantly improving the accuracy of the experimental analysis. The capillary pressure evolution during the drainage phase demonstrated an initial stabilisation around 14.2 ± 0.03 kPa, corresponding to a gas saturation of 0.85 ± 0.02 as illustrated in Fig 5.16. As imbibition progressed, a reduction in capillary pressure was observed, with values decreasing to 3.82 ± 0.03 kPa, 2.16 ± 0.03 kPa, and 1.77 ± 0.03 kPa for the first, second, and third imbibition cycles, respectively. This decline in capillary pressure is accompanied by a reduction in residual gas saturation, highlighting the progressive reorganisation and reconnection of the gas phase, which facilitated enhanced displacement during subsequent cycles.

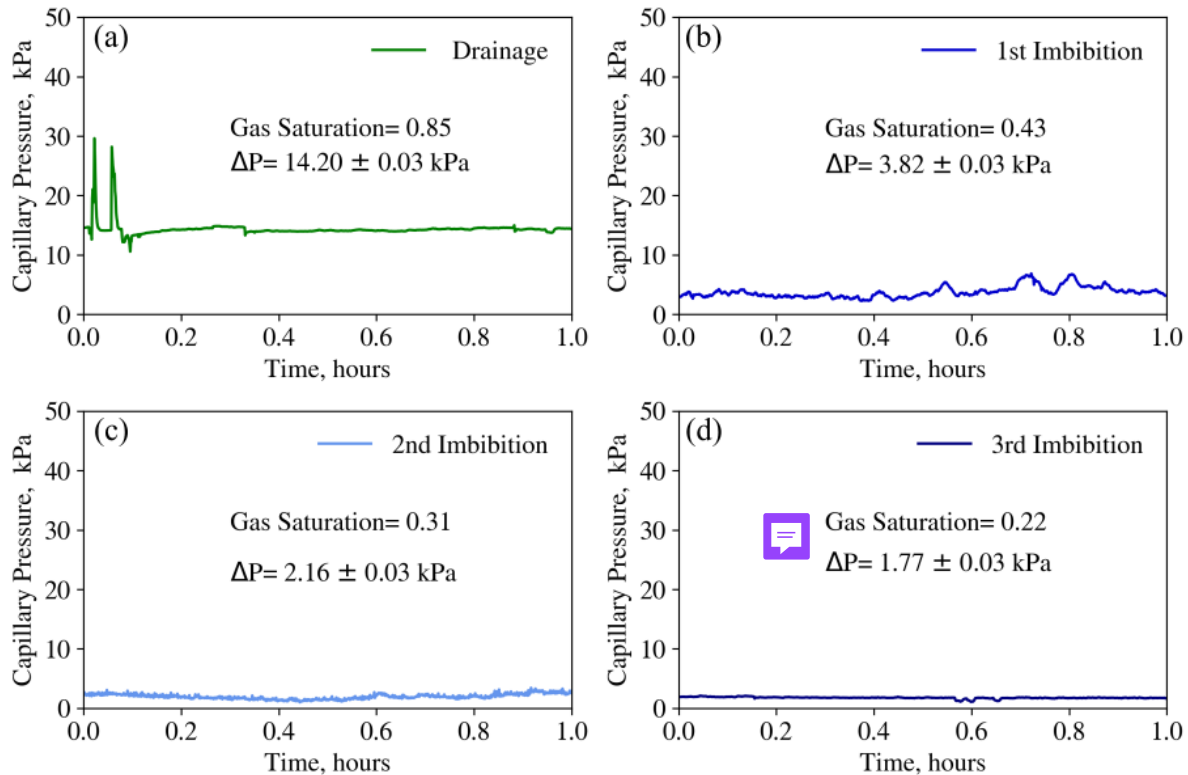


Figure 5.16: Measured capillary pressure evolution during drainage and successive imbibition cycles, with a precision of ± 0.03 kPa. The drainage phase shows an initial stabilisation at 14.2 kPa with a gas saturation of 0.85 (a). During subsequent imbibition cycles (b-d), capillary pressure and gas saturation progressively decrease, indicating improved fluid connectivity and reduced gas trapping. A 2% error applies to the gas saturation due to the segmentation method.

The capillary pressure values derived from direct experimental measurements align closely with those obtained from curvature-based estimations, see Figure 5.17. The comparison further confirms that the curvature-based approach remains a reliable method for capillary pressure quantification, as the experimental and estimated data exhibit consistent trends. The results indicate a significant reduction in hysteresis between drainage and imbibition cycles, particularly in later stages, which suggests that gas redistribution mechanisms, such as Ostwald ripening, may contribute to achieving a near-equilibrium capillary state. Furthermore, the experimental capillary pressure endpoints correspond well with independent literature data, including mercury injection capillary pressure (MICP) [22] measurements and previous studies by Raeesi et al. [14], reinforcing the validity of the methodology employed in this study.

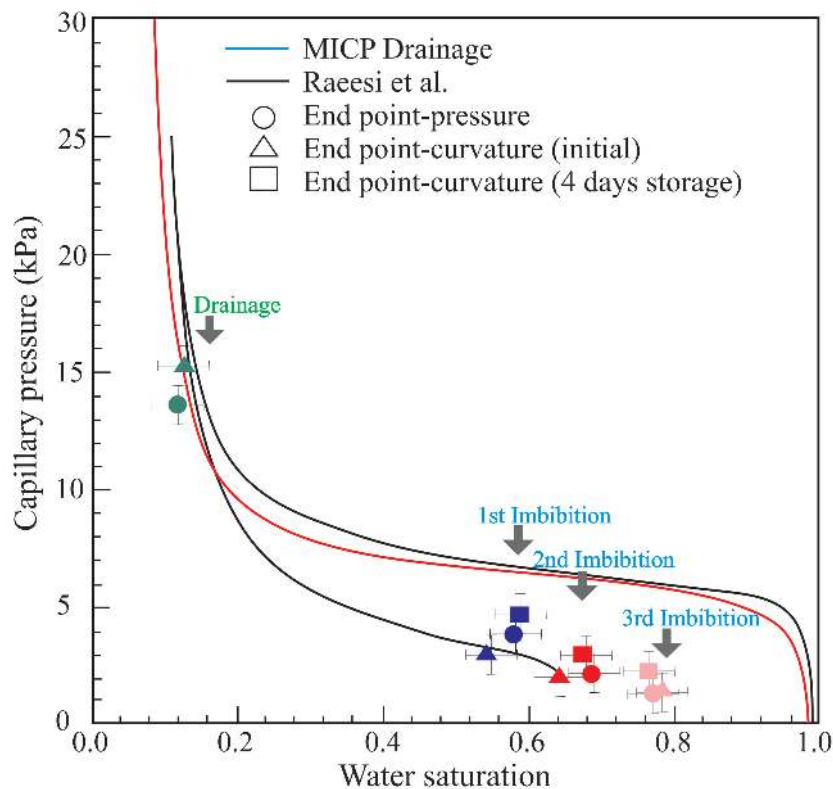


Figure 5.17: Estimated capillary pressure for drainage and imbibition measured on a 600^3 voxel subvolume in the middle of the sample. The black lines represent independent experimental measurements from the literature [14, 22] where Ostwald ripening is not considered. The data points correspond to our direct pressure measurements and curvature-derived values, with error bars indicating uncertainty in the determination of capillary pressure and saturation from segmented images. The results demonstrate a reduction in hysteresis in later imbibition cycles, attributed to enhanced gas redistribution and pore-scale connectivity.

The observed reduction in residual gas saturation across successive imbibition cycles supports the hypothesis that improved pore-scale fluid connectivity facilitates more efficient gas displacement. The ability to directly measure capillary pressure with the porous plate ~~setup~~ provides deeper insight into the pore-scale processes governing multiphase flow in porous media. These findings emphasise the advantages of the refined experimental approach in capturing the dy-

namic evolution of capillary pressure and saturation, demonstrating a marked improvement over previous methodologies.

5.4 Health and Safety

The health and safety measures for this chapter are identical to those in Chapter 4, Section 4.4, as the experimental setup and procedures remained the same. Standard precautions for hydrogen handling, brine storage, and X-ray safety were followed. Additionally, all safety protocols for operating the Reactor under high-pressure conditions were strictly maintained, including pressure monitoring, leak testing and controlled gas injection.

5.5 Final Remarks

This study examined contact angle, curvature, and capillary pressure in a 37 mm-long Bentheimer sandstone sample using a porous plate experiment with hydrogen injection and three waterflooding cycles at high pressure. High-resolution imaging was used to capture fluid distribution, and a four-day storage period enabled observation of hydrogen redistribution. Direct pressure measurements from the experiment showed that, as imbibition progressed, capillary pressure decreased to 3.82 ± 0.03 kPa, 2.16 ± 0.03 kPa, and 1.77 ± 0.03 kPa for the first, second, and third imbibition cycles, respectively. The contact angle was measured at approximately 50° , and meniscus curvature provided an independent estimate of capillary pressure, which was compared to experimental values obtained using hydrophilic and hydrophobic porous plates. Results demonstrated gas redistribution through Ostwald ripening, leading to a more uniform local capillary pressure and enhanced gas connectivity. This often resulted in the formation of a single large ganglion, as evidenced by a decrease in the Euler characteristic, indicating improved connectivity. Capillary pressure measurements deviated from traditional hysteresis models, as repeated imbibition cycles reduced the residual gas saturation.

In addition, this work could be compared to the results of pore-scale modelling which has proposed an equilibrium model of displacement accounting for Ostwald ripening and a methodology to convert measurements of capillary pressure and relative permeability made without this effect to account for ganglion rearrangement, quantifying the decrease in residual saturation and hysteresis [206].

Chapter 6

Conclusions and Future Work

6.1 Conclusions

This thesis explored the role of hysteresis in multiphase flow, with a focus on hydrogen storage in porous media. Understanding hysteresis is crucial for optimising storage efficiency, minimising gas trapping, and improving recovery. Unlike hydrocarbon-based systems, hydrogen—due to its smaller molecular size and different surface tension characteristics—is highly susceptible to capillary forces and Ostwald ripening, leading to significant phase redistribution over time. Traditional models frequently fail to account for these dynamics, resulting in inaccurate predictions of hydrogen retention and connectivity.

By utilising high-resolution X-ray imaging and Minkowski functionals, this research provided a novel perspective on fluid topology and connectivity. Experimental studies using Bentheimer sandstone allowed for direct measurement of contact angle, curvature, and capillary pressure, which were compared against conventional hysteresis models. These findings provide a deeper understanding of gas trapping mechanisms and highlight the role of Ostwald ripening in enhancing gas-phase connectivity.

Chapter 1: In this experimental study, we investigated hydrogen and brine trapping and redistribution in a sandstone sample, showing that hydrogen behaves as a non-wetting phase, preferentially occupying larger pore spaces. Water injection led to hydrogen trapping in large ganglia, which underwent gradual redistribution even in the absence of flow. This phenomenon was attributed to Ostwald ripening, where dissolved gas in the aqueous phase diffused to equilibrate capillary pressure, leading to the coalescence of hydrogen into larger connected structures. The storage time for this experiment was 16 hours, allowing for significant redistribution and improved connectivity. Our findings under unsteady-state two-phase flow in a large sample of Bentheimer sandstone can be summarised as follows:

- Hydrogen tends to occupy large pores and is trapped during water injection.
- Over time, even without external flow, gas redistributes at the pore scale, likely due to Ostwald ripening.

- This redistribution enhances gas connectivity, reducing isolated clusters and forming a dominant ganglion.
- The observed changes in connectivity, quantified using the Euler characteristic, suggest that hydrogen storage may exhibit less hysteresis than conventional hydrocarbon-based models predict.
- These results imply that traditional trapping models may overestimate hydrogen retention, as Ostwald ripening can facilitate more efficient gas recovery.

Chapter 2: In the second experimental study, we investigated capillary pressure and saturation changes during repeated hydrogen injection and water flooding cycles. We improved the experimental procedure and conducted a porous plate experiment, allowing us to directly measure capillary pressure and compare these measurements with values inferred from meniscus curvature in high-resolution images. The storage time for this experiment was also 16 hours, which allowed sufficient time for redistribution to occur and for hysteresis effects to be observed and quantified. The main conclusions from this study are as follows:

- Hydrogen redistribution does not alter the total gas volume but improves connectivity over time.
- Capillary pressure measurements revealed deviations from conventional hysteresis models, indicating that residual saturation decreased with successive imbibition cycles.
- Pore-scale gas rearrangement facilitated improved gas connectivity, leading to more efficient withdrawal of stored hydrogen.
- The experimental results support the hypothesis that ongoing redistribution processes may lead to lower hysteresis in hydrogen storage systems.
- These findings suggest that existing models for gas trapping in porous media, which typically ignore post-injection redistribution, may need to be revised for hydrogen storage applications.

Chapter 3: In the last experimental study, we improved the experimental protocol by using two porous plates—hydrophilic and hydrophobic—to control the flow and achieve uniform saturation. We investigated contact angle, curvature, and Minkowski functionals in pore-scale analysis. The final experimental study focused on wettability characterisation, capillary pressure estimation based on curvature, and the role of Minkowski functionals in describing fluid topology. Contact angle measurements confirmed that Bentheimer sandstone is water-wet, which influenced the spatial distribution of hydrogen and brine. The storage time for this experiment was extended to 4 days, allowing us to investigate the long-term effects of storage on hysteresis and fluid connectivity. Significant findings include:

- Contact angle measurements ($\approx 50^\circ$) supported the classification of the rock as water-wet.

- Curvature measurements provided an independent estimate of capillary pressure, which was consistent with experimental values.
- Analysis of Minkowski functionals (saturation, interfacial area, mean curvature, and Gaussian curvature) offered a comprehensive description of fluid connectivity and topological changes over time.
- Repeated imbibition cycles reduced residual saturation, reinforcing the hypothesis that hysteresis in hydrogen storage differs from conventional expectations.
- This study demonstrated that combining high-resolution imaging with Minkowski functionals enhances our understanding of fluid connectivity and provides a new approach for characterising hysteresis in multiphase flow.

6.2 Future Work

Although this research has provided valuable insights into hydrogen storage dynamics, several key areas require further exploration to fully understand and optimise the process:

1. Pore-Scale Modeling and Validation

- Future studies should compare experimental results with advanced pore-scale models that incorporate Ostwald ripening.
- Equilibrium displacement models could be refined to account for ganglion rearrangement effects, enhancing their predictive accuracy.
- Additional research should quantify how redistribution influences capillary pressure-saturation relationships across different rock types.

2. Further Experimental Studies

- Additional experiments under varying pressure and temperature conditions could assess how reservoir conditions affect hysteresis and gas recovery efficiency.
- Investigating a wider variety of rock types, such as carbonates and shales, would help generalise these findings to a broader range of storage formations.

3. Integration with Large-Scale Storage Models

- Connecting detailed pore-scale observations with field-scale hydrogen storage models could significantly enhance predictions of performance and efficiency in commercial-scale storage operations.
- Incorporating Minkowski functionals into numerical simulations may improve our ability to model multiphase flow in porous media, offering a more accurate representation of fluid connectivity and topology.

4. Advancing Imaging Techniques

- (a) Employing higher-resolution imaging techniques, such as synchrotron-based tomography, could offer more detailed insights into interfacial curvature and phase connectivity at the pore scale.
- (b) Real-time imaging during dynamic injection and withdrawal cycles could provide further validation for the redistribution mechanisms observed in this study.

This research has demonstrated that hydrogen storage exhibits unique multiphase flow behaviour distinct from hydrocarbon systems. The role of Ostwald ripening in redistributing trapped gas challenges conventional hysteresis models and suggests a higher potential for recovery. High-resolution imaging and Minkowski functionals have provided valuable tools for understanding fluid topology and connectivity at the pore scale. Future work integrating these findings with advanced pore-scale modelling and large-scale simulations will be critical for optimising underground hydrogen storage strategies, improving efficiency, and reducing uncertainties in commercial-scale applications.

Bibliography

- [1] A. Jahanbakhsh, A. L. Potapov-Crighton, A. Mosallanezhad, N. T. Kaloorazi, and M. M. Maroto-Valer, “Underground hydrogen storage: A uk perspective,” *Renewable and sustainable energy reviews*, vol. 189, p. 114001, 2024.
- [2] G. Wilson, “Great britain’s energy daily data.” Tableau Public, 2024. [Online]. Available: <https://public.tableau.com/app/profile/grant.wilson/viz/GreatBritainsenergydailydata/GBenergyperday?publish=yes>.
- [3] P. Saha, F. A. Akash, S. M. Shovon, M. U. Monir, M. T. Ahmed, M. F. H. Khan, S. M. Sarkar, M. K. Islam, M. M. Hasan, D.-V. N. Vo, *et al.*, “Grey, blue, and green hydrogen: A comprehensive review of production methods and prospects for zero-emission energy,” *International Journal of Green Energy*, vol. 21, no. 6, pp. 1383–1397, 2024.
- [4] T. R. Society, “large scale electricity storage report.” The Royal Society, 2021. [Online]. Available: <https://royalsociety.org/-/media/policy/projects/large-scale-electricity-storage/large-scale-electricity-storage-report.pdf>, note=Accessed: 2024-08-15.
- [5] N. Ma, W. Zhao, W. Wang, X. Li, and H. Zhou, “Large scale of green hydrogen storage: Opportunities and challenges,” *International Journal of Hydrogen Energy*, vol. 50, pp. 379–396, 2024.
- [6] S. Mao, B. Chen, M. Malki, F. Chen, M. Morales, Z. Ma, and M. Mehana, “Efficient prediction of hydrogen storage performance in depleted gas reservoirs using machine learning,” *Applied Energy*, vol. 361, p. 122914, 2024.
- [7] I. Gomez Mendez, W. M. El-Sayed, A. H. Menefee, and Z. T. Karpyn, “Insights into underground hydrogen storage challenges: A review on hydrodynamic and biogeochemical experiments in porous media,” *Energy & Fuels*, 2024.
- [8] S. Skjæveland, L. Siqveland, A. Kjosavik, W. Thomas, and G. Virnovsky, “Capillary pressure correlation for mixed-wet reservoirs,” *SPE Reservoir Evaluation & Engineering*, vol. 3, no. 01, pp. 60–67, 2000.
- [9] A. M. Alhammadi, A. AlRatout, B. Bijeljic, and M. J. Blunt, “Pore-scale imaging and characterization of hydrocarbon reservoir rock wettability at subsurface conditions using

x-ray microtomography,” *JoVE (Journal of Visualized Experiments)*, no. 140, p. e57915, 2018.

[10] B. Schweizer, “Hysteresis in porous media: modelling and analysis,” *Interfaces and Free Boundaries*, vol. 19, no. 3, pp. 417–447, 2017.

[11] S. C. Lee, H. K. Kim, I. K. Chun, M. H. Cho, S. Y. Lee, and M. H. Cho, “A flat-panel detector based micro-ct system: performance evaluation for small-animal imaging,” *Physics in Medicine & Biology*, vol. 48, no. 24, p. 4173, 2003.

[12] M. Precision, “Micro-ct scanners software.” Matsusada Precision, 2024. [Online]. Available: <https://www.matsusada.com/product/xray/micro-ct-scanners/micro-ct-software/>.

[13] kocurekindustries, “Berea cores sandstone.” kocurekindustries, note = [Online]. Available: <https://kocurekindustries.com/our-products/berea-sandstone>, 2023.

[14] B. Raeesi, N. R. Morrow, and G. Mason, “Capillary pressure hysteresis behavior of three sandstones measured with a multistep outflow–inflow apparatus,” *Vadose Zone Journal*, vol. 13, no. 3, 2014.

[15] S. Higgs, Y. Da Wang, C. Sun, J. Ennis-King, S. J. Jackson, R. T. Armstrong, and P. Mostaghimi, “Direct measurement of hydrogen relative permeability hysteresis for underground hydrogen storage,” *International Journal of Hydrogen Energy*, vol. 50, pp. 524–541, 2024.

[16] A. Yekta, J.-C. Manceau, S. Gaboreau, M. Pichavant, and P. Audigane, “Determination of hydrogen–water relative permeability and capillary pressure in sandstone: application to underground hydrogen injection in sedimentary formations,” *Transport in Porous Media*, vol. 122, no. 2, pp. 333–356, 2018.

[17] M. Boon and H. Hajibeygi, “Experimental characterization of H₂/water multiphase flow in heterogeneous sandstone rock at the core scale relevant for underground hydrogen storage (UHS),” *Scientific Reports*, vol. 12, no. 1, p. 14604, 2022.

[18] S. Goodarzi, Y. Zhang, S. Foroughi, B. Bijeljic, and M. J. Blunt, “Trapping, hysteresis and Ostwald ripening in hydrogen storage: A pore-scale imaging study,” *International Journal of Hydrogen Energy*, vol. 56, pp. 1139–1151, 2024.

[19] E. M. Thaysen, I. B. Butler, A. Hassanpouryouzband, D. Freitas, F. Alvarez-Borges, S. Krevor, N. Heinemann, R. Atwood, and K. Edlmann, “Pore-scale imaging of hydrogen displacement and trapping in porous media,” *International Journal of Hydrogen Energy*, vol. 48, no. 8, pp. 3091–3106, 2023.

[20] N. K. Jha, A. Al-Yaseri, M. Ghasemi, D. Al-Bayati, M. Lebedev, and M. Sarmadivaleh, “Pore scale investigation of hydrogen injection in sandstone via x-ray micro-tomography,” *International Journal of Hydrogen Energy*, vol. 46, no. 70, pp. 34822–34829, 2021.

[21] M. Boon, T. Rademaker, C. W. Winardhi, and H. Hajibeygi, “Multiscale experimental study of H₂ brine multiphase flow in porous rock characterizing relative permeability hysteresis, hydrogen dissolution, and Ostwald ripening,” *Scientific Reports*, vol. 14, no. 1, pp. 1–15, 2024.

[22] Q. Lin, B. Bijeljic, R. Pini, M. J. Blunt, and S. Krevor, “Imaging and measurement of pore-scale interfacial curvature to determine capillary pressure simultaneously with relative permeability,” *Water Resources Research*, vol. 54, no. 9, pp. 7046–7060, 2018.

[23] J. S. . Son, “Diamond light source source extention building.” SISK, 2024. [Online]. Available: <https://www.johnsiskandson.com/news/sisk-set-to-deliver-25m-diamond-light-source-extension-building>.

[24] keller, “Pressure transducer-series pd-33x.” Keller, note = [Online]. Available: <https://keller-druck.com/en/products/pressure-transmitters/differential-pressure-transmitters/series-pd-33x>, 2024.

[25] P. I. Company, “Series 4520 bench top reactors, 1 2 l.” Parr Instrument Company, 2024. [Online]. Available: <https://www.parrinst.com/products/stirred-reactors/series-4520-1-2l-bench-top-reactors/>.

[26] D. Zivar, S. Kumar, and J. Foroozesh, “Underground hydrogen storage: A comprehensive review,” *International Journal of Hydrogen Energy*, vol. 46, no. 45, pp. 23436–23462, 2021.

[27] Y. Zhang, B. Bijeljic, Y. Gao, S. Goodarzi, S. Foroughi, and M. J. Blunt, “Pore-scale observations of hydrogen trapping and migration in porous rock: Demonstrating the effect of Ostwald ripening,” *Geophysical Research Letters*, vol. 50, no. 7, p. e2022GL102383, 2023.

[28] A. Alhosani, A. M. Selem, Q. Lin, B. Bijeljic, and M. J. Blunt, “Disconnected gas transport in steady-state three-phase flow,” *Water Resources Research*, p. e2021WR031147, 2021.

[29] H₂Tools, “Hydrogen properties,” 2015. <https://h2tools.org/hyarc/hydrogen-properties>, 1 3, 2023.

[30] Y. Gao, Q. Lin, B. Bijeljic, and M. J. Blunt, “X-ray microtomography of intermittency in multiphase flow at steady state using a differential imaging method,” *Water resources research*, vol. 53, no. 12, pp. 10274–10292, 2017.

[31] Y. Chow, G. C. Maitland, and J. Trusler, “Erratum to “Interfacial tensions of (H₂O + H₂) and (H₂O + CO₂ + H₂) systems at temperatures of (298 to 448) K and pressures up to 45 MPa” [Fluid Phase Equil. 475 (2018) 37–44],” *Fluid Phase Equilibria*, vol. 503, p. 112315, 2020.

[32] N. Energy, “Hynet north west project.” NS Energy, 2024. [Online]. Available: <https://www.nsenergybusiness.com/projects/hynet-north-west-project/?cf-view>.

[33] UK Government, “UK Hydrogen Strategy.” <https://www.gov.uk/government/publications/uk-hydrogen-strategy/uk-hydrogen-strategy-accessible-html-version>, Aug. 2021. Department for Business, Energy & Industrial Strategy, London, UK. [Accessed: Aug. 14, 2024].

[34] National Grid Electricity System Operator, “Future energy scenarios.” <https://www.nationalgrideso.com/document/283101/download>, 2023. Accessed: Aug. 16, 2024.

[35] R. Tarkowski and B. Uliasz-Misiak, “Towards underground hydrogen storage: A review of barriers,” *Renewable and Sustainable Energy Reviews*, vol. 162, p. 112451, 2022.

[36] N. S. Muhammed, B. Haq, D. Al Shehri, A. Al-Ahmed, M. M. Rahman, and E. Zaman, “A review on underground hydrogen storage: Insight into geological sites, influencing factors and future outlook,” *Energy Reports*, vol. 8, pp. 461–499, 2022.

[37] G. Lagioia, M. P. Spinelli, and V. Amicarelli, “Blue and green hydrogen energy to meet european union decarbonisation objectives. an overview of perspectives and the current state of affairs,” *International Journal of Hydrogen Energy*, vol. 48, no. 4, pp. 1304–1322, 2023.

[38] H. UK, “Hydrogen storage: Delivering on the uk’s energy needs,” December 2022. [Accessed: Aug. 18, 2024].

[39] E. Commission, “Towards net-zero emissions in the eu energy system: Insights from scenarios in line with 2030 and 2050 ambitions of the european green deal,” tech. rep., European Union, 2021. [Accessed: Aug. 18, 2024].

[40] U.S. Department of Energy, “U.s. national clean hydrogen strategy and roadmap,” tech. rep., Office of Energy Efficiency and Renewable Energy (EERE), 2023. [Accessed: Aug. 18, 2024].

[41] I. Inovyn, “Keuper gas storage project.” Ineos Inovyn, 2024. [Online]. Available: <https://www.kgsp.co.uk/>.

[42] Recharge, “First industrial-scale hydrogen storage.” [Online]. Available: <https://www.rechargenews.com/energy-transition/first-industrial-scale-hydrogen-storage-uniper-to-build-pilot-salt-cavern...>, 2024. [Accessed: Aug. 20, 2024].

[43] Uniper, “Hydrogen pilot cavern krummhörn.” Uniper.energy, 2024. [Online]. Available: <https://www.uniper.energy/hydrogen-pilot-cavern>.

[44] A. Züttel, “Hydrogen storage methods,” *Naturwissenschaften*, vol. 91, no. 4, pp. 157–172, 2004.

[45] M. McPherson, N. Johnson, and M. Strubegger, “The role of electricity storage and hydrogen technologies in enabling global low-carbon energy transitions,” *Applied Energy*, vol. 216, pp. 649–661, 2018.

[46] J. Taylor, J. Alderson, K. Kalyanam, A. Lyle, and L. Phillips, “Technical and economic assessment of methods for the storage of large quantities of hydrogen,” *International Journal of Hydrogen Energy*, vol. 11, no. 1, pp. 5–22, 1986.

[47] R. Tarkowski, “Underground hydrogen storage: Characteristics and prospects,” *Renewable and Sustainable Energy Reviews*, vol. 105, pp. 86–94, 2019.

[48] N. Heinemann, J. Alcalde, J. M. Miocic, S. J. Hangx, J. Kallmeyer, C. Ostertag-Henning, A. Hassancouryouzband, E. M. Thaysen, G. J. Strobel, C. Schmidt-Hattenberger, *et al.*, “Enabling large-scale hydrogen storage in porous media—the scientific challenges,” *Energy & Environmental Science*, vol. 14, no. 2, pp. 853–864, 2021.

[49] K. Cyran, “The influence of impurities and fabrics on mechanical properties of rock salt for underground storage in salt caverns—a review,” *Archives of Mining Sciences*, vol. 66, no. 2, 2021.

[50] N. Dopffel, S. Jansen, and J. Gerritse, “Microbial side effects of underground hydrogen storage—knowledge gaps, risks and opportunities for successful implementation,” *International Journal of Hydrogen Energy*, vol. 46, no. 12, pp. 8594–8606, 2021.

[51] M. AbuAisha and J. Billiotte, “A discussion on hydrogen migration in rock salt for tight underground storage with an insight into a laboratory setup,” *Journal of Energy Storage*, vol. 38, p. 102589, 2021.

[52] B. Pan, X. Yin, Y. Ju, and S. Iglauer, “Underground hydrogen storage: Influencing parameters and future outlook,” *Advances in Colloid and Interface Science*, vol. 294, p. 102473, 2021.

[53] E. M. Thaysen, S. McMahon, G. J. Strobel, I. B. Butler, B. T. Ngwenya, N. Heinemann, M. Wilkinson, A. Hassancouryouzband, C. I. McDermott, and K. Edlmann, “Estimating microbial growth and hydrogen consumption in hydrogen storage in porous media,” *Renewable and Sustainable Energy Reviews*, vol. 151, p. 111481, 2021.

[54] A. I. Osman, N. Mehta, A. M. Elgarahy, M. Hefny, A. Al-Hinai, A. H. Al-Muhtaseb, and D. W. Rooney, “Hydrogen production, storage, utilisation and environmental impacts: a review,” *Environmental Chemistry Letters*, pp. 1–36, 2021.

[55] O. Fandiño, J. M. Trusler, and D. Vega-Maza, “Phase behavior of (CO₂ + H₂) and (CO₂ + N₂) at temperatures between (218.15 and 303.15) k at pressures up to 15 mpa,” *International journal of greenhouse gas control*, vol. 36, pp. 78–92, 2015.

- [56] S. Chabab, P. Théveneau, C. Coquelet, J. Corvisier, and P. Paricaud, “Measurements and predictive models of high-pressure H₂ solubility in brine (H₂O+ NaCl) for underground hydrogen storage application,” *International Journal of Hydrogen Energy*, vol. 45, no. 56, pp. 32206–32220, 2020.
- [57] R. Beckmüller, M. Thol, I. H. Bell, E. W. Lemmon, and R. Span, “New equations of state for binary hydrogen mixtures containing methane, nitrogen, carbon monoxide, and carbon dioxide,” *Journal of Physical and Chemical Reference Data*, vol. 50, no. 1, 2021.
- [58] E. J. Peters, *Advanced petrophysics: Dispersion, interfacial phenomena*, vol. 2. Greenleaf Book Group, 2012.
- [59] L. Paterson, “The implications of fingering in underground hydrogen storage,” *International journal of hydrogen energy*, vol. 8, no. 1, pp. 53–59, 1983.
- [60] K. Alms, B. Ahrens, M. Graf, and M. Nehler, “Linking geological and infrastructural requirements for large-scale underground hydrogen storage in germany,” *Frontiers in Energy Research*, vol. 11, p. 1172003, 2023.
- [61] R. Lenormand, E. Touboul, and C. Zarcone, “Numerical models and experiments on immiscible displacements in porous media,” *Journal of fluid mechanics*, vol. 189, pp. 165–187, 1988.
- [62] M. Piri and M. J. Blunt, “Three-phase threshold capillary pressures in noncircular capillary tubes with different wettabilities including contact angle hysteresis,” *Physical review E*, vol. 70, no. 6, p. 061603, 2004.
- [63] Y. Gao, Q. Lin, B. Bijeljic, and M. J. Blunt, “Pore-scale dynamics and the multiphase Darcy law,” *Physical Review Fluids*, vol. 5, no. 1, p. 013801, 2020.
- [64] M. J. Blunt, *Multiphase flow in permeable media: A pore-scale perspective*. Cambridge University Press, 2017.
- [65] I. Fatt and H. Dykstra, “Relative permeability studies,” *Journal of Petroleum Technology*, vol. 3, no. 09, pp. 249–256, 1951.
- [66] J. Hommel, E. Coltman, and H. Class, “Porosity–permeability relations for evolving pore space: a review with a focus on (bio-) geochemically altered porous media,” *Transport in Porous Media*, vol. 124, no. 2, pp. 589–629, 2018.
- [67] V. Joekar-Niasar, S. M. Hassanzadeh, and H. Dahle, “Non-equilibrium effects in capillarity and interfacial area in two-phase flow: dynamic pore-network modelling,” *Journal of Fluid Mechanics*, vol. 655, pp. 38–71, 2010.
- [68] M. Andrew, B. Bijeljic, and M. J. Blunt, “Pore-by-pore capillary pressure measurements using x-ray microtomography at reservoir conditions: Curvature, snap-off, and remobilization of residual co 2,” *Water Resources Research*, vol. 50, no. 11, pp. 8760–8774, 2014.

[69] Y. Zhang, B. Bijeljic, Y. Gao, Q. Lin, and M. J. Blunt, “Quantification of nonlinear multiphase flow in porous media,” *Geophysical Research Letters*, vol. 48, no. 5, p. e2020GL090477, 2021.

[70] L. Treiber and W. Owens, “A laboratory evaluation of the wettability of fifty oil-producing reservoirs,” *Society of petroleum engineers journal*, vol. 12, no. 06, pp. 531–540, 1972.

[71] S. Strand, E. J. Høgnesen, and T. Austad, “Wettability alteration of carbonates—effects of potential determining ions (ca^{2+} and so^{42-}) and temperature,” *Colloids and Surfaces A: Physicochemical and Engineering Aspects*, vol. 275, no. 1-3, pp. 1–10, 2006.

[72] Y. Wu, P. J. Shuler, M. Blanco, Y. Tang, and W. A. Goddard, “A study of wetting behavior and surfactant eor in carbonates with model compounds,” in *SPE Improved Oil Recovery Conference?*, pp. SPE-99612, SPE, 2006.

[73] D. Avraam and A. Payatakes, “Flow regimes and relative permeabilities during steady-state two-phase flow in porous media,” *Journal of Fluid Mechanics*, vol. 293, pp. 207–236, 1995.

[74] R. Holtzman, M. Dentz, R. Planet, and J. Ortín, “The origin of hysteresis and memory of two-phase flow in disordered media,” *Communications Physics*, vol. 3, no. 1, pp. 1–7, 2020.

[75] J. Pickell, B. Swanson, and W. Hickman, “Application of air-mercury and oil-air capillary pressure data in the study of pore structure and fluid distribution,” *Society of Petroleum Engineers Journal*, vol. 6, no. 01, pp. 55–61, 1966.

[76] R. Paustian, L. Andersson, J. O. Helland, and D. Wildenschild, “On the relationship between capillary pressure, saturation, and interfacial area for three-phase flow in water-wet porous media,” *Advances in Water Resources*, vol. 151, p. 103905, 2021.

[77] R. Lenhard and J. Parker, “Experimental validation of the theory of extending two-phase saturation-pressure relations to three-fluid phase systems for monotonic drainage paths,” *Water Resources Research*, vol. 24, no. 3, pp. 373–380, 1988.

[78] V. Hassani, T. Tjahjowidodo, and T. N. Do, “A survey on hysteresis modeling, identification and control,” *Mechanical Systems and Signal Processing*, vol. 49, no. 1-2, pp. 209–233, 2014.

[79] T. W. Teklu, Z. Zhou, X. Li, and H. Abass, “Experimental investigation on permeability and porosity hysteresis in low-permeability formations,” in *SPE Low Perm Symposium*, vol. 49, pp. 1–30, 180226, OnePetro, 2016.

[80] S. Wheeler, R. Sharma, and M. Buisson, “Coupling of hydraulic hysteresis and stress-strain behaviour in unsaturated soils,” *Géotechnique*, vol. 53, no. 1, pp. 41–54, 2003.

- [81] I. D. Mayergoyz, *Mathematical models of hysteresis and their applications*. Academic Press, 2003.
- [82] M. R. Dernaika, M. Kalam, M. Basioni, A. Dawoud, and S. M. Skjæveland, “Hysteresis of capillary pressure, resistivity index and relative permeability in carbonate rock types,” in *The International Symposium of the Society of Core Analysts*, pp. 1–12, 2011.
- [83] A. Firoozabadi and J. Hauge, “Capillary pressure in fractured porous media (includes associated papers 21892 and 22212),” *Journal of Petroleum Technology*, vol. 42, no. 06, pp. 784–791, 1990.
- [84] S. M. Hassanzadeh and W. G. Gray, “Thermodynamic basis of capillary pressure in porous media,” *Water Resources Research*, vol. 29, no. 10, pp. 3389–3405, 1993.
- [85] M. R. Dernaika, M. Z. Kalam, M. A. Basioni, and S. M. Skjæveland, “Hysteresis of capillary pressure, resistivity index and relative permeability in different carbonate rock types,” *Petrophysics-The SPWLA Journal of Formation Evaluation and Reservoir Description*, vol. 53, no. 05, pp. 316–332, 2012.
- [86] C. Evans and E. Guerrero, “Theory and application of capillary pressure,” in *SPWLA 20th Annual Logging Symposium*, OnePetro, 1979.
- [87] N. R. Morrow, “Physics and thermodynamics of capillary action in porous media,” *Industrial & Engineering Chemistry*, vol. 62, no. 6, pp. 32–56, 1970.
- [88] H. Greder, V. Gallato, P. Cordelier, D. Laran, V. Munoz, and O. d’Abridgeon, “Forty comparisons of mercury injection data with oil/water capillary pressure measurements by the porous plate technique,” *Society of Core Analysis, SCA*, vol. 9710, 1997.
- [89] G. Hassler and E. Brunner, “Measurement of capillary pressures in small core samples,” *Transactions of the AIME*, vol. 160, no. 01, pp. 114–123, 1945.
- [90] R. Wunderlich, “Imaging of wetting and nonwetting phase distributions: Application to centrifuge capillary pressure measurements,” in *SPE Annual Technical Conference and Exhibition*, pp. 1–6, 14422, OnePetro, 1985.
- [91] Z. S. Omoregbe, “Factors affecting the equivalency of different capillary pressure measurement techniques,” *SPE Formation Evaluation*, vol. 3, no. 01, pp. 146–155, 1988.
- [92] D. P. Green, J. R. Dick, M. McAloon, P. d. J. Cano-Barrita, J. Burger, B. Balcom, and C. I. U. Oaxaca, “Oil/water imbibition and drainage capillary pressure determined by mri on a wide sampling of rocks,” in *SCA2008-01 presented at the SCA conference, Abu Dhabi, UAE*, vol. 29, 2008.
- [93] J. Killough, “Reservoir simulation with history-dependent saturation functions,” *Society of Petroleum Engineers Journal*, vol. 16, no. 01, pp. 37–48, 1976.

[94] A. M. Ismail, M. Z. Kalam, and M. H. Jasser, “Giant carbonate reservoir study showing impact of capillary pressure hysteresis on history match & field development plan,” in *SPE Reservoir Characterisation and Simulation Conference and Exhibition*, pp. 1–11, 175665, OnePetro, 2015.

[95] M. Leverett, “Capillary behavior in porous solids,” *Transactions of the AIME*, vol. 142, no. 01, pp. 152–169, 1941.

[96] J. Parker and R. Lenhard, “A model for hysteretic constitutive relations governing multiphase flow: 1. saturation-pressure relations,” *Water Resources Research*, vol. 23, no. 12, pp. 2187–2196, 1987.

[97] X. Wang and V. Alvarado, “Effects of low-salinity waterflooding on capillary pressure hysteresis,” in *SPE Improved Oil Recovery Conference*, OnePetro, 2016.

[98] J. Kokkedee and V. Boutkan, “Towards measurement of capillary pressure and relative permeability at representative wettability,” *Geological Society, London, Special Publications*, vol. 84, no. 1, pp. 43–50, 1995.

[99] B. Gharedaghloo, J. S. Price, F. Rezanezhad, and W. L. Quinton, “Evaluating the hydraulic and transport properties of peat soil using pore network modeling and x-ray micro computed tomography,” *Journal of Hydrology*, vol. 561, pp. 494–508, 2018.

[100] S. Hamamoto, P. Moldrup, K. Kawamoto, T. Sakaki, T. Nishimura, and T. Komatsu, “Pore network structure linked by x-ray ct to particle characteristics and transport parameters,” *Soils and Foundations*, vol. 56, no. 4, pp. 676–690, 2016.

[101] K. Nsir and G. Schäfer, “A pore-throat model based on grain-size distribution to quantify gravity-dominated dnapl instabilities in a water-saturated homogeneous porous medium,” *Comptes Rendus Geoscience*, vol. 342, no. 12, pp. 881–891, 2010.

[102] J. Su, G. Chai, L. Wang, W. Cao, Z. Gu, C. Chen, and X. Y. Xu, “Pore-scale direct numerical simulation of particle transport in porous media,” *Chemical Engineering Science*, vol. 199, pp. 613–627, 2019.

[103] J. T. Gostick, “Versatile and efficient pore network extraction method using marker-based watershed segmentation,” *Physical Review E*, vol. 96, no. 2, p. 023307, 2017.

[104] S. M. Hassanzadeh and W. G. Gray, “Mechanics and thermodynamics of multiphase flow in porous media including interphase boundaries,” *Advances in Water Resources*, vol. 13, no. 4, pp. 169–186, 1990.

[105] K. A. Culligan, D. Wildenschild, B. S. Christensen, W. G. Gray, M. L. Rivers, and A. F. Tompson, “Interfacial area measurements for unsaturated flow through a porous medium,” *Water Resources Research*, vol. 40, no. 12, 2004.

- [106] J.-T. Cheng, L. J. Pyrak-Nolte, D. D. Nolte, and N. J. Giordano, “Linking pressure and saturation through interfacial areas in porous media,” *Geophysical Research Letters*, vol. 31, no. 8, 2004.
- [107] D. Chen, L. J. Pyrak-Nolte, J. Griffin, and N. J. Giordano, “Measurement of interfacial area per volume for drainage and imbibition,” *Water Resources Research*, vol. 43, no. 12, 2007.
- [108] M. L. Porter, M. G. Schaap, and D. Wildenschild, “Lattice-boltzmann simulations of the capillary pressure–saturation–interfacial area relationship for porous media,” *Advances in Water Resources*, vol. 32, no. 11, pp. 1632–1640, 2009.
- [109] E. Diamantopoulos, W. Durner, and T. Harter, “Prediction of capillary air-liquid interfacial area vs. saturation function from relationship between capillary pressure and water saturation,” *Advances in Water Resources*, vol. 97, pp. 219–223, 2016.
- [110] L. M. Anovitz and D. R. Cole, “Characterization and analysis of porosity and pore structures,” *Reviews in Mineralogy and geochemistry*, vol. 80, no. 1, pp. 61–164, 2015.
- [111] D. Tiab and E. C. Donaldson, *Petrophysics: theory and practice of measuring reservoir rock and fluid transport properties*. Elsevier, 2024.
- [112] M. Sahimi, *Flow and transport in porous media and fractured rock: from classical methods to modern approaches*. John Wiley & Sons, 2011.
- [113] H. Hematpur, R. Abdollahi, S. Rostami, M. Haghghi, and M. J. Blunt, “Review of underground hydrogen storage: Concepts and challenges,” *Advances in Geo-Energy Research*, vol. 7, no. 2, pp. 111–131, 2023.
- [114] J. A. de Chalendar, C. Garing, and S. M. Benson, “Pore-scale modelling of Ostwald Ripening,” *Journal of Fluid Mechanics*, vol. 835, pp. 363–392, 2018.
- [115] X. Li and X. Fan, “Effect of CO₂ phase on contact angle in oil-wet and water-wet pores,” *International Journal of Greenhouse Gas Control*, vol. 36, pp. 106–113, 2015.
- [116] D. M. Anderson, G. B. McFadden, and A. A. Wheeler, “Diffuse-interface methods in fluid mechanics,” *Annual review of fluid mechanics*, vol. 30, no. 1, pp. 139–165, 1998.
- [117] F. Civan, *Reservoir formation damage: fundamentals, modeling, assessment, and mitigation*. Gulf Professional Publishing, 2023.
- [118] J. Bear, *Dynamics of fluids in porous media*. Courier Corporation, 2013.
- [119] Y. Gao, A. Georgiadis, N. Brussee, A. Coorn, H. van Der Linde, J. Dietderich, F. O. Alpak, D. Eriksen, M. Mooijer-van Den Heuvel, M. Appel, *et al.*, “Capillarity and phase-mobility of a hydrocarbon gas-liquid system,” *Oil & Gas Science and Technology–Revue d’IFP Energies nouvelles*, vol. 76, p. 43, 2021.

[120] S. Berg, Y. Gao, A. Georgiadis, N. Brussee, A. Coorn, H. van der Linde, J. Dietderich, F. O. Alpak, D. Eriksen, M. Mooijer-van den Heuvel, *et al.*, “Determination of critical gas saturation by micro-ct,” *Petrophysics*, vol. 61, no. 02, pp. 133–150, 2020.

[121] H.-J. Vogel, U. Weller, and S. Schlüter, “Quantification of soil structure based on minkowski functions,” *Computers & Geosciences*, vol. 36, no. 10, pp. 1236–1245, 2010.

[122] C. H. Arns, M. A. Knackstedt, and K. R. Mecke, “Boolean reconstructions of complex materials: Integral geometric approach,” *Physical Review E—Statistical, Nonlinear, and Soft Matter Physics*, vol. 80, no. 5, p. 051303, 2009.

[123] R. T. Armstrong, M. L. Porter, and D. Wildenschild, “Linking pore-scale interfacial curvature to column-scale capillary pressure,” *Advances in Water resources*, vol. 46, pp. 55–62, 2012.

[124] B. P. Flannery, H. W. Deckman, W. G. Roberge, and K. L. D’AMICO, “Three-dimensional x-ray microtomography,” *Science*, vol. 237, no. 4821, pp. 1439–1444, 1987.

[125] M. Knackstedt, P. Jaime, A. R. Butcher, P. W. Botha, J. Middleton, and R. Sok, “Integrating reservoir characterization: 3d dynamic, petrophysical and geological description of reservoir facies,” in *SPE Asia Pacific Oil and Gas Conference and Exhibition*, OnePetro, 2010.

[126] D. Wildenschild and A. P. Sheppard, “X-ray imaging and analysis techniques for quantifying pore-scale structure and processes in subsurface porous medium systems,” *Advances in Water resources*, vol. 51, pp. 217–246, 2013.

[127] M. J. Blunt, B. Bijeljic, H. Dong, O. Gharbi, S. Iglauer, P. Mostaghimi, A. Paluszny, and C. Pentland, “Pore-scale imaging and modelling,” *Advances in Water Resources*, vol. 51, pp. 197–216, 2013.

[128] UKResearch and Innovation, “Diamond light source.” STFC, 2024. [Online]. Available: <https://www.ukri.org/news/uks-national-synchrotron-facility-reports-2-6-billion-impact/>.

[129] Science and T. F. Council, “Synchrotrons dimond ligh,” 2016. <https://stfc.ukri.org/research/accelerator-science/synchrotron/#:~:text=The%20UK%20made%20a%20large,STFC%20Daresbury%20Laboratory%20in%20Cheshire.>, 20, 2020.

[130] F. A. Dullien, *Porous media: fluid transport and pore structure*. Academic press, 2012.

[131] M. J. Blunt, “Flow in porous media—pore-network models and multiphase flow,” *Current opinion in colloid & interface science*, vol. 6, no. 3, pp. 197–207, 2001.

[132] G. Pinder and W. Gray, “Essentials of multiphase flow and transport in porous media, a john wiley & sons,” *Inc., Hoboken, New Jersey*, 2008.

- [133] A. Alhosani, A. Scanziani, Q. Lin, S. Foroughi, A. M. Alhammadi, M. J. Blunt, and B. Bijeljic, “Dynamics of water injection in an oil-wet reservoir rock at subsurface conditions: Invasion patterns and pore-filling events,” *Physical Review E*, vol. 102, no. 2, p. 023110, 2020.
- [134] M. Andrew, H. Menke, M. J. Blunt, and B. Bijeljic, “The imaging of dynamic multi-phase fluid flow using synchrotron-based x-ray microtomography at reservoir conditions,” *Transport in Porous Media*, vol. 110, no. 1, pp. 1–24, 2015.
- [135] A. Q. Raeini, M. J. Blunt, and B. Bijeljic, “Modelling two-phase flow in porous media at the pore scale using the volume-of-fluid method,” *Journal of Computational Physics*, vol. 231, no. 17, pp. 5653–5668, 2012.
- [136] Z. Jangda, H. Menke, A. Busch, S. Geiger, T. Bultreys, H. Lewis, and K. Singh, “Pore-scale visualization of hydrogen storage in a sandstone at subsurface pressure and temperature conditions: Trapping, dissolution and wettability,” *Journal of Colloid and Interface Science*, vol. 629, pp. 316–325, 2023.
- [137] K. K. Singh, D. N. Singh, and R. P. Gamage, “Effect of sample size on the fluid flow through a single fractured granitoid,” *Journal of Rock Mechanics and Geotechnical Engineering*, vol. 8, no. 3, pp. 329–340, 2016.
- [138] C. Garing, J. A. de Chalendar, M. Voltolini, J. B. Ajo-Franklin, and S. M. Benson, “Pore-scale capillary pressure analysis using multi-scale X-ray micromotography,” *Advances in Water Resources*, vol. 104, pp. 223–241, 2017.
- [139] S. Higgs, Y. Da Wang, C. Sun, J. Ennis-King, S. J. Jackson, R. T. Armstrong, and P. Mostaghimi, “Comparative analysis of hydrogen, methane and nitrogen relative permeability: Implications for underground hydrogen storage,” *Journal of Energy Storage*, vol. 73, p. 108827, 2023.
- [140] S. Iglauder, M. Ali, and A. Keshavarz, “Hydrogen wettability of sandstone reservoirs: Implications for hydrogen geo-storage,” *Geophysical Research Letters*, vol. 48, no. 3, p. e2020GL090814, 2021.
- [141] L. Hashemi, W. Glerum, R. Farajzadeh, and H. Hajibeygi, “Contact angle measurement for hydrogen/brine/sandstone system using captive-bubble method relevant for underground hydrogen storage,” *Advances in Water Resources*, vol. 154, p. 103964, 2021.
- [142] S. Higgs, Y. Da Wang, C. Sun, J. Ennis-King, S. J. Jackson, R. T. Armstrong, and P. Mostaghimi, “In-situ hydrogen wettability characterisation for underground hydrogen storage,” *International Journal of Hydrogen Energy*, vol. 47, no. 26, pp. 13062–13075, 2022.
- [143] W. van Rooijen, L. Hashemi, M. Boon, R. Farajzadeh, and H. Hajibeygi, “Microfluidics-based analysis of dynamic contact angles relevant for underground hydrogen storage,” *Advances in Water Resources*, p. 104221, 2022.

[144] E. M. Thaysen, I. B. Butler, A. Hassanpourouzband, D. Freitas, F. Alvarez-Borges, S. Krevor, N. Heinemann, R. Atwood, and K. Edlmann, “Pore-scale imaging of hydrogen displacement and trapping in porous media,” *International Journal of Hydrogen Energy*, 2022.

[145] Z. Jangda, H. Menke, A. Busch, S. Geiger, T. Bultreys, and K. Singh, “Subsurface hydrogen storage controlled by small-scale rock heterogeneities,” *International Journal of Hydrogen Energy*, vol. 60, pp. 1192–1202, 2024.

[146] M. Lysyy, G. Ersland, and M. Fernø, “Pore-scale dynamics for underground porous media hydrogen storage,” *Advances in Water Resources*, vol. 163, p. 104167, 2022.

[147] M. Arif, M. Lebedev, A. Barifcani, and S. Iglauer, “CO₂ storage in carbonates: Wettability of calcite,” *International Journal of Greenhouse Gas Control*, vol. 62, pp. 113–121, 2017.

[148] S. Krevor, M. J. Blunt, S. M. Benson, C. H. Pentland, C. Reynolds, A. Al-Menhali, and B. Niu, “Capillary trapping for geologic carbon dioxide storage—from pore scale physics to field scale implications,” *International Journal of Greenhouse Gas Control*, vol. 40, pp. 221–237, 2015.

[149] A. AlRatrou, M. J. Blunt, and B. Bijeljic, “Spatial correlation of contact angle and curvature in pore-space images,” *Water Resources Research*, vol. 54, no. 9, pp. 6133–6152, 2018.

[150] M. Lysyy, T. Føyen, E. B. Johannessen, M. Fernø, and G. Ersland, “Hydrogen relative permeability hysteresis in underground storage,” *Geophysical Research Letters*, vol. 49, no. 17, p. e2022GL100364, 2022.

[151] A. L. Herring, L. Andersson, and D. Wildenschild, “Enhancing residual trapping of supercritical CO₂ via cyclic injections,” *Geophysical Research Letters*, vol. 43, no. 18, pp. 9677–9685, 2016.

[152] D. S. Kumbhat and A. Ebigbo, “Effect of relative permeability hysteresis on plume dynamics, wellbore flow regime, and storage efficiency in underground hydrogen storage,” *International Journal of Hydrogen Energy*, vol. 91, pp. 243–255, 2024.

[153] B. Pan, K. Liu, B. Ren, M. Zhang, Y. Ju, J. Gu, X. Zhang, C. R. Clarkson, K. Edlmann, W. Zhu, *et al.*, “Impacts of relative permeability hysteresis, wettability, and injection/withdrawal schemes on underground hydrogen storage in saline aquifers,” *Fuel*, vol. 333, p. 126516, 2023.

[154] M. Lysyy, M. A. Fernø, and G. Ersland, “Effect of relative permeability hysteresis on reservoir simulation of underground hydrogen storage in an offshore aquifer,” *Journal of Energy Storage*, vol. 64, p. 107229, 2023.

[155] M. I. Khan, M. V. B. Machado, A. Khanal, and M. Delshad, “Evaluating capillary trapping in underground hydrogen storage: A pore-scale to reservoir-scale analysis,” *Fuel*, vol. 376, p. 132755, 2024.

[156] B. S. Shiran, M. Aarra, K. Djurhuus, N. Zamani, J. Solbakken, N. Dopffel, and H. Hajiheygi, “Underground Hydrogen Storage: Effect of Cyclic Flow and Flow rate on H₂ Recovery Efficiency,” in *85th EAGE Annual Conference & Exhibition (including the Workshop Programme)*, vol. 2024, pp. 1–5, European Association of Geoscientists & Engineers, 2024.

[157] M. Bahrami, H. Mahani, D. Zivar, and S. Ayatollahi, “Microfluidic investigation of pore-scale flow behavior and hysteresis in underground hydrogen storage in sandstones,” *Journal of Energy Storage*, vol. 98, p. 112959, 2024.

[158] S. Yu, M. Hu, C. I. Steefel, and I. Battiato, “Unraveling residual trapping for geologic hydrogen storage and production using pore-scale modeling,” *Advances in Water Resources*, vol. 185, p. 104659, 2024.

[159] H. Song, Y. Zhou, Z. Xie, J. Lao, and M. Yue, “A Pore-Scale Simulation of the Effect of Heterogeneity on Underground Hydrogen Storage,” *Water*, vol. 16, no. 22, p. 3264, 2024.

[160] J. Wang, Y. Yang, S. Cai, J. Yao, and Q. Xie, “Pore-scale modelling on hydrogen transport in porous media: Implications for hydrogen storage in saline aquifers,” *International Journal of Hydrogen Energy*, vol. 48, no. 37, pp. 13922–13933, 2023.

[161] M. J. Blunt, “Ostwald ripening and gravitational equilibrium: Implications for long-term subsurface gas storage,” *Physical Review E*, vol. 106, no. 4, p. 045103, 2022.

[162] D. Singh, H. A. Friis, E. Jettestuen, and J. O. Helland, “A level set approach to ostwald ripening of trapped gas bubbles in porous media,” *Transport in Porous Media*, vol. 145, no. 2, pp. 441–474, 2022.

[163] D. Singh, H. A. Friis, E. Jettestuen, and J. O. Helland, “Pore-scale ostwald ripening of gas bubbles in the presence of oil and water in porous media,” *Journal of Colloid and Interface Science*, vol. 647, pp. 331–343, 2023.

[164] J. Colonna, F. Brissaud, and J. Millet, “Evolution of capillarity and relative permeability hysteresis,” *Society of petroleum engineers journal*, vol. 12, no. 01, pp. 28–38, 1972.

[165] N. R. Morrow and C. C. Harris, “Capillary equilibrium in porous materials,” *Society of Petroleum Engineers Journal*, vol. 5, no. 01, pp. 15–24, 1965.

[166] J. Kleppe, P. Delaplace, R. Lenormand, G. Hamon, and E. Chaput, “Representation of capillary pressure hysteresis in reservoir simulation,” in *SPE Annual Technical Conference and Exhibition?*, pp. SPE-38899, SPE, 1997.

[167] A. J. Bouchard and J. T. Hawkins, “Reservoir-engineering implications of capillary-pressure and relative-permeability hysteresis,” *The Log Analyst*, vol. 33, no. 04, 1992.

[168] A. L. Herring, L. Andersson, D. Newell, J. Carey, and D. Wildenschild, “Pore-scale observations of supercritical CO₂ drainage in Bentheimer sandstone by synchrotron x-ray imaging,” *International Journal of Greenhouse Gas Control*, vol. 25, pp. 93–101, 2014.

[169] Y. Li, Y. Yang, M. Dong, J. Wang, W. Jing, J. Yao, K. Zhang, H. Sun, J. Zhong, L. Zhang, *et al.*, “Micro-scale experimental investigations of CO₂-wag injection and ostwald ripening analysis in carbonate rocks with different pore structures,” *Geoenergy Science and Engineering*, vol. 241, p. 213092, 2024.

[170] A. Rezaei, A. Hassanpouryouzband, I. Molnar, Z. Derikvand, R. S. Haszeldine, and K. Edlmann, “Relative permeability of hydrogen and aqueous brines in sandstones and carbonates at reservoir conditions,” *Geophysical Research Letters*, vol. 49, no. 12, p. e2022GL099433, 2022.

[171] W. Dokhon, S. Goodarzi, H. M. Alzahrani, M. J. Blunt, and B. Bijeljic, “Pressure decline and gas expansion in underground hydrogen storage: A pore-scale percolation study,” *International Journal of Hydrogen Energy*, vol. 86, pp. 261–274, 2024.

[172] K. Bijay, L. P. Frash, N. M. Creasy, C. W. Neil, P. Purswani, W. Li, M. Meng, U. Iyare, and M. R. Gross, “Laboratory study of cyclic underground hydrogen storage in porous media with evidence of a dry near-well zone and evaporation induced salt precipitation,” *International Journal of Hydrogen Energy*, vol. 71, pp. 515–527, 2024.

[173] O. E. Medina, J. F. Gallego, I. Moncayo-Riascos, M. Lysyy, P. N. Benjumea, F. B. Cortés, and C. A. Franco, “Salinity influence on underground hydrogen storage: Insights from molecular dynamics and pore-scale analysis,” *International Journal of Hydrogen Energy*, vol. 60, pp. 959–975, 2024.

[174] A. E. Peksa, K.-H. A. Wolf, and P. L. Zitha, “Bentheimer sandstone revisited for experimental purposes,” *Marine and Petroleum Geology*, vol. 67, pp. 701–719, 2015.

[175] P. Lai and S. Krevor, “Pore scale heterogeneity in the mineral distribution and surface area of berea sandstone,” *Energy Procedia*, vol. 63, pp. 3582–3588, 2014.

[176] R. Kareem, P. Cubillas, J. Gluyas, L. Bowen, S. Hillier, and H. C. Greenwell, “Multi-technique approach to the petrophysical characterization of berea sandstone core plugs (cleveland quarries, usa),” *Journal of Petroleum Science and Engineering*, vol. 149, pp. 436–455, 2017.

[177] I. Song and J. Renner, “Hydromechanical properties of fontainebleau sandstone: Experimental determination and micromechanical modeling,” *Journal of Geophysical research: solid earth*, vol. 113, no. B9, 2008.

[178] R. Huang, A. L. Herring, and A. Sheppard, “Effect of saturation and image resolution on representative elementary volume and topological quantification: an experimental study on bentheimer sandstone using micro-ct,” *Transport in Porous Media*, vol. 137, pp. 489–518, 2021.

[179] Q. Lin, B. Bijeljic, S. Berg, R. Pini, M. J. Blunt, and S. Krevor, “Minimal surfaces in porous media: Pore-scale imaging of multiphase flow in an altered-wettability bentheimer sandstone,” *Phys. Rev. E*, vol. 99, p. 063105, 2019.

[180] R. A. Ketcham and W. D. Carlson, “Acquisition, optimization and interpretation of x-ray computed tomographic imagery: applications to the geosciences,” *Computers & Geosciences*, vol. 27, no. 4, pp. 381–400, 2001.

[181] R. Szeliski, *Computer vision: algorithms and applications*. Springer Nature, 2022.

[182] M. D. Abràmoff, P. J. Magalhães, and S. J. Ram, “Image processing with imagej,” *Bio-photonics international*, vol. 11, no. 7, pp. 36–42, 2004.

[183] J. Schindelin, I. Arganda-Carreras, E. Frise, V. Kaynig, M. Longair, T. Pietzsch, S. Preibisch, C. Rueden, S. Saalfeld, B. Schmid, *et al.*, “Fiji: an open-source platform for biological-image analysis,” *Nature methods*, vol. 9, no. 7, pp. 676–682, 2012.

[184] S. Schlüter, A. Sheppard, K. Brown, and D. Wildenschild, “Image processing of multiphase images obtained via X-ray microtomography: a review,” *Water Resources Research*, vol. 50, no. 4, pp. 3615–3639, 2014.

[185] A. Buades, B. Coll, and J.-M. Morel, “A non-local algorithm for image denoising,” in *2005 IEEE computer society conference on computer vision and pattern recognition (CVPR'05)*, vol. 2, pp. 60–65, Ieee, 2005.

[186] A. L. Herring, J. Middleton, R. Walsh, A. Kingston, and A. Sheppard, “Flow rate impacts on capillary pressure and interface curvature of connected and disconnected fluid phases during multiphase flow in sandstone,” *Advances in Water Resources*, vol. 107, pp. 460–469, 2017.

[187] A. Herring, V. Robins, and A. Sheppard, “Topological persistence for relating microstructure and capillary fluid trapping in sandstones,” *Water Resources Research*, vol. 55, no. 1, pp. 555–573, 2019.

[188] C. Hemme and W. Van Berk, “Hydrogeochemical modeling to identify potential risks of underground hydrogen storage in depleted gas fields,” *Applied Sciences*, vol. 8, no. 11, p. 2282, 2018.

[189] S. Foroughi, B. Bijeljic, Q. Lin, A. Q. Raeini, and M. J. Blunt, “Pore-by-pore modeling, analysis, and prediction of two-phase flow in mixed-wet rocks,” *Physical Review E*, vol. 102, no. 2, p. 023302, 2020.

[190] Q. Lin, Y. Al-Khulaifi, M. J. Blunt, and B. Bijeljic, “Quantification of sub-resolution porosity in carbonate rocks by applying high-salinity contrast brine using X-ray microtomography differential imaging,” *Advances in water resources*, vol. 96, pp. 306–322, 2016.

[191] A. Q. Raeini, B. Bijeljic, and M. J. Blunt, “Generalized network modeling: Network extraction as a coarse-scale discretization of the void space of porous media,” *Physical Review E*, vol. 96, no. 1, p. 013312, 2017.

[192] H. Dong and M. J. Blunt, “Pore-network extraction from micro-computerized-tomography images,” *Physical Review E*, vol. 80, no. 3, p. 036307, 2009.

[193] U. D. of Energy, “Hydrogen safety protocols.” U.S. Department of Energy, 2021. [Online]. Available: <https://www.hydrogen.energy.gov/safety.html>.

[194] E. C. H. Alliance, “Ehsp guidance on hydrogen safety engineering.” European Clean Hydrogen Alliance, 2023. [Online]. Available: <https://www.clean-hydrogen.europa.eu/system/files/2023-05/EHSP%20Guidance%20on%20Hydrogen%20Safety%20Engineering%20-%20v1-Final.pdf>.

[195] S. Safety365, “Sodium chloride solution - safety data sheet.” Sevron Safety365, 2023. [Online]. Available: <https://safety365.sevron.co.uk/substances/accessSDS/SDS-25835-59266261c23b31.45615516>.

[196] C. GmbH, “Sodium chloride - safety data sheet.” Chemos GmbH, 2023. [Online]. Available: https://www.chemos.de/import/data/msds/GB_en/7647-14-5-A0216639-GB-en.pdf.

[197] S. P. Power, F. Moloney, M. Twomey, K. James, O. J. O’Connor, and M. M. Maher, “Computed tomography and patient risk: Facts, perceptions and uncertainties,” *World journal of radiology*, vol. 8, no. 12, p. 902, 2016.

[198] U. Food and D. Administration, “Medical x-ray imaging.” U.S. Food and Drug Administration, 2022. [Online]. Available: <https://www.fda.gov/radiation-emitting-products/medical-imaging/medical-x-ray-imaging>.

[199] R. Moghadasi, S. Goodarzi, Y. Zhang, B. Bijeljic, M. J. Blunt, and A. Niemi, “Pore-scale characterization of residual gas remobilization in CO₂ geological storage,” *Advances in Water Resources*, p. 104499, 2023.

[200] T. R. Jones, A. Carpenter, and P. Golland, “Voronoi-based segmentation of cells on image manifolds,” in *International Workshop on Computer Vision for Biomedical Image Applications*, pp. 535–543, Springer, 2005.

[201] R. T. Armstrong, J. E. McClure, V. Robins, Z. Liu, C. H. Arns, S. Schlüter, and S. Berg, “Porous media characterization using Minkowski functionals: Theories, applications and future directions,” *Transport in Porous Media*, vol. 130, pp. 305–335, 2019.

- [202] N. S. Muhammed, B. Haq, D. Al Shehri, S. O. Badmus, A. R. Adebayo, and M. Mahmoud, “Hydrogen injection and withdrawal performance in depleted gas reservoirs,” *International Journal of Hydrogen Energy*, vol. 96, pp. 427–442, 2024.
- [203] Y. Da Wang, L. Kearney, M. J. Blunt, C. Sun, K. Tang, P. Mostaghimi, and R. T. Armstrong, “In situ characterization of heterogeneous surface wetting in porous materials,” *Advances in Colloid and Interface Science*, p. 103122, 2024.
- [204] G. Garfi, C. M. John, M. Rücker, Q. Lin, C. Spurin, S. Berg, and S. Krevor, “Determination of the spatial distribution of wetting in the pore networks of rocks,” *Journal of Colloid and Interface Science*, vol. 613, pp. 786–795, 2022.
- [205] T. Akai, Q. Lin, A. Alhosani, B. Bijeljic, and M. J. Blunt, “Quantification of uncertainty and best practice in computing interfacial curvature from complex pore space images,” *Materials*, vol. 12, no. 13, p. 2138, 2019.
- [206] A. I. Adebimpe, S. Foroughi, B. Bijeljic, and M. J. Blunt, “Percolation without trapping: How Ostwald ripening during two-phase displacement in porous media alters capillary pressure and relative permeability,” *Physical Review E*, vol. 110, no. 3, p. 035105, 2024.

Appendix A

Scientific Background

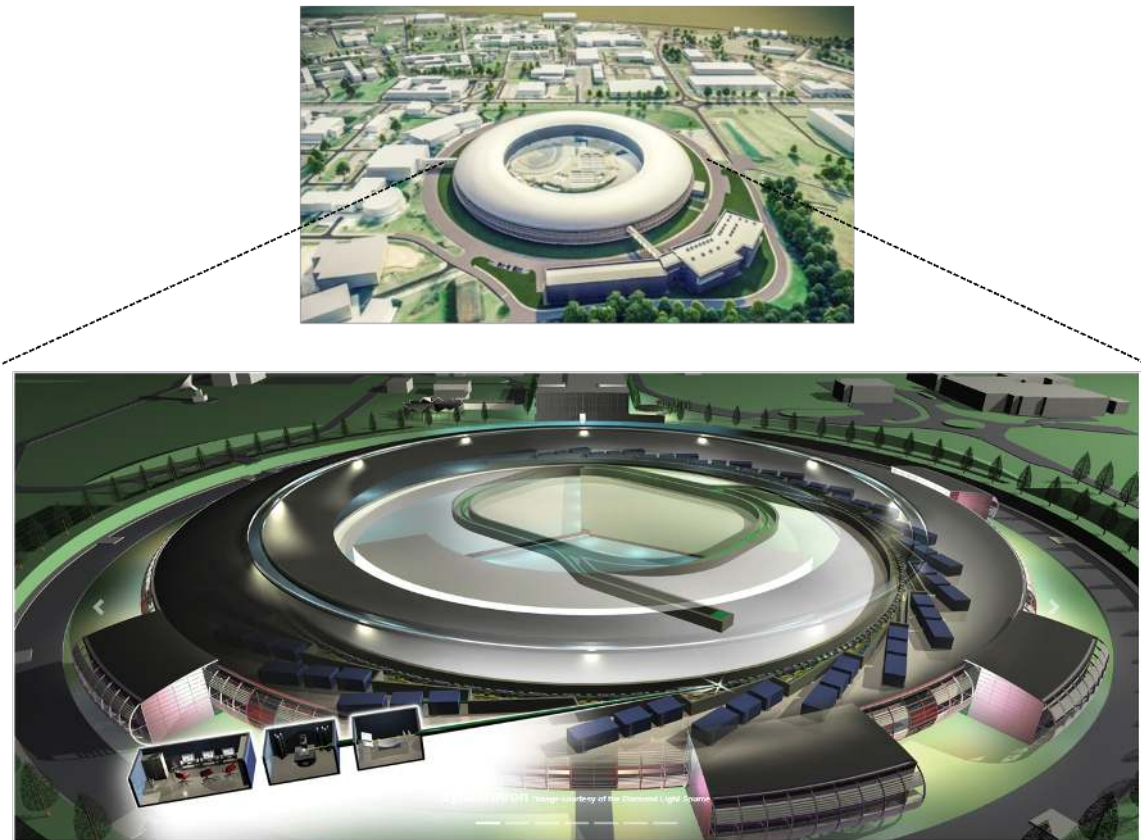


Figure A.1: Diamond Light Source building, a large ring-shaped facility that accelerates electrons to produce intense beams of synchrotron light, enabling the study of atoms and molecules in extraordinary detail [23].

Appendix B

~~Trapping, Hysteresis and Ostwald Ripening in Hydrogen Storage ...~~

B.1 Sample preparation



Figure B.1: Example of a rubber sleeve (Viton, nitrile, or silicone) used for enclosing the sample, sealed with PTFE tape to prevent gas leakage and ~~Aluminium~~ foil at the ends for additional sealing. This setup ensures a secure environment for the experimental process, minimising fluid and gas escape.

~~B.2 Absolute permeability measurement~~

Absolute permeability was determined using a steady-state flow experiment conducted in several stages to ensure accurate and reliable results. First, brine was injected into the Bentheimer sandstone sample at a low flow rate to achieve full saturation. This step ensured that all pore spaces were completely filled with brine, eliminating any residual air or other fluids that could affect the permeability measurement. Once full saturation was achieved, the brine flow rate was increased by doubling the flow rate for each subsequent measurement. At each flow rate, the pressure drop across the sample was recorded using differential pressure transducers. This step ensured that the relationship between flow rate and pressure drop remained linear, as expected under Darcy's law, and verified that the system was operating within the laminar flow regime. The process was repeated 3 to 5 times for each flow rate to reduce variability and account for potential measurement errors. This iterative approach also ensured consistency across measurements and helped confirm the homogeneity of the sample. The permeability was calculated from

the recorded data using Darcy's law (Eq. 2.1). The final permeability values, calculated from the multiple trials and flow rates, ranged between 1 and 2 Darcy ($1 - 2 \times 10^{-12} \text{ m}^2$). These results are consistent with the highly homogeneous pore structure of Bentheimer sandstone, as reported in the literature [63, 64].

B.3 PEEK tubing, valves, and pumps

In high-pressure experiments, such as those involving hydrogen and nitrogen gase, selecting appropriate tubing, valves, and pumps is critical to ensuring the reliability, safety, and accuracy of the experimental setup. These components must meet the dual requirements of chemical resistance and mechanical integrity under extreme conditions. PEEK (polyetheretherketone) tubing was chosen for its excellent chemical resistance, flexibility, and smooth internal surface, which is advantageous for high-pressure fluid dynamics. Specifically, Idex 1533XL Chromatography Tubing was used in this study due to its ability to withstand pressures up to ~~5000~~ psi. Unlike stainless steel tubing, PEEK tubing minimises turbulence, which helps maintain fluid resolution and reduces the risk of blockages caused by residue build up. Additionally, its flexibility and ease of cutting allow for quick adjustments during setup or maintenance.

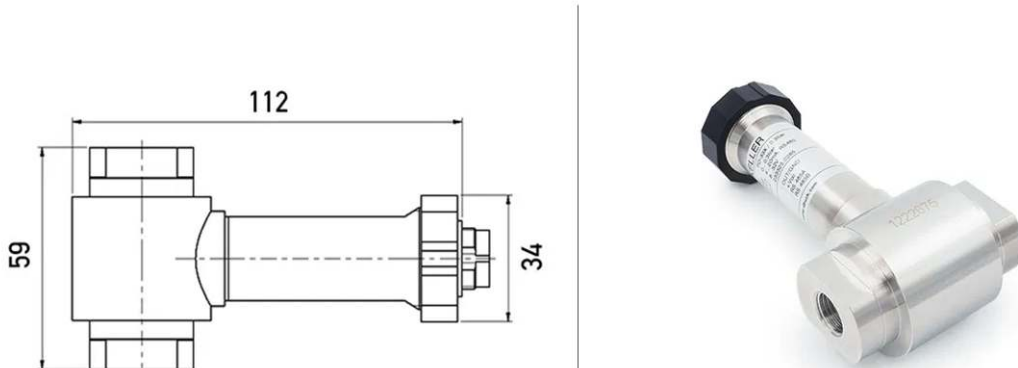
The experiments employed Teledyne Isco D-Series Pumps, which are well-suited for precise flow control under high pressures. These pumps provide the necessary reliability and performance for maintaining steady flow rates of experimental gases or fluids, which is critical when studying pressure-sensitive phenomena. The D-Series pumps were configured to handle high pressures safely while delivering consistent performance across the range of flow rates required for the study. Proper calibration and regular maintenance of the pumps were conducted to ensure their accuracy and to mitigate risks associated with fluctuating pressures.

To control fluid flow effectively in a high-pressure environment, Swagelok Stainless Steel 40G Series 3-Way Ball Valves were selected. These valves offer robust performance and a compact design, making them suitable for laboratory setups where space is a constraint. The choice of a stainless steel construction ensured compatibility with hydrogen and other experimental gases while providing mechanical strength. The valve's ability to withstand high pressures and its low internal volume were significant considerations. Regular cleaning of the valves was performed to prevent contamination, especially when switching between nitrogen and hydrogen experiments. Cleaning involved disassembling the valves and using solvents to remove residues, followed by drying with inert gas to prevent moisture accumulation, which could react with hydrogen.

B.4 Differential pressure measurement

To measure the pressure drop across the Bentheimer sandstone sample, differential pressure transducers (Keller PD-33X) with a precision of $\pm 0.03 \text{ kPa}$ were connected to the sample's inlet and outlet. This transducer was used for all experiments, including both absolute permeability measurements and core flooding experiments, where it played a crucial role in ensuring accurate pressure measurements. In the permeability experiment, the pressure difference between the inlet

and outlet of the core sample was recorded, allowing for the calculation of permeability using Darcy's law. To account for pressure losses in the flow system itself, a separate measurement was conducted with the sample removed from the core holder. The pressure drop across the system (tubing and fittings) was recorded under the same flow conditions, and this value was subtracted from the total pressure drop observed with the sample in place, isolating the pressure drop due to the core itself.



Pressure Transducer-Series PD-33X

Figure B.2: Pressure transducer (Keller PD-33X) used in the experiments. The left side shows a sketch of the setup with dimensions in millimetres, while the right side shows the actual pressure transducer used for measuring pressure during the experiments [24].

Additionally, during ~~core~~-flooding experiments, the pressure transducer was used to both impose the desired pressure and monitor the pressure at the inlet of the fluid, alongside the imposed flow rate, which allowed for the measurement of capillary pressure during fluid injection. The Keller PD-33X transducer's high precision and reliability were essential for capturing the pressure fluctuations required to accurately determine capillary pressure and analyse fluid distribution in the core. This comprehensive use of the Keller PD-33X transducer across various experiments ensured that all pressure measurements were precise and consistent, facilitating accurate calculations of permeability and capillary pressure.

B.5 Micro-computed tomography

Computed Tomography (CT) imaging is a powerful tool for non-destructive visualisation of internal structures at high resolution. Its ability to distinguish between phases (e.g., gas, liquid, and solid) makes it invaluable for studying pore-scale processes in rock samples. The theoretical basis and benefits of CT imaging have been discussed in detail in the Scientific Background section 2.3. In this study, two advanced micro-CT scanners were ~~utilised~~ to capture high-resolution images:

- **Zeiss Xradia 510 X-ray Scanner:** This scanner features a flat-panel detector, enabling

high-resolution imaging of rock samples. Its optimised design ensures a wide field of view, advanced phase-enhancing contrast, and superior image quality for larger samples, see Fig. B.3.

- **Heliscan Micro-CT Scanner:** This system features a helical scanning design, minimising artifacts and enabling uniform imaging of cylindrical samples. It is particularly suited for capturing high-precision pore-scale details, even in heterogeneous rock structures, ensuring continuous imaging along the sample's length.

After acquiring the CT scans, the images were reconstructed to create three-dimensional representations of the rock and fluid phases for each cycle [184]. For scans acquired using the Zeiss Versa X-ray scanner, the field of view limitations required partial scanning of the sample. Overlapping regions were carefully considered during scanning, and the individual sections were later stitched together to generate a complete high-resolution image.

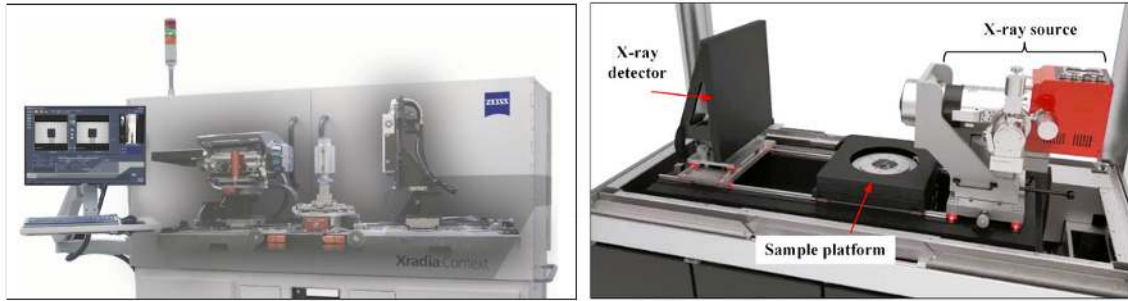


Figure B.3: Images of the two advanced micro-CT scanners used in this study. Left: The Zeiss Xradia 510 X-ray Scanner, equipped with a flat-panel detector. Right: The Heliscan micro-CT scanner, featuring a helical scanning setup with an X-ray source, detector, and sample platform, enabling seamless imaging without artifacts.

B.6 Micro-CT scanning parameters

Before conducting micro-CT imaging, careful adjustment of scanning parameters is crucial to ensure high-quality, artifact-free images. Key settings, such as projection number, exposure time, and voltage, directly influence image resolution, contrast, and overall scan accuracy. Projection Number is the number of projections that refers to the total number of 2D X-ray images captured during a scan as the sample rotates through 360 degrees. This parameter significantly impacts the resolution and accuracy of the reconstructed 3D images. For Zeiss Xradia 510, the projection number is typically adjustable depending on the desired resolution and scan duration. A higher projection number increases the angular sampling density, resulting in more detailed reconstructions, but it also lengthens the scanning time. In helical scanning, the projection number is determined by the pitch and sampling rate. Uniform projection density is achieved throughout the sample, ensuring accurate reconstructions even for cylindrical samples.

Exposure time controls how long the X-ray source illuminates the sample for each projection. Longer exposure times improve the signal-to-noise ratio, enhancing image quality but increasing

scan duration. Typical exposure times range from a few milliseconds to several seconds, depending on the sample's density and the imaging contrast required. Longer exposures are beneficial for dense or low-contrast materials. Voltage determines the energy of the X-ray beam, while current affects its intensity. These parameters must be optimised based on the material composition and thickness of the sample. Voltage settings typically range from 40 to 160 kV, with lower voltages used for soft or low-density materials to enhance contrast and higher voltages for dense samples to ensure penetration.

The voxel size determines the spatial resolution of the scan. For the Zeiss Xradia 510, voxel sizes can be adjusted based on the optical magnification system. The Heliscan scanner offers consistent voxel sizes due to its helical design, even for long cylindrical samples. Both systems have tools to minimise beam-hardening artefacts, such as filtering X-rays through a thin metal plate or using software correction. Balancing high resolution with practical scan times is critical, particularly when scanning large or multiple samples. By optimising these parameters, the micro-CT systems can deliver highly detailed reconstructions of internal rock structures, enabling precise measurements of pore-scale properties.

Appendix C

~~Ostwald Ripening Leads to Less Hysteresis during Hydrogen Injection ...~~

C.1 Reactor



Figure C.1: Parr Instrument Company Bench Top Reactor, featuring a 1L capacity chamber and advanced controls for precise temperature and pressure adjustments. This reactor is designed for high-pressure and high-temperature experiments, ensuring reliable and safe operation in laboratory settings [25].

C.2 ~~Bubble~~ size and cumulative distribution

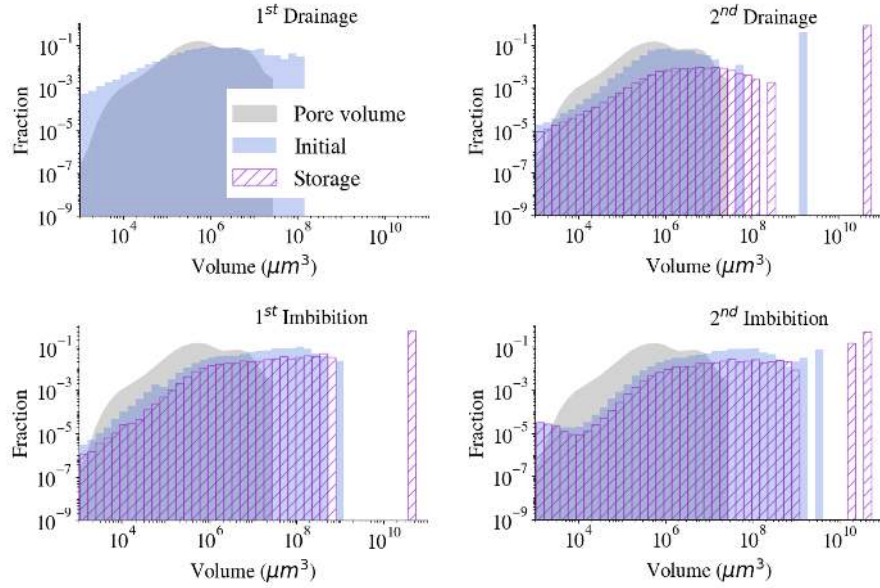


Figure C.2: The volume-weighted size distribution of ganglia is illustrated for the two cycles of gas and brine injection, with a uniformly spaced bin size in logarithmic space. These graphs compare the initial stage with the distribution after 16 hours of storage. The shaded grey area represents the volume distribution across all pores.

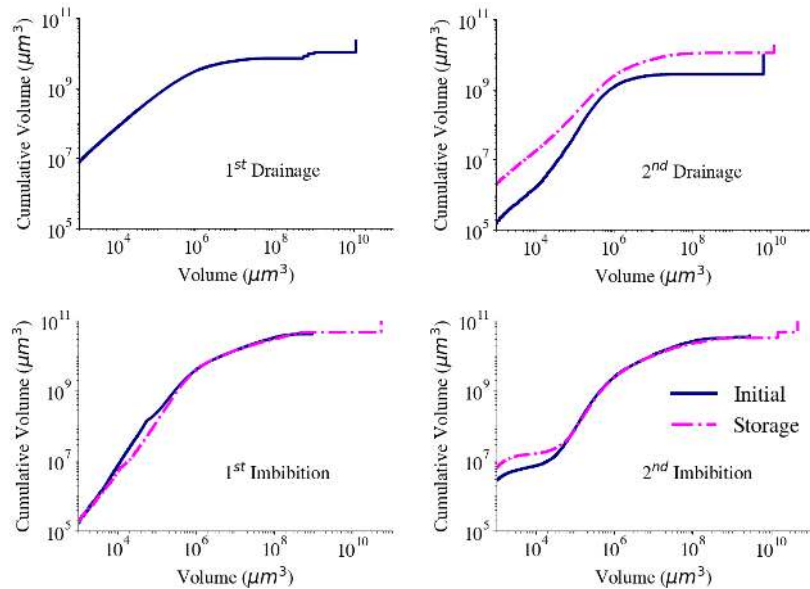


Figure C.3: The cumulative volume distribution of ganglia is illustrated across two cycles of gas and brine injection. These graphs compare the initial stage with the distribution after 16 hours of storage. A distinct vertical segment indicates the emergence of a single large ganglion, which dominates the volume following the storage period.

C.3 Pore and throat occupancy

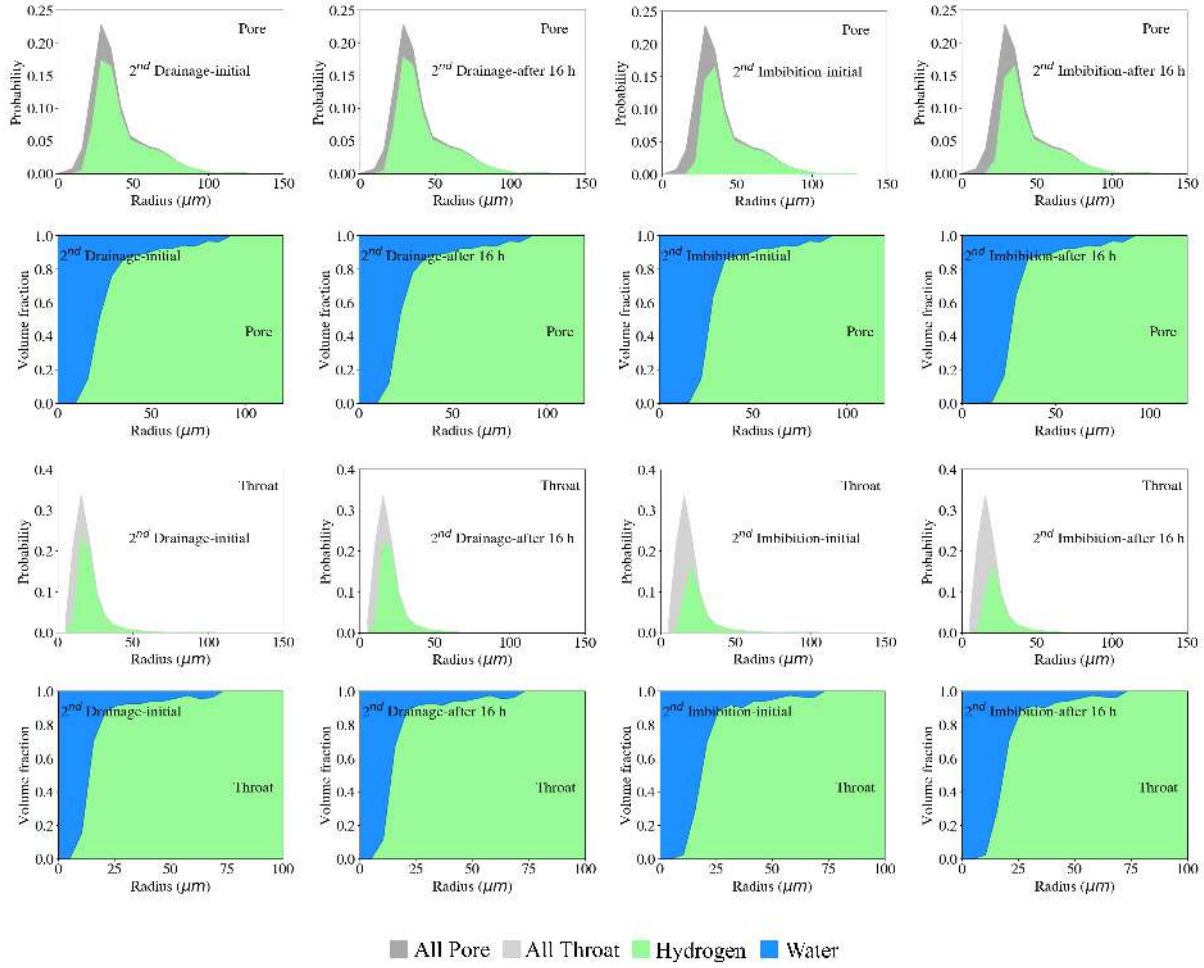


Figure C.4: Volume-weighted histograms of gas occupancy as a function of pore radius, plotted for the second cycle of gas injection following water flooding. Green indicates gas, blue indicates water, and grey represents the size distribution of all pores. Each plot corresponds to a specific cycle of injection and flooding, shown for both the initial stage and after a 16-hour storage period.

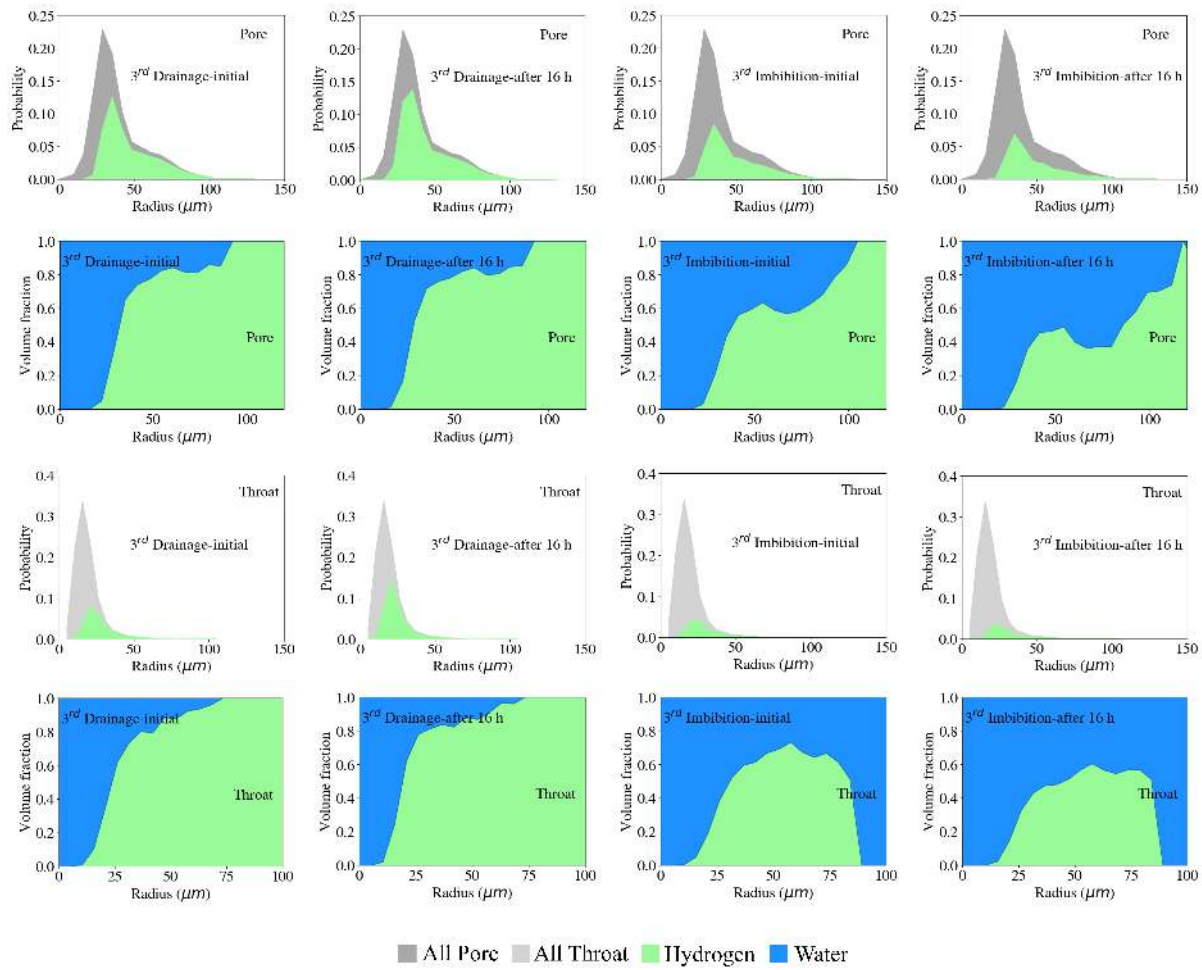


Figure C.5: Volume-weighted histograms of gas occupancy as a function of pore radius, plotted for the third cycle of gas injection following water flooding. Green indicates gas, blue indicates water, and grey represents the size distribution of all pores. Each plot corresponds to a specific cycle of injection and flooding, shown for both the initial stage and after a 16-hour storage period.

Appendix D

Pore-scale Insights into Wettability for Hydrogen Storage



D.1 Image processing

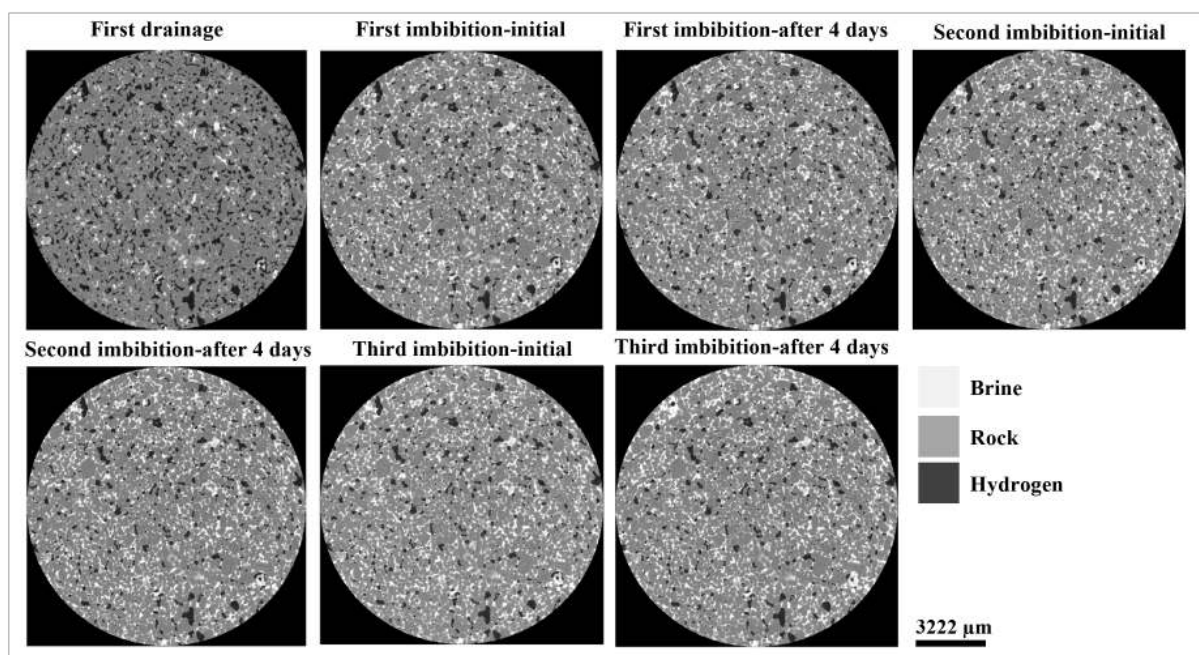


Figure D.1: Two-dimensional cross-sections of three-dimensional raw images of the Bentheimer sandstone sample showing the distribution of rock, gas and brine during three cycles of hydrogen and brine injection. The images compare initial and post-4-day stages for each cycle, with a scale bar representing 3222 μm .